Synchronous Machine Field Excitation Utilizing a Single-Phase Matrix Converter Excited Rotary Transformer

by

Jianyang Liu

A dissertation submitted in partial fulfillment of the
requirements for the degree of

Doctor of Philosophy
(Electrical Engineering)

at the
UNIVERSITY of WISCONSIN-MADISON
2018

Date of final oral examination: May 10, 2018

The dissertation is approved by the following members of the Final Oral Committee:
Thomas A. Lipo, Emeritus Professor, Electrical and Computer Engineering
Thomas M. Jahns, Professor, Electrical and Computer Engineering
Bulent Sarlioglu, Associate Professor, Engineering Professional Development
Zhenqiang Ma, Professor, Electrical and Computer Engineering
Eric L. Severson, Assistant Professor, Electrical and Computer Engineering

Abstract

This thesis introduces a Single-Phase Matrix Converter (SPMC) excited rotary transformer system to replace the Slip-Rings of traditional Would Field Synchronous Machine (WFSM). Compared to an inverter excited rotary transformer system, the matrix converter is compact due to the absence of a bulky DC Link capacitor. In this thesis, the proposed SPMC uses a new constant volt per Hz modulation method that generates a medium frequency voltage waveform to reduce the size and loss of a rotary transformer. The new modulation method maintains the flux in the rotary transformer over each switching cycle to be a nearly constant value so that the loss and the size of the rotary transformer are minimized. A new commutation strategy is also developed to ensure safe commutation of the converter switches.

A novel optimization procedure for the rotary transformer is also proposed in this thesis, which will generate a rotary transformer with both minimum power loss and minimum weight while also keeping its leakage inductance at a minimum level.

The simulation results for the proposed excitation system are discussed and a hardware prototype of the same system is also built to verify the simulated results.

Acknowledgement

First and foremost, I would like to express my sincere and deepest gratitude to my Ph.D. advisor, Professor Thomas Lipo, for his full support and patient guidance on my research work. I will not move forward without his encouragement and passion.

I would also like to thank my official UW advisor, Professor Thomas Jahns, all my committee and WEMPEC faculty members, Professor Zhenqiang Ma, Professor Bulent Sarlioglu, Professor Eric Severson and Professor Giri Venkataramanan, for their patience and suggestions on my research.

I would also like to thank for the help I obtained from all my WEMPEC friends, especially Hao Jiang, on the help of my hardware set up.

Lastly, I would like to thank my parents for all these years' understanding. Without their kindness and spiritual and financial support, I would not be where I was today.

Table of Contents

Chapter 1

Chapter 2

Chapter 3

Chapter 4

Chapter 7

List of Figures

List of Tables

Chapter 1

INTRODUCTION AND STATE-OF-ART-REVIEW

1.1 Introduction

Since the price for rare earth metal is increasing drastically recently, the motor industry is beginning to look for a good substitution for permanent magnet machines. Wound field synchronous machine(WFSM) is a promising alternative because both permanent magnet machines and WFSM belong to the synchronous machine categories, and there is no need to use rare earth metal to construct a WFSM [1]. However, there are some problems that constrain the using of the WFSM. One of the most critical issues is the use of slip rings for WFSM which increases the maintenance requirement.

In this research project, a method of using a single phase matrix converter with a rotary transformer as a substitution for slip rings is proposed. As in the matrix converter family the bulky capacitor is not needed, the system is not only efficient but compact.

1.2 Brushes and slip-rings exciter

1.2.1 Introduction to brushes and slip-rings

Brushes and slip-rings systems are widely used in industry for transferring power from a stationary part to a rotary part. The applications of brushes and slip-rings include wound field synchronous machines, wound field DC machine, double fed induction machines[2], sealing rollers, satellites and so on.

A typical brush and slip-rings system is shown in Fig 1.1[2] and Fig 1.2[3]. The brushes are a stationary portion excited by a voltage source through two cables. They act as an interface with the slip-rings to deliver power from the stationary portion of the machine to the rotary part. Slip-rings are rotary components mounted on the shaft which rotates along with the rotor of a wound field synchronous machine or the rotor of a double fed induction machine or other type of rotary components.

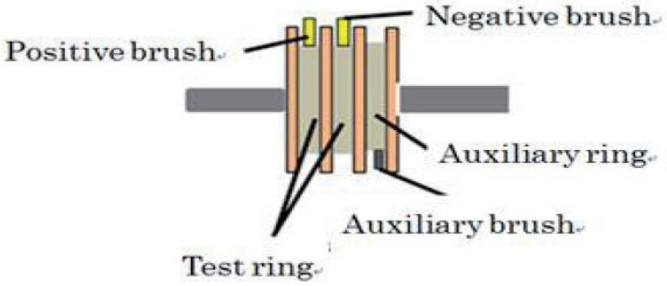

Figure 1.1. Typical brush and slip-ring system [2]

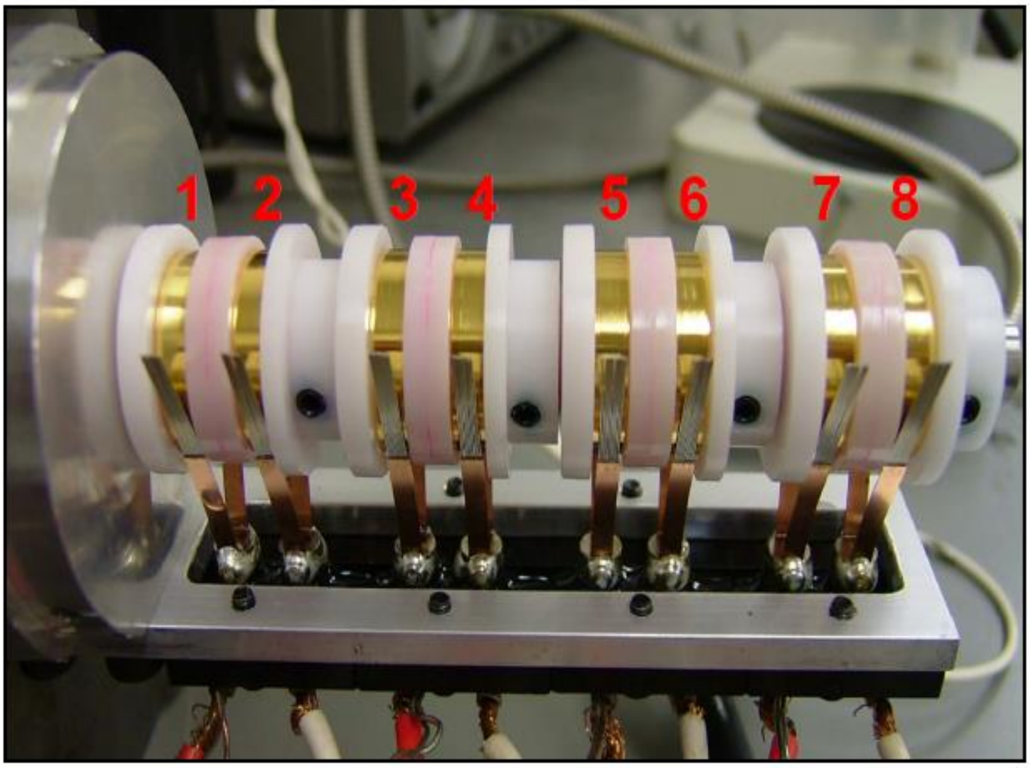

Figure 1.2. Slip-rings and brush system [3]

1.2.2 Static exciter system

Since the field winding of a wound field synchronous machine is generally mounted on the rotor side, brushes and slip rings are commonly used to supply the field current. The so-called static exciter system is a type of this brush and slip-ring system. The system structure is shown is Figure 1.3[4]. Transformers are used to step down the ac input voltage and connected to the controlled rectifier bridge, which is used to adjust the field current of the main wound field synchronous machine from the stator side. The output of the controlled rectifier bridge is then connected to the brush and slip rings to supply the rotor side current. Since the vibration of the large synchronous machine may cause failure of the brushless exciter, most of the applications for the static exciters are on large generators. For small machines, a dc source like a battery is directly connected to the brushes and slip ring system to supply the field current, while the regulation of the field current can be done by a chopper circuit.

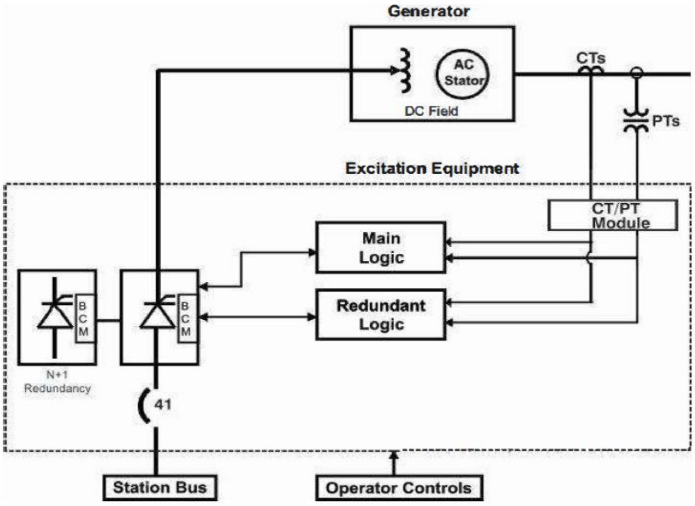

Figure 1.3. Static exciter system for a large machine[4]

1.2.3 Brush and slip-rings system summary

There are several advantages of this system. First, no power converter is needed since the voltage seen from the rotor and stator is the same, which means the overall system efficiency is high. Second, the voltage applied to the stator will be the same as the voltage applied on the rotor, so the response time for this system is fast. Third, system structure is simple, and cost is low.

However, the degradation process of the slip ring and the maintenance of brushes significantly reduce the reliability of the system [2, 3, 5]. Even with the lubricant, the life time for this kind of system is still short (1000-7000 hours)[3]. The use of gold material for slip-rings and brushes can reduce the resistance of the slip-rings and brushes and thus can increase the overall system efficiency, and also increase the reliability of the system [2], but lubricant is still required and the cost for this system remains high.

1.3 Traditional brushless exciter

1.3.1 Traditional three-stage brushless exciter

Among the types of brushless excitation system, the most common one in industry is the brushless exciter, having a small synchronous machine with field winding in stator and armature winding in rotor. Compared to the brush and slip-ring system, this brushless exciter system has the advantages of increased reliability[6] and reduced maintenance requirement[7].

The overall system structure is shown in Fig 1.3[8]. This kind of excitation system is also called a three-stage system because the current must build up in the field winding of the exciter stator to produce armature current in the rotor, and the armature current is then rectified to supply the main wound field synchronous machine’s field current.

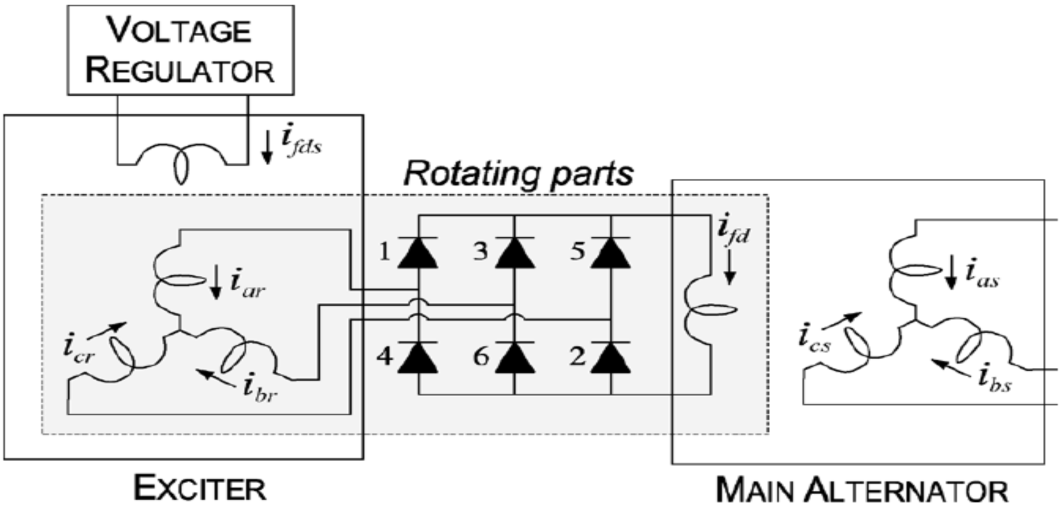

Figure 1.4. Three stage brushless exciter system[8]

There are several disadvantages of the three-stage brushless exciter system [9]. First, to supply the power to the field winding of the exciter, a battery or a DC Link system is still needed. Second, owing to the inductance of the exciter field winding, it takes time for the flux to build up in the exciter rotor winding. This extra stage will delay the overall system response time.

1.3.2 Two-stage exciter with permanent magnets

Researchers have developed a two-stage system to reduce the response time of the stator field winding [9-14]. In comparison with the three-stage system, permanent magnets are embedded in the exciters stator as a substitution for the exciter stator field winding. A hybrid topology with both stator field winding and permanent magnets is also proposed by some researchers [9, 14], where magnetic flux created by the magnets will induce a voltage on the rotor at low speed to supply the main rotor's field current. At the rated speed operation, the exciter stator field winding will be used to provide the magnetics flux. Fig 1.5 shows the hybrid exciter system for 3 Kw wound field synchronous machine.

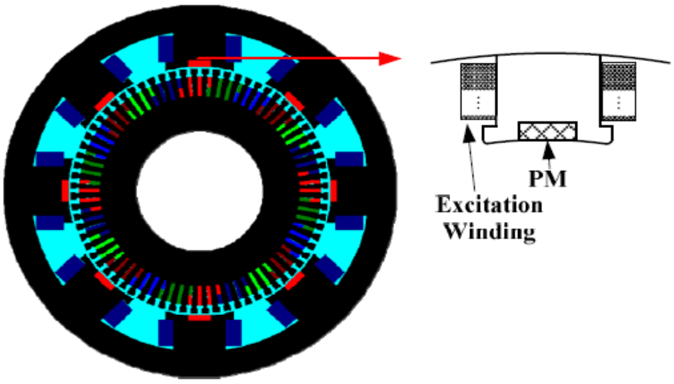

Figure 1.5. Hybrid brushless exciter [14]

For large wound field synchronous machines (mining or aircraft application), due to the MW power level of the main machine (generator), a pre-exciter is added to excite the main exciter [10]. The so-called pre-exciter in fact is a small permanent magnet generator, which provides the field power to the main exciter from its stationary armature winding. A chopper circuit is also connected to the main exciter to control the main exciter’s field current. Since the system becomes more complex for larger wound field synchronous machine, people in industry even begin to change the brushless system to main field static exciter system[4] recently. The overall system structure is shown in Fig.1.6.

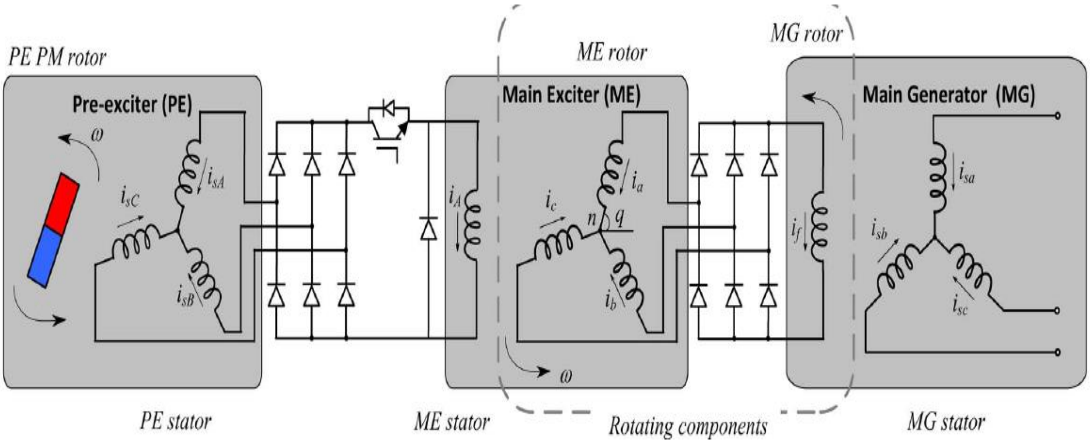

Figure 1.6. 0.2MW aircraft generator system [10]

1.3.3 Poly-phase exciter system

Poly-phase exciter systems have also been proposed to increase the performance of the overall system [15, 16]. An eleven phase brushless exciter was proposed by Xiaochuan Jia[15]. The advantages of the multiphase system include less output voltage ripples, small voltage and current harmonics, lower voltage rating device, fast system response, and low winding insulation voltage. The system structure is shown in Figure 1.7. And the advantages of the multiphase exciter system were also verified in [16].

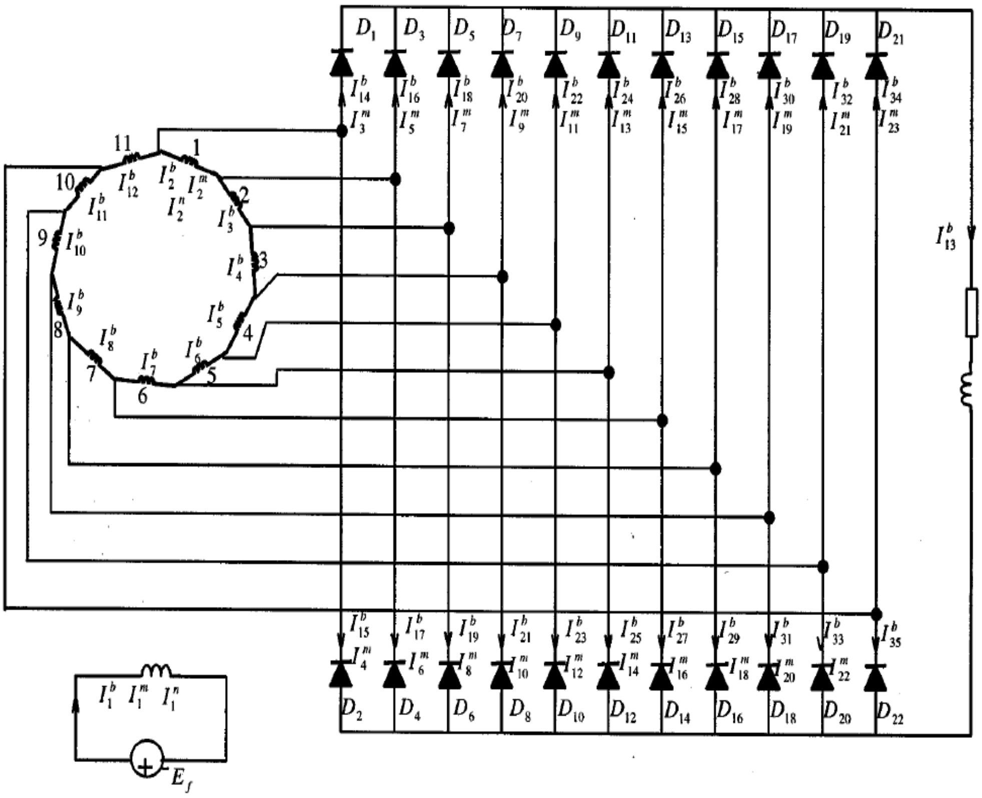

Figure 1.7. Eleven phase brushless exciter system[15]

1.3.4 Regulation of brushless excitation system

Regulation of the main field winding current is always an important part for wound field synchronous machines [17-19]. Passive rotary diode bridges are the most common rectifier bridges for brushless excitation, for it is difficult to directly control the elements in a rotating part. However, this kind of system has a slow dynamic response compared to a controlled rectifier bridge. Thus, researchers have also begun to use thyristor[20] or transistor[21] as an active rectifier. A typical thyristor based topology and a transistor based topology are shown is Fig 1.8. In order to control the active switches on the rotating part, wireless communication such as Bluetooth[22] and opto-coupler is used, but these approaches make the system more complex, and the delay of the wireless communication can create a fault for the active switch, so synchronization of the active rectifier bridge is another issue which needs to be considered.

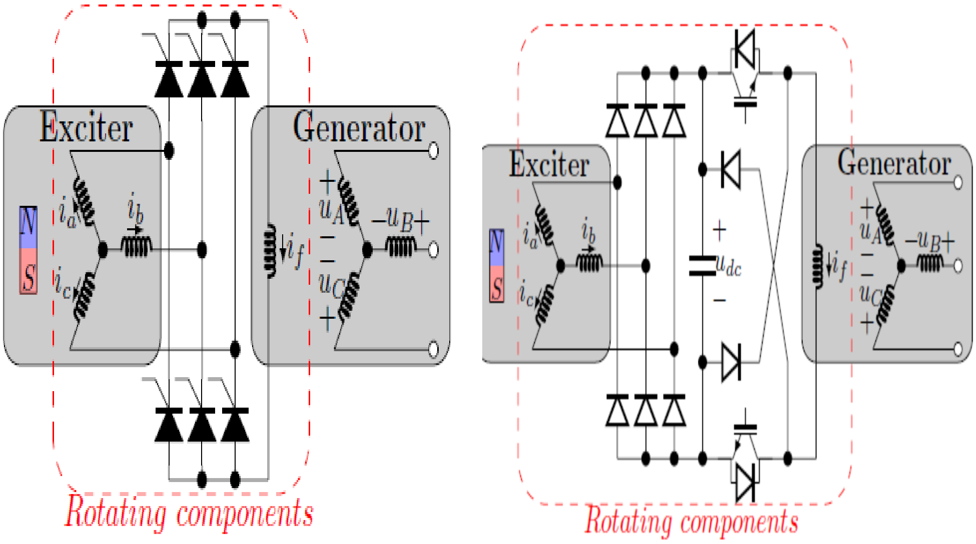

Figure 1.8. Thyristor and transistor based rectifier bridge[17]

The control and the model for the brushless exiter with the main wound field machine were designed in [18, 19]. Fig 1.9. shows the control diagram for the three stage system. Besides an innner control loop for field current and an outer control loop for output voltage, a feed-forward loop was also created for the d-axis current to compensate the load disturbance. Better damping stability, dynamics and more uniform response have been obtained by this control method.[19]

During the generating mode of the wound field synchrnous machine, a short circuit of the main stator winding can create serious problems. Reseachers have begun to use the extra (fourth) winding in the main stator to detect the fault condition[23]. The voltage information of this fourth winding and the line to line output voltage information of the main stator winding are fed to the brushless exciter together in order to prevent this fault condition from happening. The system structure is shown in Fig 1.10.

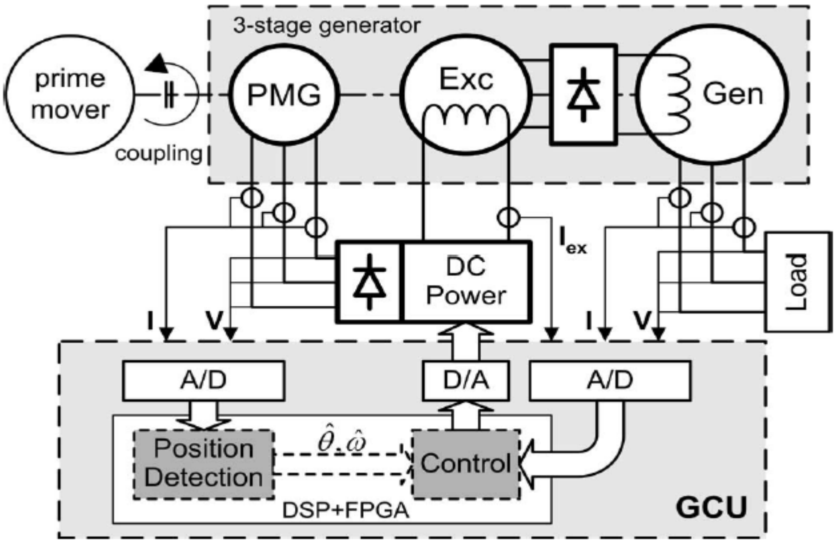

Figure 1.9. Control loop for the brushless exciter[19]

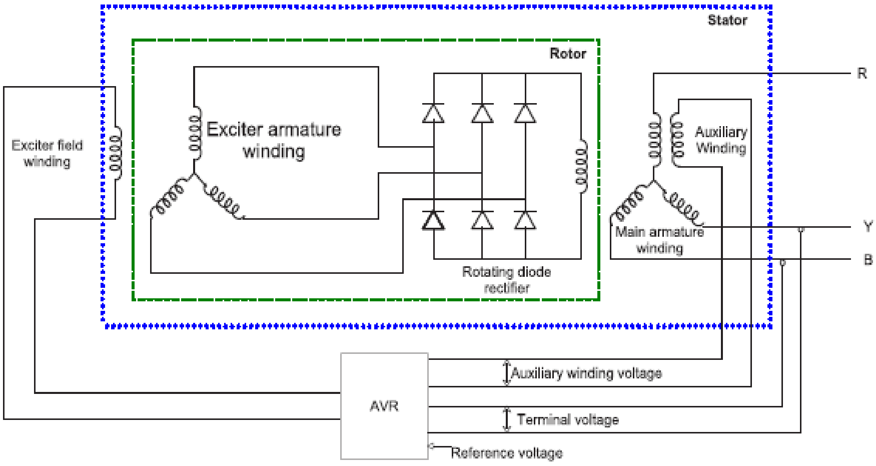

Figure 1.10. Schematic of wound field synchronous machine with auxiliary winding[23]

1.3.5 Brushless exciter system summary

Although all these kinds of brushless exciter systems are widely used in industry, there are yet many prominent defects. First, the size of these brushless exciter is much bigger than a brush and slip-ring system. Also, the power density is much smaller. For a 255 Watts brushless exciter, the weight is normally over 10 pounds only for the stator portion. Second, the cost for the brushless system is also higher than a brush and slip-ring system, if self-excited permanent magnet material is taken into consideration, whose cost is even higher. Third, due to the extra power conversion stages (at least two and sometime three), power loss is also higher than that of a slip-ring system. Lastly, the exciter frequency is speed dependent, which makes it impossible to utilize for high speed application like traction drive.

1.4 Additional rotor winding exciter

1.4.1 Additional rotor winding exciter overview

Since the traditional brushless exciter needs extra space and length on the shaft and makes the overall system structure more complex, researches begin to look for substitution for the traditional brushless exciter system [24-31].

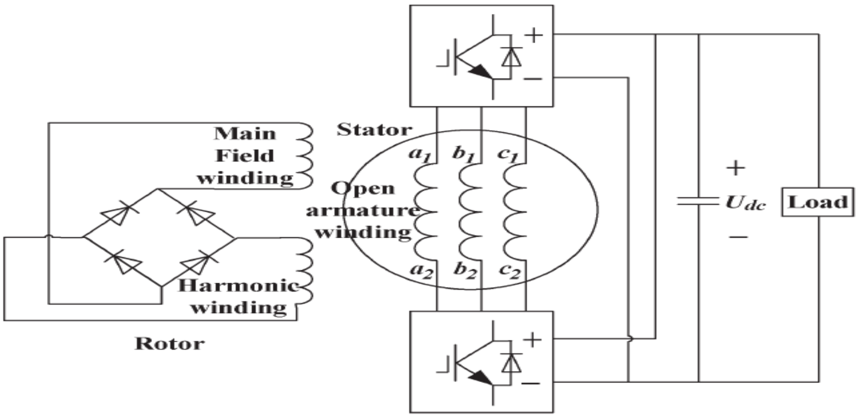

Figure 1.11. Typical structure of an additional rotor winding exciter [28]

A third harmonics current injection method is proposed in [24, 28, 30]. In these research project, they used the same inverter for the stator winding to generate a third harmonic current to induce a back EMF in the additional rotor winding. The induced back EMF in the additional rotor winding is then rectified by the rotary diode bridge to supply the dc current for the main field winding. A typical system structure of this kind of system is shown in Fig 1.11. Machine structure with the additional winding is shown in Fig 1.12., and researches have concluded that a 4 poles, 18 slots, pitch of 4 structure is best for this kind of brushless excitation method[30].

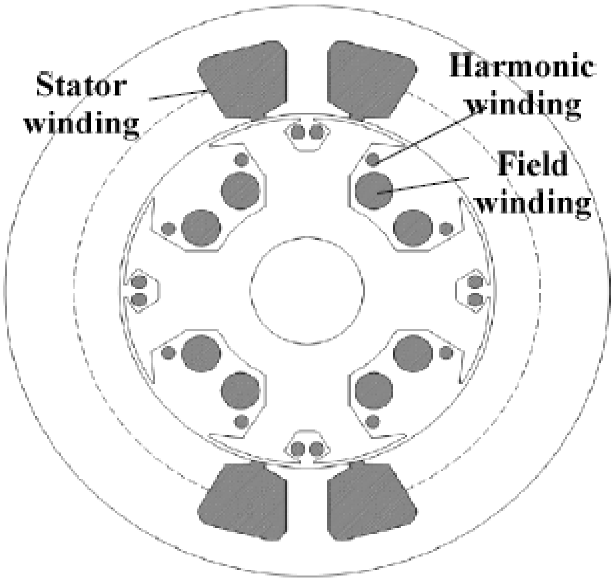

Figure 1.12. Machine structure with additional rotor winding[30]

However, by using this kind of excitation system, the power requirement for the inverter will also increase since the inverter must provide power to both armature and field winding, and the initial magnetic field of the machine is difficult to build up [27]. Thus, another topology with additional stator winding to excite the additional rotor winding is also proposed to reduce the stress of the main inverter [27]. The system structure is shown in Figure 1.13.

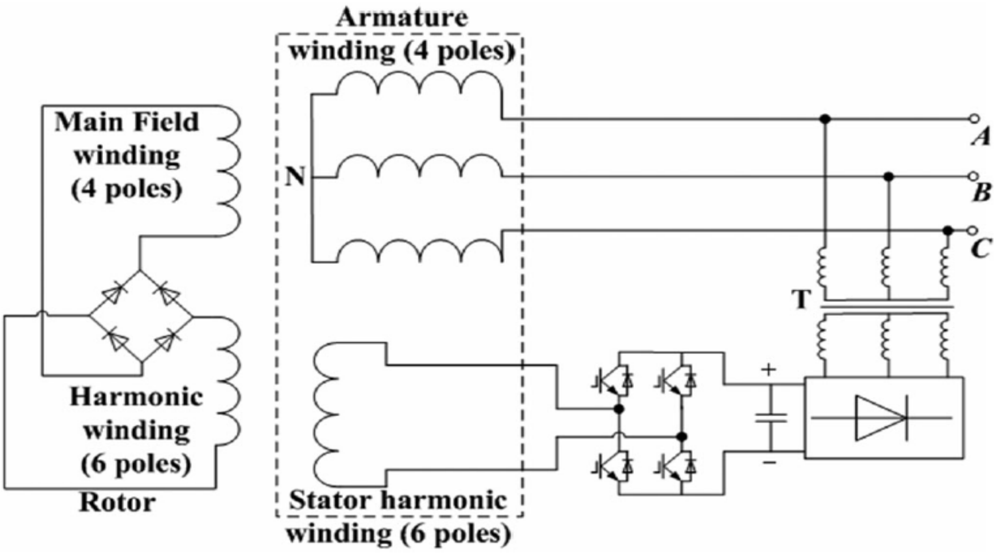

Figure 1.13. Machine structure with additional stator winding [27]

Thyristors can also be used to generate the third order harmonic current in the stator winding.[26]. The system structure is shown in Fig 1.14. Fig 1.15 (a) shows the input three phase current to the stator winding and Fig 1.15 (b) shows the zero-sequence current of the neutral point. This zero-sequence third harmonic current will then be used to induce the back EMF in the additional rotor winding. The additional rotor winding will supply the power of main field winding through the rotary diode bridge.

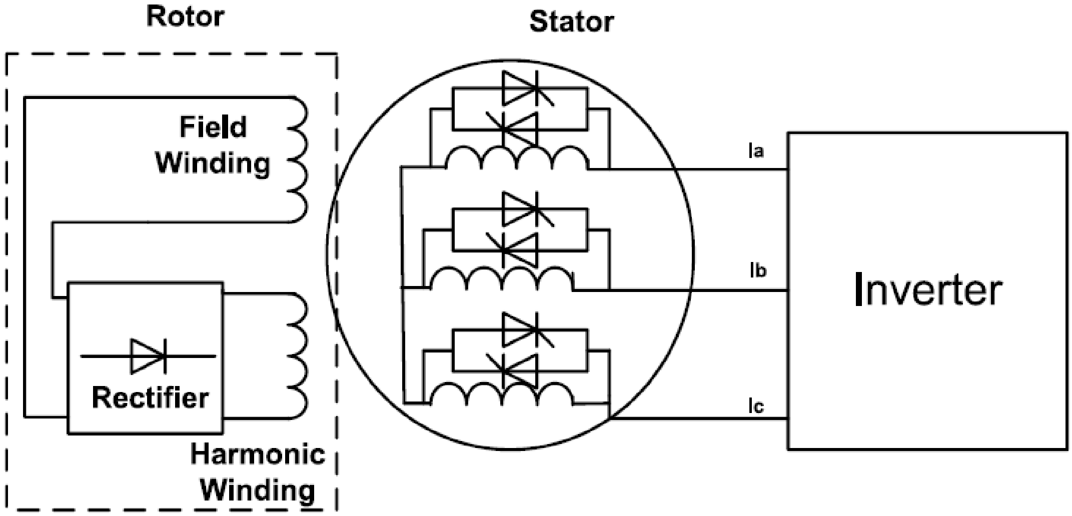

Figure 1.14. Machine structure with additional stator winding [26]

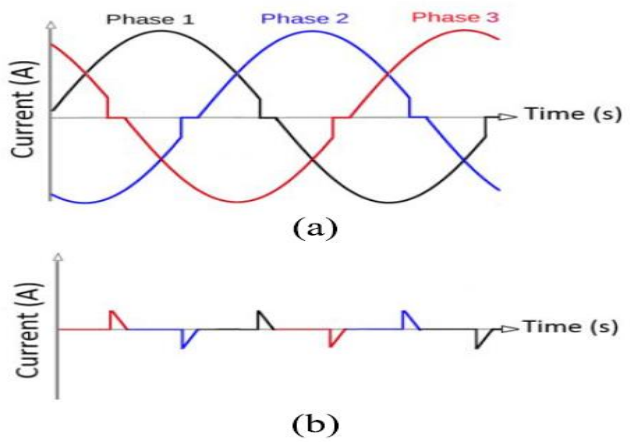

Figure 1.15 (a) Three phase current. (b) zero-sequence current of the neutral [26]

In addition to this third or higher order harmonics current injection method, a subharmonic excitation method has been proposed[31]. In this system, the stator winding is divided into two parts, where two separate inverters supply part of the input current and the unbalance of the inverter current in magnitude generates the subharmonic MMF in the stator, which will create an EMF in the additional rotor winding for main field excitation shown in Fig.1.16.

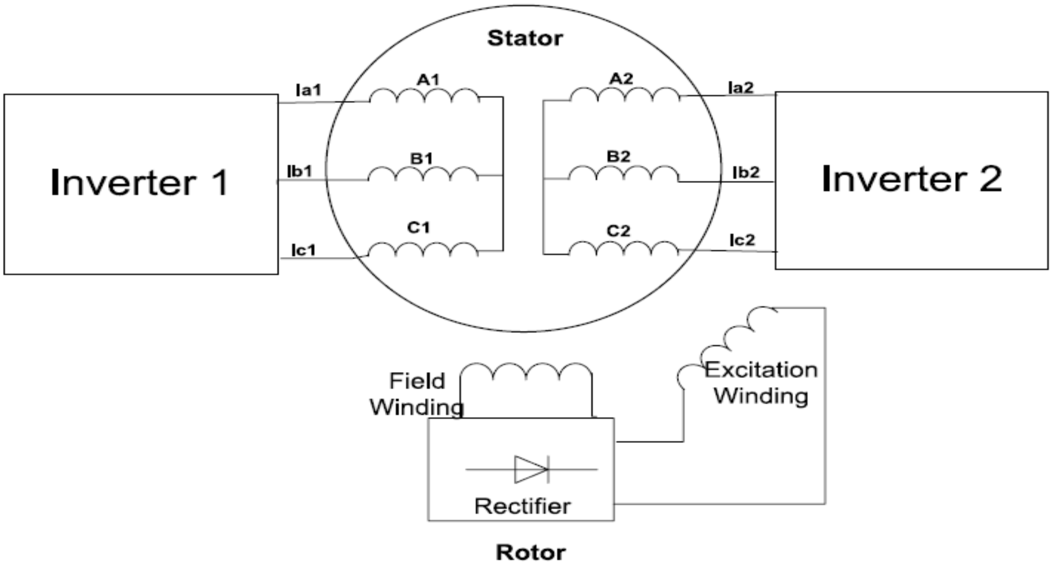

Figure 1.16. Subharmonics excitation system structure[31]

1.4.2 Additional rotor winding exciter summary

Additional rotor winding exciter does offer some great advantages like reducing the total system volume, simple system structure and the decrease of the shaft length, but the application may also be limited since the motor structure needs to be reconfigured based on this approach. Moreover, the additional windings on the rotor also consume additional space in the rotor, which could reduce the power density of the overall system.

1.5 Capacitor coupling brushless exciter

1.5.1 Capacitive brushless exciter

The application of capacitive coupling on a wound field synchronous machine excitation is a relatively new idea [32, 33]. Instead of suppling the field power inductively like a traditional brushless exciter, this system uses rotary capacitors to supply the field power. The system structure is shown in Fig 1.17.

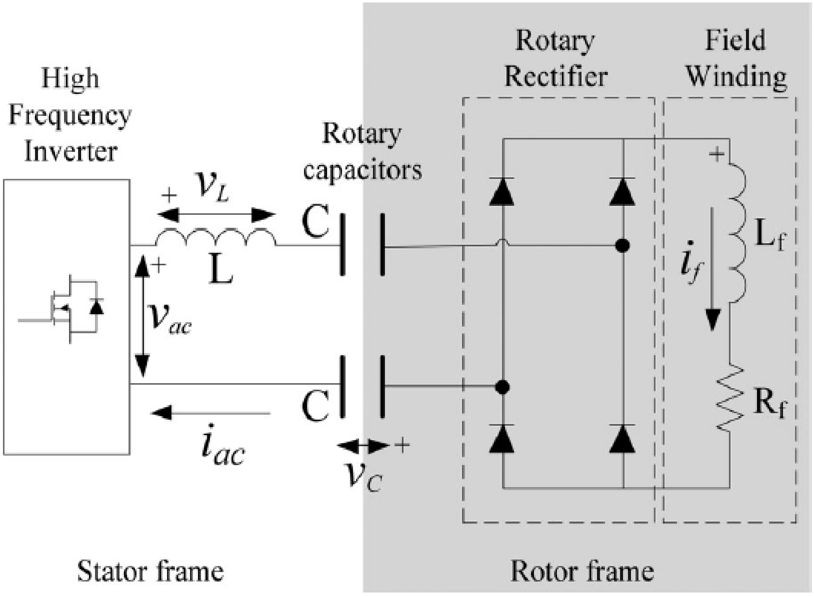

Figure 1.17. Capacitive brushless exciter system structure [32]

For the above system, an inverter generates the high frequency ac output to reduce the size of the resonant LC tank. Capacitors in LC tank is composed of a stationary part and a rotary part mounted on the shaft along with the main rotor, which is shown in Fig.1.18. The output of this LC tank will be connected to the rotary diode bridge thus to supply the dc current to the main field winding. Benefits of using the capacitive brushless exciter include absence of copper winding and ferrous material within the machine. Moreover, the high mechanical integrity of physical structure makes the system applicable to high speed applications, and the cost of the system is relatively low compared to the traditional brushless exciter.

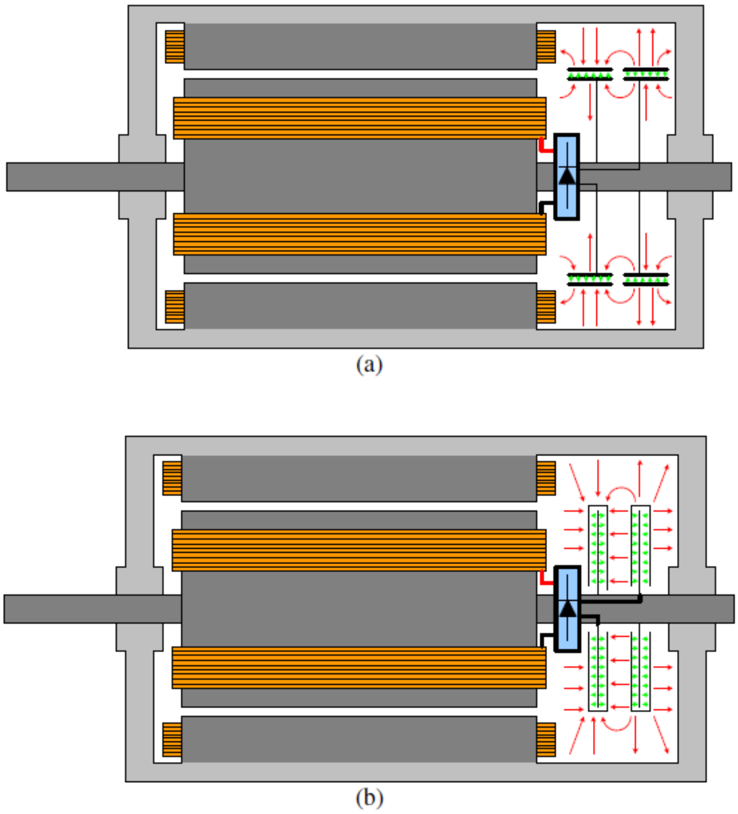

Figure 1.18. Rotary capacitors (a) concentric type (b) axial type [32]

Researchers have successfully increased the power level of the capacitive brushless exciter recently [34-36], by which 314 watts power has been delivered to the wound field synchronous machine in [36]. A comparison between the size of a traditional brushless exciter and a capacitive one is shown in Fig 1.19. Compared to a fifteen-pound of a traditional brushless exciter, the three-pound capacitive exciter is not only compact in volume but also significantly light in weight. In [34], a high-power density wound field synchronous machine is manufactured with a peak power of 80kw at rated 4000 rpm speed. The field excitation system uses an axial flux hydrodynamic capacitive power coupler, which is also a type of the capacitive brushless exciter. [35] pointed out the possibility of integrating the capacitive brushless exciter into the hydrodynamic journal bearing to further integrate the system.

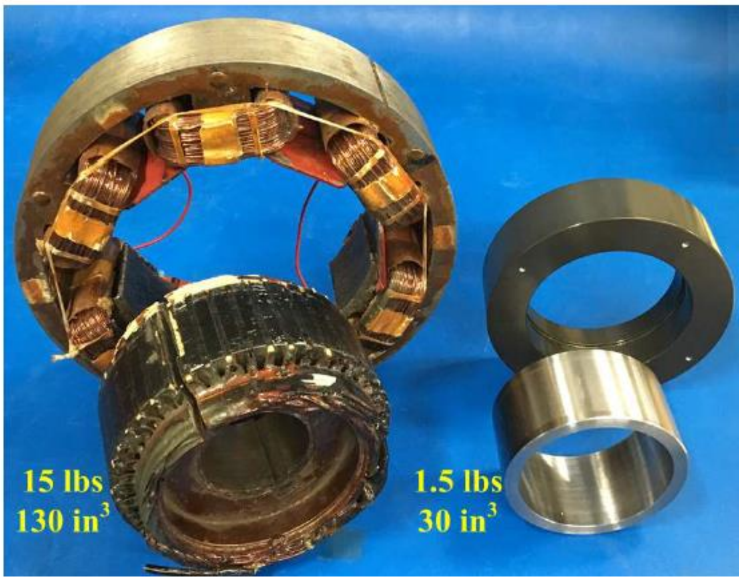

Figure 1.19. A comparison of a traditional brushless exciter with a capacitive brushless exciter [36]

1.5.2 Capacitive brushless exciter summary

Although the capacitive brushless exciter has the advantages like compact system, and being insensitive to speed, yet there are many limitations on this kind of excitation system. First, the typical airgap length between the two capacitors is less than 0.2mm, while a typical airgap length between the rotor and the stator in wound field synchronous machine is 0.5 to 1 mm. Thus, if the machine is operated in an excessive vibration environment, this could severely damage the exciter and cause system failure. Second, parasitic capacitance between the capacitor plates and chassis ground will cause the high frequency AC voltage to bypass the diode bridge, which creates additional field current ripple[33].Third, series ESR in the resonant tank reduces the overall system efficiency. Fourth, for a capacitor brushless exciter, the output current is generally less than 5 Amps because large output current charges the capacitor voltage to kilo-volts level. Not only does the insulation between the capacitor plates become a huge problem, but also the switches used in this power circuit must have higher voltage rating. More importantly, the small output current, high voltage field winding requires many more turns in the field winding thereby requiring additional space for winding insulation reducing the effectiveness of the field winding flux producing capability.

1.6 Rotary transformer based brushless exciter

1.6.1 Rotary transformer overview

Rotary transformer is another great substitution for brush and slip-ring system. Unlike the brushless exciter system, rotary transformer is not a synchronous machine but only a simple transformer system with a little airgap between the primary stator side core and secondary rotor side core. Thus, the winding structure is much simpler compared with the traditional brushless exciter system. The rotary transformer exciter system concept was proposed by Gibson[37] and was first built by Landsman in 1971[38]. At that time the application is mainly for satellites[39]. However, it was not given much attention for motor drives until recently owing to the price fluctuation of the permanent magnet~~ic~~ materials.

The general system structure for rotary transformer exciter system is shown in Fig 1.20. When an ac input source is required to supply the power for the transformer, windings from the secondary side of the transformer is connected to the rectifier bridge for delivering the DC power to the main field winding. The ac source used to excite the rotary transformer which can be either high frequency or line frequency depends on the application requirement. Medium to high frequency ac signal is preferred for compact system design but additional power electronics components will be required.

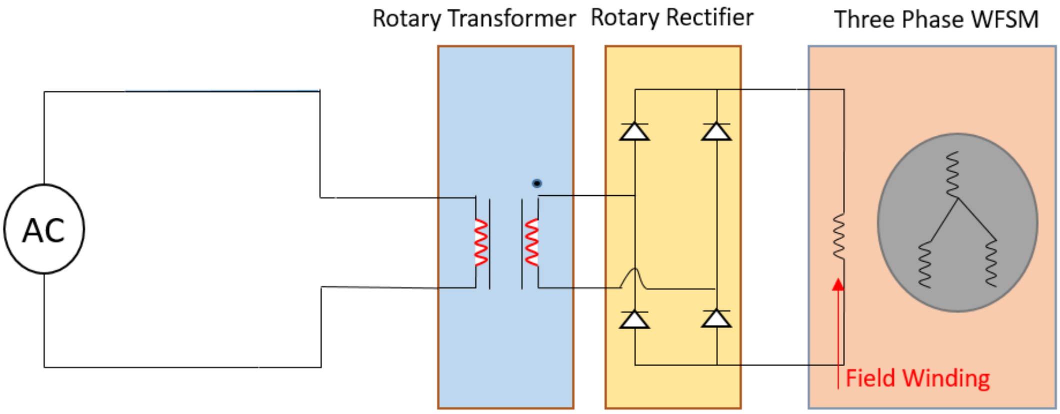

Figure 1.20. Typical system structure of a rotary transformer brushless exciter

1.6.2 Rotary transformer excitation circuit

In addition to the line frequency excitation, researchers are focusing on the inverter based excitation, the input dc source for the inverter is either a low voltage battery [40] (typical below 36 volts) or a dc link formed by the rectified input ac voltage [41]. The advantage of using battery is that no outside ac source is required, but the low voltage level means that a high input current is required to sustain the overall output power.

Owing to the large magnetizing current in the rotary transformer and this large input current resulting from the low battery voltage, the system efficiency will become a problem. A proper cooling method should also be considered in this case.

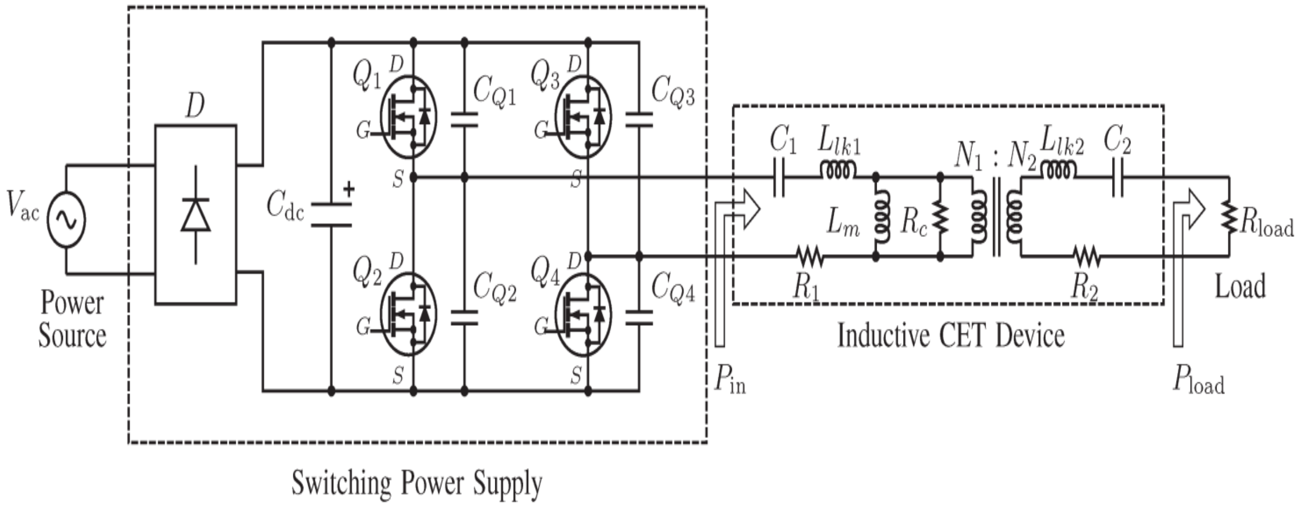

Figure 1.21. Typical system structure for an inverter based exciter system [42]

A typical ac input excitation system is shown in Fig 1.21. Input current could be much lower by using this kind of system structure in contrast with battery. The main limitation is the bulky dc link capacitors which increase the overall system size.

Series capacitors has also been added to the primary and secondary side of the transformer by some researchers in order to firm a resonant tank [40, 43, 44], since there are several benefits of using a resonant converter topology in the rotary transformer. Firstly, due to the large airgap region and the long distance between the primary and secondary side winding, a large leakage inductance exists. Resonant tank could greatly compensate this leakage inductance and improve the power transfer availability[42]. Secondly, the adding of the resonant tank will also increase the overall system power factor. Thirdly, soft switching could also be achieved by using a resonant converter. Fourthly, because a small dc bias voltage at the transformer side will saturate the transformer and create a large dc bias current, adding a LC resonant tank blocks the DC component which prevents the rotary transformer from this event.

As a resonant converter is very sensitive to the load magnitude, the adjustable load range is narrow. Second, over-current is most likely to happen in the resonant converter at start-up, which can damage the switches in the power circuit if no proper control algorithm is applied. The series capacitor will also bring additional ESR which decreases the overall efficiency. More importantly, since the current level in the capacitor is large for high power applications, the requirement for capacitor quality is extremely high compared with other applications. Lastly, the high $\frac{dv}{dt}, \frac{di}{dt}$ due to the high switching frequency will create additional stress for semiconductor power switches.

On account of the above disadvantages of resonant converters, there is another converter topology called phase-shifted full bridge inverter which can achieve the same soft switching performance without a LC resonant tank at the load side [45]. The converter structure and the soft switching waveform is shown in Fig.1.22.

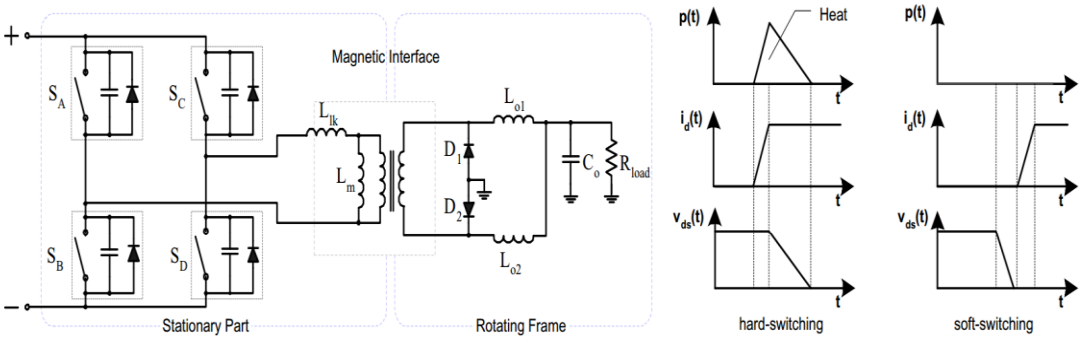

Figure 1.22. Phase-shifted full bridge converter topology with soft switching waveform [45]

Because of the system structure (large airgap) of rotary transformer, it has a large leakage inductance and poor coupling factor. This large leakage inductance with the small magnetizing inductance can be utilized by the phase-shifted converter to achieve soft switching. In contrast to traditional resonant converter topology, no extra capacitor is needed at either side of the transformer. Moreover, no inrush current caused by the LC tank will exist. Thus, no complex control algorithm is needed for this topology, which simplifies the system structure.

However, since the phase-shifted converter loses its advantage during a light load condition, another circuit topology based on the existing phase-shifted full bridge converter is presented in [46]. The system structure is shown in Fig.1.23., compared to Fig 1.22., where a chopper switch is added at the front end of the inverter to ensure the Zero Voltage Switching under every load condition. The drawback of this topology is evident, for the additional power switch not only increases total cost, but also increases the control complexity of the overall system.

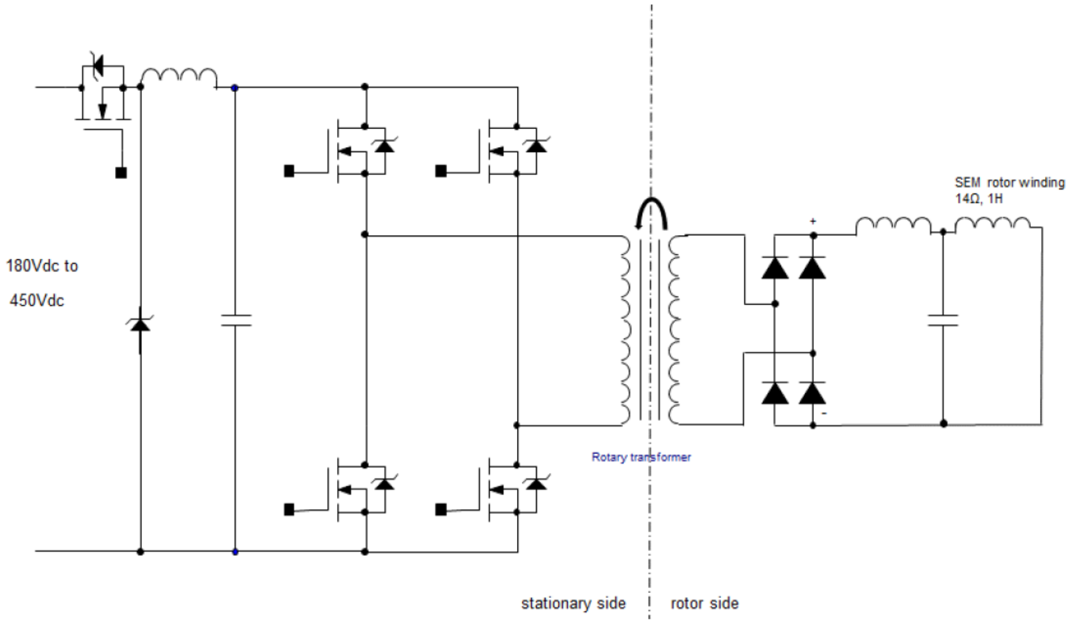

Figure 1.23. Added chopper circuit to ensure ZVS [46]

1.6.3 Material used for the rotary transformer

The two major types of the materials used for the rotary transformer are ferrite and laminated iron. Ferrite material has the merits of low volume mass density typical around 5g/cm^3, and low core loss which makes it possible to operate to MHz level. Thus the size for the ferrite material type rotary transformer is small. However, the main constraint for the ferrite material is its poor tensile strength, which will make it hard to operate on a large diameter shaft for high speed applications[47], but recently, researchers have also proposed a ferrite material rotary transformer for high speed traction application[46].

Laminated steel has both the merit of robust operation for high speed, and of the low cost. Besides these, the saturation flux density in an iron core is usually larger than 1.5 Tesla, which makes it possible to operate at line frequency. The down side of iron material is the low volume resistivity, so a lamination procedure is required for medium frequency ac input. Therefore, at certain medium frequency (around 1000Hz), the lamination cost plus the iron material cost becomes comparable to the cost of the ferrite material.

In conclusion, laminated steel is better for low frequency excited rotary transformer, while ferrite is better for high frequency rotary transformer. There are two major structures of the rotary transformer, one of which is the concentric cylinder structure, and the other of which is the pot core type structure, which will be discussed in detail at the following section.

1.6.4 Concentric cylinder type rotary transformer

The 3D structure and the cut view of the concentric cylinder type rotary transformer are shown in Figure 1.24.

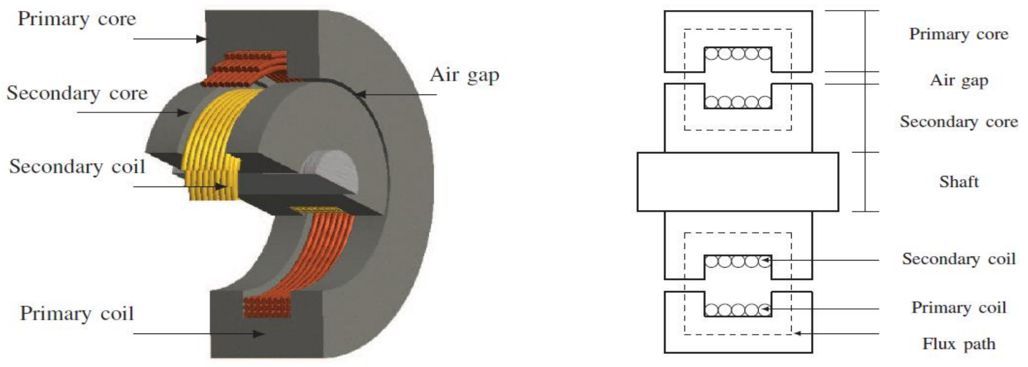

(a) (b)

Figure 1.24. (a) Concentric cylinder type rotary transformer (b) cut view [48]

Forces between the core pieces are radial symmetrical[38], so that the bearings will not be required to take the axial load. This increases the system stability in a vibration environment. In comparison with the pot core type of transformers, the other advantage is for the same number of turns, the concentric cylinder type will have a smaller radius which reduces the length of the wire. Hence, for the same amount of wire resistance, the concentric cylinder type rotary transformer can have more turns, which means more magnetizing inductance. This is very important for there is an airgap in the rotary transformer. A small magnetizing inductance means a large magnetizing current[49], which not only brings additional winding loss but also increases the overall temperature. The increase of the overall temperature will decrease the saturation flux density in the core, which may induce large inrush current, and eventually cause system failure. Since the magnetic intensity H is directly related to the magnetizing current and the magnetic density B is directly related on the applied voltage, the B-H curve for the rotary transformer with and without the airgap is presented in Fig 1.25 to show the increase of magnetizing current with airgap length. Fig 1.25 (c) also shows the magnetizing current increases more when a larger airgap is presented, compared to a smaller airgap one shown in Fig 1.24 (b).

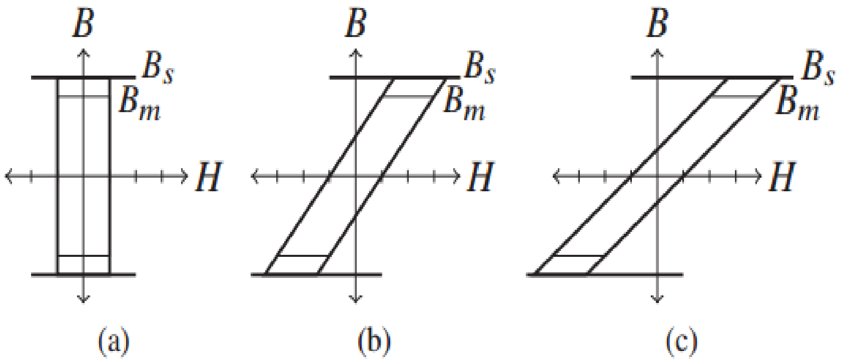

Figure 1.25. (a) No airgap (b)small airgap (c) large airgap[50]

The detailed design procedure for a ferrite based concentric cylinder type rotary transformer was first proposed by Landsman[38]. A 1.4 kW, seven-pound prototype is built with an airgap of 0.lmm with 92 percent of efficiency. Based on his model, the total power loss is 17.4 watts, but the prototype has a total loss of 112 watts. This significant difference is mainly caused by the standard gauge wire he used. In his rotary transformer system, six fourteen gauge wires are paralleled to form one turn of the wire. Since the operating frequency is 2 kilo-hertz, a high skin effect would occur in his design to increase the rotor resistance more than two times. Apart from the skin effect, the loss caused by the magnetizing current is also ignored in his design procedure which further increases the total loss in the prototype. Third, winding fill factor is not included in his model either, which further widens the gap between the theoretical power loss and the experimental result.

A silicon iron type of concentric rotary transformer is presented in [40], Table 1.1 shows the design parameter for the rotary transformer. From Table.1, the author has confirmed that the 800 watts concentric rotary transformer has a smaller size compared to the 100 watts brush and slip-ring system.

Table 1.1. Design specification for the silicon iron type of RT[40]

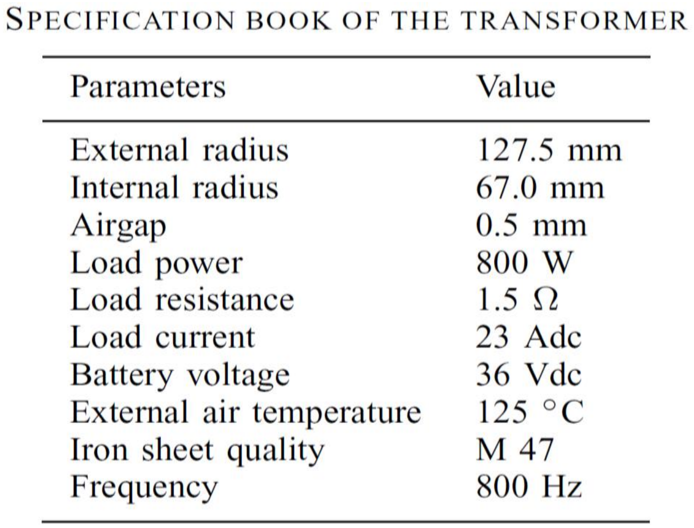

SPECIFICATION BOOK OF THE TRANSFORMER

Parameters	Value
External radius	127.5 mm
Internal radius	67.0 mm
Airgap	0.5 mm
Load power	800 W
Load resistance	1.5 Ω
Load current	23 Adc
Battery voltage	36 Vdc
External air temperature	125 °C
Iron sheet quality	M 47
Frequency	800 Hz

Table 1.2. shows the current value for the designed system. Based on Table.2, the overall rotary transformer system has an efficiency of 78 percent. Compared to the 90 percent efficiency of the brush and slip-ring system, the difference results from the large magnetizing current from the primary side of the transformer, but the efficiency can be increased by reducing power level to 100 watts. Higher efficiency can also be obtained by using a wound field synchronous machine with large field resistance.

Table 1.2. Current level for the silicon iron RT [40]

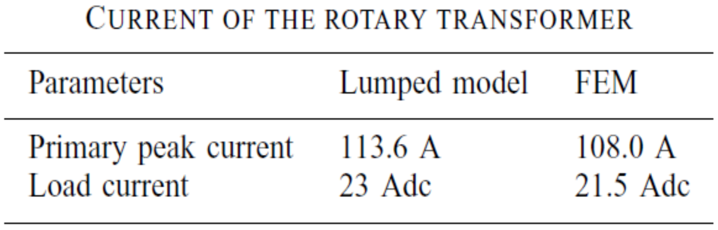

CURRENT OF THE ROTARY TRANSFORMER

Parameters	Lumped model	FEM
Primary peak current	113.6 A	108.0 A
Load current	23 Adc	21.5 Adc

A concentric rotary transformer made by radially oriented electric steel is proposed in [47]. In this paper, a segmented rotor and stator core rotary transformer are designed and manufactured. The 3d structure and the cut view of this rotary transformer is shown in Fig.1.26 and Fig.1.27. The benefit of this rotary transformer includes robustness in structure and ease in manufacture.

Figure 1.26. Concentric RT made by radially oriented electric steel [47]

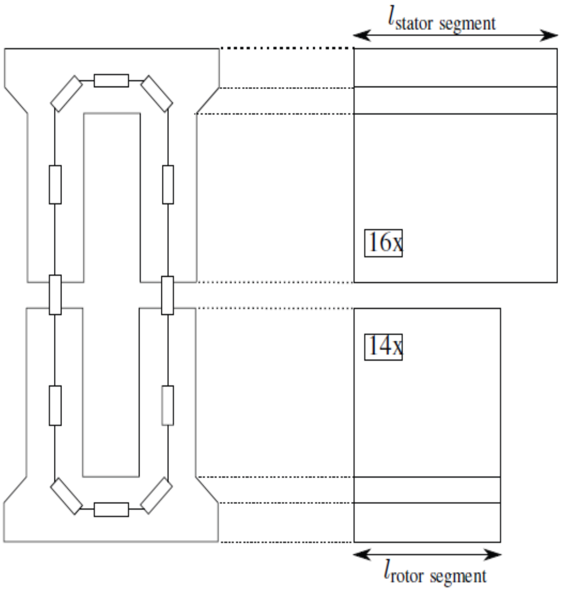

Figure 1.27. Cut view of concentric RT made by radially oriented electric steel [47]

Table 1.4 shows the prototype parameters for this segmented rotary transformer. Compared to a ferrite type, its size and weight is much bigger, but the special manufactured laminated iron makes the transformer eligible to operate at 5 kilo-hertz.

Table 1.3. Segmented RT Prototype Parameters [47]

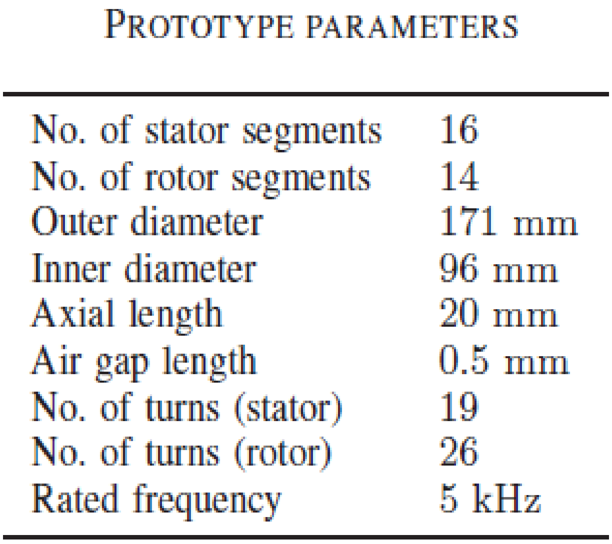

PROTOTYPE PARAMETERS

No. of stator segments	16
No. of rotor segments	14
Outer diameter	171 mm
Inner diameter	96 mm
Axial length	20 mm
Air gap length	0.5 mm
No. of turns (stator)	19
No. of turns (rotor)	26
Rated frequency	5 kHz

Table 1.4 shows the calculated inductance for this radially oriented electric steel type rotary transformer. According to table 1.4, the leakage inductance is almost 30 percent of the mutual inductance, which will create a huge voltage drop at the load side if there is no resonant tank to compensate. This is mainly due to the radically distributed winding structure and the segmentation core shape.

Table 1.4. Calculated and measured inductance value [47]

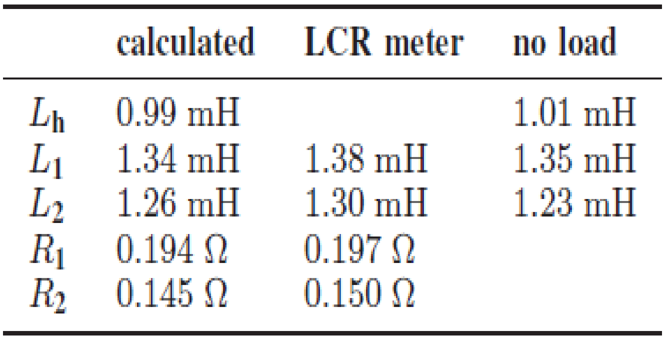

	calculated	LCR meter	no load
L_h	0.99 mH		1.01 mH
L_1	1.34 mH	1.38 mH	1.35 mH
L_2	1.26 mH	1.30 mH	1.23 mH
R_1	0.194 Ω	0.197 Ω	
R_2	0.145 Ω	0.150 Ω	

A line frequency concentric rotary transformer was built by Zietsman [48] for double fed induction machine application. Figure.1.28 shows the complete assembly of the rotary transformer in the project.

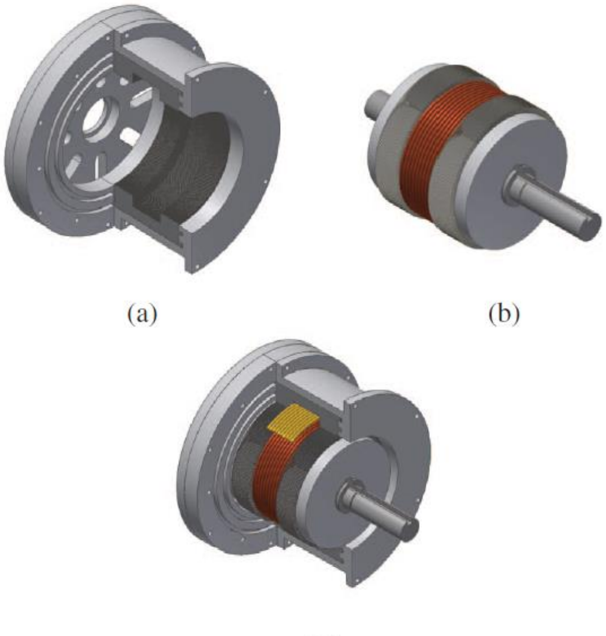
(a) (b)

(c)

Figure 1.28. Line frequency concentric RT (a) primary core assembly (b) secondary core assembly (c) overall system structure[48]

Table 1.5. Dimension of the line frequency RT[48]

DIMENSIONS OF 1.2 KVA AXIAL RT

Secondary Side			
D_{si}	50 mm	l_w	39.76 mm
D_{so}	126.04 mm	l_g	0.5 mm
d_{ws}	13.27 mm	l_1	89.27 mm
Primary Side			
D_{pi}	127.04 mm	D_{po}	169.66 mm
d_{wp}	13.27 mm		

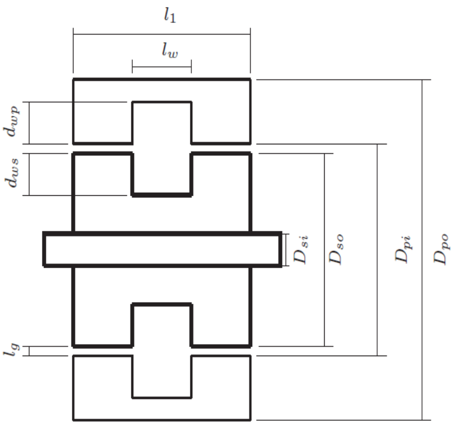

Table 1.5 shows the dimensions of this line frequency rotary transformer. Because of the low 60 Hertz line frequency, the transformer size is much larger than the previous

one; but this rotary transformer has an advantage that no power electronics is required. There are several other reseachers also pointing out the possibility of replacing the brush and slip-ring system in double fed induction machine system [51, 52]. However, because of the low line frequency characteristics, the size of the transformer is much bigger than that of the medium to high frequency excited rotary transformer.

Among concentric cylinder type rotary transformers, there are several topologies that share the same design principle of the conentric cylinder rotary transformer. Fig.1.29. shows a rotary transformer with a small rotor part proposed by Studer and Paulkovich [53]. The advantage of this structure is mainly on the mechanical side, for it reduces the axial force on the bearing and the size of the rotor core. However, because the transformer has a larger radial length, the flux density in the radial direction is not so evenly distributed that core material is not fully utilized, which increases the overall size and creates additional loss in the winding.

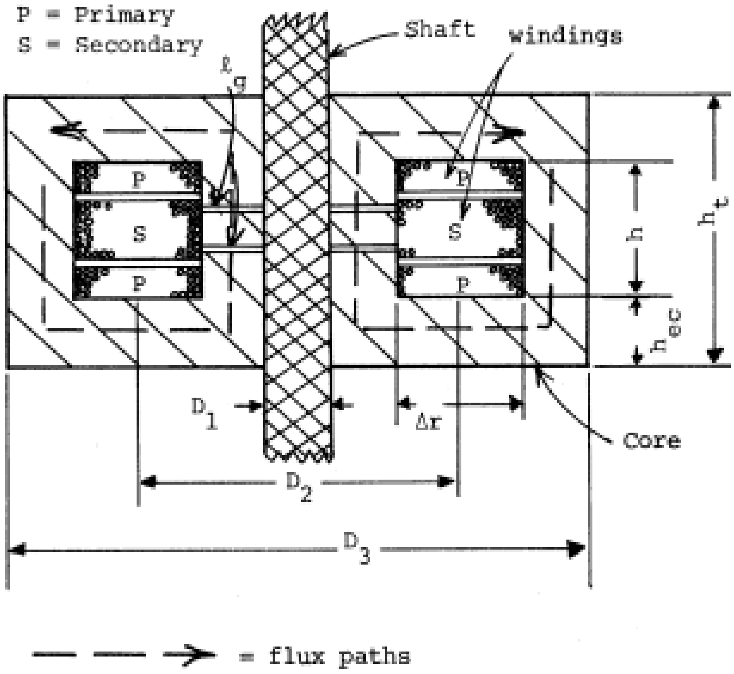

Figure 1.29. Studer and Paulkovich concentric rotary transformer [53]

An L type rotary transformer is another attractive structure. In [43], the L type rotary transformer is directly mounted on the ball bearings as an integrated system. Figure.1.30. shows 3D structure of this kind of system. In this research project, litz wire was used to reduce the high frequency resistance of winding and an output power of 20W was achieved by using resonant converter topology.

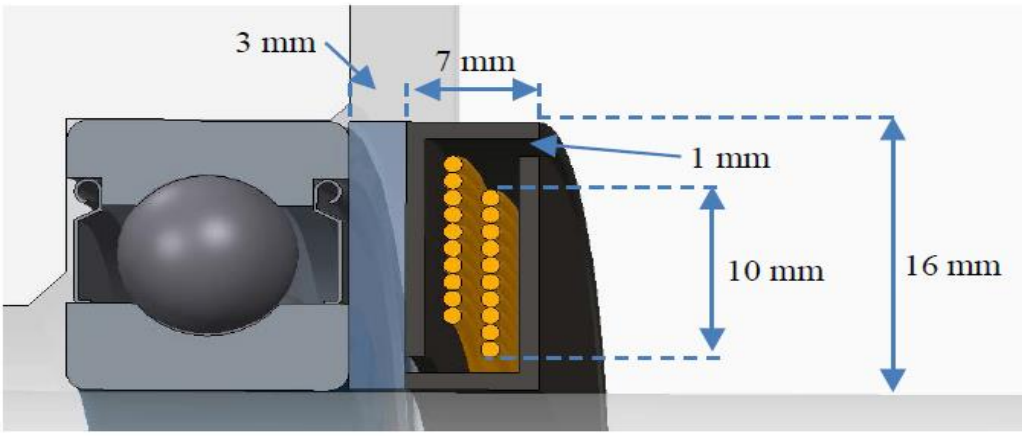

Figure 1.30. Integrated L type RT with ball bearing [43]

High power L shape transformer is also prototyped by H. Krupp and A. Mertens[44, 54] shown in Figure 1.31, where the transformer had a rating of 400 watts continuous power at 100 ◦C (212 ◦F). Since the designed L shape transformer is operated at a high frequency range (100-1000 kilo-hertz), the skin and proximity loss on the winding will be the dominant loss term. They also proposed a general semi-analytical loss model for the rotary transformer with different structures on those papers, which can predict the winding loss caused by high frequency harmonics components from several finite element method simulation results. In addition, they also introduced a displacement factor to their model, in which shaft displacement at extreme condition was also considered.

There are also some limitations in their model. First, the core geometric has to be previously determined before the model is set. Second, the model assumes the magnetizing current only flows through the primary winding, but this is not accurate when zero state is introduced. Third, the model only applies to the flat copper winding, hence the use of standard gauge round wire is not mentioned in these papers.

Figure 1.31. 400 watts L type rotary transformer [54]

1.6.5 Pot core type rotary transformer

Figure. 1.32 shows a typical pot core type rotary transformer. In comparison with the axial distributed winding in the concentric cylinder structure, generally, the pot core transformer has a winding distribution in the radial direction [55]. The radial direction distributed winding has a significant disadvantage of large leakage inductance, but some applications can use it to achieve soft switching as previously discussed [45, 46, 56]. Additionally, the radial distributed winding reduces the axial (shaft) length of the transformer, which will benefit some applications that have a strong requirement for the short shaft length.

Ease in manufacture is the most attractive feature of using the pot core type rotary transformer. Compared to the manufacture of concentric rotary transformer which needs extra grounding work, when the output power of the pot core transformer is set, one can easily get the corresponding ferrite pot core from the market. The other advantage of the pot core type rotary transformer is its rotational symmetry, but bearings have to take axial load, which reduces its performance in harsh vibrational environment.

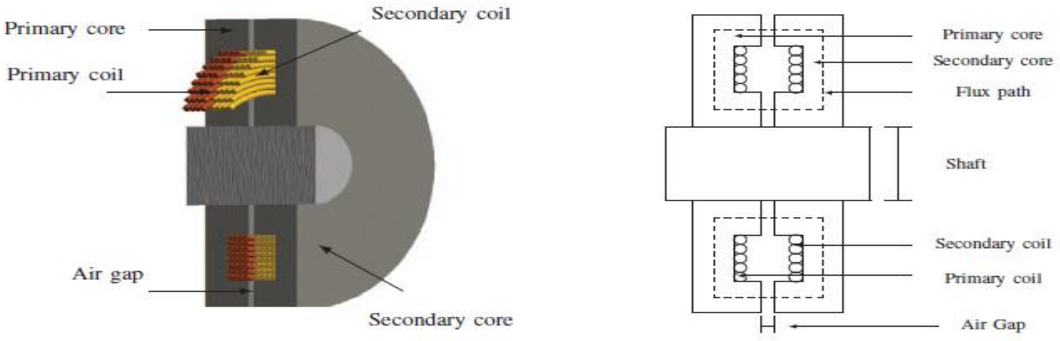

(a) (b)

Figure 1.32. (a) Pot core type transformer (b) cut view [48]

In order to reduce the effect of the larger leakage inductance resulting from the radial distributed winding, a co-axial winding arrangement for the pot core type of transformer is proposed in [45, 57, 58]. Fig 1.33 shows the traditional adjacent winding structure and Fig 1.34 shows proposed co-axial winding structure. The proposed co-axial winding structure which could greatly reduce the winding leakage inductance is shown in Fig 1.35.

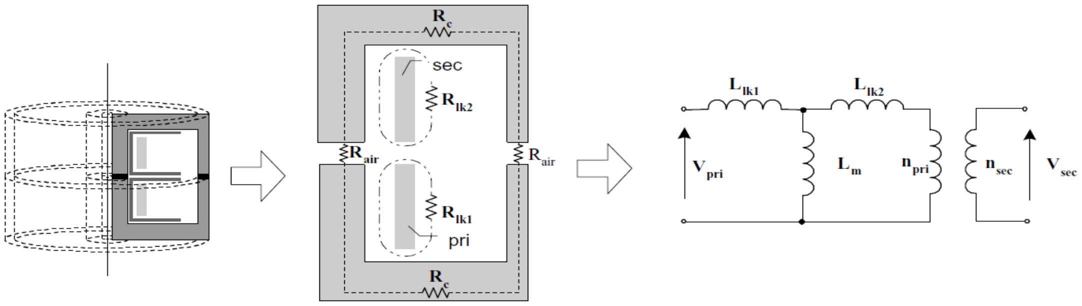

Figure 1.33. Adjacent winding for pot core type RT [45]

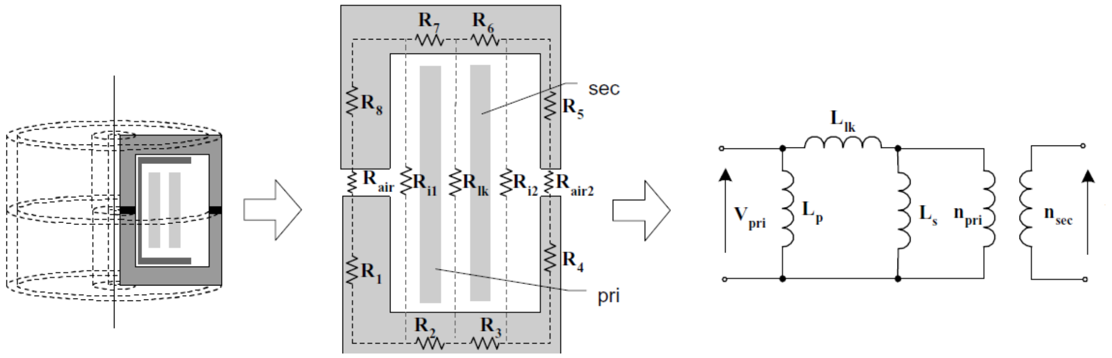

Figure 1.34. Co-axial winding for pot core type RT [45]

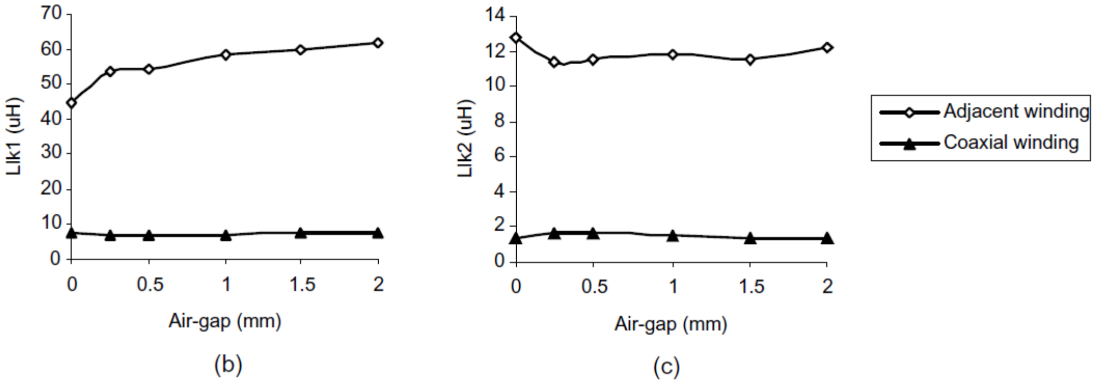

Figure 1.35 Leakage inductance comparison between adjacent winding and co-axial winding [45]

A one thousand watt prototype is built from the proposed co-axial winding topology with a total loss of a hundred watts. The total loss could be reduced by increasing the winding area but due to the pot core type structure the leakage inductance will also be increased. Another pot core type rotary transformer system based on the same converter topology is realized by a group of researcher at General Motors[46]. In this research project, a 5.1 kW pot core transformer prototype was built with an efficiency of 92 percent. Printed circuit board winding was used in this transformer to supply the field power, and the prototype was tested on a wound field synchronous machine for hybrid vehicle traction drive successfully.

Owing to the fragile properties of ferrite material, it is not applicable to high speed operation due to the high mechanical stress. Researchers have proposed a pot core type transformer with new structure in [59]. Figure 1.36 (a) shows the prototype of the proposed system and Figure 1.36 (b) shows the cut view and the overall system structure. A 200W 70 kHz, 60,000 RPM prototype is realized in this paper, while the main constraint to this structure is the additional airgap by the rotor that will create a large magnetizing current which could significantly reduce efficiency.

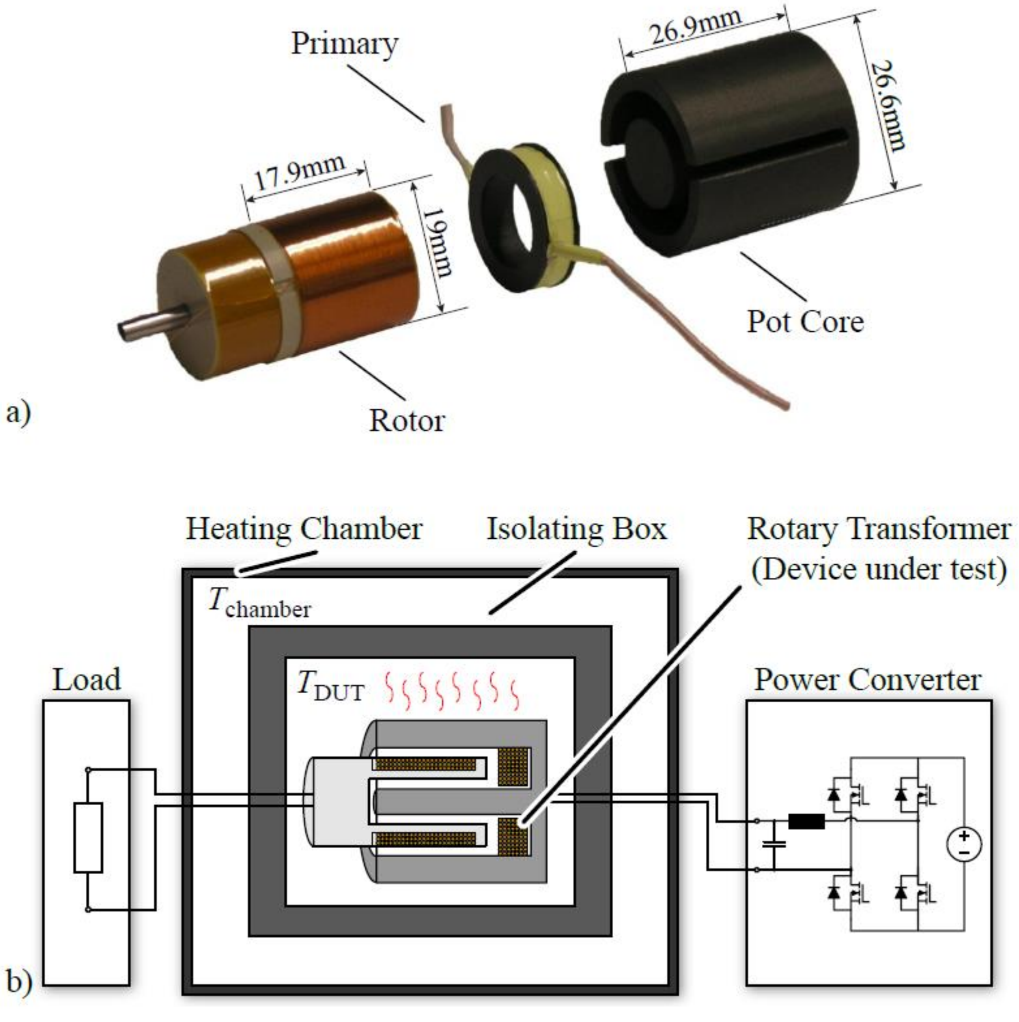

Figure 1.36. (a) Rotor side plastic material pot core rotary transformer prototype (b) cut view of the RT and overall system structure[59]

In addition to the specially designed rotor part, they also compared two different winding structures in order to increase the magnetic coupling factor [60]. Fig.1.37 shows the proposed different winding structure. From Table 1.6, it could be concluded that compared to the type one winding structure, type two winding structure has a better magnetic coupling factor, but the manufacture cost for type two is also higher than type one on account of an additional stator core. Moreover, due to the better magnetic coupling in type two, it also has a larger magnetizing inductance which reduces the magnetizing current and the total loss. However, the lower coupling factor in type one winding could be compensated by adding a series capacitor. In short, type one structure is better for industry application where total cost is a key factor and type two structure is better for a system which needs higher efficiency and better magnetic coupling factor.

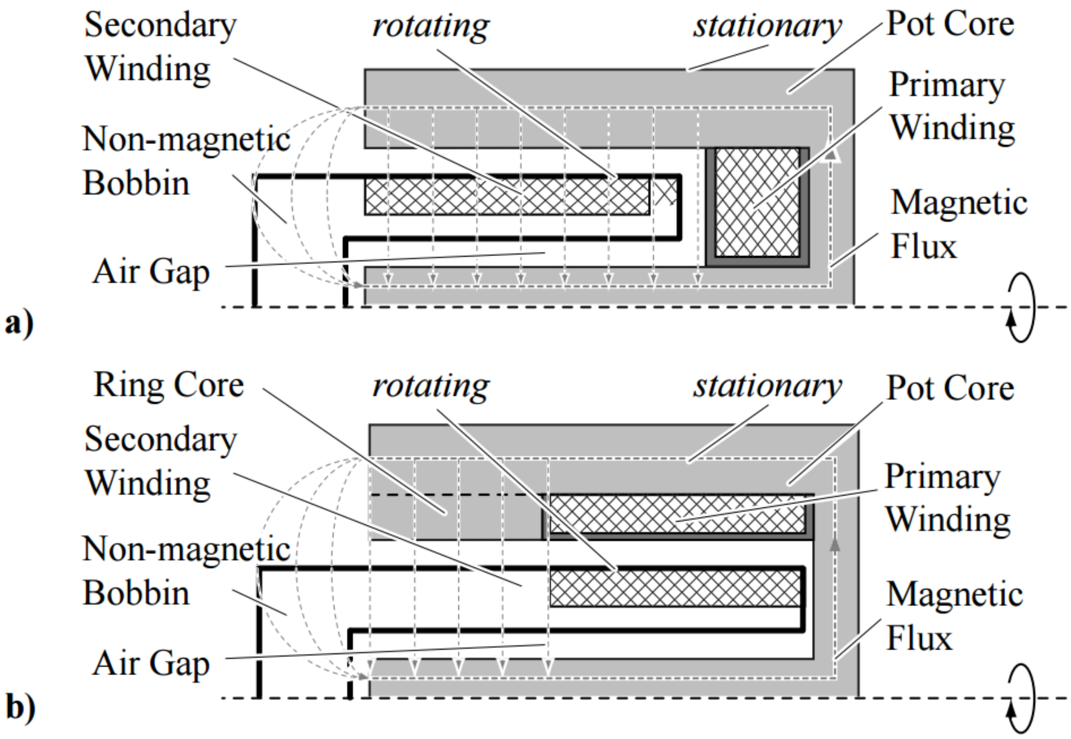

Figure 1.37. (a) Type one winding structure (b) type two winding structure [60]

Table 1.6 Inductance for different winding structure [60]

	Calculated	*Measured*	*Relative Error*
L_1 of concept 1	13.9 µH	14.0 µH	−0.2 %
L_2 of concept 1	7.1 mH	6.5 mH	9.7 %
L_1 of concept 2	23.3 µH	25.5 µH	−8.6 %
L_2 of concept 2	8.6 mH	8.3 mH	3.6 %

[61] gives an introduction to four kinds of resonant topology which could be applied to pot core type rotary transformer. Owing to the additional inductor at the input DC link, input parallel resonant tank is not applicable. For this reason, the paper compares the Serial-Serial resonant tank topology with the Serial-Parallel one. Although the Serial-Parallel tank has the advantage of wide load range, it is sensitive to the value change of the magnetizing inductance. Therefore, the Serial-Serial resonant tank is preferred. However, a small filter capacitor is still needed at the load side for Serial-Serial case.

As stated before, a pot core transformer has a large disadvantage that the flux density distribution is not even through the transformer core, because a large part of core is placed in the radial direction. This could cause a part of the transformer material to go into the saturation region while the rest is not as shows in Fig.1.38.

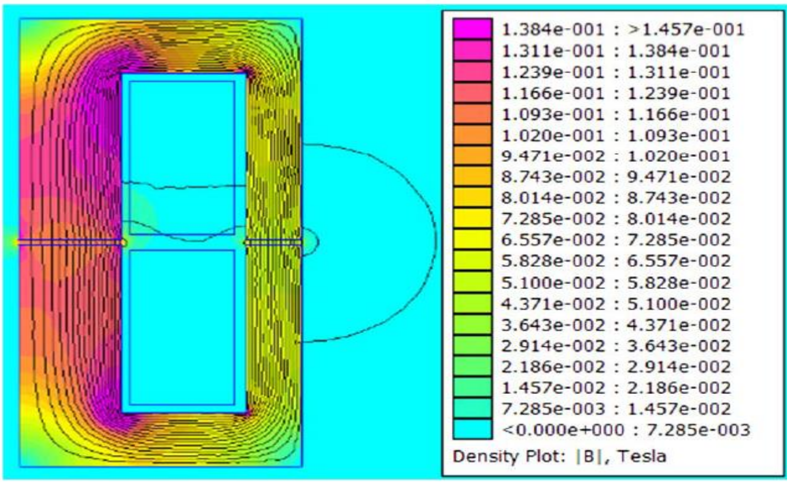

Figure 1.38. Typical pot core type RT flux density distribution [42]

1.6.6 Rotary transformer summary

A comparison with the concentric cylinder and the pot core type rotary transformer is performed by Mipo [62]. The results from Table 1.7 shows the optimized pot core type ferrite transformer has higher efficiency and smaller size than the optimized concentric cylinder type rotary transformer.

Table 1.7 Comparison of a concentric and pot core type RT [62]

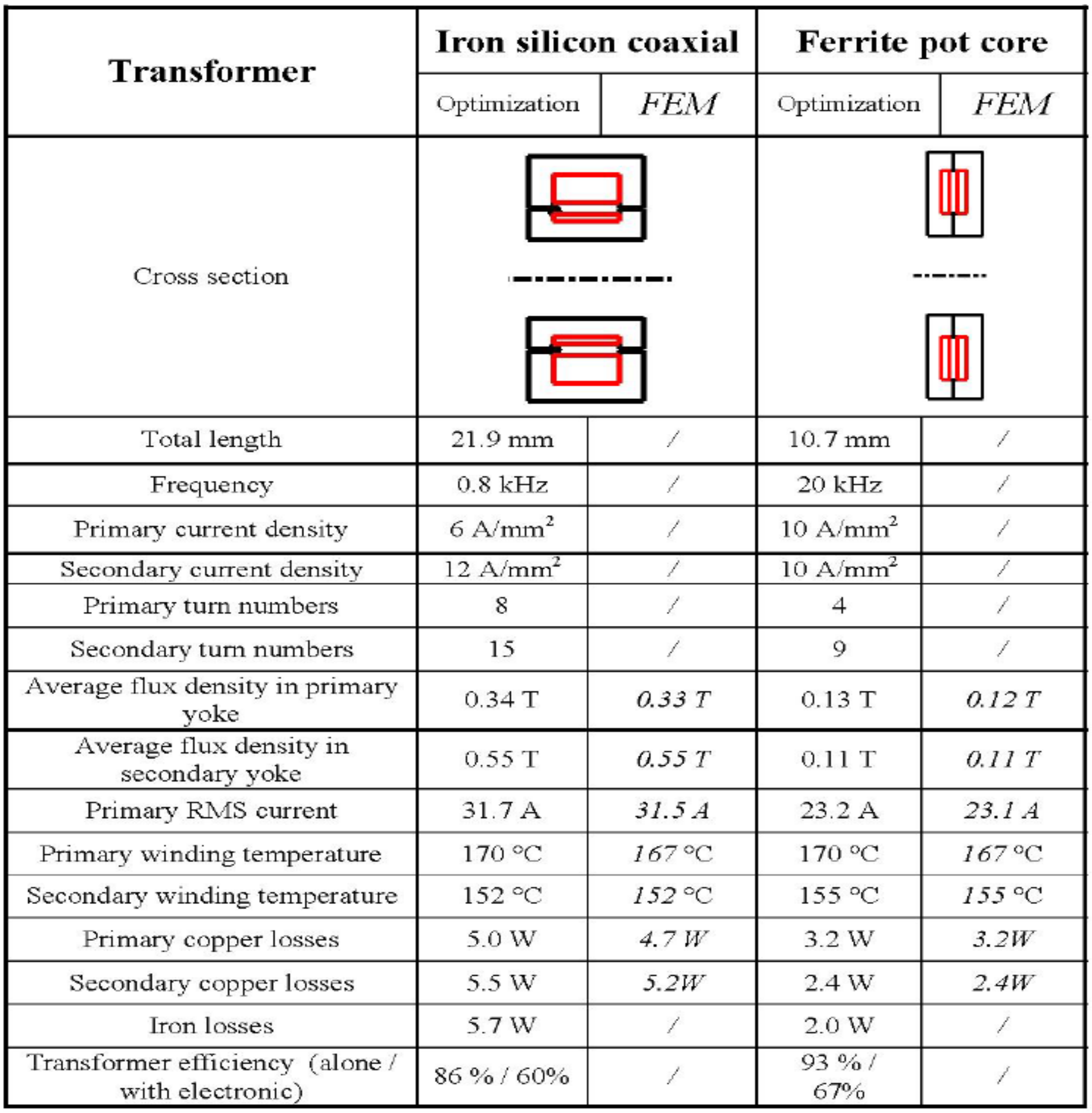

Transformer	Iron silicon coaxial		Ferrite pot core	
	Optimization	*FEM*	Optimization	*FEM*
Cross section				
Total length	21.9 mm	/	10.7 mm	/
Frequency	0.8 kHz	/	20 kHz	/
Primary current density	6 A/mm^2	/	10 A/mm^2	/
Secondary current density	12 A/mm^2	/	10 A/mm^2	/
Primary turn numbers	8	/	4	/
Secondary turn numbers	15	/	9	/
Average flux density in primary yoke	0.34 T	*0.33 T*	0.13 T	*0.12 T*
Average flux density in secondary yoke	0.55 T	*0.55 T*	0.11 T	*0.11 T*
Primary RMS current	31.7 A	*31.5 A*	23.2 A	*23.1 A*
Primary winding temperature	170 °C	*167 °C*	170 °C	*167 °C*
Secondary winding temperature	152 °C	*152 °C*	155 °C	*155 °C*
Primary copper losses	5.0 W	*4.7 W*	3.2 W	*3.2W*
Secondary copper losses	5.5 W	*5.2W*	2.4 W	*2.4W*
Iron losses	5.7 W	/	2.0 W	/
Transformer efficiency (alone / with electronic)	86 % / 60%	/	93 % / 67%	/

However, since the material type is different, it cannot be concluded that the pot core type is a better geometry than the concentric cylinder. Moreover, the core loss for the silicon iron is much higher than that for the ferrite core. Because the high frequency excitation reduces the input volts per Hz to ferrite core, the size is also minimized for the pot core type.

In conclusion, the rotary transformer is a great substitution for the existing brushless exciter system on account of the following reasons. Firstly, more compact in size (generally 60 percent reduction) because of the high frequency excitation. Secondly, manufacture cost is low since both winding and core structure are much simpler. Thirdly, there is no speed dependence for the rotary transformer system. When compared to the capacitive brushless exciter system, the rotary transformer has an advantage of allowing higher load current, owing to the insulation problem associated with high voltage in the capacitor. This is important because many wound field synchronous machines use a low voltage battery as a field excitation source, the current in the load side has to be high in order to maintain the same output power.

1.7 AC brushless exciter

AC brushless exciter is another significant topic due to the absence of bulky dc link capacitor. However, this has not been drawn much attention until K. Veszpremi proposed a brushless exciter based on ac chopper circuit [63-66].

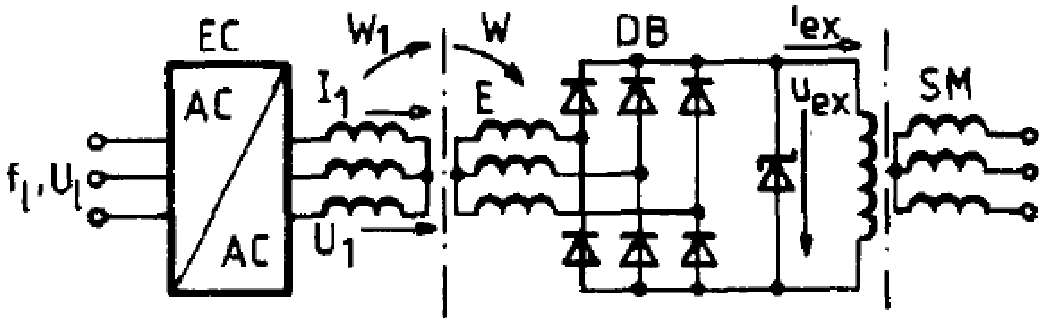

Figure 1.39. AC chopper based brushless exciter system [65]

The system structure for the proposed brushless exciter is shown in Fig 1.39. Although the author claimed the system to be a chopper based rotating transformer brushless exciter, he used an induction machine instead, since in industry, people sometimes refer the induction machine to be a rotating transformer. Thus, the exciter is still not compact due to the large volume of the induction machine. Furthermore, the overall system is still speed dependent like a traditional brushless exciter. Additionally, for an induction machine, the rotor operates at the slip frequency but not synchronous frequency, which makes the system even larger. For a small wound field synchronous machine whose field inductance is not large, an additional link capacitor behind the diode bridge is required to stabilize the output voltage on account of the low slip frequency on the rotor.

1.8 Scope of the thesis

- In Chapter 2, the proposed novel brushless exciter system structure with the theoretical foundation and applications for the single phase matrix converter and its modulation methods are explained.
- In Chapter 3, the proposed new modulation method with different topologies of single phase matrix converter and their operational mechanism based on the rotary transformer will be covered.
- In Chapter 4, a novel optimized design procedure of the rotary transformer system is proposed, the important characteristics of the rotary transformer during the optimization procedure will be illustrated.
- In Chapter 5, a comparison of the proposed modulation strategy with existing

modulation strategies will be covered, and a comparison of the proposed modulation strategy with two different operating frequency will also be explained in detail.

- In Chapter 6, the prototype of the single phase matrix converter based rotary transformer system is presented and the experiment results are analyzed.
- In Chapter 7, the conclusion and suggested future work are presented.

Chapter 2

SINGLE PHASE MATRIX CONVERTER BASED BRUSHLESS EXICTER SYSTEM WITH THE STATE OF ART REVIEW ON SINGLE PHASE MATRIX CONVERTER

2.1 Proposed system and introduction to single phase matrix converter

A single phase matrix converter based rotary transformer brushless exciter has been proposed in this thesis to supply the field power of a wound field synchronous machine. The overall system structure is shown in Fig. 2.1.

Direct ac to ac converter not only simplifies the two-system stage, an ac to dc to ac, to a single system stage but also brings the benefit of compact size due to the absence of bulky DC link capacitor. Thus, the overall system will share both the advantages of a rotary transformer and a single phase matrix converter.

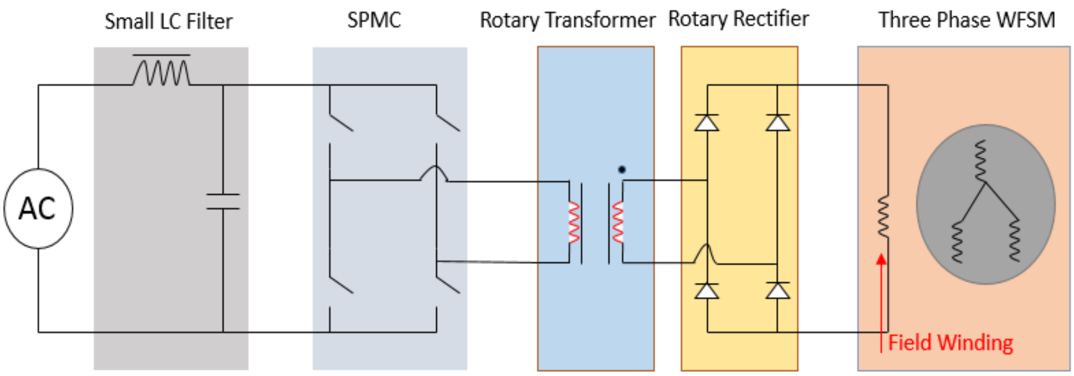

Figure 2.1. Proposed SPMC based brushless exciter system structure

The transformer operating frequency is a very important factor in this system, because it determines the overall system's efficiency and the power density. Lower frequency (below 60Hz) operation increases the magnetizing current, and therefore increases the copper and switch's conduction loss. Furthermore, a large volume transformer is required to constrain the maximum flux density in the core. High frequency (10kHz or higher) operation will decrease the size of the transformer but increase the core loss and the switching loss, thus a resonant circuit is required for soft switching. It should be noted that the relationship between the size of the transformer and the operating frequency is not linear. A ten times increase in operation frequency will not yield a ten times reduction in volume for a transformer at kHz level as the operation flux density has to be smaller at high frequency. Moreover, high frequency operation will also increase the input EMI which requires additional filtering part at input [67, 68].

On the other hand, medium frequency (400-1000 Hz) operation takes the advantage of both smaller transformer size and a good overall system efficiency [67]. Based on the above reasons, the system is designed to operate at a fundamental frequency of 960Hz.

2.2 Introduction to the single phase matrix converter

The matrix converter was first proposed by Gyugyi [69] in 1976 as a generalized converter. The first single phase matrix converter was built by Zuckerberger [70] in 1997. After that, Saiful has applied the SPWM method to achieve better output current waveform [71]. The principle of the commutation for the single phase matrix converter was proposed by Idris[72]. In that paper, Idris claimed the safe commutation had been achieved by following his commutation method. However, there is an important commutation state he did not state clearly in that paper which can cause significant voltage stress in the switch which will be discussed in section 2.4.

The benefits of using matrix converter are listed below.

1. The absence of the reactive power storage component makes the converter system more compact and have a higher power density compared to traditional ac to dc to ac inverter system [73].
2. Due to the unique switch topology, the matrix converter has the ability of bi-directional power transfer [74].
3. It can achieve unity power factor (adjustable input power factor) with sinusoidal input current [75].
4. It has a fast system response and have a more reliable system owing to the absence of the DC link capacitor [76].
5. The frequency and waveform on the input and output side are independent of each other.
6. It has high efficiency and variable frequency operation capability.

Compared to the inverter based system, the matrix converter has a lower voltage transfer ratio (86 percent). However, this will not be the case if the application is required to step down the voltage. Moreover, a transformer can be used to adjust the output voltage. Secondly, a limitation of the matrix converter results from the complex control algorithm of bi-directional switches. Lastly, the matrix converter has a low ride through capability when a voltage sag happens from the input side.

2.3 Bi-direction switches

Since the matrix converter the switches must have the ability to conduct bi-direction current and to block bi-direction voltage, a proper switch has to be chosen for this application. Unfortunately, there is no single product in the market which could fulfill this function until recently. Thus, a combination of several single switches has been proposed by people to realize the desired capability.

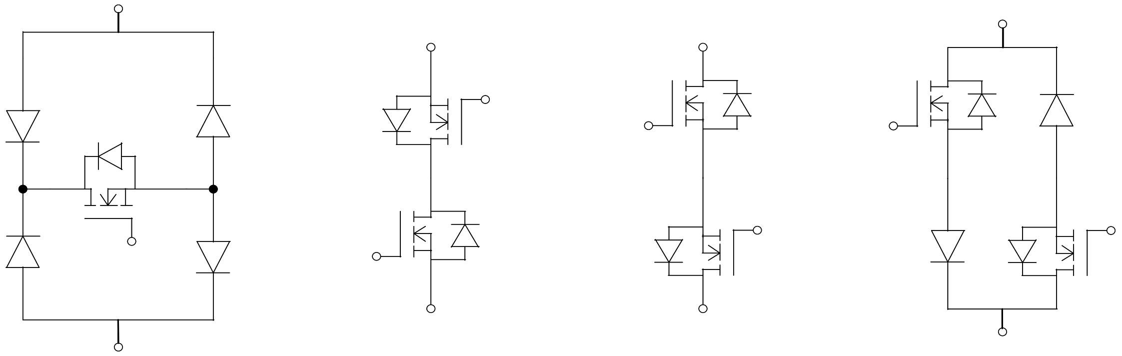
(a) (b) (c) (d)

Figure 2.2. Bi-directional switches

(a) Rectifier bridge (b-d) back to back connection

Fig. 2.2. shows the four different topologies for a MOSFET based bi-directional switches. The rectifier bridge connection is shown in (a), where the benefit of using this topology includes reducing the number of active switches by half (MOSFET). Thus, the overall control will be easier, and the total cost will also be lower. However, by using the bridge connection topology, the switch conduction loss will increase due to the additional forward voltage drop of the diode. Also, owing to the single active switch structure, the bridge topology will have higher stress than the back to back connection topology at transition (dead time) and commutation event which will be discussed in

the next section. Based on the above reasons, a snubber circuit is required for the bridge topology to limit the switch stress because of the stray inductance. Back to back bi-directional switch topologies are shown in (b) to (d). It should be noted that they all share a common characteristic that the current passes one of the active switch with a series diode when the switch conducts. Thus, the total switching loss is the same for all these three topologies. Using the topology shown in (c) could help to reduce the number of isolated power supply by half for the gate drive circuit. Also, a commercialized bi-directional anti-parallel IGBT set based on topology (d) has come on the market recently.

2.4 Commutation strategy

2.4.1 Back to back connection

A single phase matrix converter with RL load is shown in Fig. 2.3. The detailed commutation strategy based on this circuit will be discussed in this section. Although the figure shows the bi-direction switch set as an anti-parallel connection topology, in fact the commutation strategy will be the same for all back to back topologies. Thus, the commutation method for the series back to back topology will not be discussed in this thesis since they share the same behavior of the anti-parallel connection.

A series resistor and inductor are used as the output of this circuit to model the inductive load like machines or loosely coupled transformers. In this section, the commutation strategy for step up frequency operation will be covered for the rotary transformer requires a medium frequency input. Because the step-down frequency operation follows the same commutation procedure, it will not be discussed in this section.

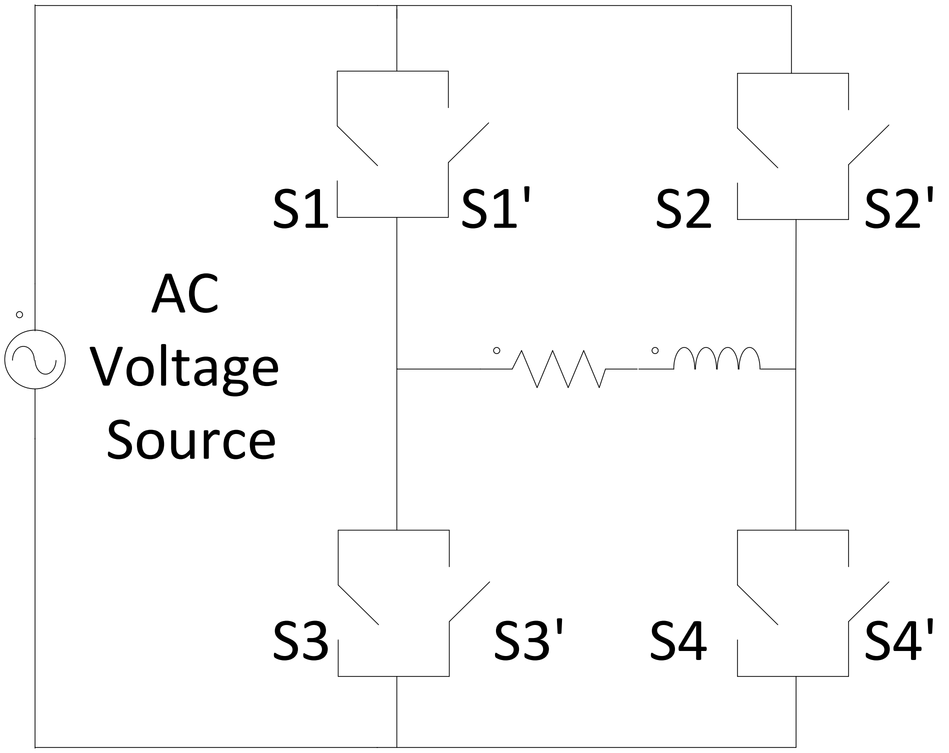

Figure 2.3. Anti-parallel switch set single phase matrix converter with RL load

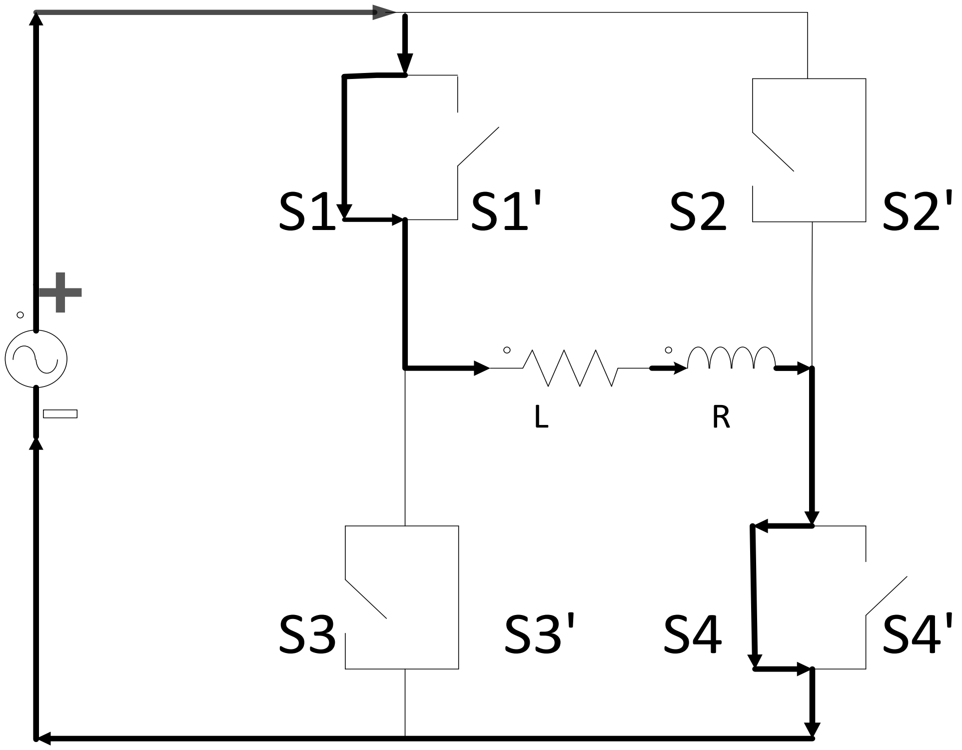

Figure 2.4. State 1

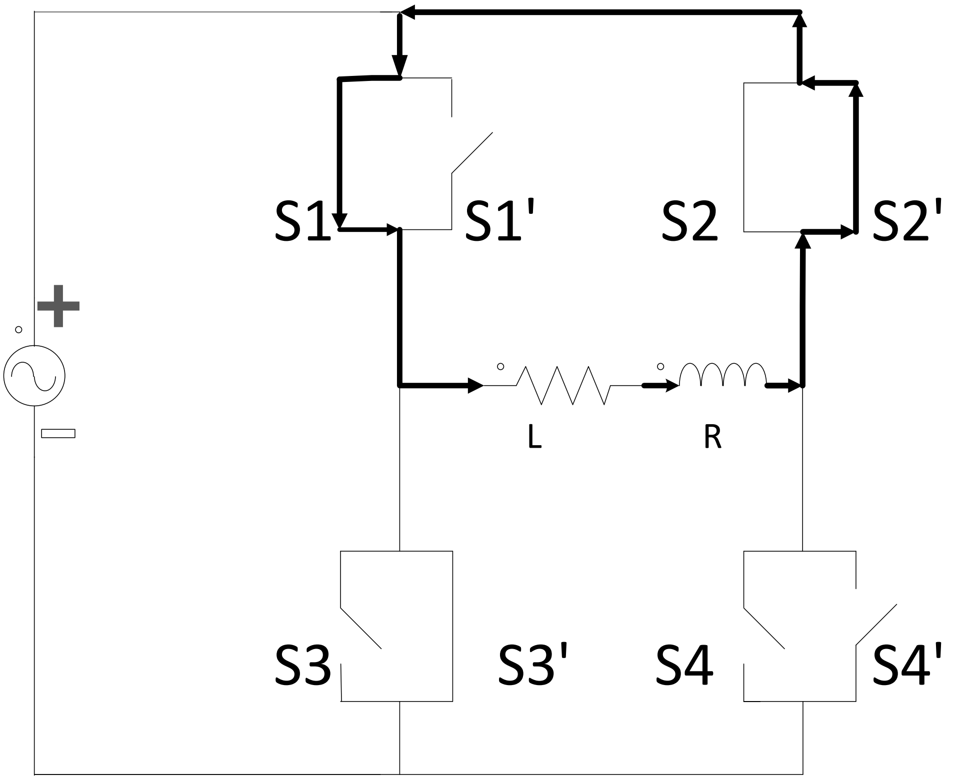

Figure 2.5. State 2

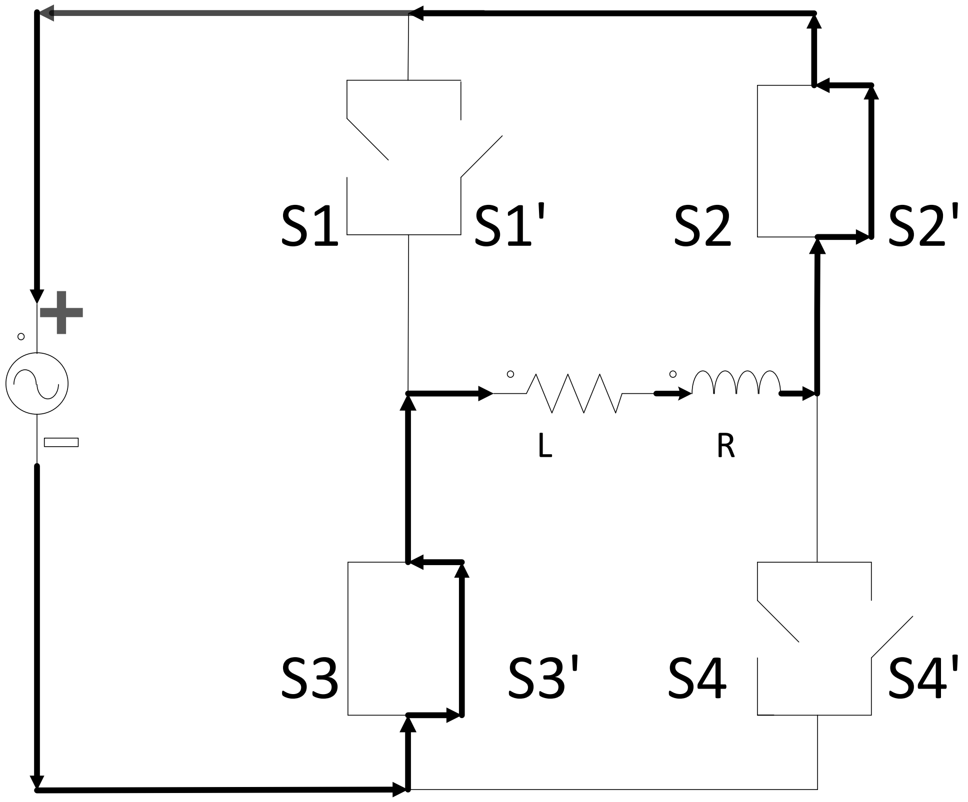

Figure 2.6. State 3

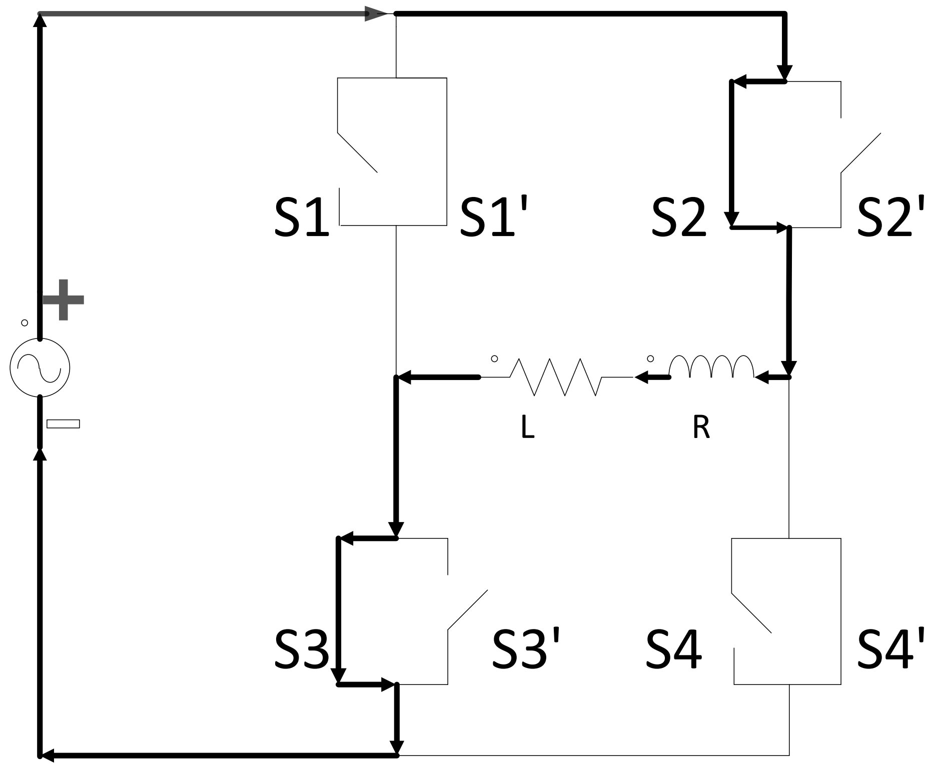

Figure 2.7. State 4

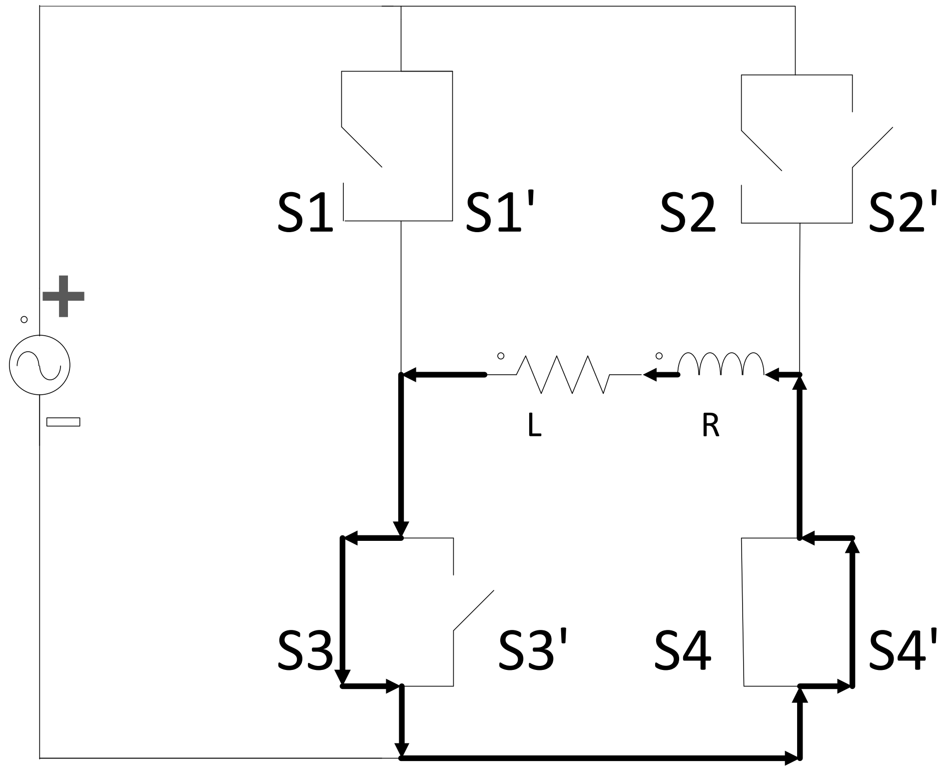

Figure 2.8. State 5

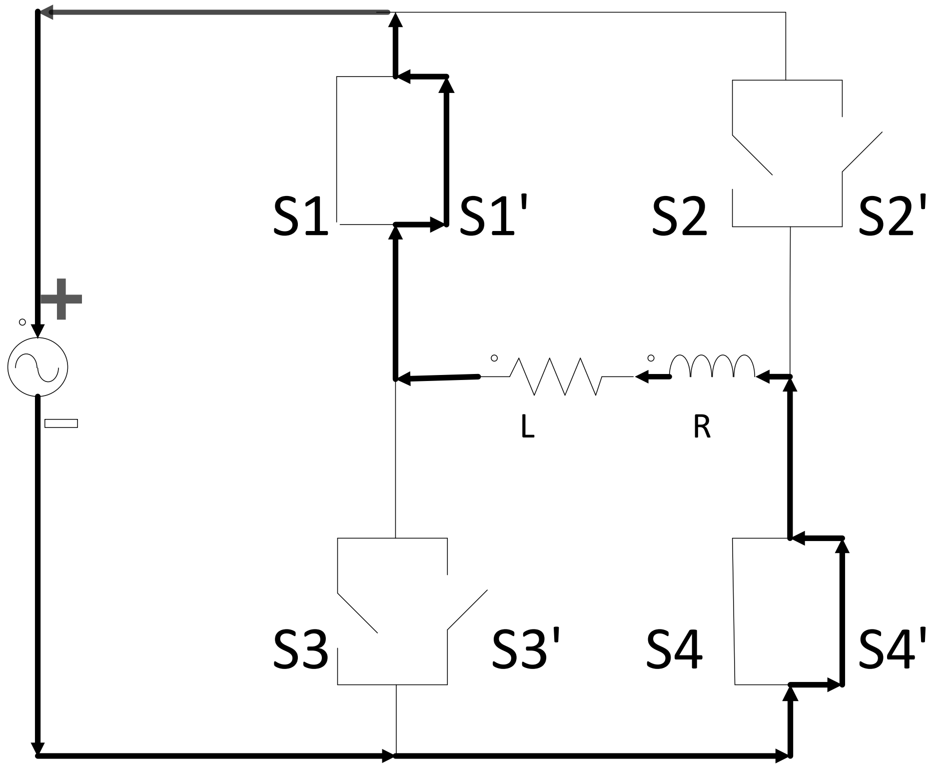

Figure 2.9. State 6

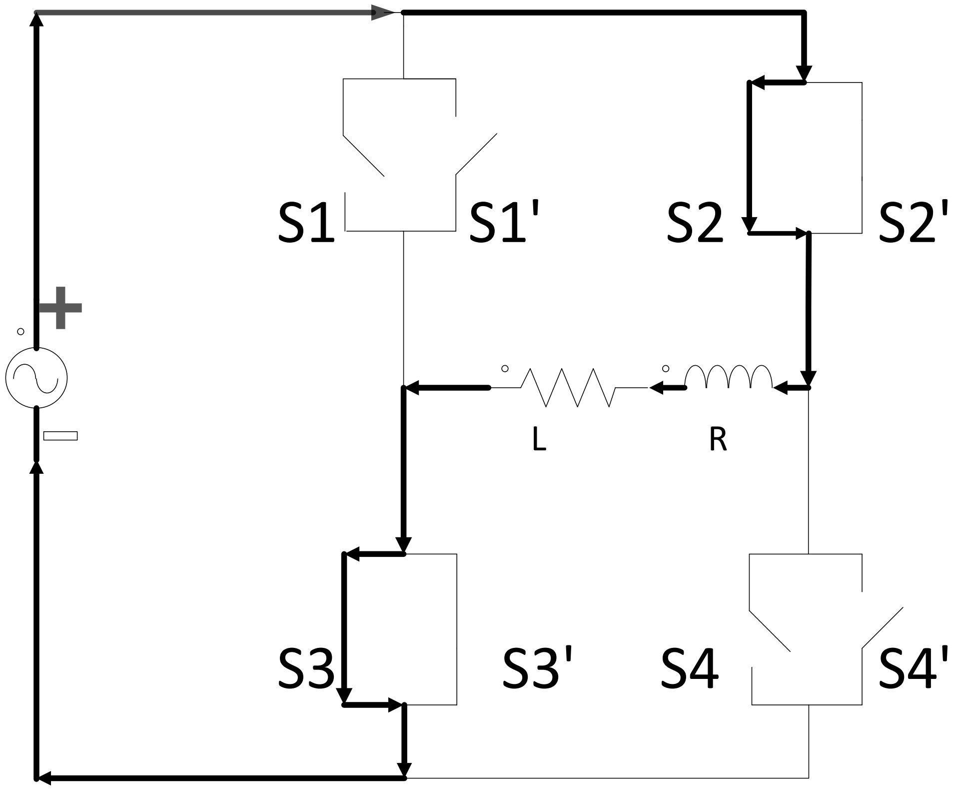

Figure 2.10. Revised State 3 when input polarity is about to change from positive to negative (Output frequency is even times the input frequency)

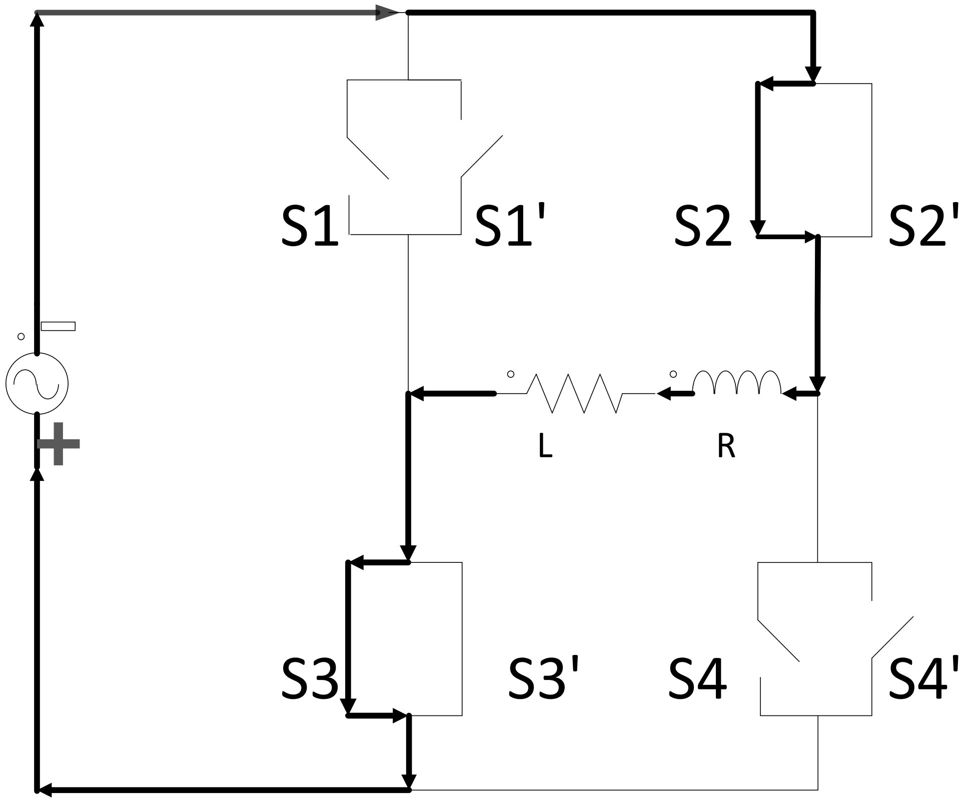

Figure 2.11. State 7 when input polarity changes from positive to negative

(Output frequency is even times the input frequency)

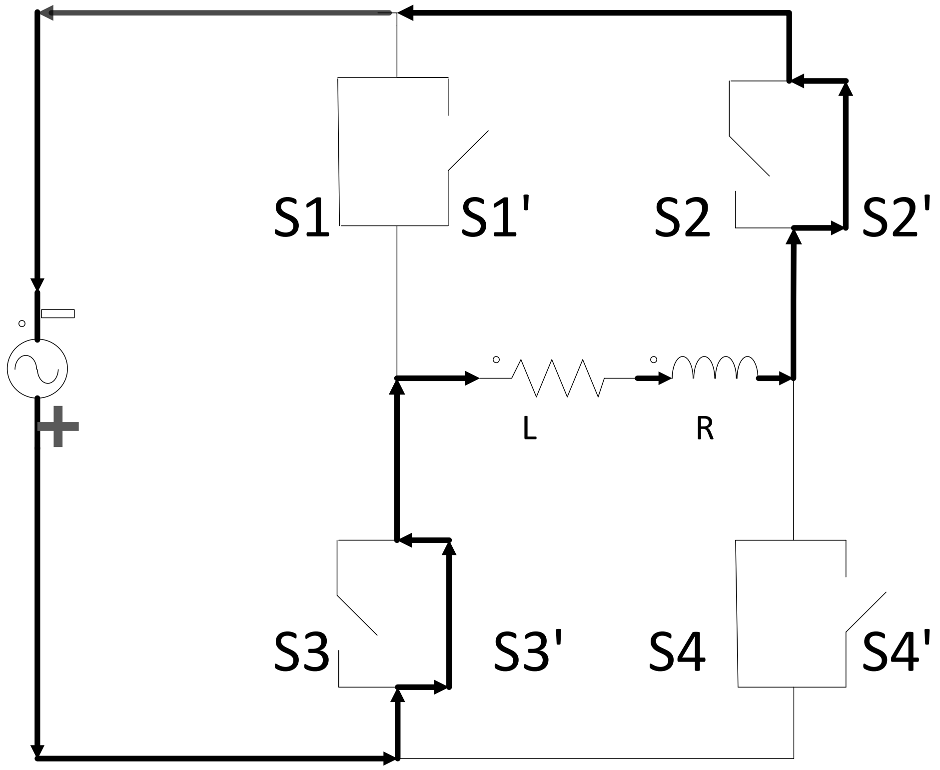

Figure 2.12. State 8

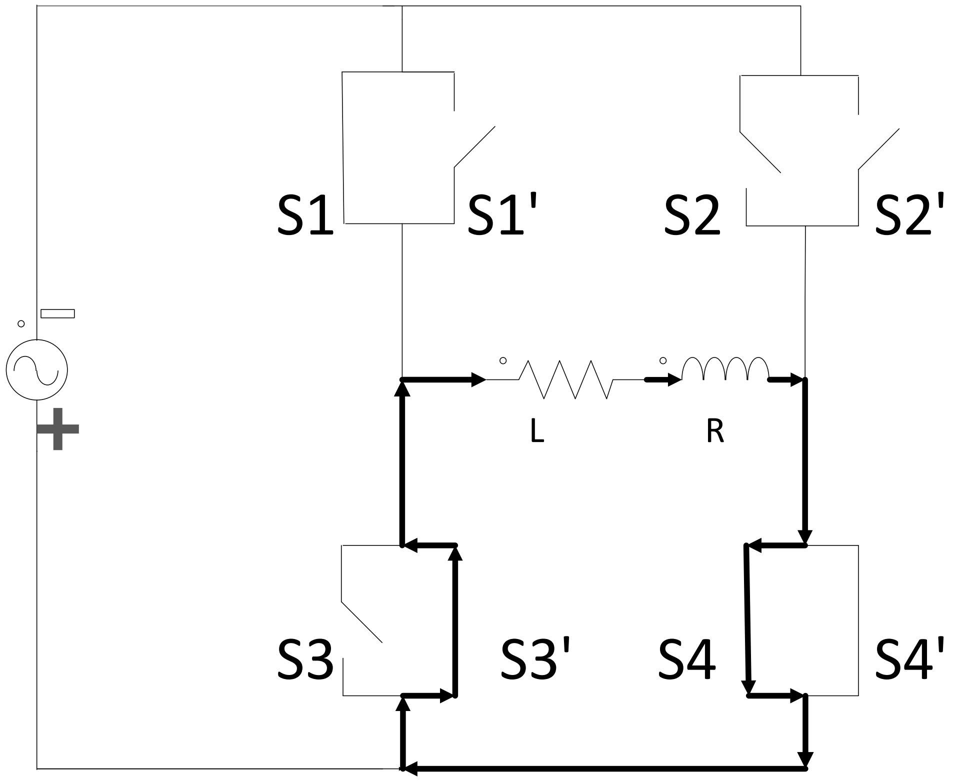

Figure 2.13. State 9

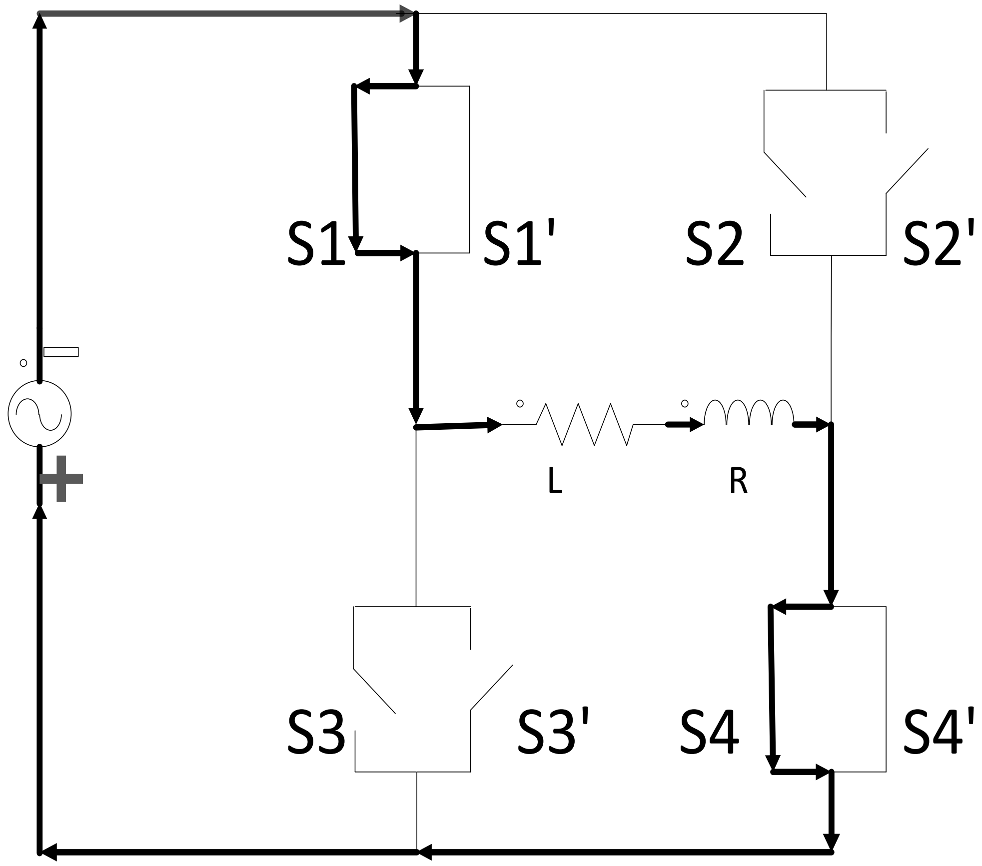

Figure 2.14. State 10

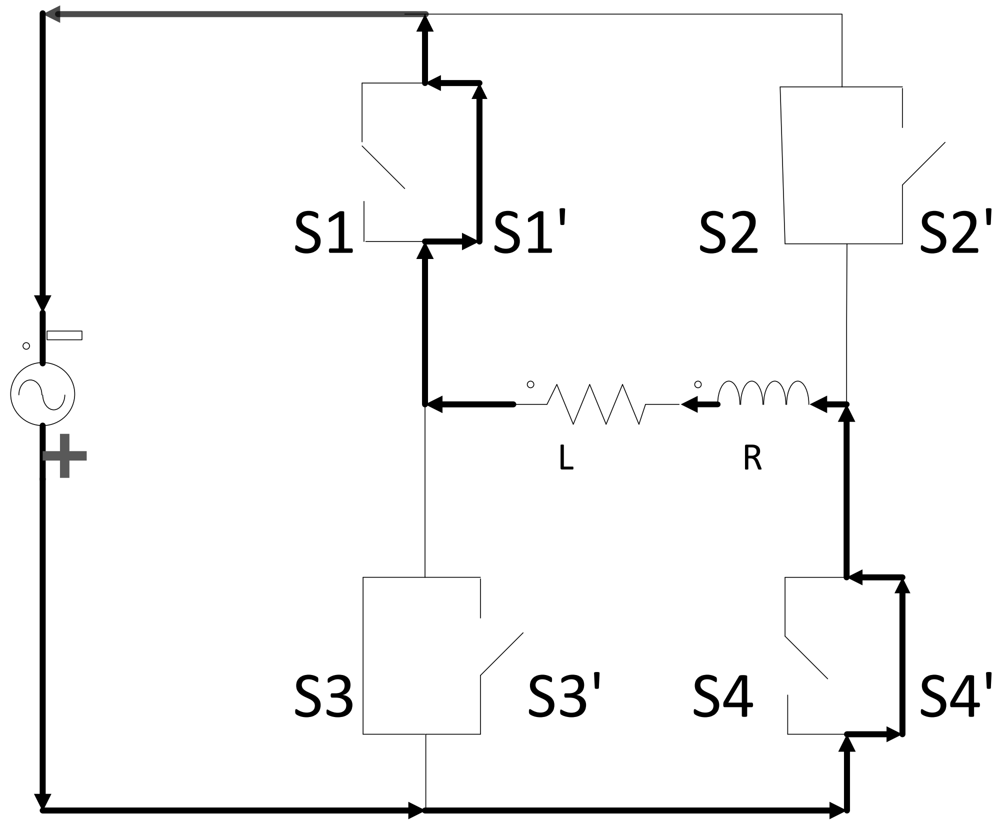

Figure 2.15. State 11

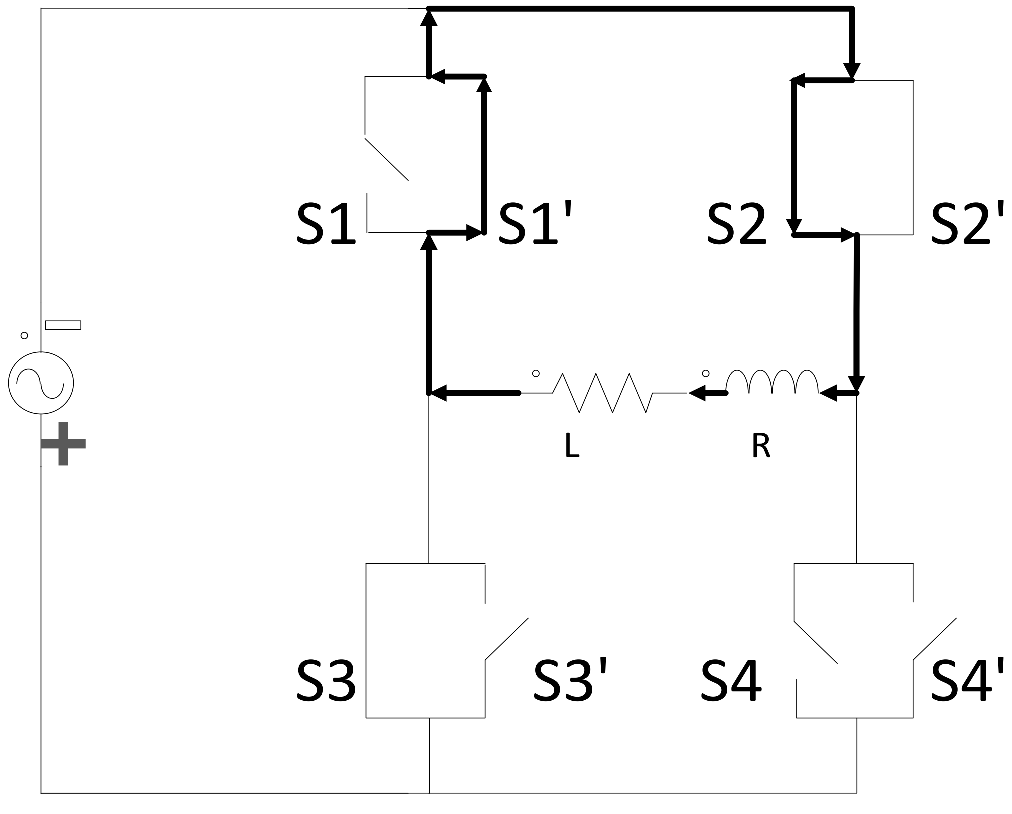

Figure 2.16. State 12

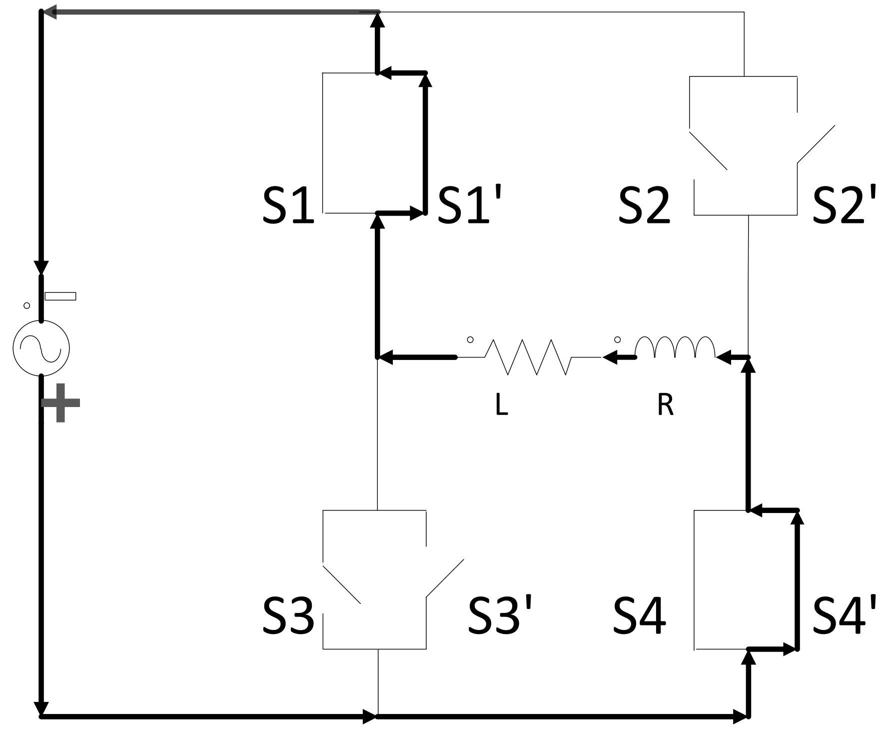

Figure 2.17. Revised State 10 when input polarity is about to change from negative to positive (Output frequency is even times the input frequency)

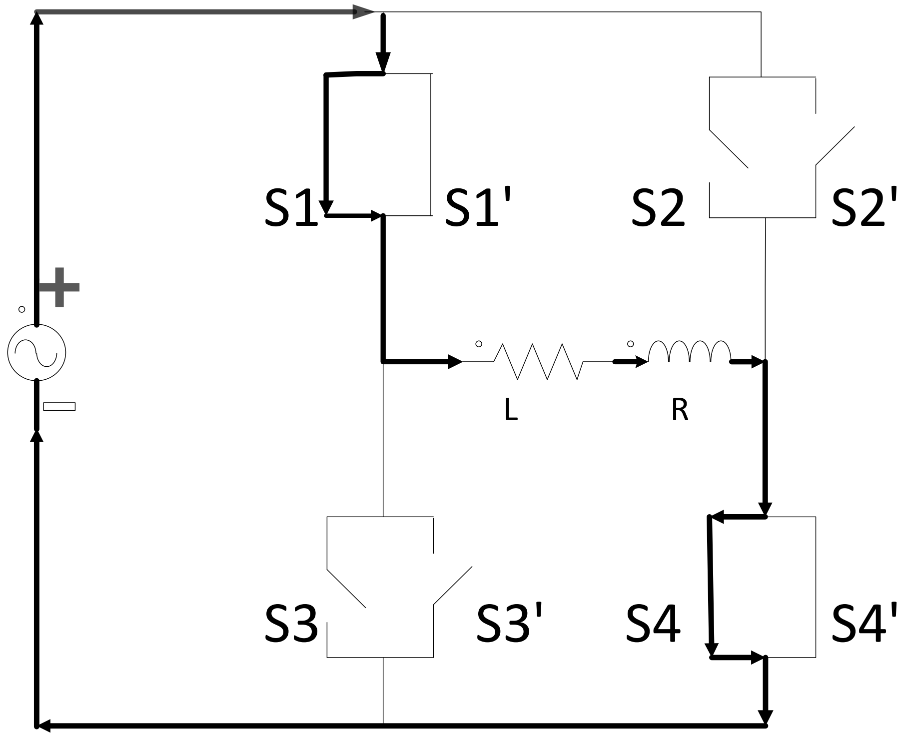

Figure 2.18. Revised State 6 when input polarity is about to change from positive to negative (Output frequency is odd times the input frequency)

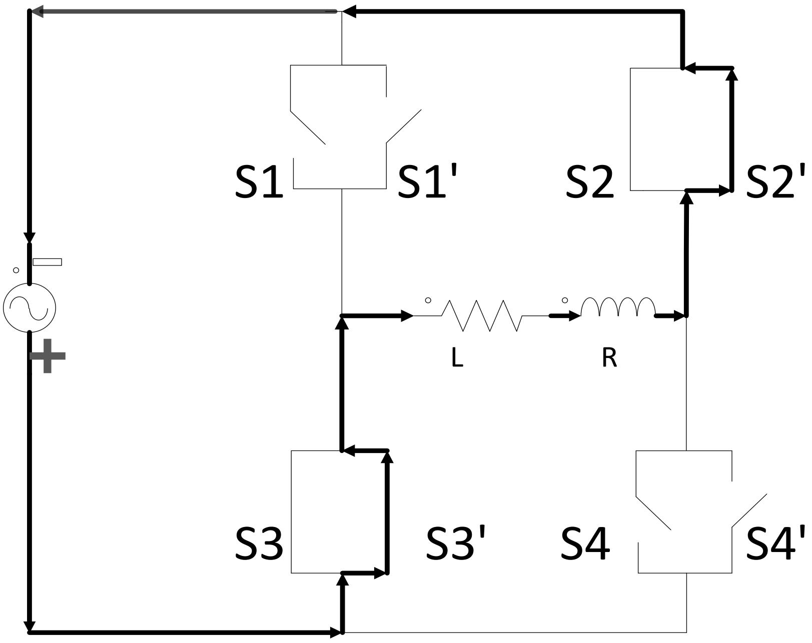

Figure 2.19. Revised State 7 when input polarity is about to change from negative to positive (Output frequency is odd times the input frequency)

The 12 possible safe commutation states are listed in Fig.2.4 to Fig. 2.16. The safe commutation strategy based on proposed modulation method of this thesis (with zero state) will be explained below, and the safe commutation strategy for the widely-used modulation method (no zero state) will also be illustrated.

1. Commutation strategy for proposed modulation method (including zero state)

Before going to the detailed commutation strategy, it should be noted that S1 to S4 are modeled as switches capable of conducting current from top to bottom direction and S1' to S4' are switches capable of conducting current from bottom to top direction, and S1 and S3, S2 and S4, S1' and S3', S2' and S4' are complementary switches.

It assumes the circuit is energized by an ac source with positive voltage applied to the load in state 1 as Fig.2.4 shows. The positive voltage is applied to the load and current begins to flow in the load through S1 and S4, S2' and S3' are also turned on in order to prepare for the next state. When state 1 ends and state 2 begins, S4 is open and S2 is on while the other switches remain in the same condition. The load current will naturally commutate to freewheeling state through S2' and S1 after the turn off event of S4, since S2' is already turned on in state 1. When a negative voltage is required at the load at state 3, S1 turns off and S3 turns on. Due to the nature of the inductive load, the current still flows in the positive direction through S2' and S3' when S1 is off while the negative voltage applies. When the positive current dies out, the negative current will naturally commutate through S2 and S3 in state 4. In state 4 S2' and S3' are off, and S1' and S4' are on in order for the preparation of state 5. It should be noted the time when the current commutates through state 3 to state 4 is determined by the value of the inductive load. In the extreme case when the load is purely inductive, this moment will occur in the 90 degree of the negative cycle output voltage, in other words, this moment will occur when the applied area of V/Hz is half to the total applied area of V/Hz during state 3 and 4. Thus, to guarantee the safe commutation for all inductive load conditions, S2' and S3' have to be turned off after this half V/Hz area point. When state 4 ends, S2 is off and S4 is on, the negative current naturally commutates to S3 and S4' for freewheeling operation. State 6 will begin when the positive voltage is required at the load. In state 6, S3 is off and S1 is on, the negative current will again naturally commutate to switches of S1' and S4'. When this negative current dies out, the system will change back to State 1 with S1' and S4' turned off, the load current will naturally commutate to S1 and S4 again for conducting the positive current.

When the polarity of the input voltage is negative, the switching sequence of S1, S3' exchanges (S1 follows S3's switching sequence in the positive case, and S3' follows S1's switching sequence in the positive case), the switching sequence of S2, S4' exchanges, the switching sequence of S1', S3 exchanges, and the switching sequence of S2', S4 exchanges. The commutation strategy follows the same procedure as in the positive polarity case. Therefore, the detailed commutation strategy will not be explained, and the summarized turn-on and turn-off sequence is presented in Table 2.1.

Table 2.1 Truth table for each state during positive and negative polarity

Input Polarity	State	Switch on	Switch off
Positive	1	**S1**, **S4**, S2', S3'	S2, S3, S1', S4'
	2	**S1**, **S2'**, S3', S2	S3, S4, S1', S4'
	3	**S2'**, **S3'**, S2, S3	S1', S4', S1, S4
	4	**S2**, **S3**, S4', S1'	S1, S4, S2', S3'
	5	**S3**, **S4'**, S1', S4	S1, S2, S2', S3'
	6	**S4'**, **S1'**, S1, S4	S2', S3', S2, S3
	If the input voltage is still positive, next state is 1 again		
Negative	7	**S2**, **S3**, S2', S3'	S1, S4, S1', S4'
	8	**S2'**, **S3'**, S4, S1	S1', S4', S2, S3
	9	**S3'**, **S4**, S1, S4'	S2, S3, S1', S2'
	10	**S4**, **S1**, S1', S4'	S2, S3, S2', S3'
	11	**S1'**, **S4'**, S2, S3	S1, S4, S2', S3'
	12	**S1'**, **S2**, S3, S2'	S1, S4, S3', S4'
	If the input voltage is still negative, next state is 7 again		

If the output frequency is even times the input frequency, when the input voltage changes from positive to negative, the positive switching sequence will end at state 3. In this discussion, this state is called a Rev state 3 since it is different from state 3 where the current will flow in the positive direction finally shown in Fig.2.10. It should be noted that during the transition from Rec state 3 to state 7 there is no switch sequence change and no current commutation happens either. Thus, the commutation during the input voltage polarity change will also be smooth. When the input voltage changes from negative to positive, it follows the same procedure, in which the negative switching sequence will end at Rev state 10 which is shown in Fig.2.17 and followed by the positive sequence state 6 to create a natural commutation of voltage. The summary for the switching sequence for these events is shown in Table 2.2.

Table 2.2 Truth table for each state during input polarity change when output frequency is even times the input frequency

	State	Switch on	Switch off
Input change from positive to negative	Rev. 3	S2’, S3’, **S2, S3**	S1, S4, S1’, S4’
	7	**S2**, **S3**, S2’, S3’	S1, S4, S1’, S4’
Input change from negative to positive	Rev. 10	**S4’**, **S1’**, S1, S4	S2’, S3’, S2, S3
	6	**S4’**, **S1’**, S1, S4	S2’, S3’, S2, S3

When the output frequency is odd times the input frequency, the voltage commutation will follow the same procedure as the even times event. The only difference is the commutation states, whose detail for this event is shown is Fig.2.18 and Fig.2.19 and summarized in Table 2.3.

Table 2.3 Truth table for each state during input polarity change when output frequency is odd times the input frequency

	State	Switch on	Switch off
Input change from positive to negative	Rev. 6	**S4**, **S1,** S1’, S4’	S2, S3, S2’, S3’
	10	**S4**, **S1,** S1’, S4’	S2, S3, S2’, S3’
Input change from negative to positive	Rev. 7	**S2’**, **S3’**, S2, S3	S1’, S4’, S1, S4
	3	**S2’**, **S3’**, S2, S3	S1’, S4’, S1, S4

Table 2.4 Truth table for cyclo-converter

Input polarity	State	Switch on	Switch off
Positive	1	**S1**, **S4**, S2’, S3’	S2, S3, S1’, S4’
	3	**S2’**, **S3’**, S2, S3	S1’, S4’, S1, S4
	4	**S2**, **S3**, S4’, S1’	S1, S4, S2’, S3’
	6	**S4’**, **S1’**, S1, S4	S2’, S3’, S2, S3
	If the input voltage is still positive, next state is 1 again		
Negative	7	**S2**, **S3**, S2’, S3’	S1, S4, S1’, S4’
	8	**S2’**, **S3’**, S4, S1	S1’, S4’, S2, S3
	10	**S4**, **S1,** S1’, S4’	S2, S3, S2’, S3’
	11	**S1’**, **S4’,** S2, S3	S1, S4, S2’, S3’
	If the input voltage is still negative, next state is 7 again		

When the single phase matrix converter operates as Cyclo-converter, the only difference is there will be no zero state. Its switch sequence is summarized in Table 2.4 above. When the input polarity changes, it will follow the switching sequence summarized in Table 2.2 and 2.3.

2.4.2 Bridge connection

Fig.2.20 shows the simplified circuit for the bridge connection single phase matric converter. The commutation strategy for the bridge type matrix converter could follow the same procedure as the back to back connection topology, and its control algorithm will be even simpler due to the reduced number of active switches. However, a snubber or a clamp circuit is required in this case for safe commutation.

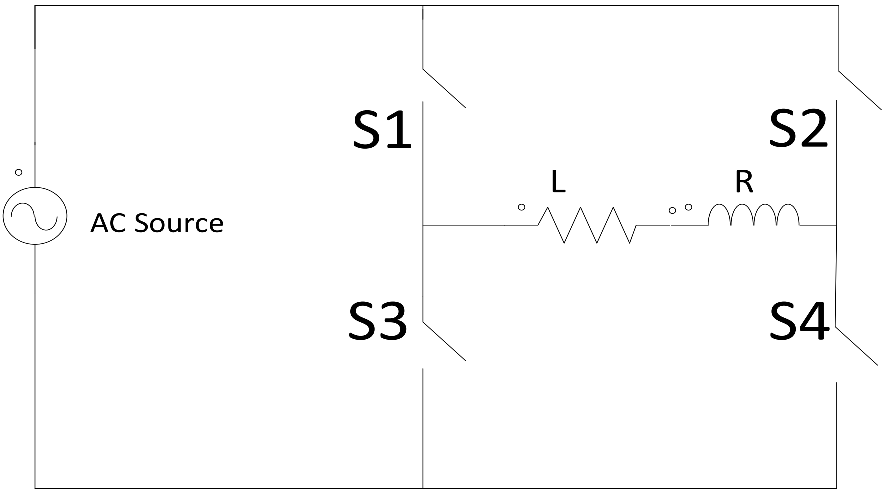

Figure 2.20. Bridge connection single phase matrix converter with RL load

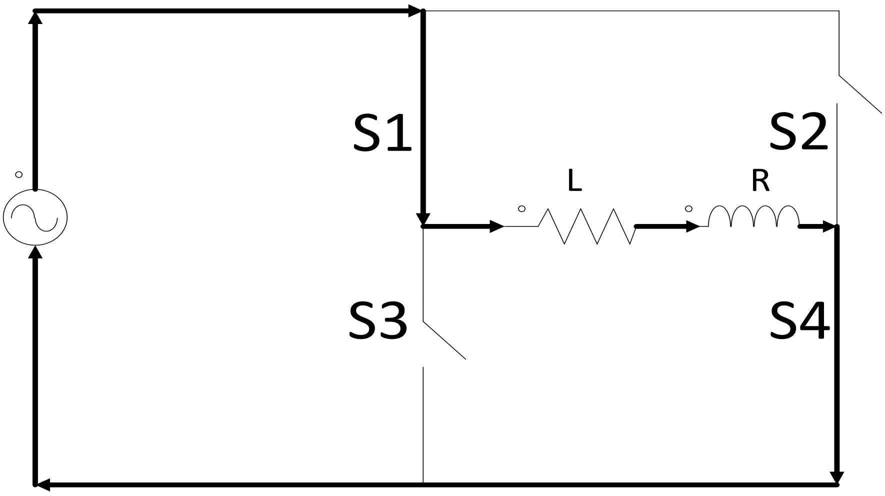

Figure 2.21. State 1 for bridge type SPMC

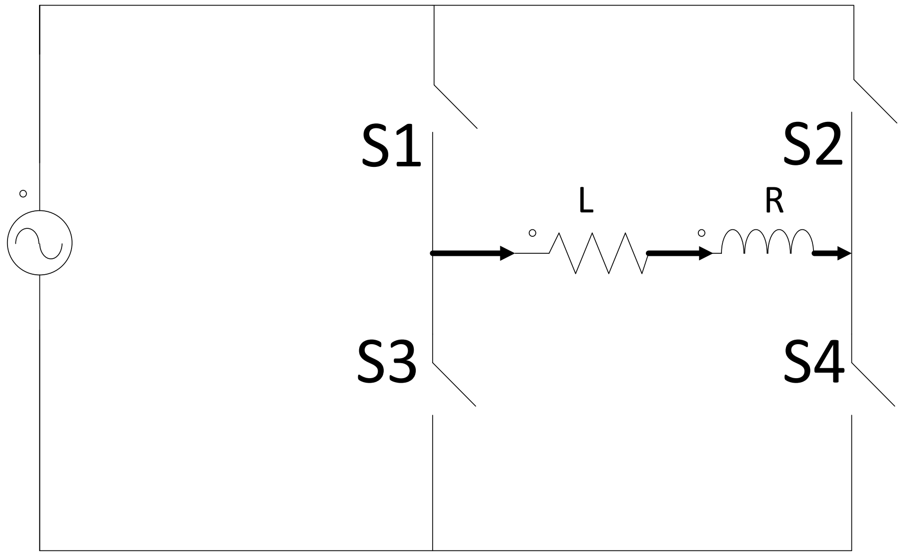

Figure 2.22. Dead time state

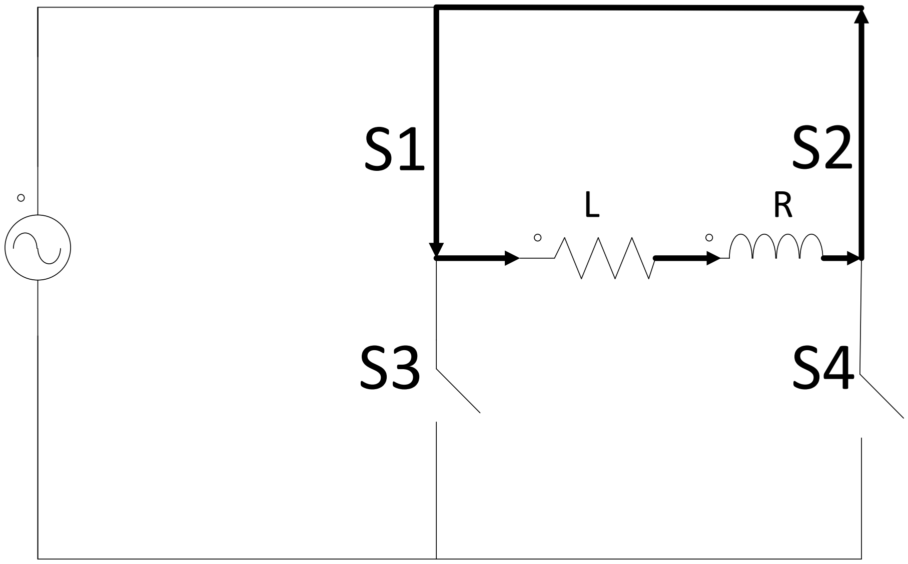

Figure 2.23. State 2 for bridge type SPMC

Fig 2.21-23 explain why a clamp circuit or a snubber circuit is required for the bridge type switches. For an ideal switch, it turns on and turns off immediately when a command is given. However, this is not true for real MOSFETs and transistors, since such switches take hundreds of Nano-seconds to several micro seconds to cut off the current (hard switching case). If one of the complementary switches (S1, S3 or S2, S4 pair) is turned on before the other one's current dies out, a short circuit will happen.

Thus, a deadtime between the complementary switches has to be added in order to avoid this short circuit condition. In contrast, adding a dead time will create a new switching state where all switches are open circuited shown in Fig. 2.22. Owing to the nature of the inductive load, this open circuit condition will create a large voltage spike which could damage the semiconductor switches if there is no path for the inductor current to flow. As a result, the clamp circuit or a proper designed snubber circuit is required to provide that path. Although the clamp circuit does provide a path for the inductive load at the deadtime state, due to the voltage difference between the ac input side and the dc load side of the clamp circuit, a small voltage spike will still be observed during this transition. Fig. 2.24 shows an example of the output voltage waveform during the dead time state.

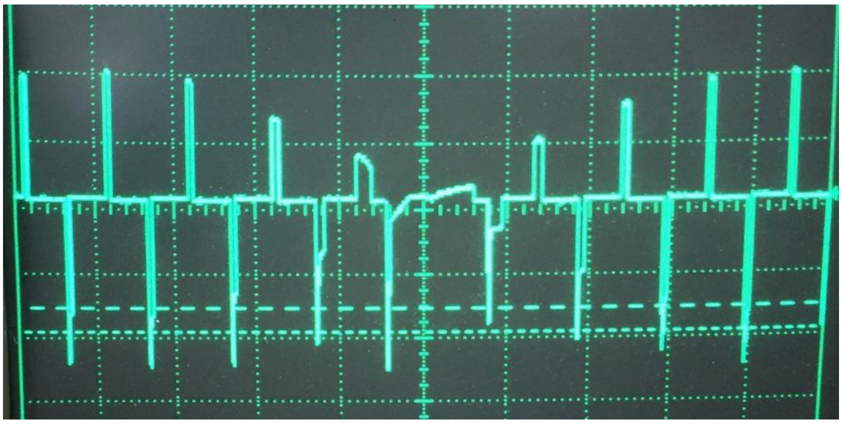

Figure 2.24. SPMC output voltage waveform during commutation

To compare the difference between the proposed commutation strategies, a safe commutation strategy proposed for the back to back topology is applied in the positive cycle of the output voltage in which a special commutation strategy for the bridge topology is applied in the negative cycle of the output voltage. A large inductive load with power factor less than 0.2 is connected to the output of the matrix converter to simulate the worst case. From Fig 2.24, it could be concluded that a safe commutation has been obtained from the proposed back to back connection strategy since no voltage spike exists at the load side during the positive cycle. In contrast, due to the dead time of the bridge type commutation, a small voltage spike will be created during the negative cycle of the output voltage. However, it should be noted again that this small voltage spike is not generated by a forced shutdown of the inductor current but caused by the voltage difference between the dc voltage of the clamp circuit and the ac input voltage.

2.5 Modulation method

In order to achieve a better output waveform, a proper modulation method must be chosen. There are many different modulation methods which could be applied to single phase matrix converter [77, 78]. Delta modulation method is claimed to have the best output waveform at higher output frequency [79]. However, since a feedback loop is required for this modulation method, which complicates the overall system structure, this thesis presentation will only cover the average method and other PWM method.

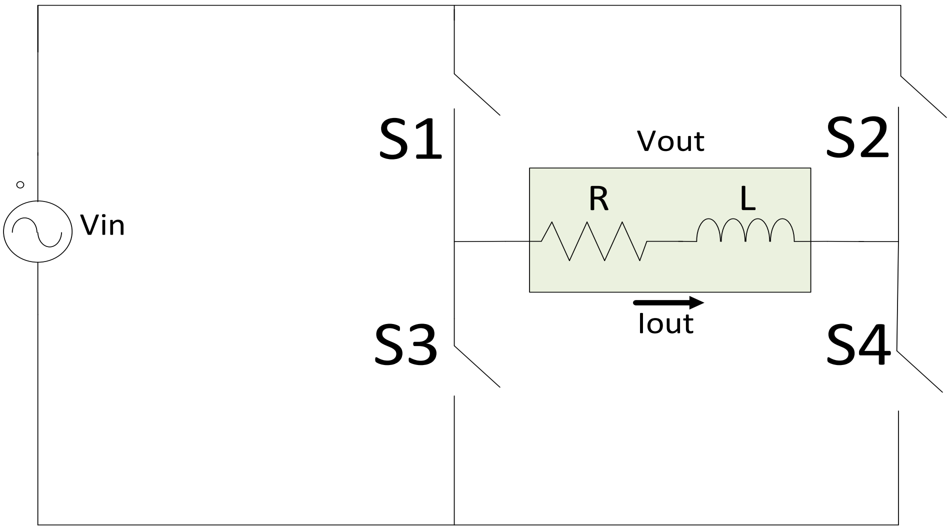

Figure 2.25 Simplified structure of SPMC

2.5.1 Average voltage method

As stated before, the first single phase matrix converter is realized by Zuckerberger and his co-workers. In his paper, a modulation method based on average voltage is proposed. Fig 2.25 is a simplified structure of a single phase matrix converter and will be used to elaborate this modulation method.

Assume the conduction time for S1 and S4 are T_1 and the conduction time for S2 and S4 are T_2. The sampling time T is defined as

$$\mathrm{T} = T_1 + T_2 \tag{2.1}$$

With an input voltage sinusoidal voltage Vin, to modulate the output voltage based on this input voltage at sampling time T, first the modulation index m_1 and m_2 (can be also called duty cycle) must be determined,

$$m_1 = \frac{T_1}{T}\ m_2 = \frac{T_2}{T} \tag{2.2}$$

$$m_1 + m_2 = 1 \tag{2.3}$$

$$V_{in} = \sqrt{2} * V_{irms} * \cos \omega_i t \tag{2.4}$$

$$V_{out} = \sqrt{2} * V_{orms} * \cos \omega_o t \tag{2.5}$$

During the switching interval m_1, the average positive output voltage and average negative output voltage can be calculated as

$$V_{out}\left(t_{op}\right) = V_{in}(t_o) * m_1 \tag{2.6}$$

$$V_{out}(t_{on}) = -V_{in}(t_o) * m_2 \tag{2.7}$$

It should be pointed out that the sampling time T is much smaller than the input voltage period and the output voltage period (at least 10 times larger than the output frequency for a frequency step up operation). Therefore, the input voltage and the output voltage at time t_o to t_o+T is assumed to be unchanged. The average output voltage at this sampling period T can then be calculated as

$$V_{out}(t_o) = V_{in}(t_o) * (m_1 - m_2) \tag{2.8}$$

According to equation 2.3 and 2.8, m_1, m_2 can be calculated as

$$m_1 = \frac{1+\frac{V_{orms}*\cos\omega_o t}{V_{irms}*\cos\omega_i t}}{2} \tag{2.9}$$

$$m_2 = \frac{1-\frac{V_{orms}*\cos\omega_o t}{V_{irms}*\cos\omega_i t}}{2} \tag{2.10}$$

$$0 \le m_1, m_2 \le 1 \tag{2.11}$$

$$\left|\frac{V_{orms}*\cos\omega_o t}{V_{irms}*\cos\omega_i t}\right| \le 1 \tag{2.12}$$

From (2.12), it can be observed that the output voltage must have a zero value when the input voltage is equal to zero, which means the output voltage must cross zero more frequently than the input voltage, which also proves that when this kind of modulation method is applied to the single phase matrix converter, the output frequency must be an integer times the input frequency.

$$\omega_0 = N * \omega_i \tag{2.13}$$

More importantly, when the input voltage is equal to zero, m_1, m_2 is calculated by

$$m_1 = \frac{1+\frac{V_{orms}*\omega_o t}{V_{irms}*\omega_i t}}{2} \tag{2.14}$$

$$m_2 = \frac{1-\frac{V_{orms}*\omega_o t}{V_{irms}*\omega_i t}}{2} \tag{2.15}$$

It could be further concluded from (2.11) and (2.14) that

$$V_o \le \frac{\omega_i}{\omega_o} V_i \tag{2.16}$$

This expression is a very important equation, since it states that based on this modulation method, for a boost in the output frequency, there will be a decrease in the maximum output voltage. For example, if the input voltage is 230 V RMS at 60 Hz, the output frequency of 960 Hz (medium frequency suitable for a rotary transformer) ac waveform’s peak value is limited to $230 * \frac{60}{960} = 13.75$ V RMS. For the application of rotary transformer, this voltage is typically too low, so that a large current will be required to supply the field power, which will create an additional loss in the transformer winding.

Apart from the shortage low output voltage at high frequency output, the switching loss will also be increased at high frequency output. Based on the above reasons, the average voltage modulation method is not suitable for this project.

Fig 2.26 shows the simulation result of the input voltage, output voltage and output current based on the average voltage modulation method. The input voltage is 60Hz 110 V peak with a RL load of 1 ohm and 200 mH. The output frequency is 120 Hz with a sampling frequency at 10 kHz. It could be observed from the output current waveform that there are more ripples in the negative cycle than in the positive cycle. These unsymmetrical ripples may create saturation in the transformer load and are caused by the unsymmetrical characteristics of the modulation method. Another modulation method proposed by Babaei is used to address this issue [80]. In his paper, sampling time T is divided into two equal time cycles to modulate an output voltage. During the positive half cycle, S1, S4 are turned on first followed by S2, S3 to modulate output voltage based on the same procedure on (2.8). During the negative half cycle, S2, S3 are turned on then followed by S1, S4 to modulate the same output voltage, shown in (2.20,21). n_1, n_2 are the duty ratios for S1, S4 and S2, S3 during the negative half cycle. Although the current waveform is better by using this modulation method, this method in fact doubles the sampling frequency which creates an additional switching loss.

$$\frac{T}{2} = T_1 + T_2 = T_3 + T_4 \tag{2.17}$$

$$m_1 = \frac{T_1}{T/2}\ m_2 = \frac{T_2}{T/2} \tag{2.18}$$

$$n_1 = \frac{T_3}{T/2}\ n_2 = \frac{T_4}{T/2} \tag{2.19}$$

$$n_1 + n_2 = 1 \tag{2.20}$$

$$V_{out}(t_o) = V_{in}(t_o) * (n_2 - n_1) \tag{2.21}$$

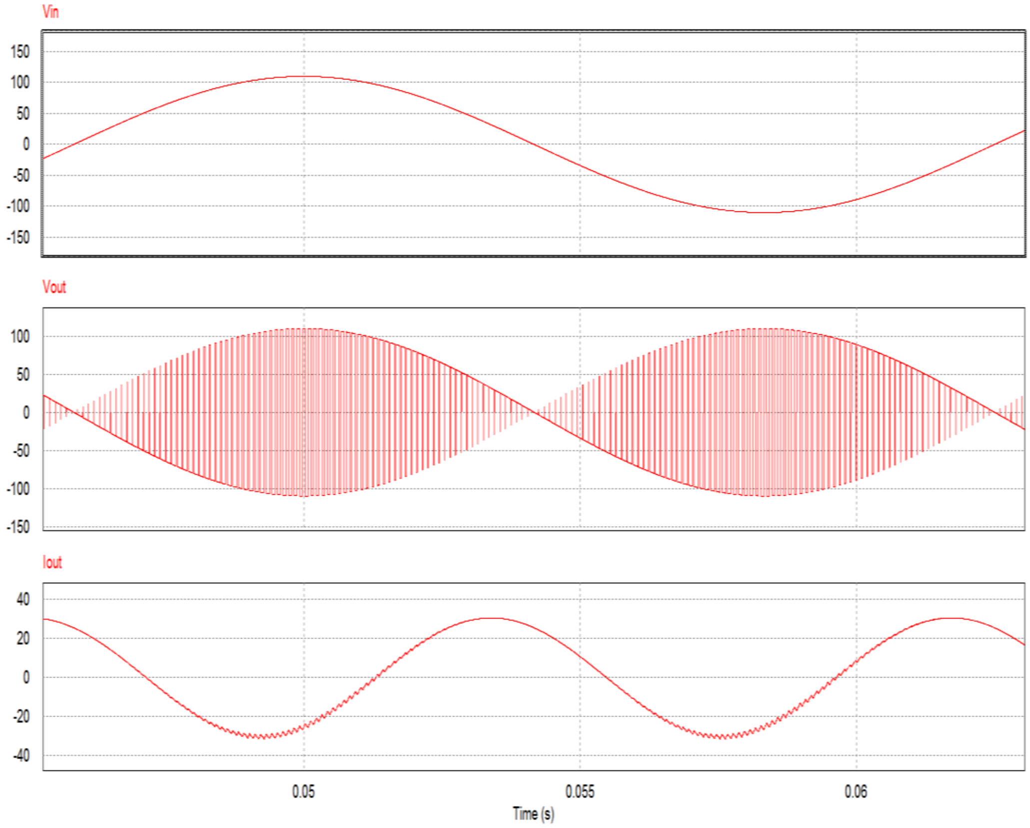

Figure 2.26. Input voltage, output voltage and output current waveform of a SPMC based on average voltage modulation method

2.5.2 Constant time modulation

Since the average voltage method will not generate enough voltage at high frequency output, a constant time modulation method is proposed to increase output voltage for the single phase matrix converter. In this method, the output high frequency voltage is generated by a square wave triggered gate signal. The conduction sequence follows the same procedure as S1, S4 and S2, S3 like in the average voltage method. However, the duty cycle m_1 is equal to the duty cycle m_2 for every switching interval. In other words, the single phase matrix converter works as a frequency step up cyclo-converter with this modulation method. Fig 2.27 shows the simulation result for the input voltage, output voltage and output current waveform based on this modulation method. The output frequency is 960 Hz, where the input voltage, input frequency and the load parameters are the same as the simulation in the average voltage method.

In order to control the output voltage and reduce the harmonics, PWM method [71, 78, 79, 81] could be applied to the constant time modulation method, but it will create an additional switching loss and complicate the commutation procedure. Researchers have concentrated on stepping up the low frequency, high voltage power line input into a medium frequency output to feed a power transformer by using the constant time modulation method. The transformer size could be reduced significantly by this approach [82-88]. However, by using this modulation method, the output volts per Hz (Volts*seconds) is not a constant value during each switching time. Thus, the medium frequency transformer core has to be designed based on the time interval which has the highest volts per Hz. Accordingly, the core material of the power transformer is not fully utilized in this switching method, which not only increases the total volume but also increases the total cost of building the transformer.

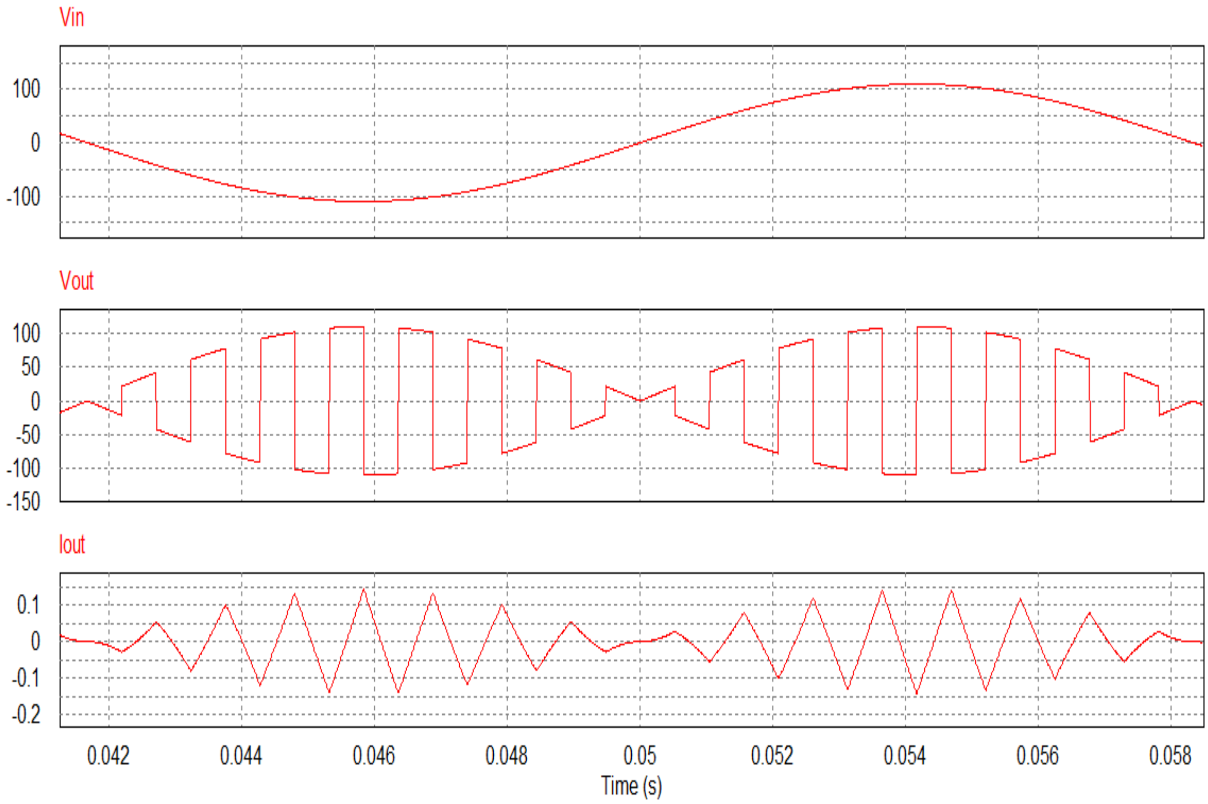

Figure 2.27. Input voltage, output voltage, and output current wave form based on constant time modulation method

2.6 Input filter requirement

The input filter is a very important part for the matrix converter, since it helps to prevent the unwanted higher order harmonic current to flow through the input side and also prevents the switching harmonics from affecting the line side voltage[89]. The input filter is generally a LC tank in the line side which is shown in Fig.2.1. On one hand, the capacitor is used to prevent a surge voltage from the line side to affect the applied voltage to the matrix converter and prevent the high voltage spike due to the high $\frac{di}{dt}$ of the inductance during the switching event. On the other hand, since the load of the matrix converter generally has an inductive behavior, which creates a low pass filter characteristic. The higher order harmonic current will flow through the input side of the matrix converter, a properly tuned inductor could filter out this harmonic current which creates a unity power factor at the input side. Note that if there is no requirement for the shape of the input current, a simple capacitor at the line side will be enough.

The three basic rules in designing the input filter are listed in [90].

1. The size of the LC filter has to be as compact as possible.
2. The inductor value must be small in order to reduce the voltage drop at the load side.
3. The filter resonant frequency has to be in the range of ten times larger than the input frequency and ten times smaller than the switching frequency.

It should be noted that for some modulation methods, for example, medium frequency output based on constant time modulation; the input frequency is 60 Hz, where the output is around 1000 Hz, and the filter tank which has a resonant value around 1000 Hz could create some resonance with the output circuit which will create an input voltage distortion. A parallel resistor with the inductor will help to damp out the energy but additional losses will be introduced. In contrast, for a system without the filter inductor, a sine voltage with less distortion could be applied to the matrix converter.

For the application of brushless excitation system in this thesis, a filter inductor is not required, because in contrast with the power consumption of main wound field synchronous machine, the field power is generally around 3 percent. Thus, the distortion to the source caused by the brushless exciter system will not be significant compared with the main drive.

2.7 Clamp circuit for matrix converter

For lack of dc link capacitor and non-passive switches in the matrix converter, a clamp circuit is generally needed to prevent the input surge voltage from affecting the output, and also prevent the output surge voltage from affecting the input. The typical clamp circuit consists of two rectifier diode bridges and a parallel resistor and capacitor shown in Fig 2.28.

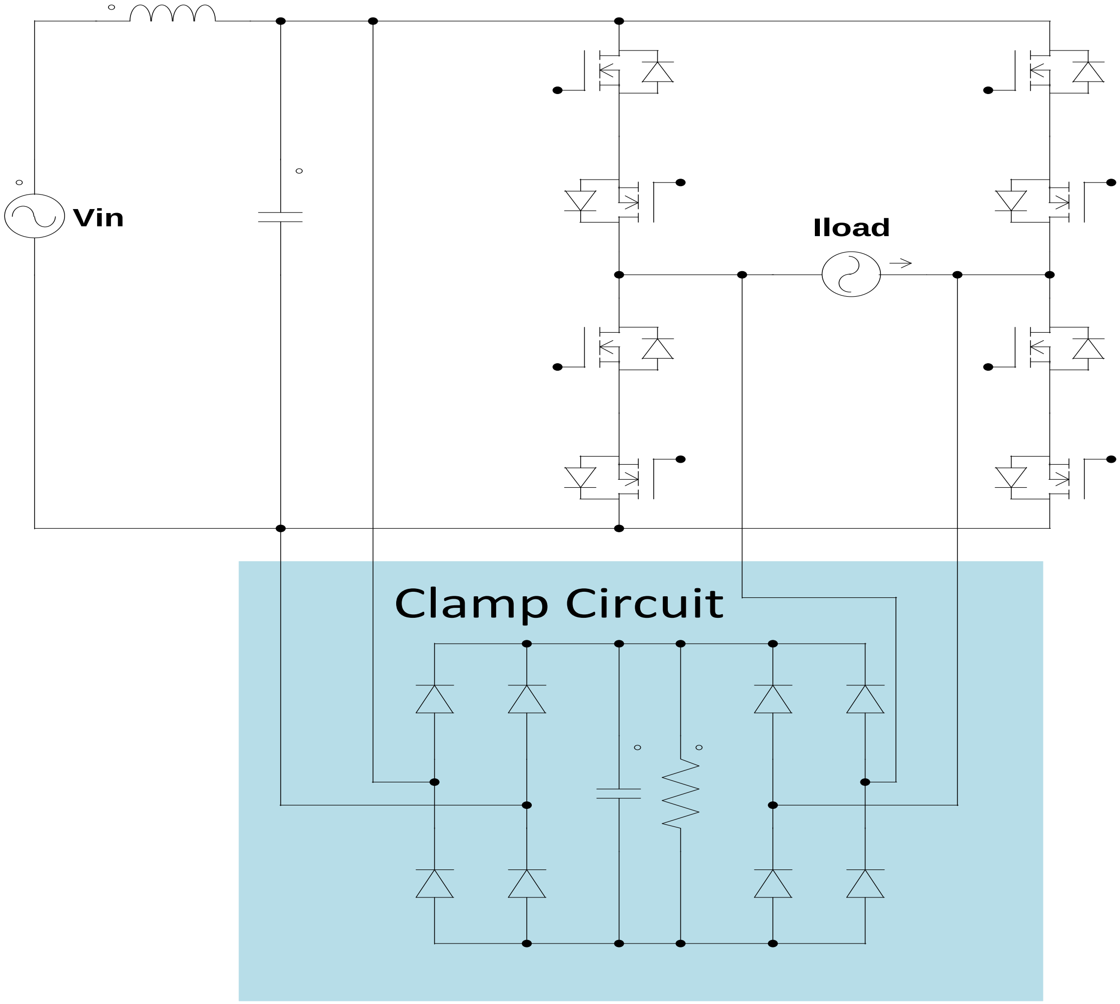

Figure 2.28. Typical clamp circuit structure for a single phase matrix converter

For an inverter based circuit, energy stored in the load could be released to the DC link capacitor through the body diodes when the system shuts down. In contrast, thanks to the ac input voltage, the energy stored in the load cannot be released to input capacitor through the passive body diodes when the system shuts down. This will create a large voltage spike to damage the semiconductor switches. The clamp circuit will help to provide a path for damping out the stored energy when this event happens which shows in Fig. 2.29. In Fig 2.29, the current direction of the load is assumed to flow from bottom to top. For this case, the current will flow through the clamp diode DC2 and DC3 to charge the clamp capacitor, and when the current of the load is reversed, it will flow through DC1 and DC4 to charge the capacitor similarly. The clamp circuit will also act as a pathway for the bridge connection switches during dead time state if there are no snubber circuits in parallel with the semiconductor switches.

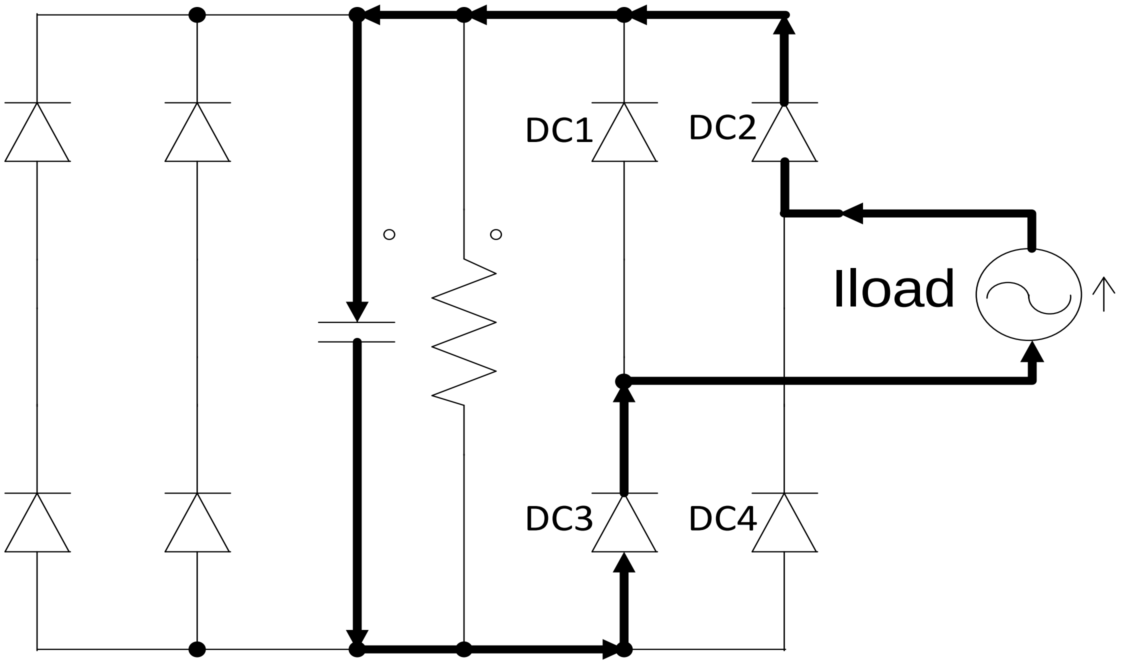

Figure 2.29. Current flow during shut down

It is important to optimize the size of the clamp circuit since the increased value of the clamp capacitor will also increase the overall system volume. To determine the minimum value of the clamp capacitor, the inductance and the current of the load must be known, since

$$E_{store} = \frac{1}{2} * L * I^2 \tag{2.22}$$

The average value of the voltage across the capacitor is

$$V_{cavg} = \frac{2\sqrt{2}}{pi} * V_{inrms} \tag{2.23}$$

It should be noted that in real case the average voltage value across capacitor may be higher than that in 2.23 since the high frequency harmonic current which exists in the matrix converter would also charge the capacitor. In theory if there is no parallel resistor, the average voltage across the capacitor will be the peak ac voltage. When the system shuts down, the stored energy is transferred into the capacitor, the increase of capacitor voltage can be calculated by

$$E_{store} = \frac{1}{2} * L * I^2 = \frac{1}{2} * C * (V_{cfinal}^2 - V_{cavg}^2) \tag{2.24}$$

$$V_{cfinal} = \sqrt{\frac{L*I^2}{C} + V_{cavg}^2} \tag{2.25}$$

Since the harmonic current may keep charging the capacitor, a parallel resistor is often present in the clamp circuit to damp out this harmonic energy. A small resistor could further reduce the size of the capacitor; however, it will also decrease the overall system efficiency.

2.8 Relative issues associated with the single phase matrix converter

Due to the absence of dc link capacitor, the matrix converter has taken the advantages of compactable size and fast system response. However, the absence of the large link capacitor also creates a few new limitations for the matrix converter.

One of the most important is the voltage transfer ratio between input and output. On one hand, for a dc to ac inverter, the voltage transfer ratio is 1 (no active front end). On the other hand, for the three-phase matrix converter, the maximum voltage transfer ratio is 0.866. Over modulation method can be applied to the three-phase matrix converter to increase the voltage transfer ratio to 1.05, but it will also add some low order harmonics to the system and cause some resonance in the circuit. The resonance may damage the switches without proper control, thus over modulation should not be applied to the matrix converter for a long period of time. For the single phase matrix converter, the voltage transfer ratio is even lower for high frequency output as stated in section 2.5.

Besides the low voltage transfer ratio, the matrix converter also requires a clamp circuit to provide a current path to dissipate the load energy when the system shuts down. Compared with an inverter based system, the extra clamp circuit in the matrix converter adds additional complexity to the system and increases the overall system size. But for an indirect matrix converter, a simple clamp circuit consists of only one diode and a capacitor could be applied [91].

Due to the energy stored in the dc link capacitor, the inverter based system will not have any ride through problems. However, this will not be the case for the matrix converter since no link capacitor is included in the system. To deal with this issue, a zero-state command is applied to the switches when the perturbation of the input happens [92]. The system will operate back to normal state when input voltage recovers.

Lastly, for a three-phase system, the unbalance of the source voltage will also create some additional low frequency harmonics to the output, but this will not be the case for the single phase matrix converter system.

2.9 Summary

The characteristics of the single phase matrix converter are demonstrated in this chapter. Although the invention of the single phase matrix converter has been almost two decades, the application of it is yet not fully discovered. Thus, a new application of the single phase matrix converter on field excitation of a wound field synchronous machine is presented in this chapter and will be explained in the next chapter.

Chapter 3

NEW CONSTANT VOLTS PER HZ MODULATION METHOD FOR SINGLE PHASE MATRIX CONVERTER

3.1 Introduction

The characteristics of the existing modulation methods for single phase matrix converter are introduced in the previous chapter. However, because the average voltage method cannot generate enough rms voltage from a 230-volt input; and the constant time modulation method creates an unequal average voltage value at each switching cycle, the transformer size is not optimized. On account of the above limitations on the existing modulations, a new modulation method for the single phase matrix converter is proposed in this thesis.

3.2 Constant volts per Hz modulation strategy

It is preferred to apply a constant volt per Hz to a transformer so that the transformer will have a balance maximum flux density at both positive and negative voltage cycle. Thus, the average voltage applied to the transformer for both positive and negative polarities should be a constant value as shows in (3.1).

$$\int_0^t \mathrm{V}\,\mathrm{dt} = N * S * \Delta B = constant \tag{3.1}$$

Where N is the primary turns number, B is the flux density, and S is the average flux area of a transformer. Fig.3.1. shows the input and output voltage waveform of the

SPMC for the proposed new constant Volt-sec modulation method. The constant Volts-secs will create a nearly constant flux linkage over each switching cycle in the transformer. By using this kind of modulation method, both the iron and copper of the transformer can be so fully utilized that a smaller and more efficient transformer can be designed.

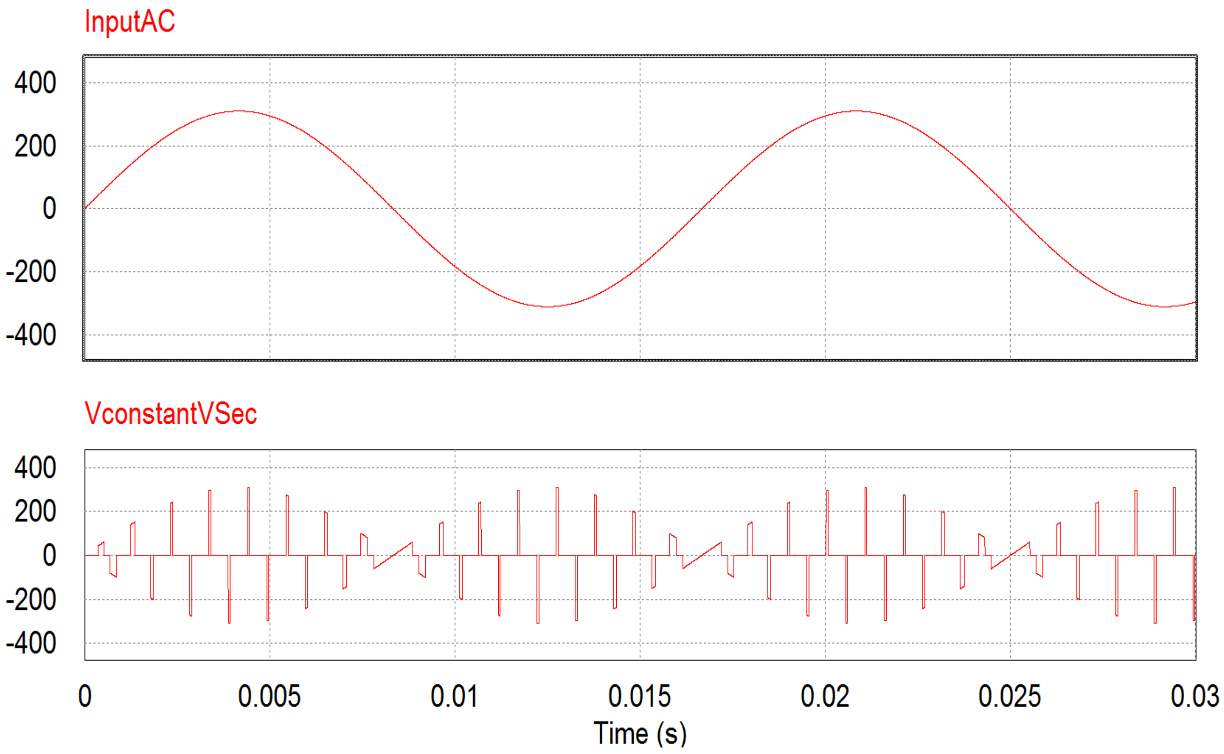

Figure 3.1. Proposed constant V/Hz modulation Method

3.3 Current flow based on constant volts per Hz modulation strategy

Unlike the traditional close area transformer, the rotary transformer has two airgaps between the stator core and the rotor core. As a consequence, a large magnetizing current will circulate in the circuit during the zero state. Hence, it is important to analyze the current flow in the proposed modulation method.

To analyze the current flow of the system, the load is modelled as a stiff current source due to the large field inductance. The transformer is modelled as a stator copper resistance, a stator leakage inductance, a rotor copper resistance, a rotor leakage inductance and a magnetizing inductance. According to the property of ferrite material, the rotary transformer will not have much core loss at medium frequency excitation, so the core loss term is not modelled as a parallel resistance with the magnetizing inductance in the proposed model shown in Fig 3.2, and the back to back connected bi-directional switch is modelled as one resistor (Rdson) in series with a body diode.

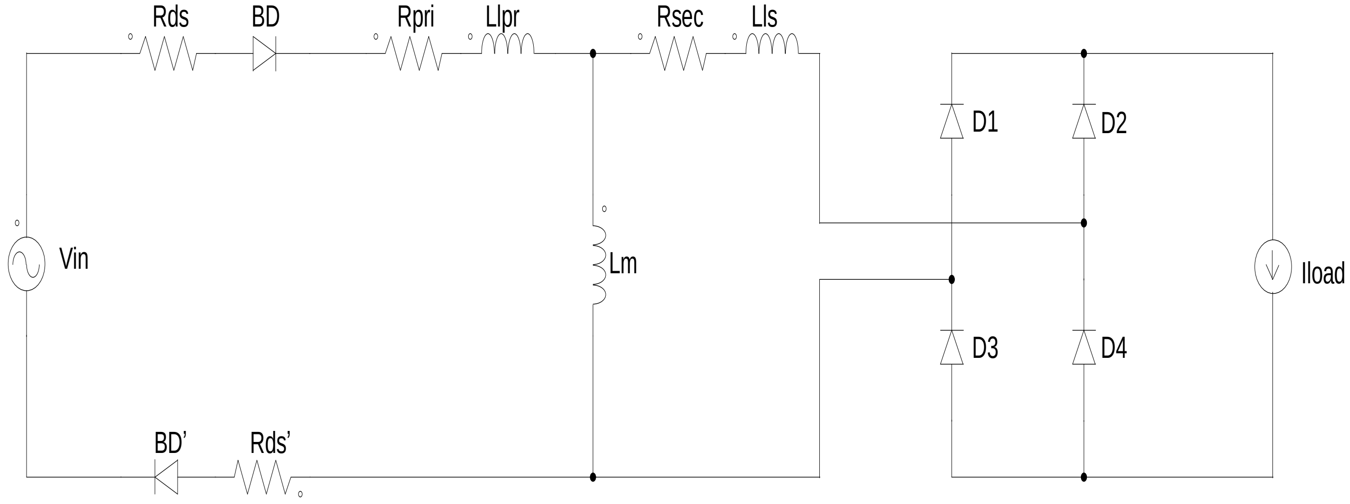

Figure 3.2 Proposed system structure with current flow

Assume the circuit works in the steady state, and the input voltage polarity is positive as shows in Fig.3.3. The magnetizing current flows from bottom to top (negative polarity magnetizing current) due to the charge by the negative polarity voltage before this state. Initially when D2 and D3 are on because of the positive polarity input voltage, the load current will be equal to the negative polarity magnetizing current plus the input current due to KCL. Due to the positive input voltage, the magnetizing current will change its polarity to positive (from top to bottom) by the end of this cycle as shown in Fig. 3.4. D2 and D3 continue conducting and the input current is equal to the load current plus the magnetizing current at this state.

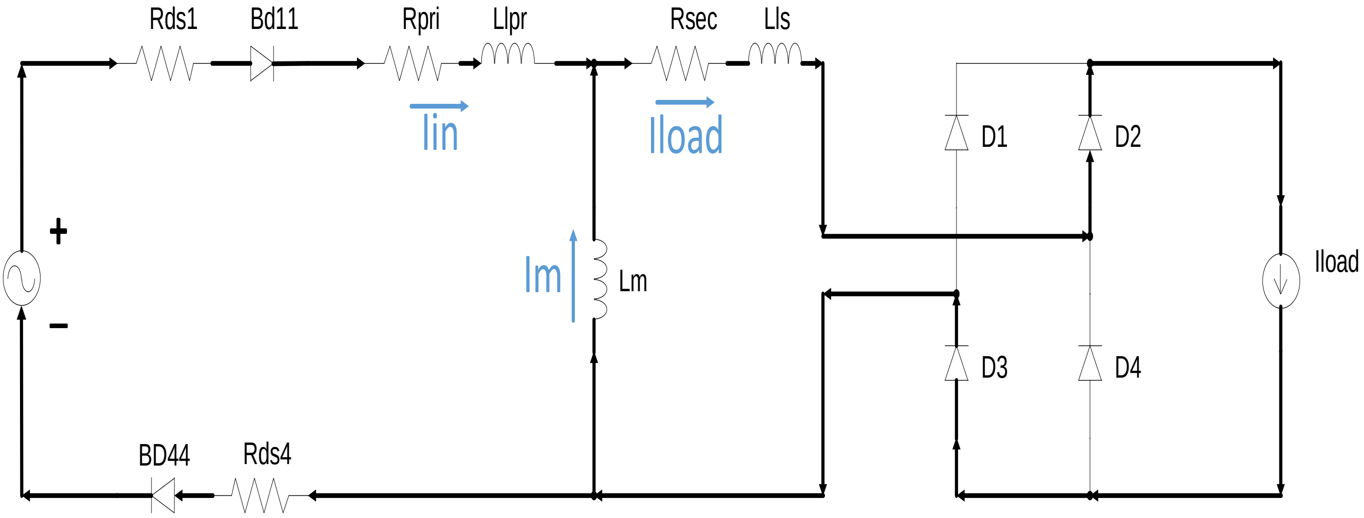

Figure 3.3 Positive input polarity state 1

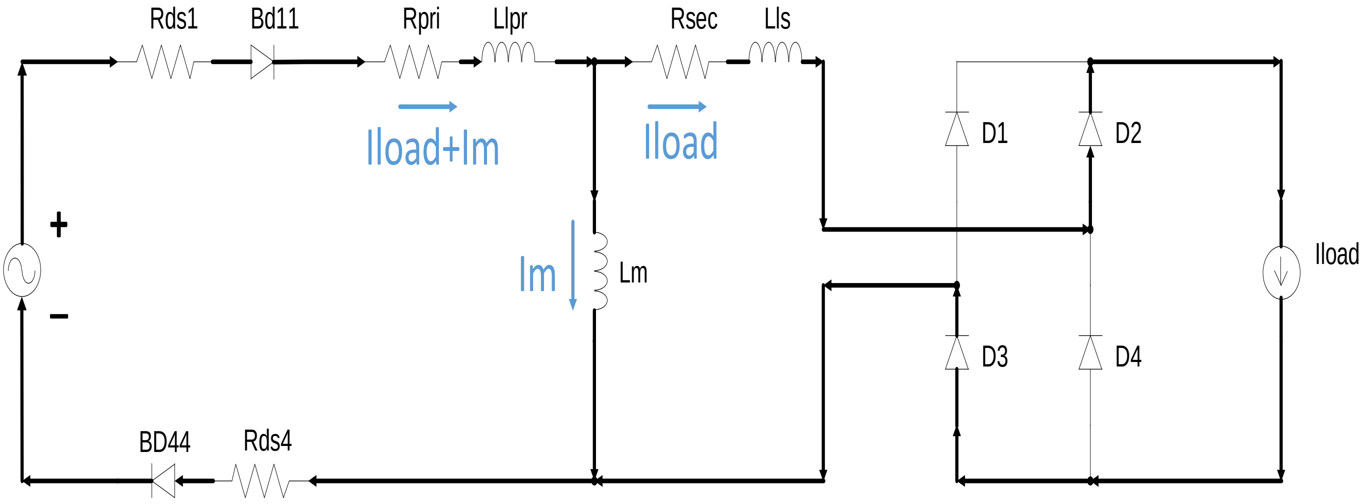

Figure 3.4 Positive input polarity state 2

The zero state (zero input voltage) will follow when the magnetizing current reaches its peak value as shown in Figure. 3.5. Due to the leakage inductance of the transformer, the input current from both the primary and secondary side will not die out immediately when the input voltage changes to zero. The load current is commutated from D3 to D4 at this state due to the dying out of the input current. It should be noted that in a real case the load current may also commutate from D2 to D1, since it depends on the distribution of the stray inductance in the circuit and the distribution of leakage inductance in the rotary transformer.

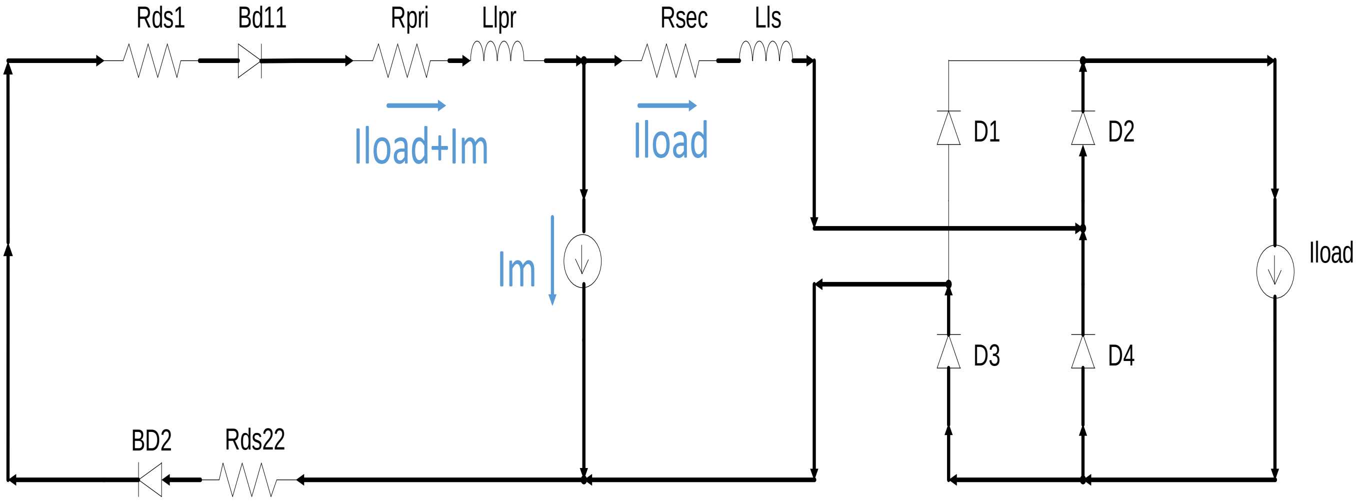

Figure 3.5 Zero state 3

When the energy stored in the transformer leakage inductance is dissipated (input current dies out), the magnetizing current is modelled as another current source shown in Fig. 3.6. And the load current is freewheeling across D2 and D4. Because there is a large zero state (freewheeling) time for the proposed modulation method, the magnetizing current will have a chance to flow on both the primary and secondary side of the rotary transformer compared to other modulation methods. The other characteristic of the proposed system structure is that the magnetizing current will tend to flow solely on the secondary side of the transformer shown in Fig.3.7 if the leakage inductance is small. Since for the magnetizing current to flow on the primary side of the transformer, it must overcome two body diodes' voltage drop plus two resistance (Rdson) caused by the MOSFETs. This will reduce the rms current on the primary side, which also reduces the size of the heat sink in PCB and increases the power density of the system. Moreover, because the secondary side of the transformer rotates with the machine, the copper wire on the secondary side will have a better air cooling to dissipate its heat caused by the loss of conducting magnetizing current.

In a real case, the primary side winding would also have a possibility to conduct partial of the magnetizing current during the zero state, which is determined by the value of the transformer primary and secondary side leakage inductance.

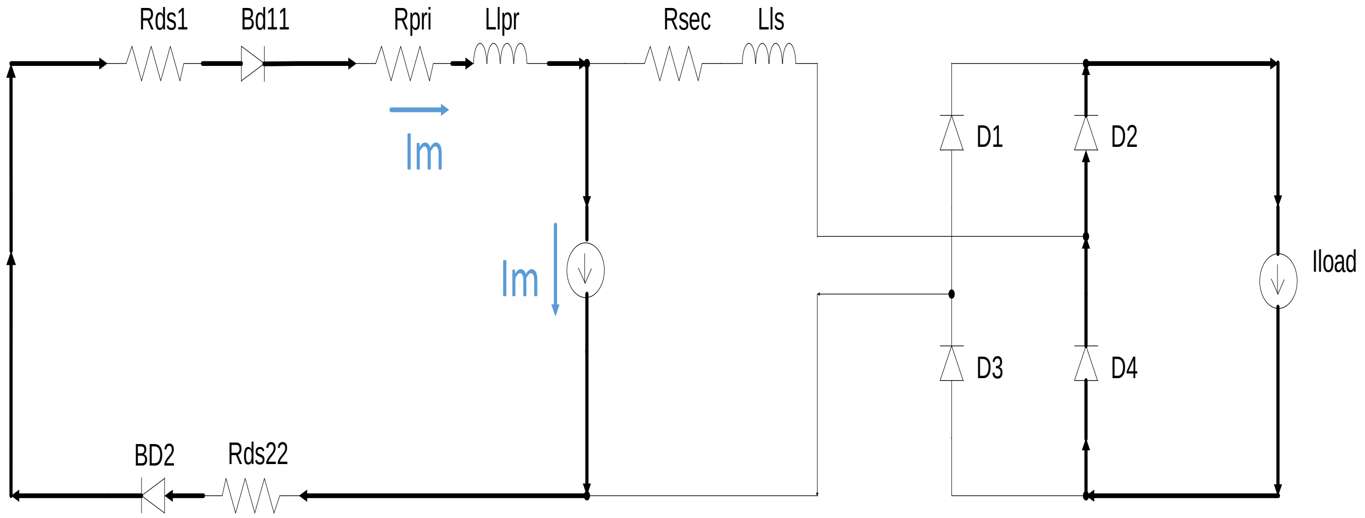

Figure 3.6 Zero state 4

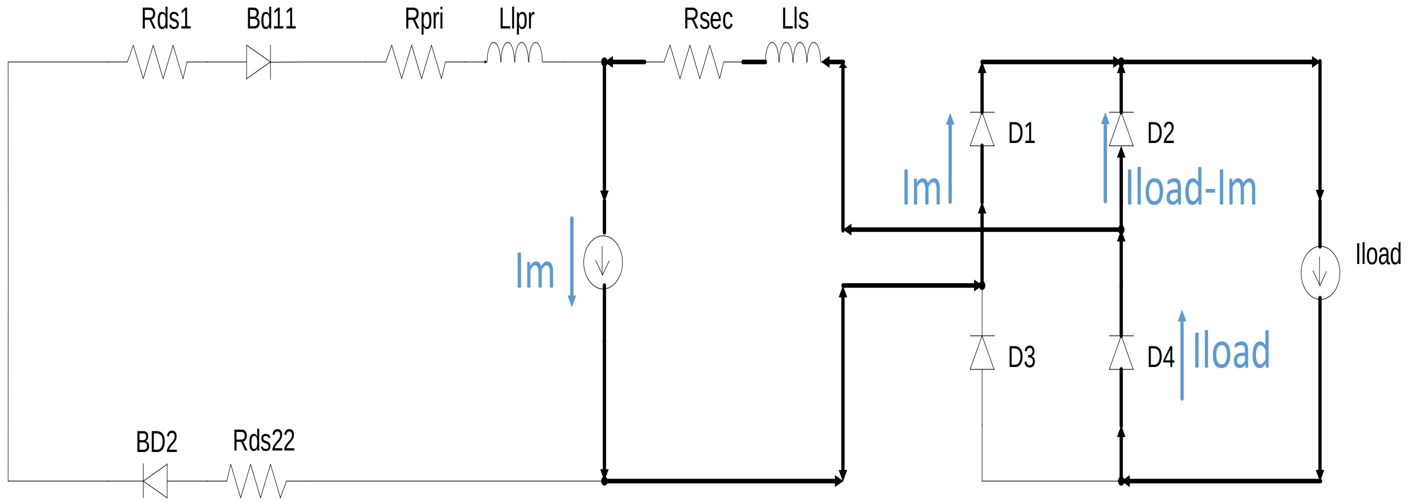

Figure 3.7 Zero state 5

Figure 3.8-12 shows the current flow when the input voltage polarity is negative, which will follow the same sequence as the positive cycle. The complementary switches will conduct the current flow on the primary side of the transformer and the complementary diodes pair D1 and D4 will conduct the current on the secondary side of the transformer this time instead of D2 and D3.

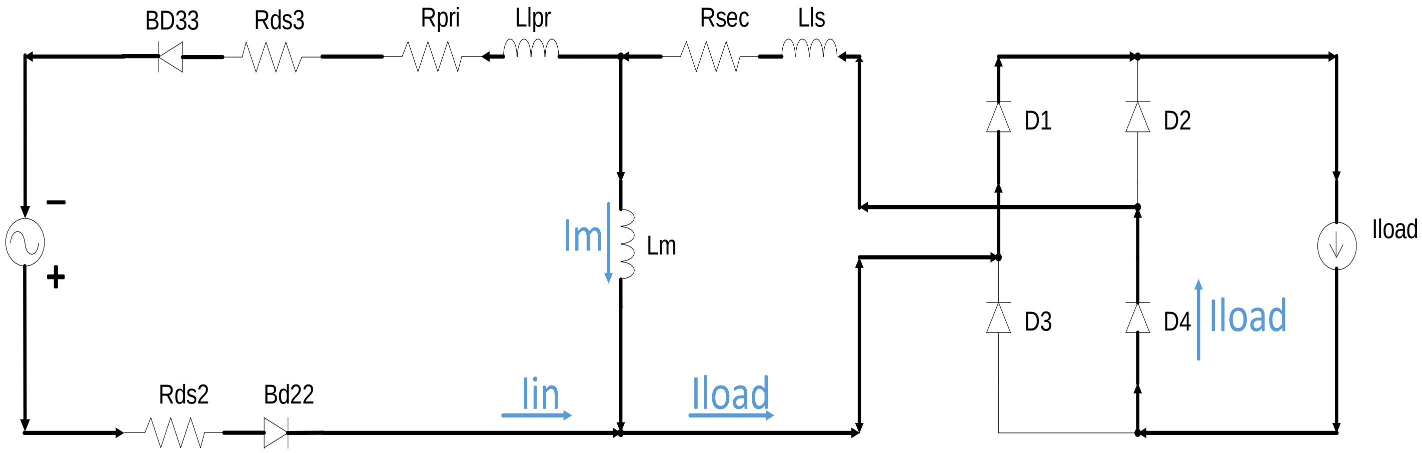

Figure 3.8 Negative input voltage polarity state 6

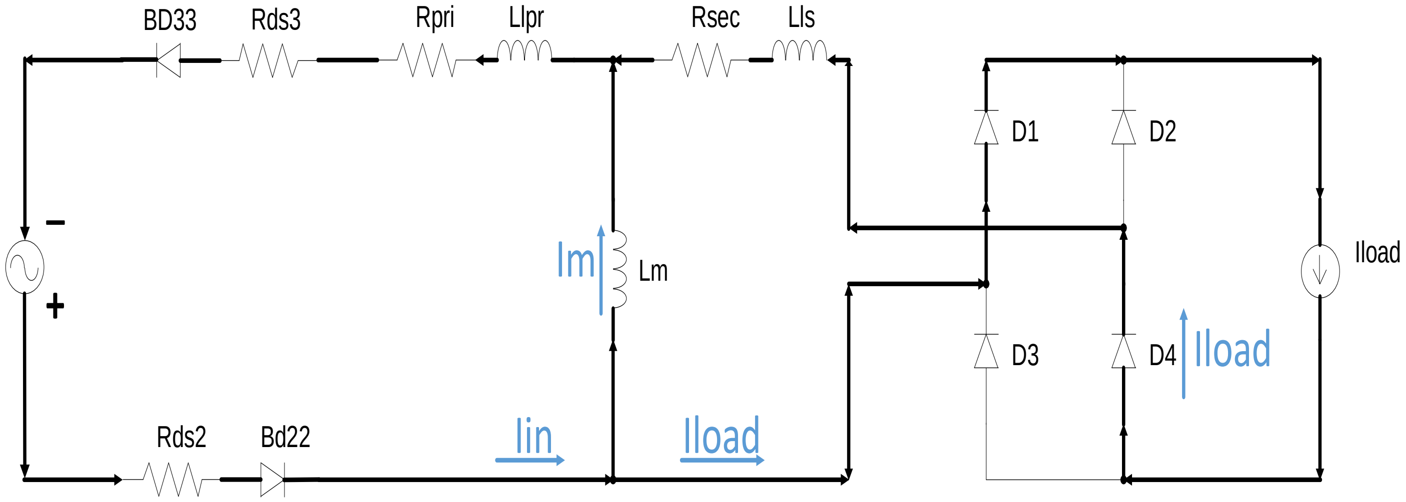

Figure 3.9 Negative input voltage polarity state 7

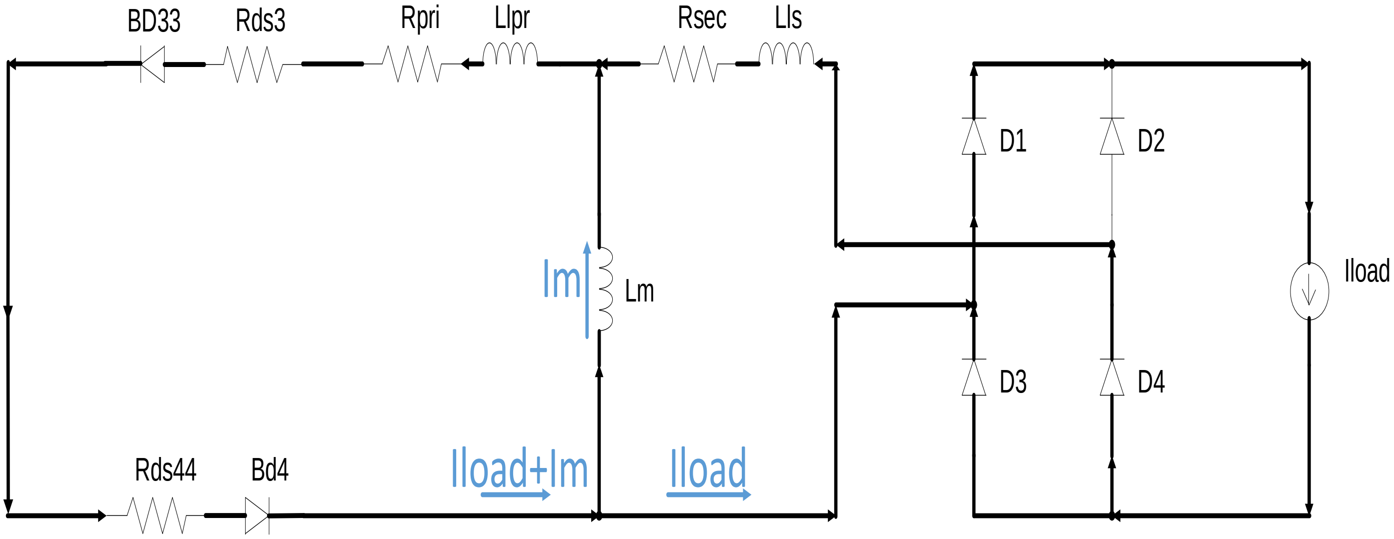

Figure 3.10 Zero state 8

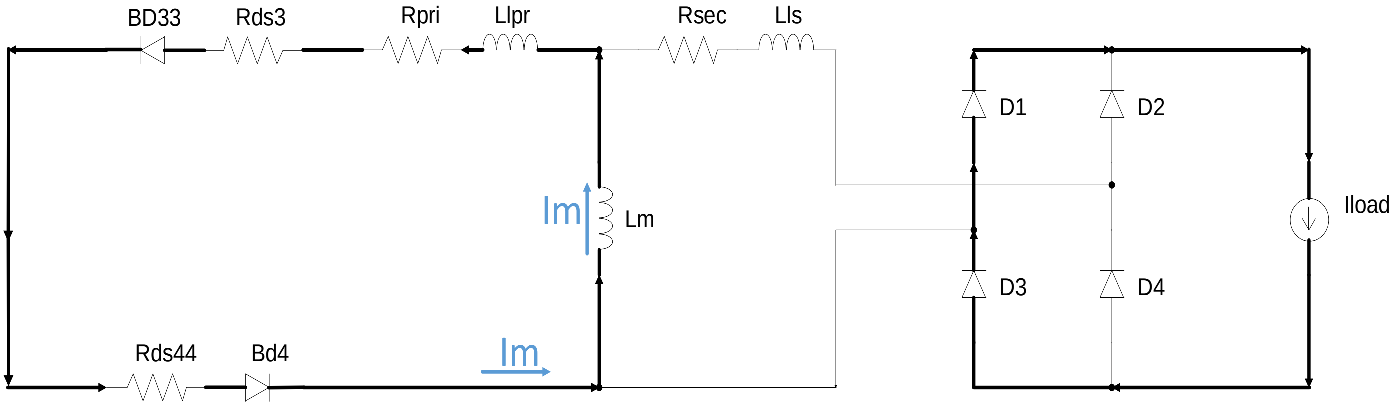

Figure 3.11 Zero state 9

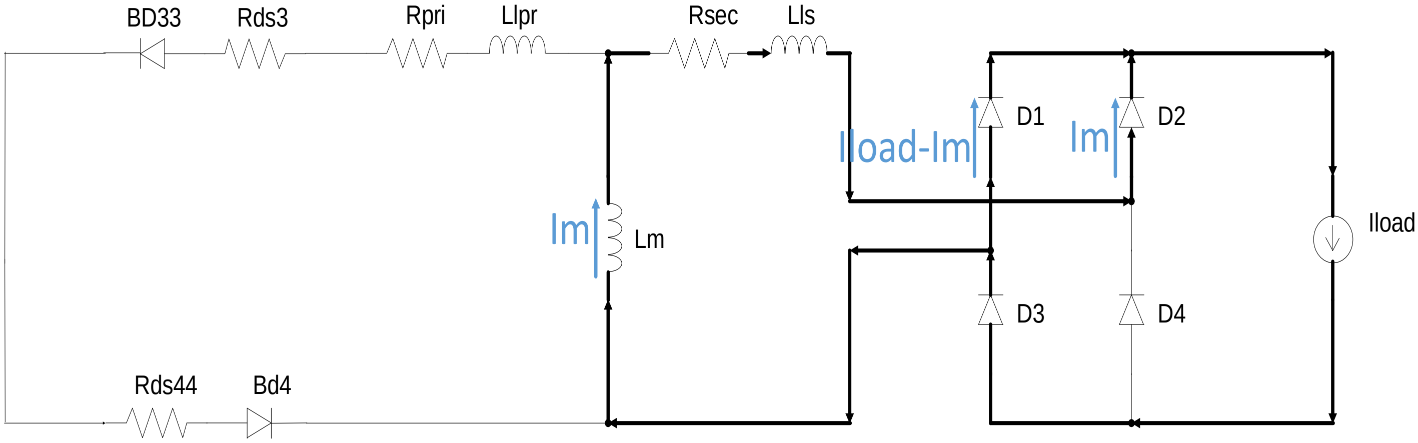

Figure 3.12 Zero state 10

3.4 Simulation result based on constant volts per Hz modulation strategy

Based on the commutation method stated in Chapter 2 and the proposed constant volts per Hz modulation method, a circuit simulation is performed on Power-sim. Table.3.1 shows the simulation parameters of circuit elements and Table.3.2 shows the simulation parameters of the rotary transformer. The field inductance in the real wound field synchronous machine could be much higher than the simulated value (in the unit of several Henries) but increasing the value of the field inductance will also significantly increase the simulation time. Thus, a smaller value of 10mH is chosen as the field inductance.

For a dual bridge matrix converter, it is not applicable to reduce the field inductance in simulation since a large field inductance can create over voltage issue during starting, but it will not be the case for the direct matrix converter topology proposed.

Table 3.1 Simulation input parameter

Input Voltage Amplitude (RMS)	230V
Input Voltage Frequency	60Hz
Fundamental Output Frequency	960Hz
Input Filter Inductance	50uH
Input Filter Capacitance	30uF
MOSFET Rds On	88mΩ
MOSFET Body Diode Forward Voltage	0.7V
Rectifier Diode Forward Voltage	0.95V
Simulated Field Inductance	10mH
Field Winding Resistance	0.3Ω

Table 3.2 Simulation rotary transformer parameter

Magnetizing Inductance	2mH
Primary Side Leakage Inductance	6uH
Primary Side Copper Resistance	88mΩ
Secondary Side Leakage Inductance (Refer to Primary Side)	6uH
Secondary Side Copper Resistance (Refer to Primary Side)	149mΩ
Primary to Secondary Turns Ratio	3

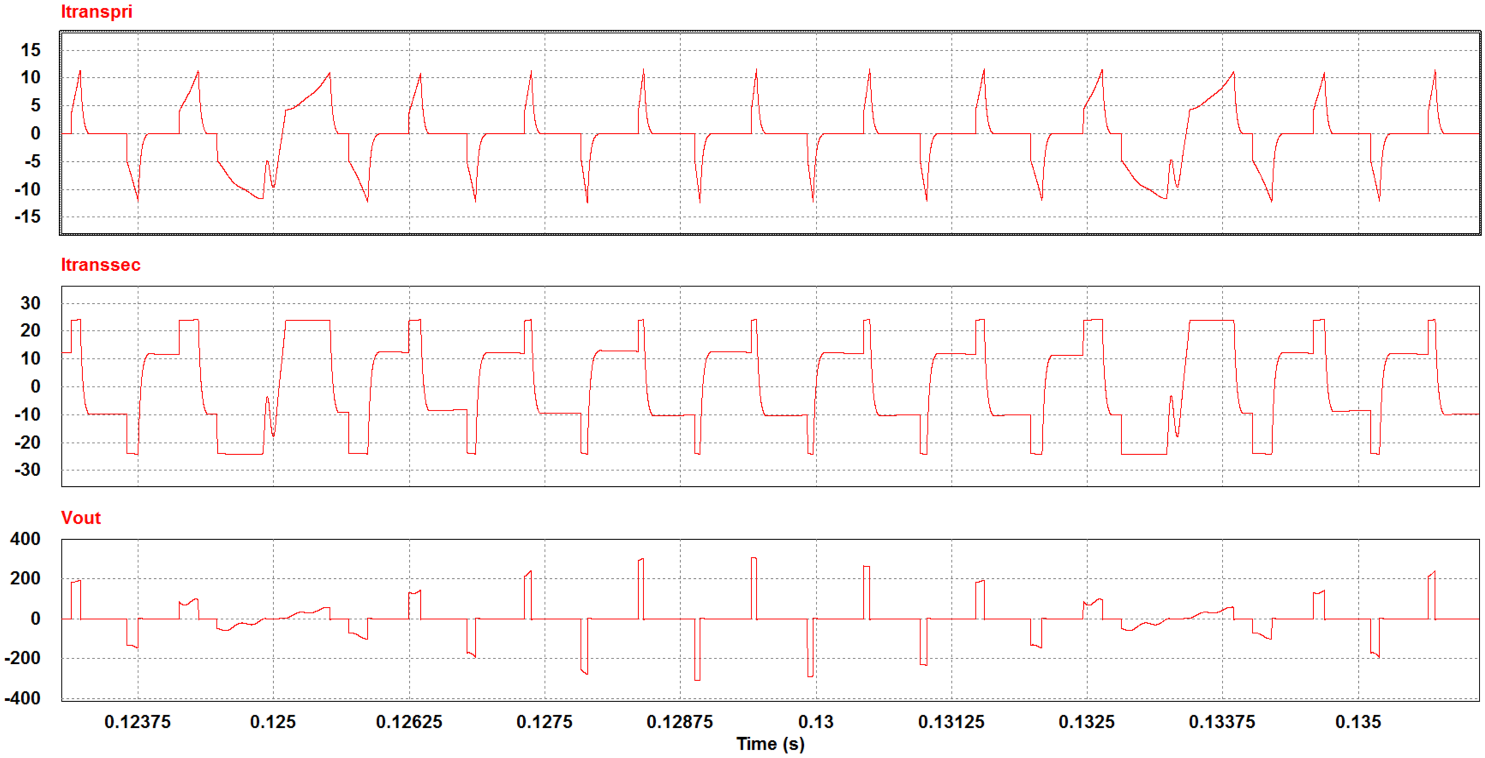

Figure 3.13 Transformer primary side current, secondary current, and input voltage (Output voltage of the matrix converter)

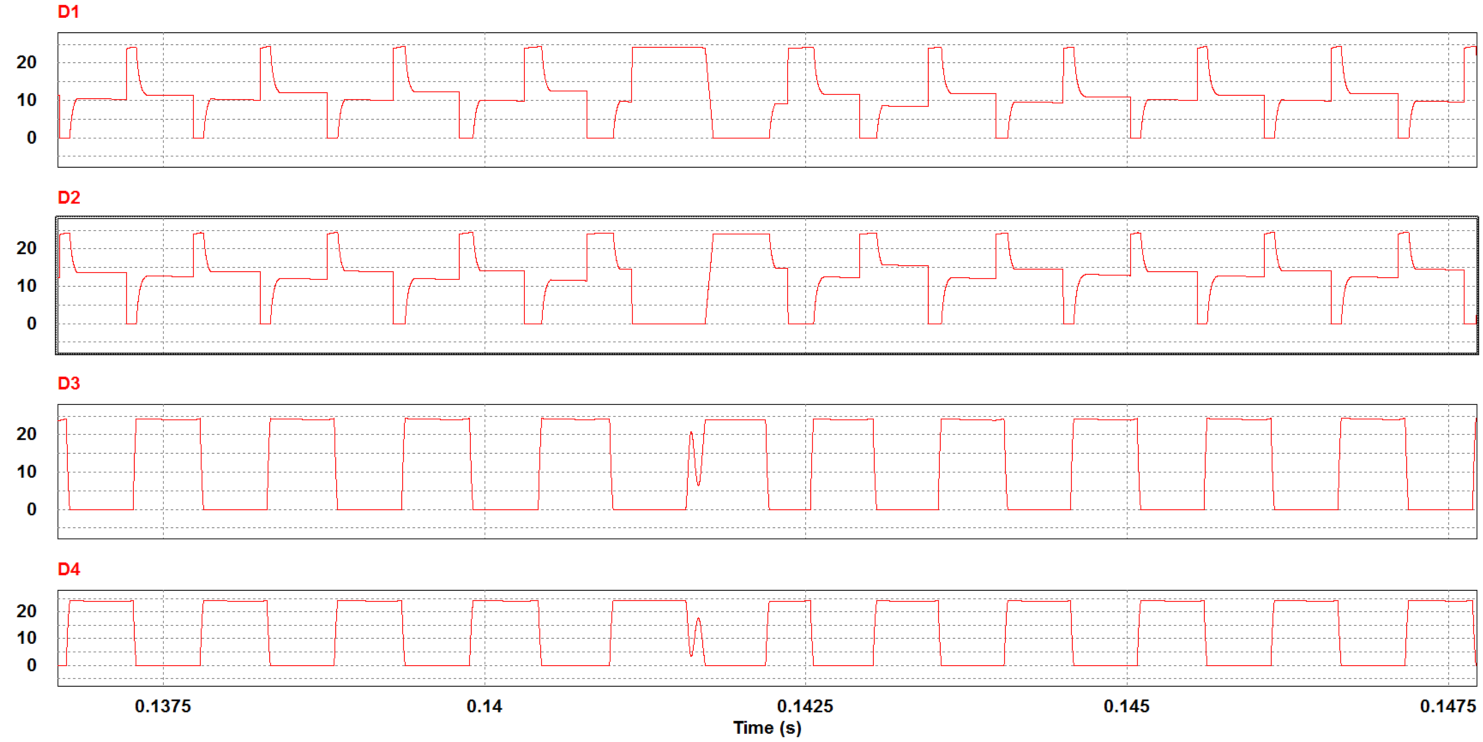

Figure 3.14 Rectifier diodes current waveform

Figure 3.13 shows the steady state input, output current and the input voltage waveform of the rotary transformer. It can be observed from the simulation result that all the magnetizing current flows on the secondary side of the transformer during the zero state. In other words, when the input voltage of the transformer is zero, there is no current flow on the primary side of the transformer, which not only reduces the current stress on the primary side active switches, but also creates a benefit for the magnetizing current to have better cooling on the secondary side of the transformer as pointed out in the last section. Figure 3.14 shows the simulation result of current waveform on the rotating diode bridges. The result for the current commutation sequence in diode bridge matches the proposed current flow sequence in the last section.

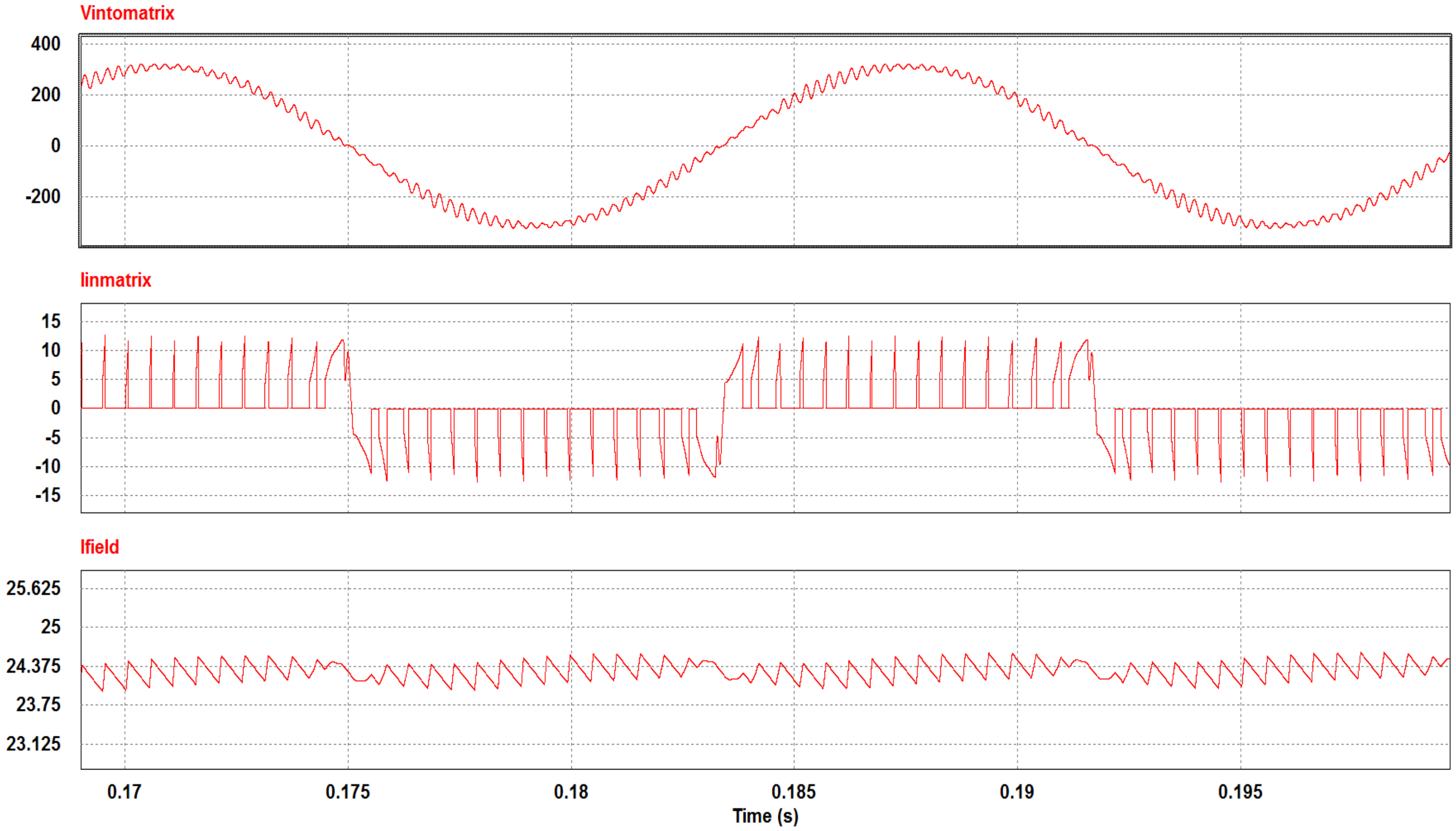

Figure 3.15 Input voltage, input current to the matrix converter and output field current waveform

The input voltage to the matrix converter is shown in Fig.3.15. Owing to the resonance of input LC filter, there is small ripple in the applied voltage. The applied voltage can be smoother by reducing the filter inductance or adding a parallel resistor to damp out the stored energy in the inductor. Fig.3.15 also shows the input current to the matrix converter and the field winding dc current.

Major simulation results are summarized in Table 3.3. The conduction loss of the active switches and copper loss of the transformer are calculated in Table 3.4 based on the simulation result. Table 3.4 also includes the output power and the calculated system efficiency. Since the overall system is operated at 960 Hz medium frequency, the switching (0.8W) and core loss (0.2W) are much smaller than the conduction and copper loss. Thus, the switching and core loss is not included in the system efficiency calculation.

Table 3.3 Summarized simulation result

Primary Side RMS Output Current	4.62A
Secondary Side RMS Output Current	15.2A
Average Output Voltage per half cycle	30.44V
RMS Output Voltage	74.4V
Field Current Ripple	0.7A
Average Field Current	24.3A

It can be observed from Table 3.4 that the major loss component in the system is the rectifier bridge (19 percent), which is caused by the large field current. Without considering the power loss in the rectifier bridge, the proposed system has an efficiency over 90 percent. Thus, the overall system efficiency is limited by the field current requirement of the machine.

Table 3.4 Summarized output power and loss

MOSFETs Conduction Loss	10.2W
RT Primary Side Copper Loss	1.88W
RT Secondary Side Copper Loss	3.83W
Rectifier Diodes Conduction Loss	45.6W
Output Power	177W
Calculated System Efficiency	74.2%
Efficiency Without Rectifier Diodes	91.8%

Chapter 4

ROTARY TRANSFORMER DESIGN PROCEDURE AND NEW OPTIMIZATION METHOD

4.1 Introduction

It has been presented in Chapter 1 that there are two major types of rotary transformer: the concentric cylinder type and pot core type. The typical structure for the rotary transformer is shown in Fig.4.1.

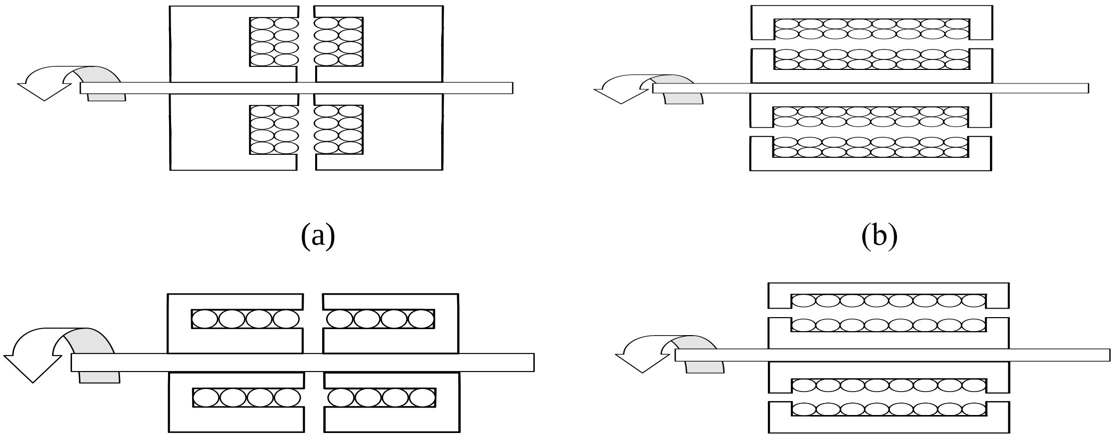

(a) (b)

(c) (d)

Figure 4.1 Typical rotary transformer structure (a) two-layer pot core type RT (b) two layer concentric cylinder RT (c) one layer pot core type RT (d) one layer concentric cylinder RT

For the single layer winding structure, the axial length for the pot core type rotary transformer will be doubled compared to the concentric cylinder type rotary transformer. To reduce the axial length for the pot core transformer, a multi-layer winding structure could be applied. However, the multi-layer winding in the rotary transformer is generally not preferred based on several reasons. First, the multilayer winding would cause high proximity effect which increases the transformer loss. Second, the increase of layers will also significantly increase the leakage inductance. Third, the radial length of the transformer must keep short since the flux density of the radial direction is not uniformly distributed, but multi-layer winding will increase the radial length of the transformer. Fourth, besides the proximity effect, the dc resistance will also be larger in a multi-layer winding owing to a larger diameter.

The design procedure for these two types of rotary transformer is the same, because the only geometry difference between these two types of transformers is the location of airgap as shown in Fig.4.2. Based on the above reasons, the concentric cylinder rotary transformer with one layer winding is chosen as an example in the optimized design of the rotary transformer in this chapter.

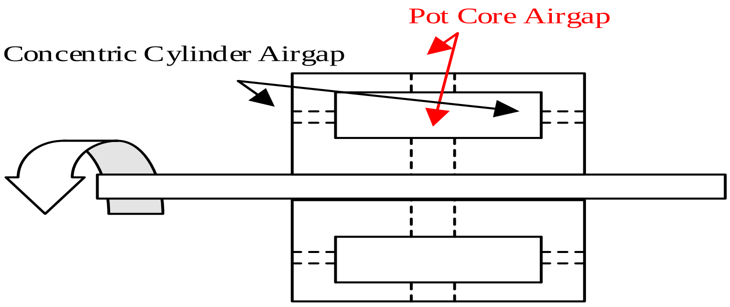

Figure 4.2 Generalized rotary transformer structure

4.2 Flux density requirement

Figure 4.3 shows the dimension of a concentric cylinder type rotary transformer with a single layer winding. The notation in this thesis will follow Landsman's paper, but the optimization procedure will be different.

The first constraint of designing a transformer results from the saturation of the magnetic materials. Laminated steel could work from 1 to 2 Tesla, whereas ferrite material typically works around 0.2 Tesla. For medium frequency applications, ferrite material is preferred owing to low eddy current loss in core. According to (3.1)

$$\Delta B = \frac{\int_0^t \mathrm{V}\,\mathrm{dt}}{N*A_m} \tag{4.1}$$

$$\mathrm{B}_{\max} = \frac{\Delta B}{2} = \frac{\int_0^t \mathrm{V}\,\mathrm{dt}}{2*N*A_m} \tag{4.2}$$

Thus, the maximum flux density in the core is constrained by the applied volts per Hz ($\int_0^t \mathrm{V}\,\mathrm{dt}$), transformer primary side turns number (N) and the core cross section area (A_m). To keep the flux density in the core less than the saturation flux density, a proper value for these three parameters must be chosen.

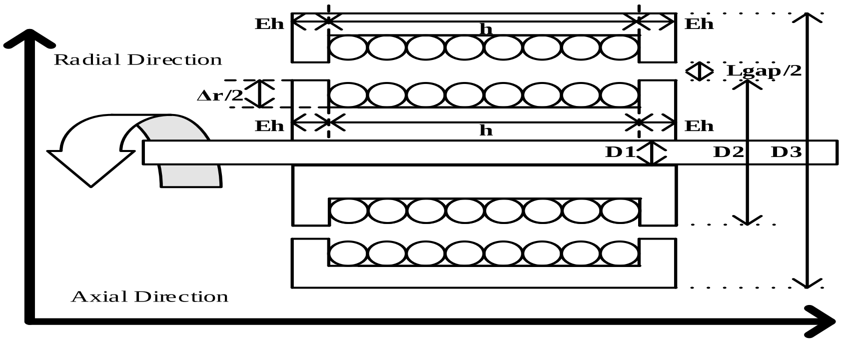

Figure 4.3 Dimensions for the concentric cylinder type rotary transformer with a single layer winding

4.3 Inductance calculation

4.3.1 Magnetizing inductance

As there are two airgaps in the rotary transformer, it has a much smaller magnetizing inductance than the traditional power transformer. Although the inductor does not consume any real power, a small magnetizing inductance will generate a large magnetizing current which significantly reduces system efficiency. Because the reluctance of the core is much less than that of the airgap, the estimated magnetizing inductance can be calculated by only considering the airgap reluctance in (4.3),

$$L_{mesti} = \frac{N_{pri}^2 * u_0 * A_m}{L_{gap}} \tag{4.3}$$

Due to the fringing effect of the airgap, the real magnetizing inductance will be larger than the estimated value in (4.3), thus an adjusting factor (Ff) is defined in (4.4) by Mclyman to include the fringing effect.

$$\mathrm{F}f = 1 + \frac{L_{gap}}{\sqrt{A_m}} * \ln(\frac{2*h}{L_{gap}}) \tag{4.4}$$

The magnetizing inductance of the rotary transformer is defined in (4.5).

$$L_m = L_{mesti} * Ff \tag{4.5}$$

4.3.2 Leakage inductance

Because the transformer is operated at 960 Hz medium frequency, it is important to consider the leakage inductance effect. It has been stated previously that multi-layer windings will have a larger leakage inductance than the single layer winding, so single winding structure is chosen to design the transformer. The leakage inductance could be calculated by the stored energy (E) of the magnetic field in the winding area.

$$E = \frac{1}{2} L_{lk} * I^2 = \frac{1}{2} \int_v B * H dv \tag{4.6}$$

Since the total MMF generated by the winding is N*I, and the MMF drop in the core is much less than the MMF drop in the air, so

$$H_{max} = \frac{N*I}{h} \tag{4.7}$$

In addition, the leakage inductance referred to the primary side can be estimated as

$$L_{lk} = {N_{turn}}^2 * \frac{u_0}{3} * \frac{\pi * D_2 * \Delta r}{h} \tag{4.8}$$

Where N_{turn} is the turns number and u_0 is the vacuum permeability. In the real case the leakage inductance could be higher than the estimated value, according to Landsman in the worst case it could be three times larger due to the leakage path which is not accounted for in the proposed model.

4.4 Loss calculation

4.4.1 Core loss

Hysteresis and eddy current loss are the two major loss components for the transformer core. Steinmetz Equation (4.9) could be used to estimate the total hysteresis loss in ferrite materials accurately.

$$P_{core} = K * f_s^{a} * B^{\beta} * V_{core} \tag{4.9}$$

Where f_s is the frequency in Hz, B is the maximum flux density in Tesla and V_{core} is the effective volume in m^3. K, α and β could be calculated based on the material datasheet.

For ferrite materials, the eddy current is almost zero due to the large resistivity, and the major core loss term is caused by the hysteresis part. Thus, in a medium frequency system, the major loss in a transformer is not core loss but copper conduction loss. For laminated iron, eddy current will be the dominant term at high frequency. As a result, it is preferred to use iron material below the kHz level.

4.4.2 Copper loss based on constant V/Hz modulation

It has been stated in the last section that copper loss will be the dominant loss term in a rotary transformer. Both the primary RMS and secondary side RMS current must be known to calculate the total copper loss. As the proposed modulation method is new, it is necessary to build a new model to estimate the winding current.

Because the input 60 Hz voltage is not applied to the load at all the time, it is useful to define a duty cycle (D) when the input voltage is applied to the load side.

$$\mathrm{D} = \frac{t_1+t_2+t_3+\cdots+t_{16}}{T/2} \tag{4.10}$$

Where t_1 to t_{16} is the time when the input voltage is applied to the transformer (at other time there is only zero voltage applied to the load, selected switches are on for freewheeling zero state). For example t_1 is from 0 to 1/1920 s, T is the period for the input voltage, which is 1/60 s in this case. The equation means for a T/2 (120Hz) interval, there are 16 voltage pulses (2 pulses per cycle) which are applied to the load to simulate the fundamental output frequency of 960 ($\frac{16}{2} * 120$) Hz.

First, the load DC current can be calculated by using the average voltage model, for the large field inductance filters all the ac voltage content.

$$\mathrm{E} = 1920 * \int_0^{1/1920} \sqrt{2} * V_{RMS} * \sin\omega t \tag{4.11}$$

$$I_{load} = \frac{\left(\frac{E}{N}-2*V_d\right)}{R_{Load}+\left(R_{sec}+\frac{R_{pri}}{N^2}+4\frac{R_{dson}}{N^2}\right)*D} \tag{4.12}$$

Where E is the average input voltage for one half cycle, which is also the output DC voltage after the rectifier diodes, N is the turns ratio between the primary side to the secondary side, Vd is the rectifier diodes voltage drop on the secondary side of the transformer. R_{Load} is the field winding resistance. R_{pri} and R_{sed} are the primary and secondary side transformer resistance, and R_{dson} is the turn on resistance of the MOSFET.

The voltage drop on the leakage inductance is not included in this model since for medium frequency transformers, the voltage drop on the leakage inductance is less than 5 percent for a leakage inductance of 100uH for a 200W load. And the maximum leakage inductance during the optimization procedure is limited to a max value of 20uH.

The maximum magnetizing current is calculated by the total volts per Hz applied to the magnetizing inductance since

$$\int \mathrm{V}\,\mathrm{dt} = \mathrm{L}_m * \Delta\mathrm{I} \tag{4.13}$$

$$\Delta\mathrm{I} = \frac{\int \mathrm{V}\,\mathrm{dt}}{\mathrm{L}_m} \tag{4.14}$$

$$I_{mmax} = \frac{\Delta\mathrm{I}}{2} = \frac{\int \mathrm{V}\,\mathrm{dt}}{2*\mathrm{L}_m} \tag{4.15}$$

Where $\int \mathrm{V}\,\mathrm{dt}$ is the volts per Hz applied to the transformer each half cycle, $\Delta\mathrm{I}$ is the peak to peak magnetizing current, and I_{mmax} is the maximum magnetizing current.

It has been discussed in Chapter 3 that the flow of the magnetizing current in the zero state is not only determined by the transformer parameter but also determined by the parasitic inductance and resistance in the Printed Circuit Board, so the actual RMS current on the primary side and secondary side is extremely hard to model. However, on the one hand, the maximum RMS current on the primary side winding and the minimum RMS current on the secondary side winding can be calculated by assuming that the magnetizing current will all flow on the primary side. On the other hand, the minimum RMS current on the primary side winding and the maximum RMS current on the secondary side winding can also be calculated by assuming the magnetizing current all flows on the secondary side. Based on the average load current and the maximum magnetizing current, the minimum input current and maximum input current can be calculated

$$I_{PRImax} = \frac{I_{load}}{N} + I_{mmax} \tag{4.16}$$

$$I_{PRImin} = \frac{I_{load}}{N} - I_{mmax} \tag{4.17}$$

The minimum primary side current occurs at the beginning of each cycle where the input voltage begins to charge the magnetizing inductance to the reverse polarity and the maximum input current occurs at the end of each cycle where the magnetizing current has been charged to the reverse polarity. The primary side RMS current can be calculated by assuming the integral of square function is the area of a trapezoid in (4.18) and (4.19)

$$I_{PRIrmsmin} = \sqrt{\left({I_{PRImax}}^2 + {I_{PRImin}}^2\right) * D/2} \tag{4.18}$$

$$I_{PRIrmsmax} = \sqrt{\left({I_{PRImax}}^2 + {I_{PRImin}}^2\right) * \frac{D}{2} + {I_{mmax}}^2 * (1 - D)} \tag{4.19}$$

The calculation of the secondary side RMS current is easier since there are only two current levels. The result is shown in (4.20) and (4.21).

$$I_{SECrmsmax} = \sqrt{I^2{}_{load} * D + (I_{mmax} * N)^2 * (1 - D)} \tag{4.20}$$

$$I_{SECrmsmin} = \sqrt{I^2{}_{load} * D} \tag{4.21}$$

It should be pointed out again that in this model the effect of the leakage inductance is not included, but even in the worst case where the circuit has a 100uH leakage inductance for a 200W load, the deviation from the calculated rms current to the simulation result is still less than 5 percent.

Based on the RMS current shown above, the copper loss for the case where magnetizing current solely flows on the primary side ($P_{copperMP}$) and for the case where magnetizing current solely flows on the secondary side ($P_{copperMS}$) can be calculated. The total copper loss (P_{copper}) can be calculated by averaging the two results.

$$P_{copperMP} = {I_{PRIrmsmax}}^2 * R_{pri} + {I_{SECrmsmin}}^2 * R_{sec} \tag{4.22}$$

$$P_{copperMS} = I_{PRIrmsmin}{}^{2} * R_{pri} + I_{SECrmsmax}{}^{2} * R_{sec} \tag{4.23}$$

$$P_{copper} = \frac{P_{copperMP}+P_{copperMS}}{2} \tag{4.24}$$

4.5 New optimization procedure

4.5.1 Introduction

A new optimization procedure for the rotary transformer based on the proposed modulation method is presented in this section. The procedure will give the transformer not only a minimum weight but also a minimum power loss with no iteration. A 200-Watt rotary transformer with a load resistance of 0.3 ohms will be used as an example in this chapter, where the maximum flux density in the transformer (B_{max}) is set to be 0.2 Tesla.

4.5.2 Wire size, Δr and turns ratio determination

The first step in the optimization procedure is to determine the wire size of the rotary transformer. It has been shown in the previous chapter that the RMS current in both the primary and secondary side winding based on constant volts per Hz method is smaller than that in the square wave method. Therefore, it is applicable to use the square wave modulation method to determine the maximum current that will flow in the rotary transformer. First, the secondary side maximum current can be calculated, where P_{out} is the load power.

$$I_{secmax} = \sqrt{\frac{P_{out}}{R_{load}}} = \sqrt{\frac{200}{0.3}}\text{A=25.8 A} \tag{4.25}$$

Thus a AWG number 12 wire will be chosen for the secondary side winding. For the primary side winding, the maximum current will be calculated by the input power and input square wave voltage. Assume the worst case, where the overall system efficiency is 70 percent, the primary maximum current could be calculated as

$$I_{primax} = \frac{P_{load}}{\eta * E} = \frac{200}{0.7 * 31.8} = 9A \tag{4.26}$$

η is the system efficiency and E is the average half cycle voltage (960 Hz 31.83V output from a 230V RMS 60Hz input). So, AWG number 14 wire will be chosen for the primary side winding. The $\Delta\mathrm{r}$ could also be determined when the wire size is set. In this case since the diameter for AWG number 12 wire is (0.106inch 2.69mm) larger than the diameter of AWG number 14 wire (0.096inch 2.44mm), so $\frac{\Delta\mathrm{r}}{2}$ is set to be 0.12 inch (ten percent larger than 0.106inch).

The turns ratio N could be set by considering the secondary side voltage

$$V_{sec} = (V_{load} + 2 * V_D) = (I_{secmax} * R_{load} + 2 * V_D) \tag{4.27}$$

$$= (25.8 * 0.3 + 0.95 * 2)V = 9.64V$$

Since there is an additional voltage drop in the MOSFET turn on resistance and the transformer winding resistance, the worst case is considered where this resistance consumes additional 10 percent of the secondary side output voltage.

$$V_{secworstcase} = V_{sec} * 1.1 = 10.604V \tag{4.28}$$

The turns ratio could then be determined by (4.29)

$$\mathrm{N} = \frac{E}{V_{secworstcase}} = 3 \tag{4.29}$$

4.5.3 Minimum weight constraint

Because the winding diameter and the turns ratio have been set, the winding window width *h* could also be determined in by (4.30) and (4.31).

$$h_{pri} = D_{pri} * N_{pri} \tag{4.30}$$

$$h_{sec} = \frac{D_{sec} * N_{pri}}{N} \tag{4.31}$$

Where h_{pri} is the minimum width for the primary side winding, and h_{sec} is the minimum width for the secondary side winding, the overall winding width h for the transformer is determined by the transformer side which has the larger winding width. Because in this case the primary minimum winding width is larger, consider the filling factor α (equal to 1.2 in this case),

$$\mathrm{h} = \alpha * h_{pri} \tag{4.32}$$

This is a very important equation for it automatically sets the transformer core to be minimum weight at every different dimension during the optimization procedure. It will be more obvious to the case where the transformer has equal number turns, since the diameter and turns number are more equally distributed on both the primary and secondary side winding. To prove the equation has successfully optimized the total size of the transformer, the weight of the transformer core is calculated below.

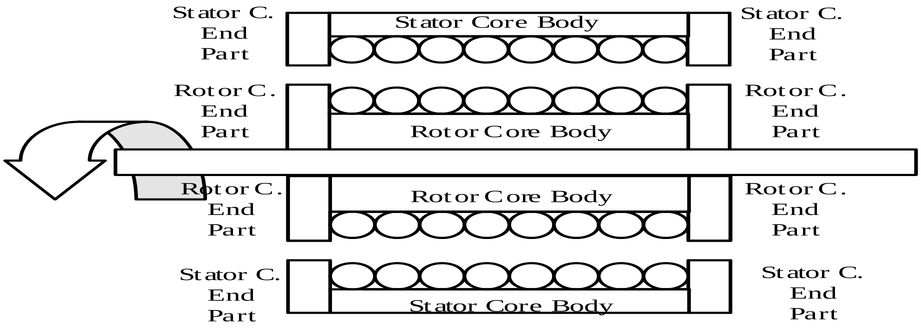

Figure 4.4. Different core part

Before the calculation of the total transformer weight, the average flux area A_m should be known. Since the average flux area in the transformer core needs to be a constant value, which maintains uniformly distributed magnetic flux density, the flux area in rotor core body, stator core body, stator core end part and rotor core end part should also be the same as shown in (4.33).

$$A_m = \pi(\frac{D_2-\Delta r}{2})^2 - \pi\left(\frac{D_1}{2}\right)^2 = \pi\left(\frac{D_3}{2}\right)^2 - \pi\left(\frac{D_2+L_{gap}+\Delta r}{2}\right)^2 = \pi * (D_2 - \Delta r) * Eh \quad (4.33)$$

Based on (4.33) the outer Diameter D_3 and the end cap height Eh could be also calculated in (4.34) and (4.35). D_1 is the required shaft diameter, which is 2.54cm (1 inch) in this example.

$$D_3 = \sqrt{(D_2 - \Delta r)^2 - D_1^2 + (D_2 + L_{gap} + \Delta r)^2} \quad (4.34)$$

$$Eh = \frac{(\frac{D_2-\Delta r}{2})^2 - \left(\frac{D_1}{2}\right)^2}{D_2-\Delta r} \quad (4.35)$$

The transformer is divided into six parts as shown in Figure 4.4 to calculate the total weight. The volume of the rotor core body and that of the stator core body are calculated in (4.36), and the volume of the two stator core end parts and that of the two rotor core end parts are calculated in (4.37) and (4.38)

$$V_{rcbd} = V_{stbd} = A_m * h \quad (4.36)$$

$$2* \mathrm{V}_{rep} = 2 * \pi * \frac{(D_2^2-D_1^2)}{4} * Eh = \pi * \frac{(D_2^2-D_1^2)}{2} * Eh \quad (4.37)$$

$$2* \mathrm{V}_{sep} = 2 * \pi * \frac{(D_3^2-(D_2+L_{gap})^2)}{4} * Eh = \pi * \frac{(D_3^2-(D_2+L_{gap})^2)}{2} * Eh \quad (4.38)$$

V_{rcbd}, V_{stbd} are the rotor and stator core body volume and V_{rep}, V_{sep} are the rotor and stator core end parts. Combining equation (4.30), (4.32) and (4.36), the relationship between the turns number and core body volume could be established in (4.39)

$$V_{rcbd} = V_{stbd} = A_m * D_{pri} * N_{pri} * \alpha \quad (4.39)$$

According to (4.2), the relationship between N_{pri} and A_m is shown in (4.40)

$$N_{pri} = \frac{\int_0^t \mathrm{V}\,\mathrm{dt}}{2*\mathrm{B_{max}}*A_m} \quad (4.40)$$

By inserting (4.40) into (4.39),

$$V_{rcbd} = V_{stbd} = A_m * D_{pri} * N_{pri} * \alpha = A_m * D_{pri} * \frac{\int_0^t \mathrm{V}\,\mathrm{dt}}{2 * \mathrm{B_{max}} * A_m} * \alpha$$

$$=D_{pri}*\frac{\int_0^t \mathrm{V\,dt}}{2*\mathrm{B_{max}}}*\alpha \tag{4.41}$$

Equation (4.41) is the most powerful equation in the procedure, for it gives the insight into why (4.32) sets the transformer total volume to be minimum at all different D2 value. It could be observed from (4.41) that once the flux density $\mathrm{B_{max}}$, input voltage V, input frequency f (which is equal to $\frac{2}{t}$ since t is equal to the half period $\frac{1}{2T}$), input current (in a linear relationship with the wire diameter D_{pri}) and the filling factor α are set, the volume of the two transformer body cores is also set no matter how D2 changes.

The total volume and weight of the transformer core are determined by (4.42) (4.43).

$$V_{transcore} = V_{rcbd} + V_{stbd} + 2 * \mathrm{V}_{rep} + 2 * \mathrm{V}_{sep} \tag{4.42}$$

$$M_{transcore} = V_{transcore} * \rho_{core} \tag{4.43}$$

where $V_{transcore}$ and $M_{transcore}$ are the total volume and weight for the transformer core. ρ_{core} is the transformer density.

Although the volume for the end part $\mathrm{V}_{rep}, \mathrm{V}_{sep}$increases with D_2, they will not be the dominant term of the total core volume for a reasonable range of D_2. Because a large D2 also means the larger the A_m and smaller in turns number shown in (4.33) (4.40), a smaller turns number will decrease the magnetizing inductance and create a huge conduction loss at larger D_2 which will be shown in the next section.

The copper weight for the primary side ($M_{scopper}$) and secondary side ($M_{rcopper}$) is calculated in (4.43) and (4.44). And the total weight (M_{tot}) for the transformer is calculated in (4.45). L_s, L_r are the stator and rotor winding length in meters and ρ_s, ρ_r are the stator and rotor winding density in kg/m. In this case, ρ_s is 12.43 pound per

1000 feet, ρ_r is 19.77 pound per 1000 feet.

$$M_{scopper} = L_s * \rho_s = N_{pri} * \pi * (D_2 + L_g + \Delta r) * \rho_s \tag{4.43}$$

$$M_{rcopper} = L_r * \rho_r = \frac{N_{pri}}{N} * \pi * (D_2) \; * \rho_r \tag{4.44}$$

$$M_{tot} = M_{scopper} + M_{rcopper} + M_{transcore} \tag{4.45}$$

4.5.4 Airgap determination

The quantity L_{gap} is the first parameter which needs to be determined before proceeding to the power optimization procedure. Although the bearings in industry nowadays could hold the tolerance less than 0.02mm, owing to the harsh environment a motor or generator may have, it is preferred to have an airgap larger than 0.1mm. For most electric machines, the airgap is generally between 0.5-2mm. However, a larger airgap also means a small magnetizing inductance and larger copper loss. In consequence, an airgap of 0.5mm (L_{gap}=2*0.5mm=1mm) is used in the optimization procedure to increase the system reliability and keep the magnetizing inductance at a reasonable value.

4.5.5 Power loss calculation

It has been discussed in section 4.4 that the transformer loss consists of the copper and core loss. Since the length for the primary and secondary side wires is determined in (4.43), the resistance of the primary (R_{pri}) and secondary (R_{sec}) winding could also be calculated. ρ_{rs} and ρ_{rr} are the resistivity for the primary and secondary side winding, which are 8.29 and 5.21mΩ/m in this case.

$$R_{pri} = L_s * \rho_{rs} \tag{4.46}$$

$$R_{sec} = L_r * \rho_{rr} \tag{4.47}$$

Based on the calculated winding resistance in (4.46) and (4.47), the total copper power loss could then be calculated by the proposed method in section 4.4.2.

Core loss could be calculated by using the Steinmetz Equation based on the datasheet provided by the manufacture. In this example, a MnZn type ferrite material is chosen, with K=0.28W/m^3, α=1.57 and β=2.2. The calculated loss density is 0.4mw/cc, considering the worst case where the loss density is doubled, the loss density L=0.8mw/cc. The total transformer core loss could then be calculated by the loss density L and the total volume in (4.48), and the total transformer loss are shown in (4.49).

$$P_{core} = V_{transcore} * L \tag{4.48}$$

$$P_{tot} = P_{core} + P_{copper} \tag{4.49}$$

All the required equations for the proposed optimization procedure have been presented. It can be observed from the above equations, except the parameters which have been defined (D_1, Dpri, B_{max} etc.), all the other parameters (D_3, Eh, h, P_{tot} etc.) which have not been defined can all be expressed by a function of D_2. Thus, to find the minimum weight and minimum power loss of the transformer, it is required to generate a plot of D2 versus those undefined parameters.

4.6 Optimization and FEM result

4.6.1 Introduction

The optimization result of the rotary transformer will be discussed in this section based on the optimization method mentioned before. Table 4.1 summarizes all the input and calculated parameters not based on D_2. Table 4.2 summarizes the wire information, and Table 4.3 summarizes the transformer dimension parameters that are determined by D_2.

Table 4.1 Parameters not determined by D_2

Input Voltage	230V
Input Voltage Frequency	60Hz
Fundamental Output Frequency	960Hz
Half Cycle Average Input Voltage	31.83V
MOSFET Rdson	88mΩ
Rectifier Diode Forward Voltage Drop	0.95 V
Shaft Diameter	1inch (2.54cm)
Winding Window Height $\frac{\Delta r}{2}$	0.12inch (0.3048cm)
Airgap Length $\frac{L_{gap}}{2}$	0.5mm
Primary Side Wire Diameter D_{pri}	2.44mm
Filling Factor α	1.2
Transformer Peak Flux Density	0.2 Tesla
Transformer Turns Ratio $\frac{N_{pri}}{N_{sec}}$	3
Duty Cycle D	0.2672
Core Loss Density L	0.8mw/cc
Core Weight Density	4.7g/cc
Desired Output Power	200W
Field winding Resistance (R_{load})	0.3Ω
Permeability of the air	1.256×10^{-6}H/m

Table 4.2 Wire information

Primary Side Wire AWG	14
Secondary Side Wire AWG	12
Primary Side Wire Resistivity	8.29mΩ/m
Secondary Side Wire Resistivity	5.21mΩ/m
Primary Side Wire Density	0.0185kg/m
Secondary Side Wire Density	0.0294kg/m
Primary Side Wire Diameter	2.44mm
Secondary Side Wire Diameter	2.69mm

Table 4.3 Rest of the dimension parameters determined by D_2

Outer Diameter D_3	$\sqrt{(D_2 - \Delta r)^2 - D_1^2 + (D_2 + L_{gap} + \Delta r)^2}$
End Cap Height Eh	$\frac{(\frac{D_2 - \Delta r}{2})^2 - \left(\frac{D_1}{2}\right)^2}{D_2 - \Delta r}$
Winding Window Length h	$N_{pri} * \alpha * D_{pri}$ $= \frac{\int_0^t V\,dt}{2 * B_{max} * A_m} * \alpha * D_{pri}$ $= \frac{\int_0^t V\,dt}{2 * B_{max} * (\pi\left(\frac{D_2 - \Delta r}{2}\right)^2 - \pi\left(\frac{D_1}{2}\right)^2)} * \alpha * D_{pri}$

4.6.2 Important optimization parameters

Now that all the input parameters and the dimensions of the rotary transformer have been defined, the last step here is to plot the desired optimization parameters with respect to a reasonable range of D_2. Table 4.4 summarizes the core optimization parameters during the optimization procedure (determined by D_2).

Table 4.4 Important optimization parameters

Transformer Core Volume ($V_{transcore}$)	$\pi * \mathrm{Eh} * (\frac{(D_2^2 - D_1^2)}{2} + \frac{(D_3^2 - (D_2 + L_{gap})^2)}{2}) + D_{pri} * \frac{\int_0^t \mathrm{V}\,\mathrm{dt}}{\mathrm{B_{max}}} * \alpha$
Transformer Core Weight ($M_{transcore}$)	$V_{transcore} * \rho_{core}$
Average Flux Area (A_m)	$\pi(\frac{D_2 - \Delta r}{2})^2 - \pi\left(\frac{D_1}{2}\right)^2$
Primary Turns Number (N_{pri})	$\frac{\int_0^t \mathrm{V}\,\mathrm{dt}}{2 * \mathrm{B_{max}} * A_m}$
Transformer Copper Weight (M_{copper})	$N_{pri} * \pi * (D_2 + L_g + \Delta r) * \rho_s + \frac{N_{pri}}{N} * \pi * (D_2) * \rho_r$
Transformer Total Weight	$M_{transcore} + M_{copper}$
Transformer Core Loss (P_{core})	$V_{transcore} * L$
Transformer Copper Loss	$\frac{P_{copperMP} + P_{copperMS}}{2}$
Transformer Total Loss	$P_{core} + P_{copper}$
Magnetizing Inductance	$L_m = L_{mesti} * Ff$
Leakage Inductance	$L_{lk} = N_{turn}{}^2 * \frac{u_0}{3} * \frac{\pi * D_2 * \Delta r}{h}$
Output Power	$I_{load}{}^2 * R_{load}$

4.6.3 Optimization result

Following the optimization procedure, the plots of all the important parameters versus D_2 are summarized in Fig.4.5. The average flux area A_m versus D_2 is shown in Fig.4.5 (a). It can be observed from the plot that with the increasing length of D_2, the average area to sustain the flux also increases. Since the average flux area increases with D2, the required turns number must decrease to keep a constant flux density.

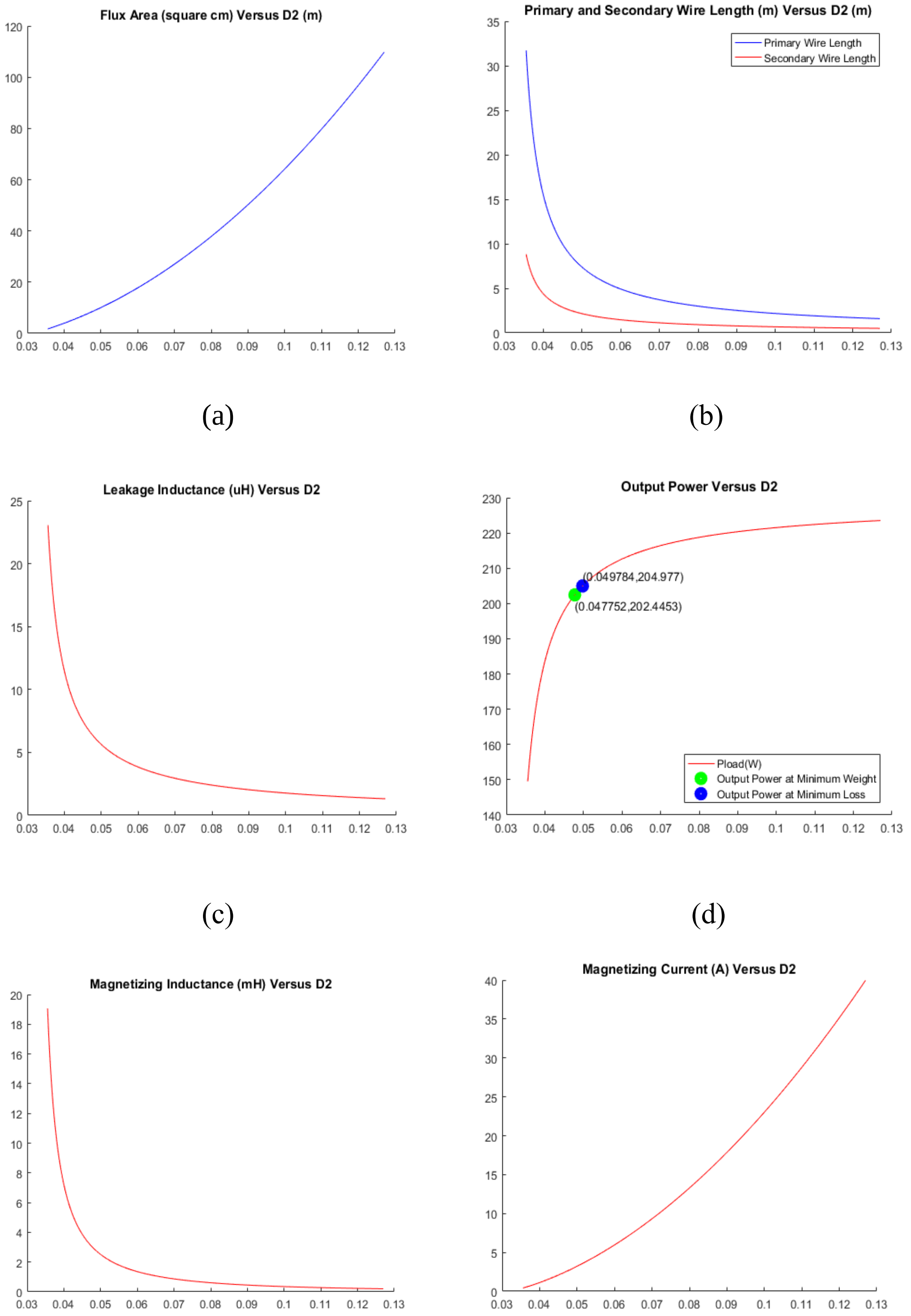

(a) (b)

(c) (d)

(e) (f)

Figure 4.5 Optimization result (a) average flux area versus D_2 (b) primary and secondary total wire length versus D_2 (c) leakage inductance versus D_2 (d) output power versus D_2 (e) magnetizing inductance versus D_2 (f) magnetizing current Versus D_2

Fig.4.5 (b) shows the total primary and secondary wire length with respect of D_2. Although the turns number decreases with D_2, it does not mean the total length of the copper wire will also decrease with D_2 since the length of the wire is equal to a constant multiplied by $N_{pri} * (D_2 + L_g + \Delta r)$ (4.43). However, N_{pri} is equal to a constant divided by A_m (4.40) and A_m is a second order function of D_2 (4.33), which proves that the copper wire length will also decrease with the increase of D_2 shown in Fig.4.5 (b).

According to (4.8) Fig.4.5 (c) shows the leakage inductance with respect to D_2. Based on the plot, the total leakage inductance will drop significantly with respect to D_2. The plot also shows for a reasonable range of D_2 (larger than 4cm), the calculated leakage inductance is far below than 50uH (less than 10uH). In consequence, the output power and copper loss model built in section 4.4.2 will be reasonable. The load power could be calculated by (4.12) shown in Fig.4.5 (d). Due to the long wire length at a small D_2 shown in Fig.4.5 (b), there will also be a large voltage drop on the winding resistance. Thus, the output power at small D_2 will be less than the designed value (200W) as shown in Fig.4.5 (d).

Although the increasing of D_2 increases the output power and decreases the transformer winding resistance, this does not mean that the larger D_2 the better performance will be achieved. Since the magnetizing inductance also drops significantly with respect to D_2 as shown in Fig.4.5 (e), the small magnetizing inductance at larger D_2 will also generate a huge magnetizing current at larger D_2 as shown in Fig.4.6 (f). As a result, a reasonable D_2 value should be chosen by considering both the magnetizing inductance and the winding resistance.

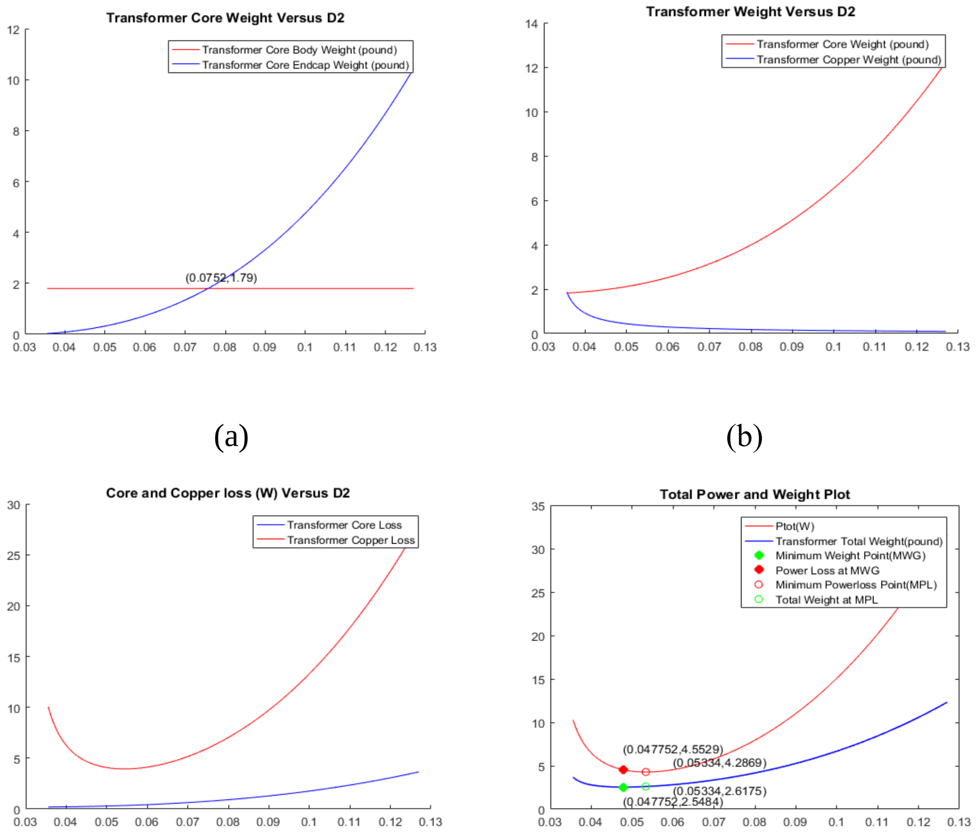

(a) (b)

(c) (d)

Figure 4.6. Optimization result of total weight and total loss (a) transformer core body and endcap weight versus D_2 (b) transformer core and copper wire total weight versus D_2 (c) transformer total core and copper loss versus D_2 (d) transformer total power and total weight versus D_2

Figure 4.6 shows the transformer weight and the loss plot versus D_2 for the designed rotary transformer. Owing to the constraint on the winding length h, the body part of the rotary transformer has a constant value of 1.79 pounds independent of D_2 shown in Fig.4.6 (a). Fig.4.6 (a) also shows that the weight of the endcap parts increases with D_2. However, for a reasonable value of D_2 (less than 6cm), the weight of the end part core is much less than that of the body part of the core. The body part and the end part core have an equal weight of 1.79 pound when D_2 is 7.5cm. However, this D_2 value will generally not be chosen for the magnetizing inductance is too small at this point.

Fig.4.6 (b) shows the total transformer core weight and total copper wire weight versus D_2, in which it has been discussed that the total length of the wire will decrease with D_2, so will the total weight of the copper wire with D_2 (since there is a linear relationship of the wire length and weight). It can also be observed from the plot that the total copper wire weight has become comparable to the weight of the transformer core at small value of D_2, which proves that there will be a specific medium value of D_2 for the rotary transformer has a minimum weight.

Fig.4.6 shows the total conduction loss and the total core loss of the designed rotary transformer. Since the transformer operates at medium frequency with ferrite material, there will be almost zero eddy current loss in the transformer core, while the only core loss part is the hysteresis loss. Thus, the copper loss is the dominant term for almost all value of D_2. The plot also shows that a large value of the conduction loss exists at both small D_2 and large D_2, because there will be a large winding resistance at small D_2, and a large magnetizing current at large D_2. This characteristic shows there will also be a specific medium value of D_2 for the transformer has a minimum total loss.

In consequence, a medium value of D_2 is required for the rotary transformer to have both a minimum weight and a minimum total power loss, so a proper chosen value of D_2 will let the rotary transformer to enjoy the benefits of both a minimum weight and a minimum power loss.

Based on this statement, a plot of the total transformer weight (core plus copper wire) and the total transformer loss (core plus copper wire) versus D_2 is displayed in

Fig.4.6 (d). The minimum weight (2.54lb 4.55W loss) is located at D_2=4.7cm and the minimum power (2.61lb 4.28W loss) is located at D_2=5.3cm based on Fig.4.6 (d). The output power in Fig.4.5 (d) for the minimum weight point is 202.44W and for the minimum power loss point is 204.97W, both of which satisfy the design requirement of 200W.

These results prove that the minimum weight point and minimum power point are in a very nearby position. Thus, the final value of D_2 could be determined by the average value of D_2 of these points, which is 5.0cm.

4.6.4 FEM verification

A FEM simulation is performed to verify the proposed model. Table 4.5 summarizes the dimensional parameters of the concentric cylinder rotary transformer based on the optimization procedure.

Table 4.5 Optimized 200W rotary transformer parameter

Shaft Diameter (D_1)	2.54cm (1inch)
Rotor Core Diameter (D_2)	5.08cm(2inch)
Stator Core Diameter (D_3)	6.86cm(2.7inch)
End Cap Height (Eh)	0.756cm(0.3inch)
Winding Window Length (h)	11.42cm(4.49inch)
Winding Window Width ($\frac{\Delta r}{2}$)	0.305cm(0.12inch)
Airgap Length ($\frac{L_{gap}}{2}$)	0.5mm(19.85mil)
Primary Turns Number	39
Secondary Turns Number	13

Table 4.6 Calculated inductance versus FEM simulated inductance

	Magnetizing Inductance	Leakage Inductance
FEM Result	2.45mH	7.7uH
Calculated Value	2.37mH	6.31uH

Table 4.6 summarizes the calculated inductance and the FEM simulated inductance value. Since the flux area in the radial direction is not uniformly distributed (flux area in the end of the core $(\pi * (D_2) * Eh)$ is larger than the average flux area A_m $(\pi * (D_2 - \Delta r) * Eh)$ shown in Fig.4.7), the magnetizing inductance in FEM is 3.4 percent larger than the calculated value.

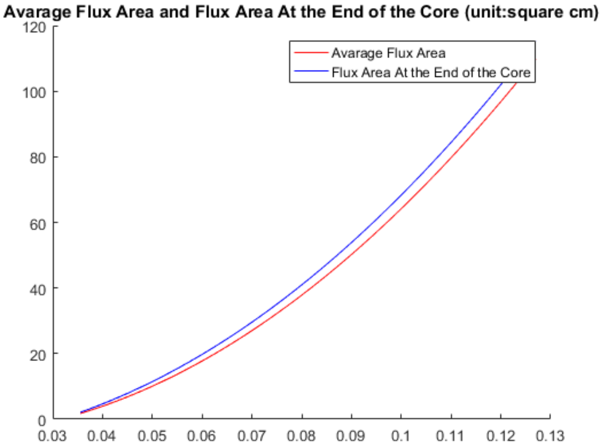

Figure 4.7 Average flux area in the core body and flux area in the end part

The leakage inductance in FEM is 1.22 times the calculated value, because there are many leakage paths that have not been included in the model. Even though the leakage inductance is much larger in the FEM case, it is still much smaller than limit of 100uH, which proves the model to be still accurate.

Figure 4.8 shows the flux density distribution of the designed rotary transformer, it can be observed from the plot that a uniformly distributed flux density is achieved from the design procedure. On account of the leakage flux, the peak flux density in the body core is slightly larger than the designed value (0.21T compared to 0.2T), but this small difference will not saturate the core since the saturation flux density for the selected material is 0.48 Tesla.

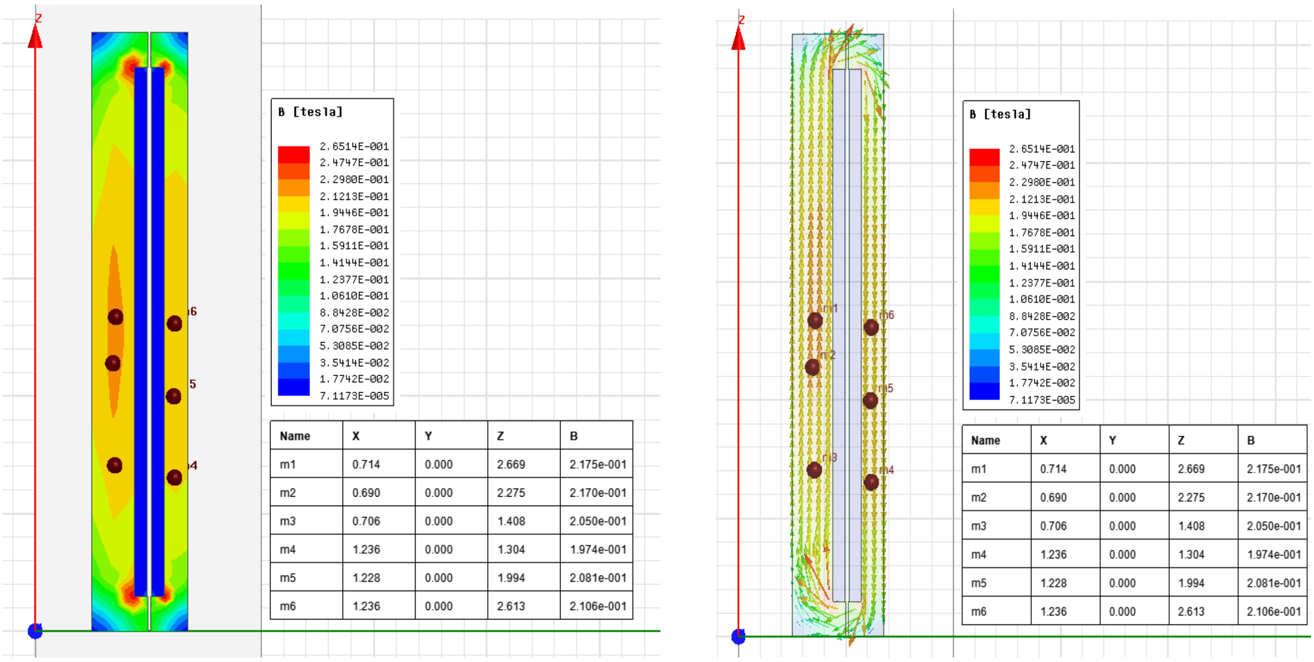

Name	X	Y	Z	B
m1	0.714	0.000	2.669	2.175e-001
m2	0.690	0.000	2.275	2.170e-001
m3	0.706	0.000	1.408	2.050e-001
m4	1.236	0.000	1.304	1.974e-001
m5	1.228	0.000	1.994	2.081e-001
m6	1.236	0.000	2.613	2.106e-001

Name	X	Y	Z	B
m1	0.714	0.000	2.669	2.175e-001
m2	0.690	0.000	2.275	2.170e-001
m3	0.706	0.000	1.408	2.050e-001
m4	1.236	0.000	1.304	1.974e-001
m5	1.228	0.000	1.994	2.081e-001
m6	1.236	0.000	2.613	2.106e-001

Figure 4.8 Flux density distribution of the designed rotary transformer

Fig.4.9 shows the plot of core loss for the designed rotary transformer based on FEM, and Table 4.7 summarizes the average core loss base on the calculated and simulated FEM result.

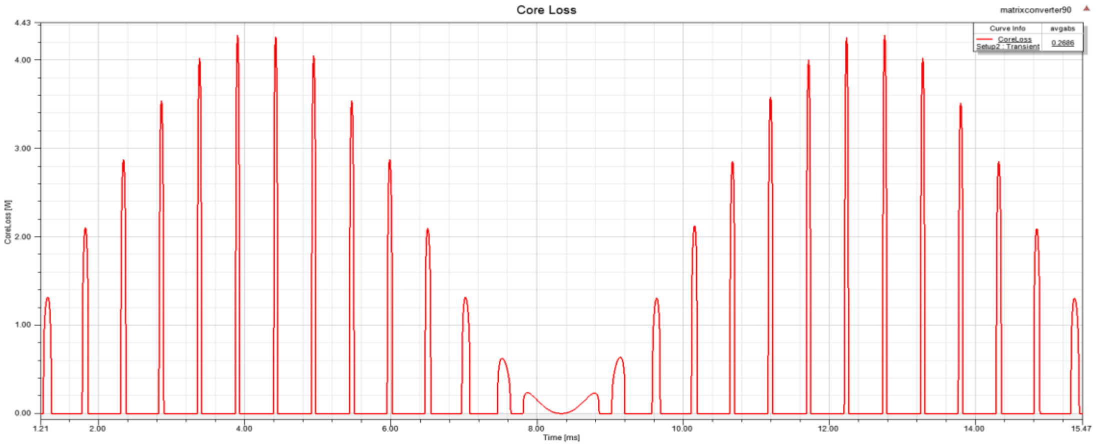

Figure 4.9 FEM result of core loss

Table 4.7 Average core loss based on FEM and calculation

	Core Loss
FEM Simulated Average Value	0.2686W
Calculated Average Value	0.1527W

According to Table 4.7, the calculated core loss value is much smaller than the simulated value, because only the fundamental component is considered during the calculation. However, this does not mean that the designed model is not accurate, because compared to the total transformer loss of 4.5 W, the core loss only accounts for less 5 percent of total loss.

4.6.5 Circuit simulation verification

To verify the copper loss model was correct, the inductance value obtained from the FEA and the calculated winding resistance were imported to the circuit simulation software. Table 4.8 summarizes the parameters of the simulated circuit. The parameters not included in Table 4.8 share the same value in Table 3.1. The important simulated results versus the calculated results are summarized in Table 4.9.

Table 4.8 Input parameters for the circuit simulation

Input Voltage	230V (RMS)
Input Frequency	60Hz
RT Primary Winding Resistance	58.8mΩ
RT Secondary Winding Resistance	10.8 mΩ
Leakage inductance	7.7uH
Magnetizing inductance	2.46mH

Table 4.9 Comparison between the calculated and simulated result

	Simulated Result	Calculated Result
Load Current (I_{load})	26.03A	26.20A
Primary Side RMS Current	4.69A	4.84A
Secondary Side RMS Current	15.29A	16.14A
Load Power	203.26W	205.9W
Transformer Copper Loss	3.818W	4.033W
Transformer Total Loss	4.0886W	4.1864W
Total transformer Efficiency	98%	97.97%

From Table 4.9, it shows that all the calculated results are slightly larger than the circuit simulation result. These differences are caused by the following reasons. First, the calculated magnetizing inductance is slightly smaller than the FEM value (which stated in section 4.6.4), so that the magnetizing current on the primary side will also be larger. Second, the proposed optimization model does not include the voltage drop on the leakage inductance, so the rectifier side voltage is slightly higher than the simulated value. Third, the effect of the leakage inductance is not included when calculating the transformer RMS current in the proposed model.

In conclusion, despite the difference, the proposed model is accurate enough to predict the total transformer loss and efficiency (with an error less than 3 percent).

4.6.6 Optimization flow chart

The flow chart for the optimization procedure is shown in Figure 4.10. It must be pointed out that based on the proposed optimization procedure, generally there is no need for any iterations in the design procedure.

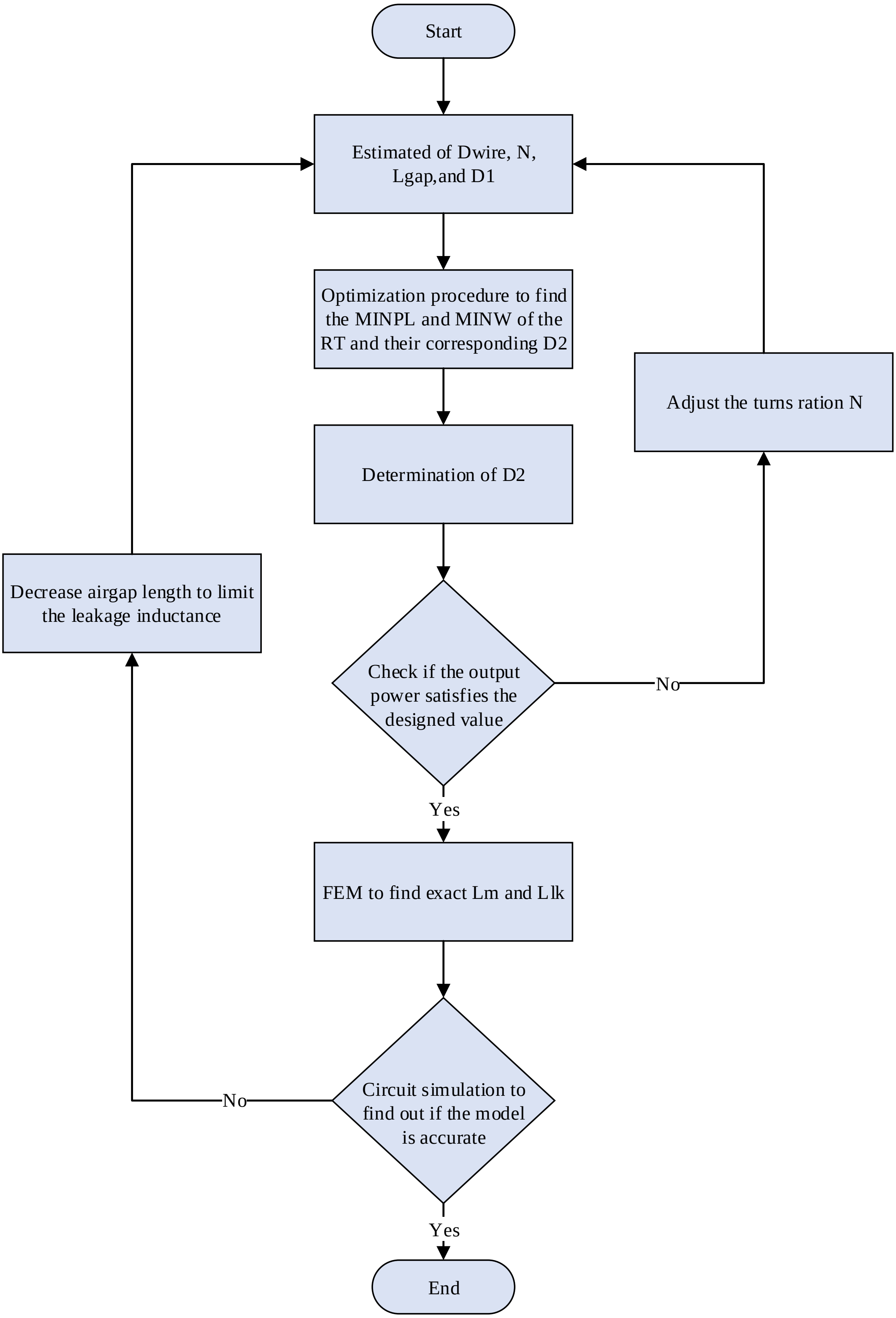

Figure 4.10 Flow chart for optimization procedure

However, because there is an estimation for the total loss in the first step of the design procedure, the output power at the end of the optimization procedure may not be the exact desired value. As a consequence, an iteration step is added to adjust the turns ratio of the transformer if the output power does not satisfy the requirement. The optimization procedure will generate a primary and secondary side maximum RMS current for the finalized D_2. If these two currents are much higher or lower (20 percent) than the estimated value in the first step, a procedure to change the wire can also be applied in this step.

A FEM simulation will be performed after the optimization procedure to finalize the inductance value and calculate the core loss. Based on the information obtained from the FEM, a circuit simulation will be operated to determine if the model is accurate. If there is too much voltage drop on the leakage inductance and the output power cannot sustain the desired value, another iteration of decreasing the airgap will be added to limit the value of the leakage inductance, because a smaller number of turns could be obtained to sustain the same magnetizing inductance for a smaller airgap (4.3), and a smaller number of turns would also significantly reduce the leakage inductance (4.8). The design of the rotary transformer is completed if the predicted model meets the circuit simulation result.

4.7 Summary

In this chapter, a model to calculate the RMS current for constant volts per Hz based rotary transformer system is firstly built. Based on the RMS current model, a new optimization procedure for rotary transformer is proposed, a medium frequency rotary transformer with compact size (2.57 pound 200W) at high efficiency (98 percent) is obtained from the optimization method.

The proposed optimization method has significantly simplified the designed procedure by reducing the design variables to one (inner core diameter D_2), which also directly optimizes the transformer weight. The method will automatically generate the dimensions for the rotary transformer with minimum loss and minimum volume in one straight forward calculation (no iteration needed). It should be noted that the proposed optimization method is not limited to the constant volts per Hz modulation method but also applicable to other modulation methods.

Chapter 5

COMPARATIVE PERFORMANCE EVALUATION

5.1 Introduction

A comparative performance evaluation will be presented in this chapter to show the advantages of the proposed modulation compared to the existing ac and dc based modulations. The benefits and side effects of increasing the proposed 960Hz to 1920Hz will also be discussed in this chapter.

5.2 Comparison with other modulation strategies based on SPMC

5.2.1 Average voltage method

It has been mentioned in Chapter 2 that if the output frequency is 960 Hz, the output voltage based on average voltage modulation method is 13.75V rms for a 230 V 60 Hz input. Consequently, to generate the output power of 177W, a minimum rms input current is $\frac{177W}{13.75V} = 12.9A$, which is 2.8 times the primary rms current in the proposed constant volts per Hz modulation method. Furthermore, when considering the conduction loss, it would be $2.8^2 = 7.84$ times more than the proposed modulation method. Additionally, to modulate a 960 Hz output waveform, while the switching frequency may be at least ten times larger, the switching loss will also be at least 10 times larger than that of the constant volts per Hz modulation method.

Based on the reasons above, the detailed comparison between the average voltage method and the constant volts per Hz modulation method will not be carried out.

5.2.2 Constant time modulation

Table 5.1 summarized the detailed input parameters for the constant time modulation method to have the same output power as the proposed modulation method. The other input parameters not included in Table 5.1 share the same value as the simulations for constant volts per Hz method in Chapter 3. It should be noted that the value of Rdson for the MOSFETS reduces from the previous case 80 mΩ to 10 mΩ, since the input voltage for the constant volts per Hz method is 230V rms and the input voltage for the constant time modulation method is 34 V rms. Hence, a MOSFET with a small Rds on can be applied to the matrix converter.

Table 5.1 Input parameters for simulation of constant time modulation method

Input Voltage Amplitude (RMS)	34V (48V peak)
Input Voltage Frequency	60Hz
Fundamental Output Frequency	960Hz
MOSFET Rds On	10mΩ
MOSFET Body Diode Forward Voltage	0.7V

Fig.5.1 shows the transformer primary side current, voltage and secondary side current waveform. It can be observed that during each 1920 (half cycle of 960Hz) Hz cycle, the average voltage applied to the transformer is not a constant value. Thus, the transformer must be designed over a half cycle which has the maximum average voltage, and for each cycle the maximum flux density will also have a different value.

It can be observed from Fig.5.1 that the field current (Iload1) has a ripple of 1.78

A compared to 0.7A in constant volts per Hz method, which is caused by the unequal average voltage. According to the output DC voltage waveform shown in Fig.5.2, this output field current will have a harmonic content of 120 Hz rather than 960 Hz, and based on the constant time modulation method, the output voltage waveform of the rectifier is the same as the 60 Hz input AC voltage.

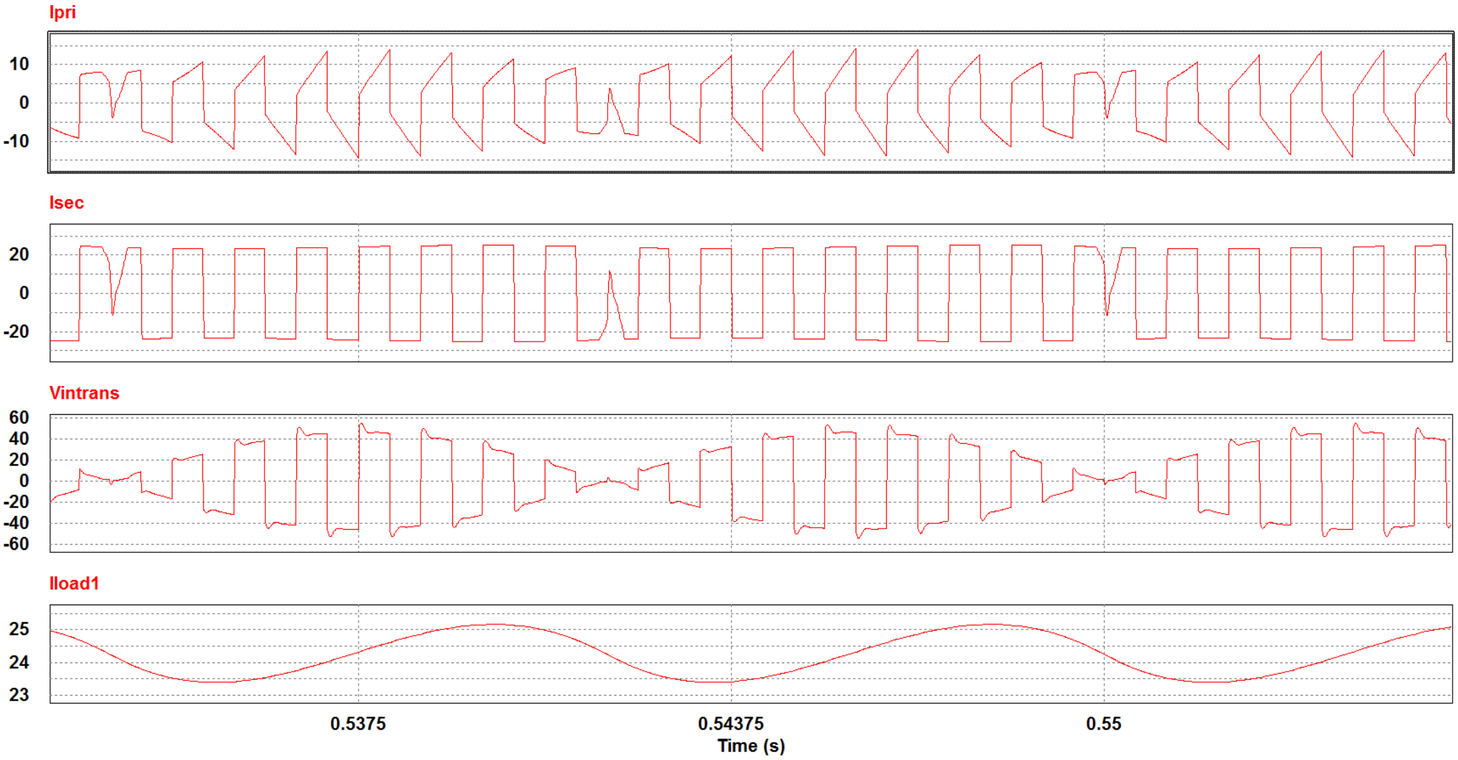

Figure 5.1 Simulation results of transformer primary, secondary side current, input voltage, and field winding current waveform

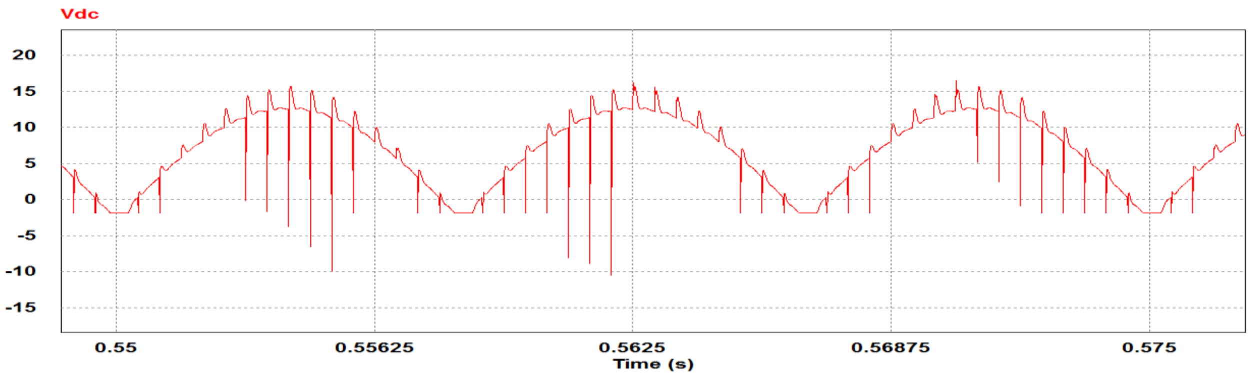

Figure 5.2 Voltage waveform after the diode bridge

The major simulation results for the constant time modulation method is summarized in Table 5.2. Based on the summarized simulation results, a loss calculation was made and is summarized in Table 5.3.

Table 5.2 Summary of the simulation results

Primary Side RMS Output Current	8.4A
Secondary Side RMS Output Current	23.8A
Max half cycle Average Output Voltage	42V
RMS Output Voltage	34V
Field Current Ripple	1.78A
Average Field Current	24.3A

Table 5.3 Summarized output power and loss

MOSFETs Conduction Loss	13.17W
RT Primary Side Copper Loss	6.23W
RT Secondary Side Copper Loss	9.4W
Rectifier Diodes Conduction Loss	45.6W
Output Power	177W
Calculated System Efficiency	70.4%
Efficiency Without Rectifier Diodes	86%

Fig.5.3 summarizes the major difference between the constant time and constant V/Hz modulation method, and the three important ones are explained below.

1. Compared to a constant V/Hz modulation method with the same output power of 177 W, the total loss is 81 percent more with a constant time modulation

method.

2. The maximum half cycle average voltage is 38 percent higher for the constant time modulation method. Although this feature does not mean that the transformer in constant time modulation method is 38 percent larger~~.~~ It proves that the transformer is better utilized in the constant volts per Hz method, and to deliver the same output power, the transformer has to be larger using the constant time modulation method.
3. The current ripple is 154 percent larger in constant time modulation, which will also create more torque ripples at the output of the wound field synchronous machine.

According to the above reasons, constant time method is also less applicable in the proposed brushless excitation system compared with constant volts per Hz method.

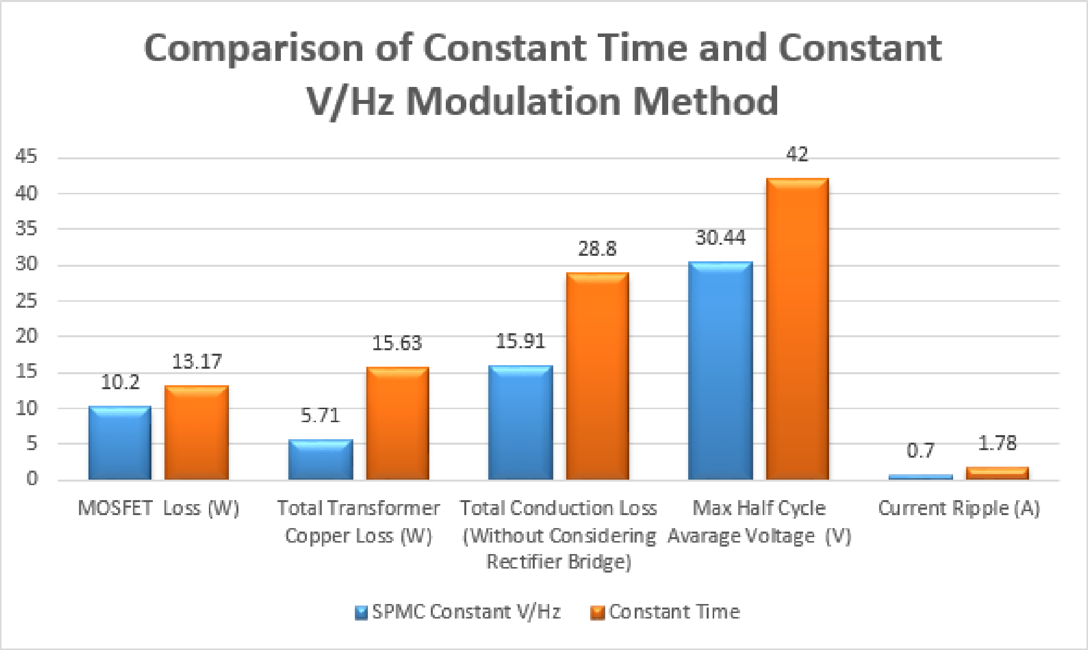

Figure 5.3 Comparison of constant time and constant volts/Hz modulation method

5.3 Comparison with 30V input square wave excitation based on inverter

Employing the square wave excited transformer system, the input dc voltage source can be either a battery or an ac voltage source through a rectifier bridge with large dc link capacitor. A chopper circuit may also be included to control the amplitude of the input dc voltage. However, instead of using the rectifier circuit with link capacitor, a stiff dc voltage source is used in simulation for simplicity. Thus, the real power loss in the overall system must be higher than in the simulated result. Table 5.4 summarizes the input parameters of the square wave inverter circuit to supply the same output power (177W) with constant volts per Hz modulation method. The transformer parameter is not included since it is the same value as in the last section.

Table 5.4 Input parameter for simulation of square wave inverter

Input Voltage Amplitude (DC)	30.2V
Fundamental Output Frequency	960Hz
MOSFET Rds On	10mΩ
MOSFET Body Diode Forward Voltage	0.7V

Figure 5.4 shows the transformer primary, secondary current and primary side voltage waveform. Similar to the constant time modulation method mentioned in the last section, the transformer has a much larger primary side current compared to the constant volts per Hz modulation method since the input RMS voltage is much lower (30.2V compared to 74.4V). However, the field current ripple is much smaller with square wave excitation (0.007 A compared to 0.7A) since there is a constant DC output voltage for the square wave case. However, owing to the large field inductance in the

real wound field synchronous machine, all modulation methods would produce a ripple less than 0.1 percent.

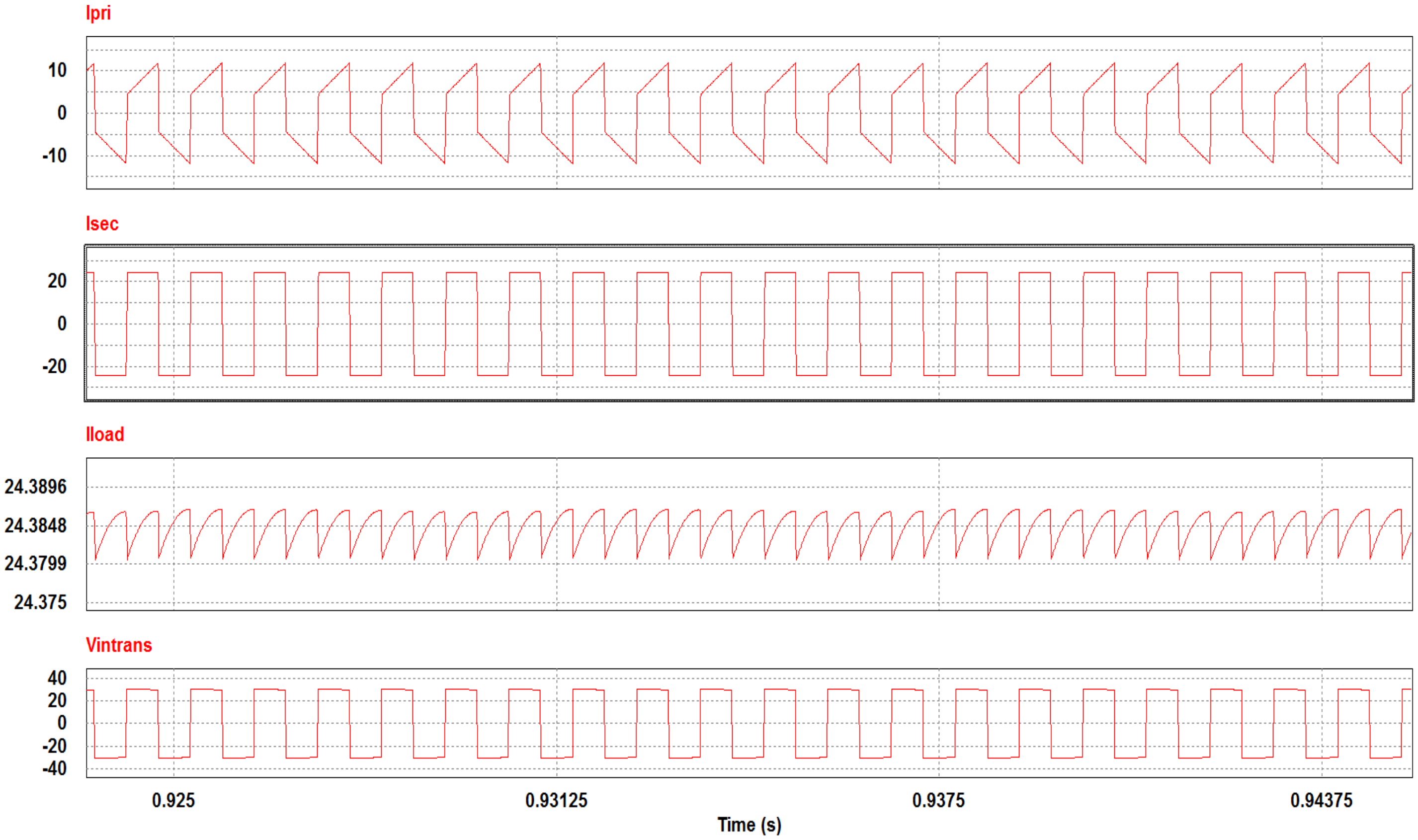

Figure 5.4 Simulation results of transformer primary, secondary side current, field winding current and transformer input voltage waveform

Table 5.5 and Table 5.6 summarize the simulated results and the calculated loss for the square wave inverter system. The average input voltage to the rotary transformer is slightly smaller than that of the constant volts per Hz method (30.2 to 30.44V), which is caused by the forward voltage drop on diodes in bi-directional switches. From the conduction loss summarized in Table 5.6, it can be concluded that the square wave inverter has the least conduction loss in MOSFETs. This occurs since current only flows through two MOSFETs when conducting, but for the matrix converter, current must flow through at least 4 MOSFETS when conducting. When a safe commutation is required, current in the matrix converter may flow through 3 MOSFETs plus 1 diode, or 2 MOSFETs plus 2 diodes which further increases the conduction loss.

Table 5.5 Summary of the simulation results

Primary Side RMS Output Current	8.42A
Secondary Side RMS Output Current	24.3A
Max half cycle Average Output Voltage	30.2V
RMS Output Voltage	30.2V
Field Current Ripple	0.007A
Average Field Current	24.3A

Table 5.6 Summary of output power and loss

MOSFETs Conduction Loss	1.418W
RT Primary Side Copper Loss	6.26W
RT Secondary Side Copper Loss	9.8W
Rectifier Diodes Conduction Loss	45.6W
Output Power	177W
Calculated System Efficiency	73.75%
Efficiency Without Rectifier Diodes	91%

Fig 5.5 shows a comparison of a SPMC based constant Volts/Hz modulation and an inverter based square wave modulation. The switching conduction loss in the square wave modulation is the smallest among the three-modulation methods (constant time, constant volts per Hz, and square wave). However, due to the increase of the output current, the rotary transformer copper loss is much larger than that in the constant volts

per Hz modulation. As a result, the overall conduction loss in the square wave modulation is still higher than that in the constant volts per Hz modulation.

Lastly, the switching loss is not included here because in medium frequency excitation, the calculated maximum hard switching loss in the square wave modulation is less than 0.1W. The switching loss could be further reduced by applying the zero-voltage switching at turn on by a phase shifted technique. However, this is not useful with medium frequency excitation since the conduction and transformer copper loss are much larger than the switching loss.

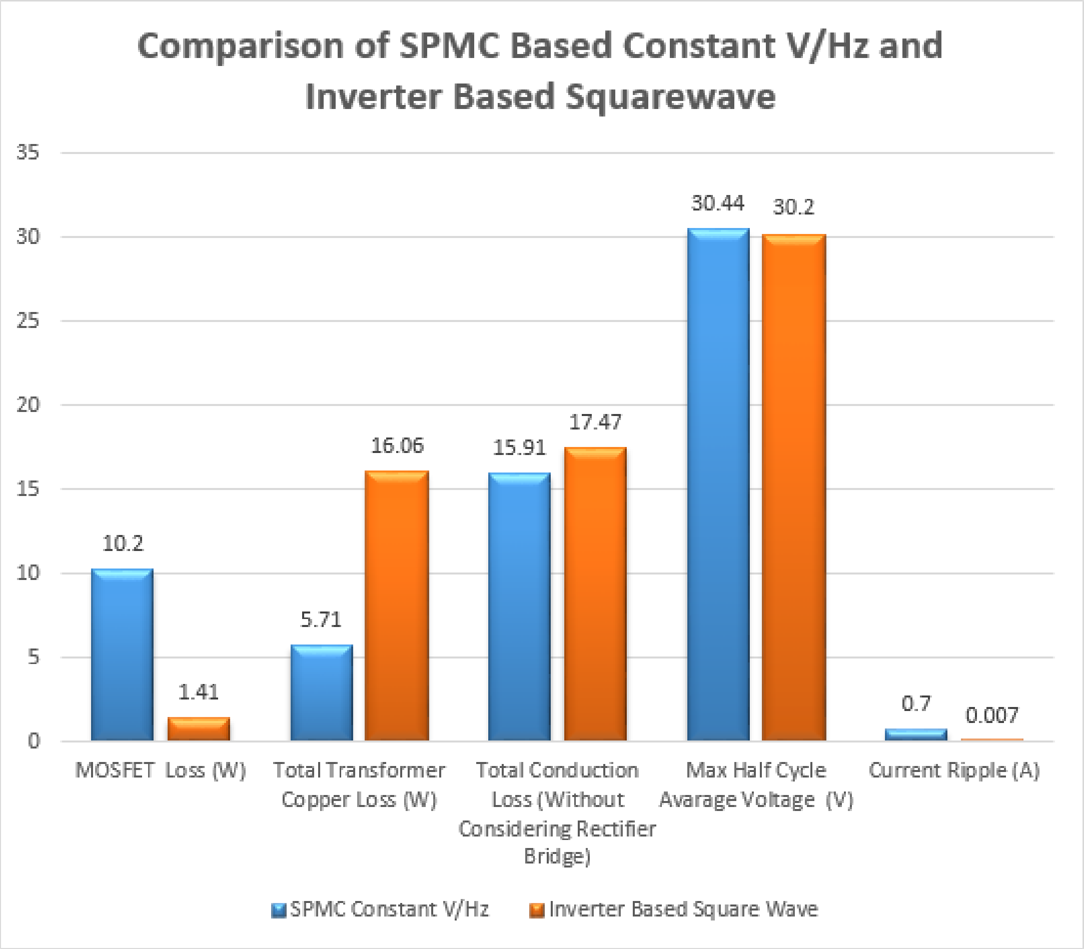

Figure 5.5. Comparison of SPMC based constant Volts/Hz modulation and inverter based square wave modulation

5.4 Comparison with ac line input based square wave excitation

It is assumed in the previous section that there is voltage step down stage in the manner of a traditional 60 Hz steady state transformer to change the input line voltage to a lower value (30 Volts). Hence, the same rotary transformer could be used for all three kinds of modulations at the same input V/Hz. However, this voltage step down stage will also increase the overall system efficiency and volume.

In this section, a more general type of inverter based square wave system shown in Fig.5.6 (two stage system: rectifier plus an inverter) will be simulated to compare with the proposed constant volts per Hz modulation, with a same input voltage of 240V rms 60Hz and a same output power of 200W. The output frequency for both modulation techniques was set to 960Hz for a fair comparison.

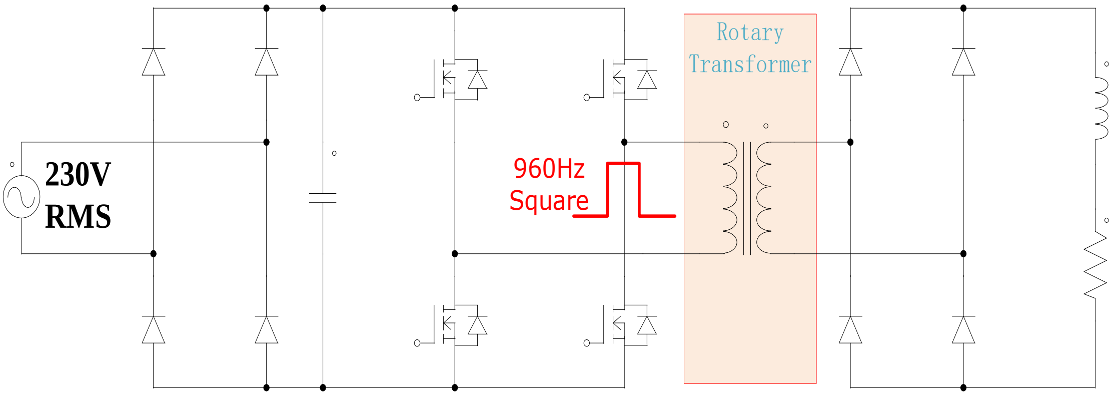

Figure 5.6. Inverter based system

Since the DC bus voltage is the peak value of the input AC voltage, in this case around 330V, the output V/Hz at 960Hz will be much higher than the proposed modulation. This means the rotary transformer must be redesigned for this system to avoid saturation. Following the same optimization procedure mentioned in the previous chapter, the optimized rotary transformers parameters for both the 330V 960Hz system and the proposed volts per Hz modulation system are summarized in Table 5.7. The electrical simulation results for the two systems are summarized in Table 5.8.

Table 5.7 Rotary transformer characteristics for the inverter based and the matrix converter based system

	Constant V/Hz	330V Square Wave
Shaft Diameter (D1)	2.54cm (1inch)	2.54cm (1inch)
Rotor Core Diameter (D2)	5.08cm (2inch)	4.55cm (1.8inch)
Stator Core Diameter (D3)	6.86cm (2.7inch)	6.09cm (2.4 inch)
Winding Window Length (h)	11.42cm (4.49inch)	23.91cm (9.41inch)
Total Weight	1.54kg (3.4lb) 480cc	2.0385kg (4.5lb) 712cc
Transformer Efficiency	97.93%	97%
Link Capacitor	10uF (16cc)	680uF (100cc 3 percent ripple)
Total Volume	496cc	812cc
Output Power	200W	200W

Table 5.8 Electrical simulation results for the inverter based and the matrix converter based system

	Constant V/Hz	330V Square Wave
Primary RMS Current	4.69A	0.76A
Secondary RMS Current	15.29A	26.3A
Output Power	200W	200W
Switch Loss	8.74W (1W switching)	7.16W (5.35 Rectifier +1.81 MOSFET)

From Table 5.7, the rotary transformer size for the inverter based system is 48 percent larger than the matrix converter based system. By considering a link capacitor to stabilize input AC voltage the difference would be even larger (65 percent). It can also be observed from Table 5.7 that the rotary transformer efficiency is almost the same for both systems. Since the primary side winding current for the inverter-based system is lower, the secondary side winding current for the constant volts per Hz system is lower as shown in Table 5.8. The overall system loss for the proposed system is slightly higher than that for the inverter based system but with a volume reduction of over 33 percent.

5.5 Comparison with different output frequency for the constant V/Hz modulation

Since the operating frequency for the constant V/Hz modulation was set to be 960Hz in the previous sections, a circuit simulation will be performed based on an operating frequency of 1920Hz in this section to show the characteristics of the proposed system when the operating frequency increased. Again, following the same optimization procedure mentioned in the last chapter, Table 5.9 summarizes the detail parameters for the optimized rotary transformer and the circuit simulation results for both 960Hz and 1920Hz.

It could be observed from Table 5.9 that the size of the rotary transformer is reduced by half if the operating frequency doubles. The overall transformer efficiency is increased in 1920Hz because for the same output power, the input duty cycle defined in the last chapter decreases, which means the active time for the secondary side of the transformer winding to conduct the same load current decreases, the rms current for the secondary side winding thus decreases. However, when the output frequency doubles, the rms output voltage also decreases by half for the constant V/Hz modulation. To generate the same output power, the output current must be doubled. Thus, it can also be observed from Table 5.9 that for a 1920Hz operation, the conduction loss for the SPMC is three times higher than that in the 960Hz case.

Table 5.9 Comparison between the 960Hz case and the 1920 Hz case

	960Hz Case V/Hz	1920Hz Case V/Hz
Shaft Diameter (D_1)	2.54cm (1inch)	2.54cm (1inch)
Rotor Core Diameter (D_2)	5.08cm (2inch)	4.37cm (1.72inch)
Stator Core Diameter (D_3)	6.86cm (2.7inch)	5.79cm (2.28inch)
Winding Window Length (h)	11.42cm (4.49inch)	7.94cm (3.12inch)
Total Weight	1.54kg (3.4lb)	0.725kg (1.6lb)
Transformer Efficiency	97.93%	99%
Primary RMS Current	4.69A	8.52A
Secondary RMS Current	15.29A	13.23A
Output Power	200W	200W
Switch Loss	8.74W (1W switching)	30W (4W switching)

5.6 Summary

In conclusion, it was determined that for the same rotary transformer at 30V/960Hz (average value per half cycle), compared to SPMC based constant time and square wave modulations, the proposed constant V/Hz modulation has the least conduction loss which shows in Fig.5.7. Moreover, the rotary transformer is also optimized based on the proposed modulation method since a constant volts/Hz is applied to the transformer at each half cycle in comparison with the constant time modulation. The switching loss is not listed below because it is much smaller (less than 10 percent) compared with the conduction loss for every modulation method at 960 Hz medium frequency.

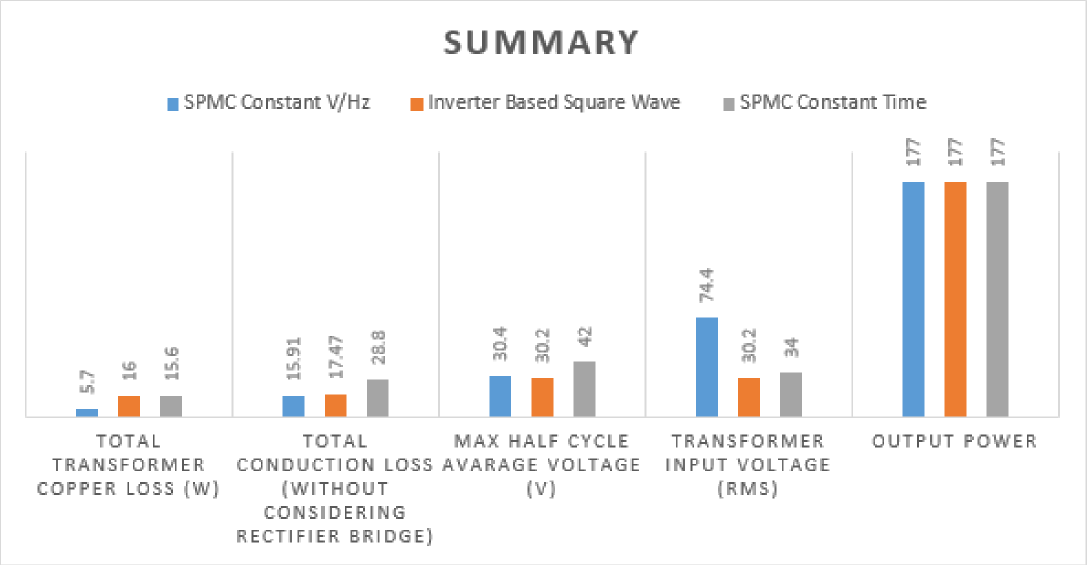

Figure 5.7 Summary of three modulation methods

For an ac line based square wave system, the transformer size will be 48 percent larger than the proposed modulation at 960Hz input; when considering the extra link capacitor, the difference will be increased to 65 percent.

Although an increasing of the output frequency for the constant V/Hz modulation will decrease the size of the rotary transformer, it will significantly increase the overall conduction loss. As a result, the final output frequency of the system should be determined by the requirements of a specific application.

Chapter 6

PROTOTYPE EXPERIMENTAL RESULT

6.1 Introduction

To prove the proposed constant V/Hz modulation and verify the new optimization procedure for the rotary transformer, a single-phase matrix converter excited rotary transformer system has been constructed to supply the field current of a WFSM. The details of the system and its experiment result will be elaborated upon in this chapter.

6.2 Software design

6.2.1 Introduction

The micro controller used in this research project is a Texas InstrumentTMS28335. An experimental kit is used in this prototype to generate gate signals for each switch and provide control and synchronization for the entire system. This DSP has 18 separate channels to generate pulse width modulation (PWM) waveform and has 16 channels of analog to digital conversion.

6.2.2 External interrupt channel for zero crossing detection

Since the input for the proposed matrix converter is 60 Hz ac but not dc, an external interrupt logic loop in DSP must be used to synchronize the system. For every 60 Hz cycle, the hardware part will generate a pulse as an input to the DSP’s General-Purpose Input/Output (GPIO) terminal for synchronization. However, the pulse for synchronization may contain some high frequency noise that have not been eliminated by the hardware filter. Hence, the GPIO terminal from the DSP could be served as a second stage digital filter.

After the digital filtering stage from the GPIO terminal, an external interrupt will be activated by the rising edge of the synchronization pulse. The counters for the PWM signal will be reset to 0 once the external interrupt is activated. Fig.6.1 shows an example of the waveform for the 60Hz synchronization pulse signal.

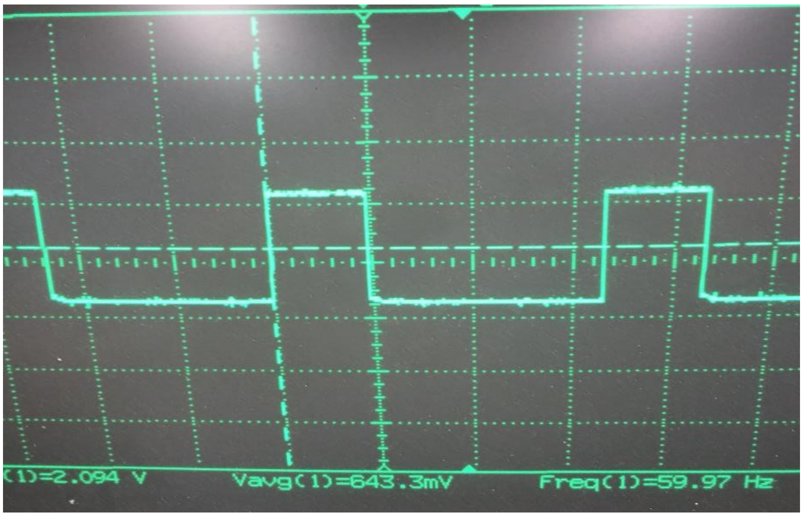

Figure 6.1 Synchronization signal for matrix converter

6.2.3 PWM signal generation

Figure 6.2 shows the PWM gate signal generated for the MOSFETS. It also shows each MOSFET turns on and turns off time. The deadtime for each switching pair is also included (1us) in this driving signal for the bridge connected switch models, because there will be a short circuit if both switches on one leg are turned on simultaneously. There must be one and only one switch which turns on at each moment to avoid an open circuit for the output because of the big inductive load.

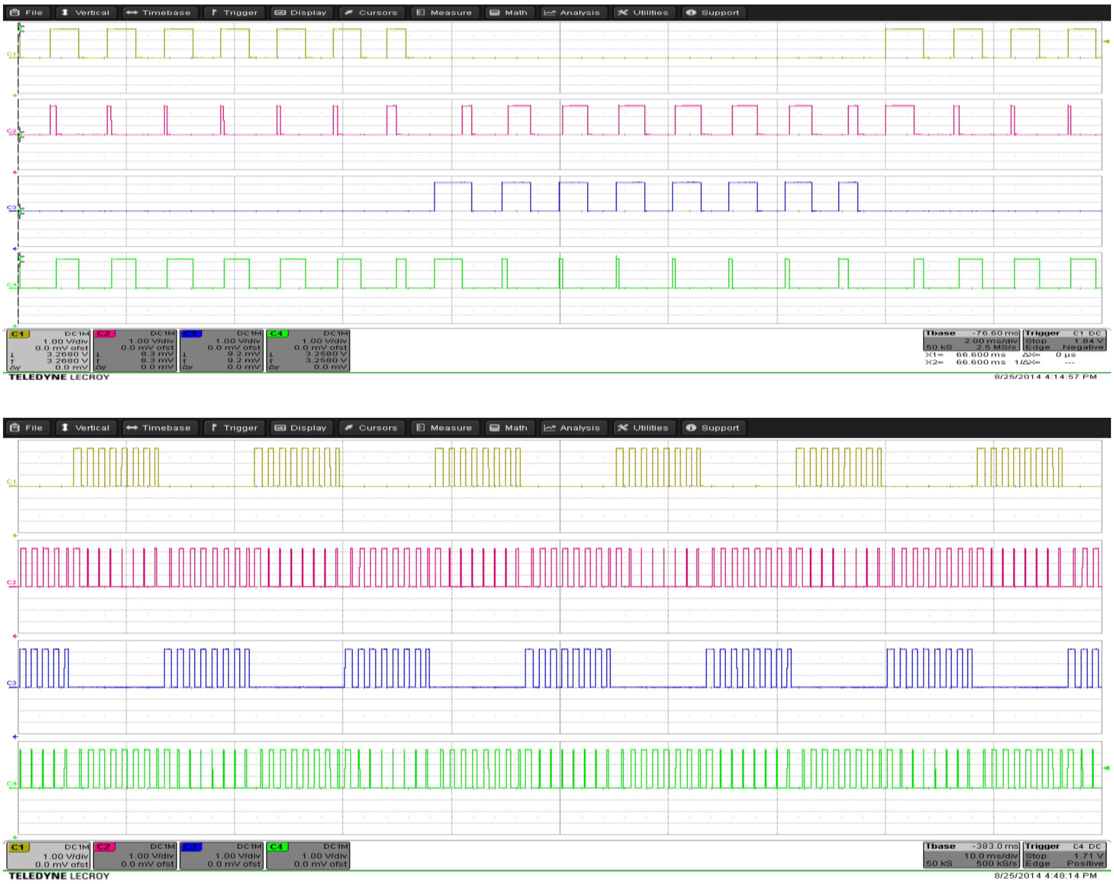

Figure 6.2 DSP output gate signal

6.3 Matrix converter design

6.3.1 Zero crossing detection circuit

It has been discussed previously that because a synchronization in each period (in this case every $\frac{1}{60}$s for a 60Hz input) is required for the matrix converter based system, two major zero crossing detection circuits are required as shown in Fig.6.3 and Fig.6.4.

The comparator based zero crossing detection circuit is shown in Fig.6.3. This circuit has the advantage of fast system response (ns level), but the main power stage and synchronization pulse signal stage are not isolated from each other. Consequently, a transformer is generally required as a buffer (isolation) stage for large power application, which increases the overall system volume.

Fig.6.4 shows the optocoupler based zero crossing detection circuit. As the optocoupler provides an isolation between the power stage and signal stage, the system is compact compared with the transformer based comparator circuit, but the system response is slower (us level) than that of the comparator circuit.

Since a compact design is required for the proposed system, a FOD2200 optocoupler based synchronization circuit is used in this project.

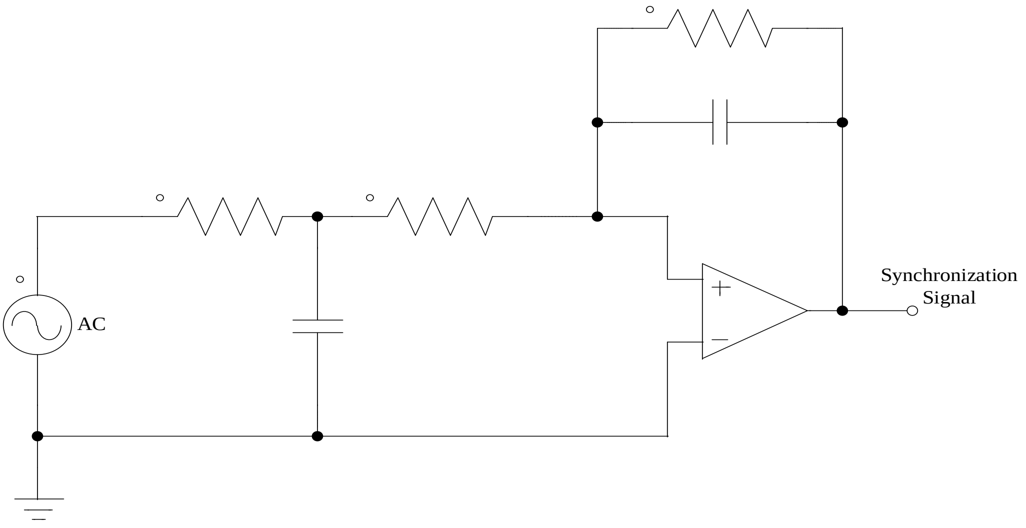

Figure 6.3 Comparator based zero crossing detection circuit

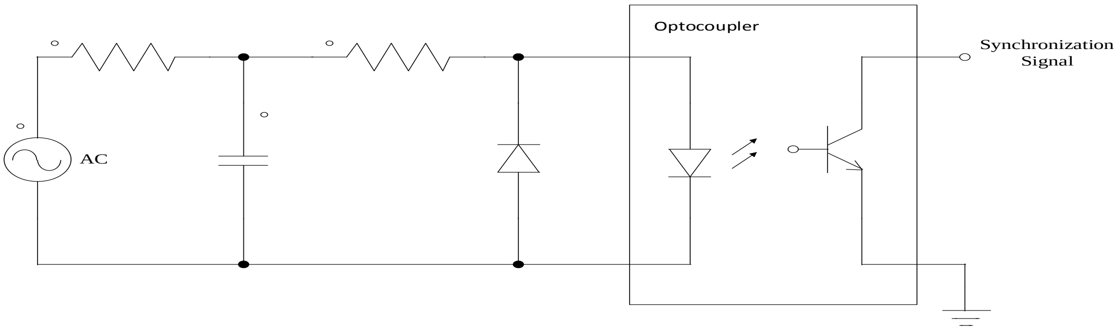

Figure 6.4 Optocoupler based zero crossing detection circuit

6.3.2 Input filter and clamp circuit

Table 6.1 summarizes the inductor, damped resistor and capacitor values for the input filter and the clamp circuit used in this project. It should be noted that the capacitor value is not optimized because the main purpose of this prototype is used to simply verify the constant volts per Hz modulation strategy.

Table 6.1 Input LC filter and clamp circuit parameters

Input LC Filter Inductance	250uH
Input LC Filter Capacitance	30uF
Clamp Circuit Capacitance	30uF
Clamp Circuit Damp Resistance	100kΩ (three 300kΩ in parallel)

6.3.3 Main power circuit

Fig.6.5 and Fig.6.6 show the main power circuit for the bridge connected topology and the back to back connected topology and Table 6.2 summarizes the information for input power supply, active switches and diodes. The input voltage of the matrix converter is adjusted by an adjustable AC drive. The input frequency is 60Hz and the fundamental output frequency is 960 Hz.

Table 6.2 Summary of power circuit information

Input Voltage	Adjustable by AC Drive up to 230 V
Input Frequency	60 Hz
MOSFETS	STP40N60M2 (V_{ds} 600V R_{dson} 88mΩ)
Diodes for Bridge Connected Topology	C3D10060A-ND (V_f 1.8V@10A)
Output Fundamental Frequency	960 Hz

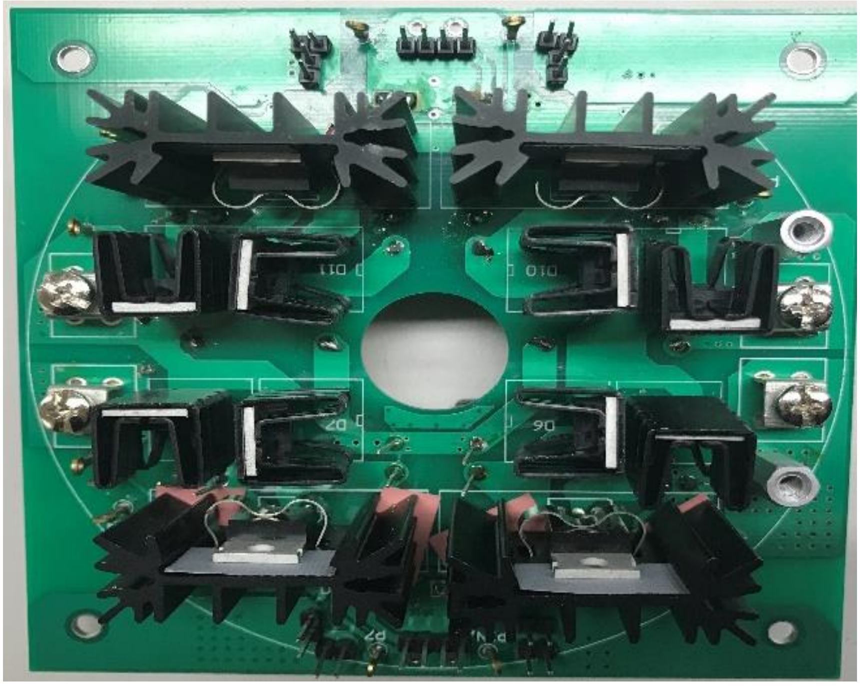

Figure 6.5 Bridge topology of SPMC

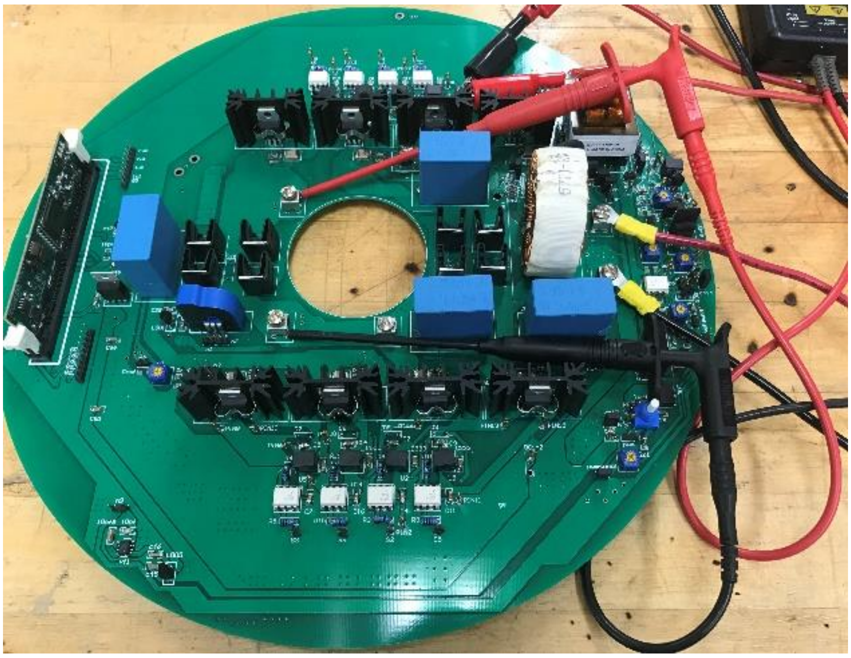

Figure 6.6 Back to back topology of SPMC

6.4 Rotary transformer and rectifier design

6.4.1 Rotary transformer core and winding

Based on the optimization procedure presented in Chapter 4, the core of the rotary transformer has been manufactured in three parts: one rotary part, and two stationary parts as shown in Fig.6.7. The two stationary parts contain one main part and a cap ring element which are shown on the left of Fig.6.7, since it will be easier to wind the wires in this two-part structure compared to a one-part structure as mentioned in Chapter 4. The detailed dimensions and material composition of the transformer core are summarized in Table 6.3.

Figure 6.7 Core of the rotary transformer

Table 6.3 Optimized 200W rotary transformer parameter

Shaft Diameter (D_1)	2.54cm (1inch)
Rotor Core Diameter (D_2)	5.48cm (2.16inch)
Stator Core Diameter (D_3)	7.28cm (2.866inch)
End Cap Height (Eh)	1.046cm (0.412inch)
Winding Window Length (h)	6.97cm (2.746inch)
Winding Window Width ($\frac{\Delta r}{2}$)	0.254cm (0.1inch)
Airgap Length ($\frac{L_{gap}}{2}$)	0.5mm (19.85mil)
Core Material	MnZn Type Ferrite Material

Fig.6.8 shows a comparison between the rotary transformer core with the existing brushless exciter. And a detailed weight and rated power comparison of the two systems are summarized in Table 6.4.

Figure 6.8 Comparison of the designed rotary transformer core to a traditional brushless exciter

Table 6.4 Comparison of the two systems in weight and rated output power

	Designed Rotary Transformer	Brushless Exciter
Total Weight	1.5kg core plus 0.6kg copper	14.4kg
Rated Output Power	400W	65W

The winded transformer core is shown in Fig.6.9 with a primary turns number of 37 and a secondary turns number of 16.

Figure 6.9 Winded transformer core

6.4.2 Rotary transformer cage

To avoid additional eddy current loss, the shaft and cage of the rotary transformer are built of the polyethylene material in a machine shop. Fig.6.10 shows the three parts of the transformer cage, which consists of two cap parts and one body part. It could also be observed from Fig.6.10 (a) that a bearing is embedded in the cap part of the transformer cage to maintain the small airgap (0.5mm). Wires on the rotary part of the transformer will be connected to the rectifier bridge through the inner side of the plastic shaft shown in Fig.6.10 (b).

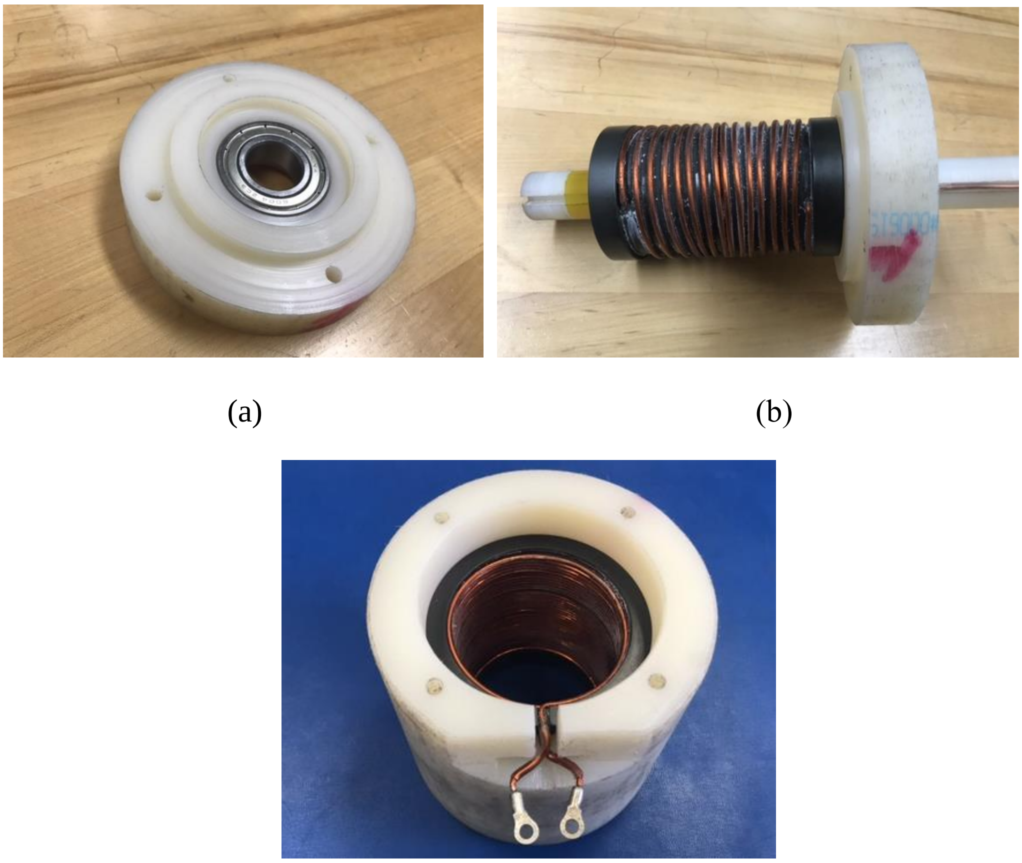

(a) (b)

(c)

Figure 6.10. Cage of the rotary transformer (a) Cap part with bearing (b) Cap part with shaft and rotary part of the transformer (c) Body part with stationary part of the transformer enclosed

Figure 6.11 shows the complete system of the rotary transformer and the detailed electrical parameters of the transformer are summarized in Table 6.5.

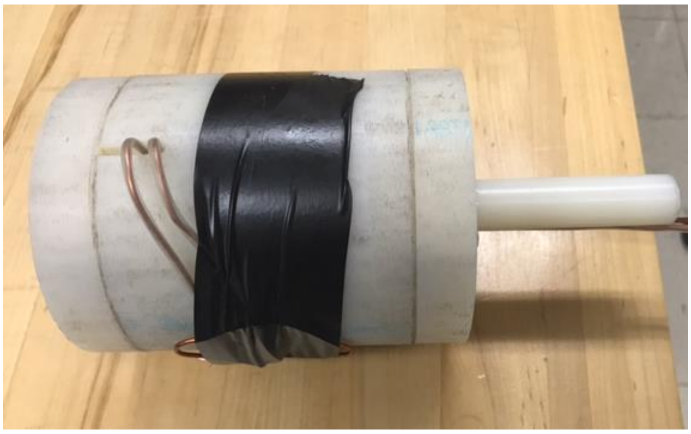

Figure 6.11. Complete rotary transformer

Table 6.5 Electrical parameters of the rotary transformer

Magnetizing Inductance	2.93mH
Leakage Inductance referred to the primary side of the transformer	194uH
Stationary side winding resistance	61.9mΩ
Rotary side winding resistance	18.39mΩ

6.4.3 Rotary diode bridge

The diode bridge is mounted on a plastic frame through the heat sink shown in Fig.6.12. It could also be observed from the right picture of Fig.6.12 that the plastic frame is attached to the shaft through a small key. The diodes used in this rectifier bridge is APT60S20BG with a forward voltage drop of 0.65V at 30 Amps with a fast reverse recovery characteristic of 55 ns.

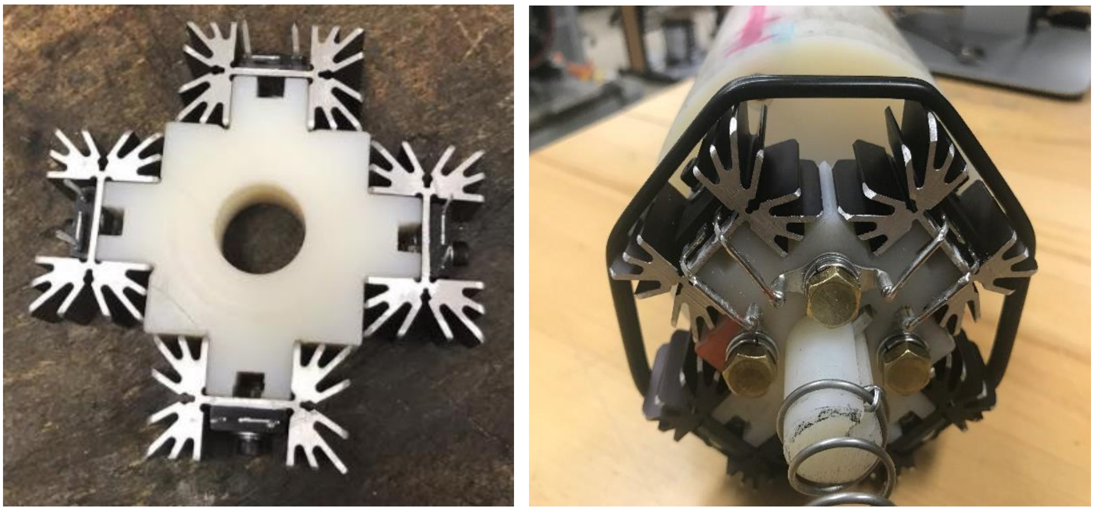

Figure 6.12 Rotary Diode Bridge

6.5 Machine and dyno set-up

6.5.1 Machine reconfiguration and set-up

The wound field synchronous machine used in this project was donated by Regal Inc., with a model number of 281PDL1722, the detailed machine parameters are summarized in Table 6.6.

Table 6.6 Parameters for the wound field synchronous machine

Pole Pair Number	2
Rated Output Power	8.8kW
Rated Voltage (Y-Connected)	240V Parallel/480V series
Field winding resistance	0.3Ω
Field winding inductance	4H

6.5.2 Set-up of the dyno

To verify the proposed system, a modification of the existing rotor structure is required. The first step is to remove the existing brushless exciter and the rotating diode bridge from the main rotor shown in Fig.6.13. The left part of Fig.6.13 shows the unconfigured rotor and the right part of Fig.6.13 shows the rotor after the unnecessary parts are removed.

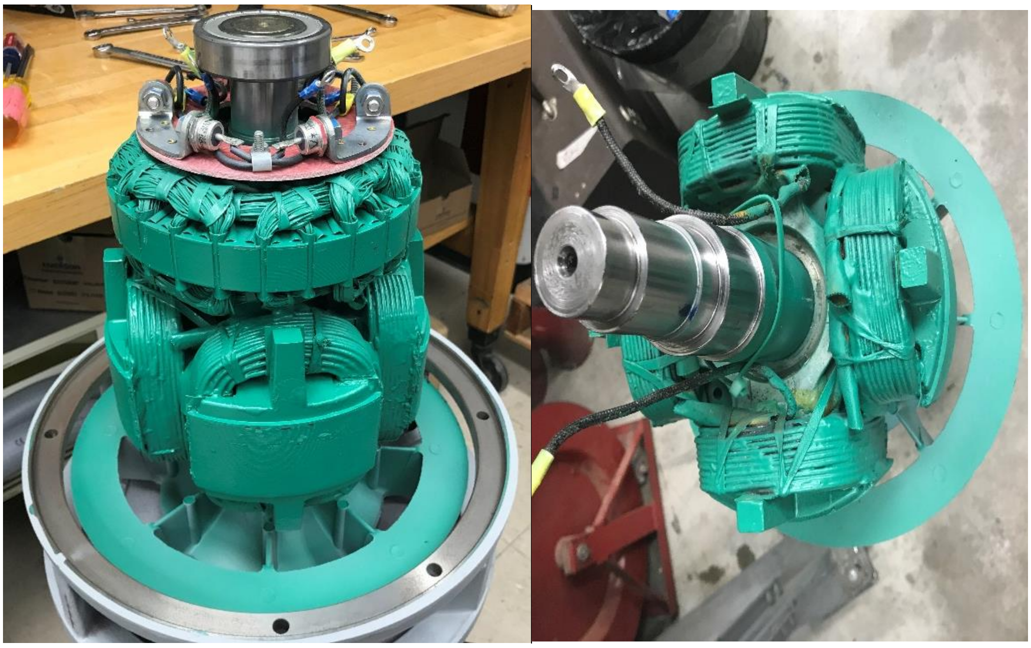

Figure 6.13 Rotor structure before and after modification

Since the goal of this experiment is to prove a concept instead of designing a mature product, it would be easier to analyze the system (for example: current measurement) if the rotary transformer is separated from the main rotor, the rotary transformer is not mounted on the same shaft as the rotor. However, the rotating transformer still needs to supply the current for the main rotor's field winding. Hence a slot is made through the main rotor's shaft to place the field winding wires for the transformer shown in Fig.6.14.

After the reconfigured rotor was placed back to its stator, the following steps to build a base for the machine and the rotary transformer so that the proposed system could be operated in an existing dyno. The base for the machine consists of three parts aluminum metal and the base for the rotary transformer is made of two parts plastic stands. The finished three parts machine base and the two-parts rotary transformer base are shown in Fig.6.15.

Figure 6.14 Reconfigured rotor shaft

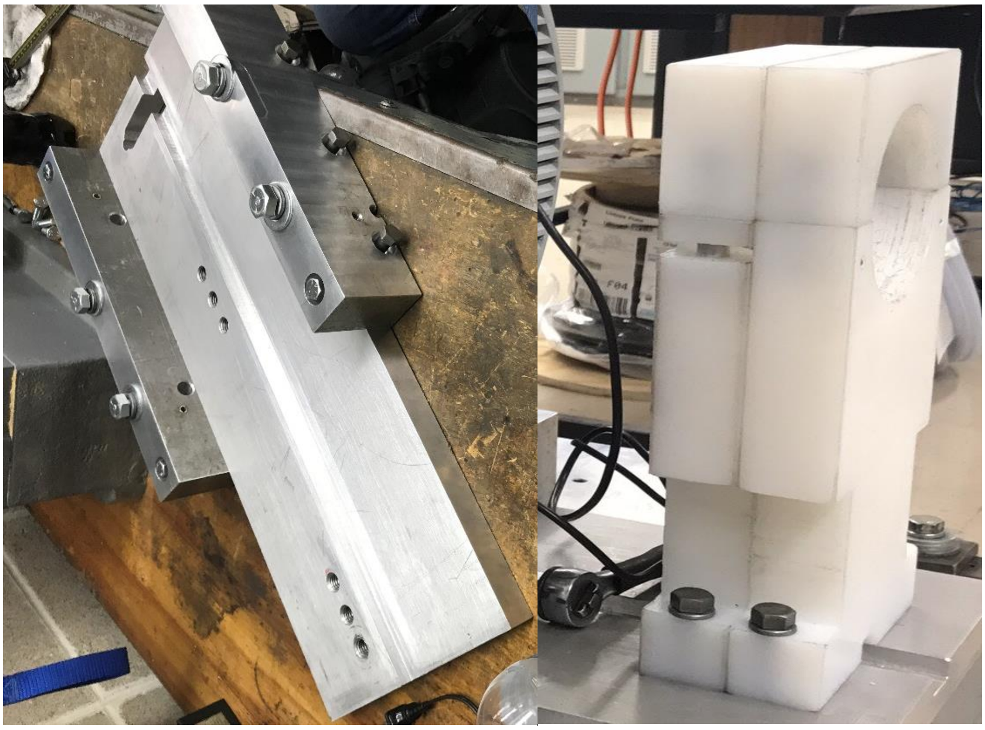

Figure 6.15 Base for the proposed system

6.5.3 Overall system structure

Fig.6.16 shows the complete rotary transformer based field excitation system with matrix converter attached to the main machine. The eight switch topology of the matrix converter is chosen in the final experiment stage because of a lower conduction loss and a guaranteed safe commutation strategy.

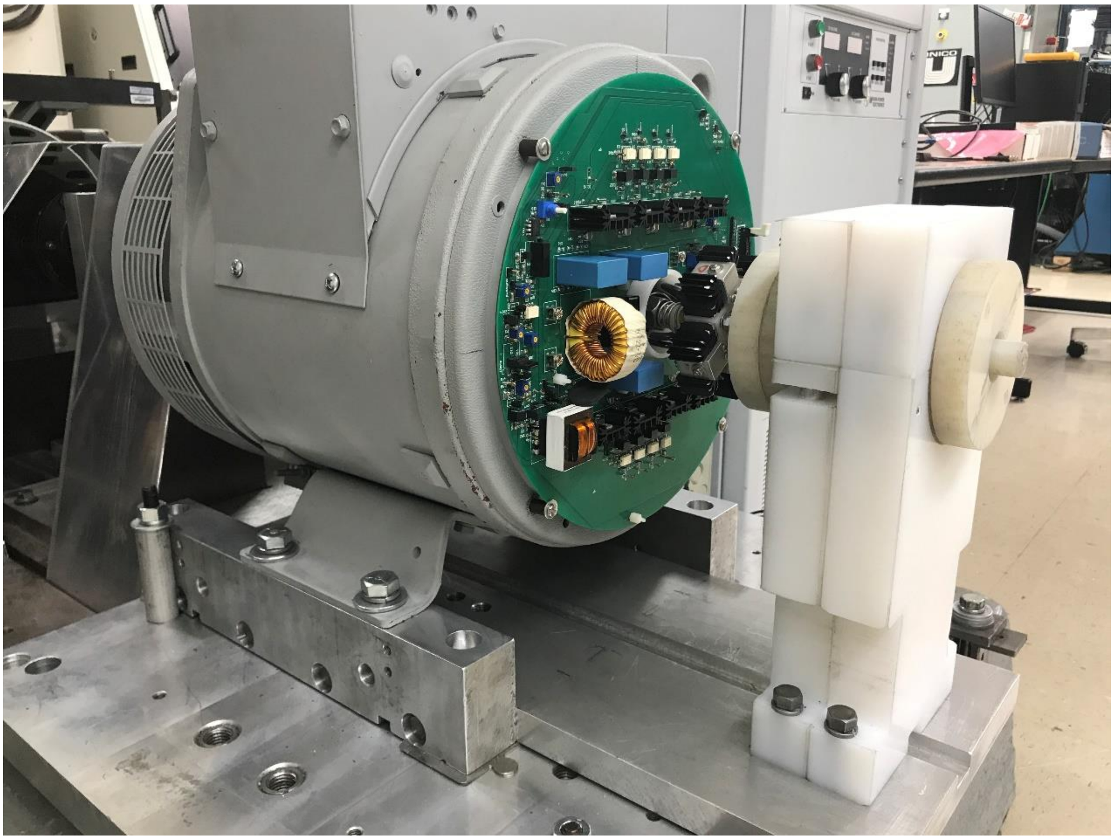

Figure 6.16. Complete excitation system

6.6 Experimental results

6.6.1 Experimental results with sinusoidal excitation

The first experiment set-up is to check the characteristics of the rotary transformer system. Thus a 960Hz sinusoidal input voltage was supplied to the transformer. Machine was at standstill in this set-up to ensure the measurement of both the transformer input voltage, current and the output voltage, current waveform.

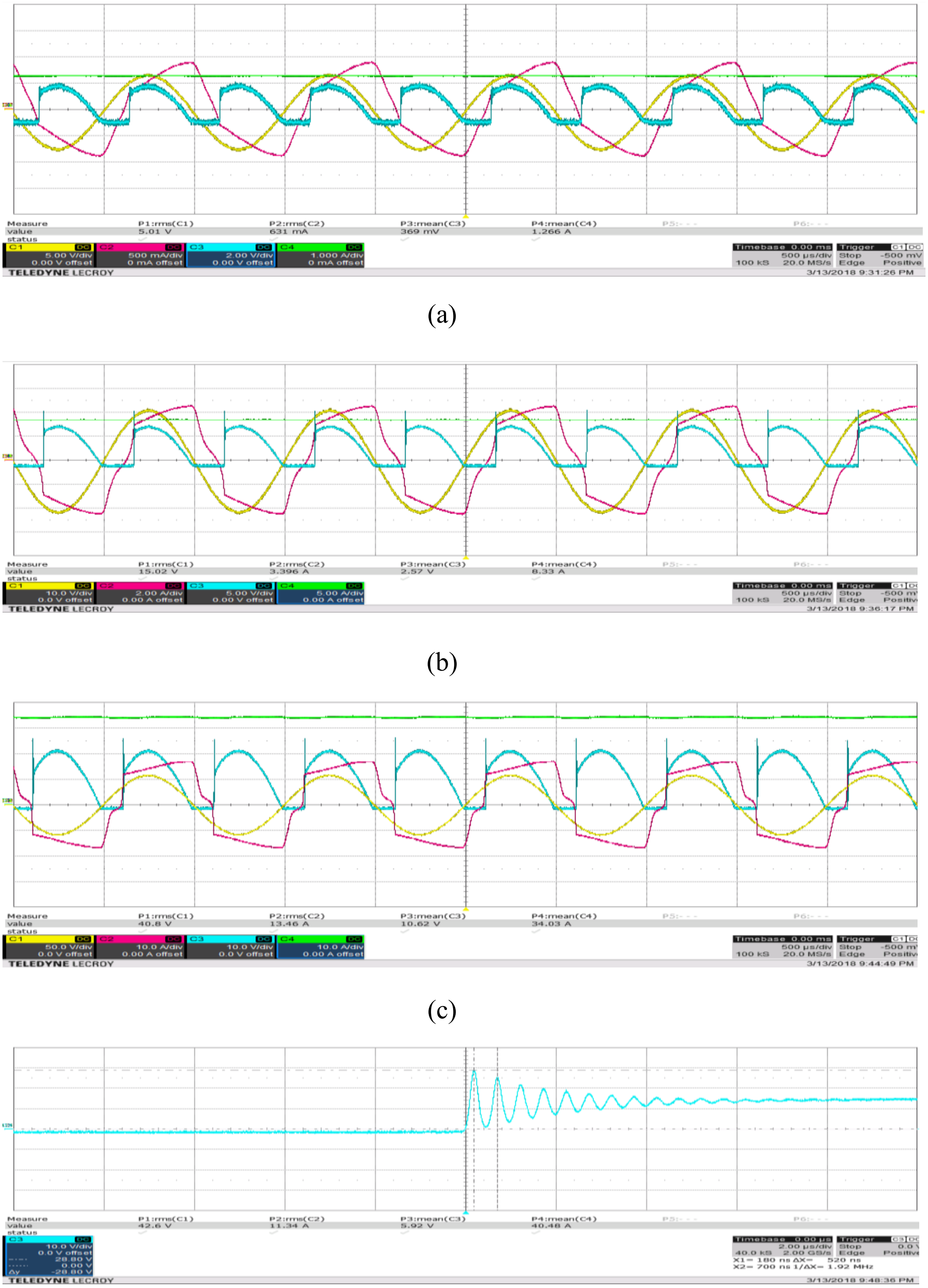

(a)

(b)

(c)

(d)

Figure 6.17. Input voltage, current and output voltage current after the rectifier bridge (a) 10V input (b) 15V input (c) 40V input (d) Reverse recovery characteristics

Fig.6.17 shows the input voltage and current waveform to the rotary transformer plus the rectified output voltage and current waveform to the machine at three input voltage level of 10, 15, and 40 V rms. It can be observed from the waveforms that due to a large field winding inductance, the field current is almost purely DC for all the cases. It could be observed from the plot that owing to the 190uH leakage inductance, the input current lags the input voltage by about 40 degrees. The voltage spike at the rectifier's output is caused by the reverse recovery characteristics of the rectifier diodes shown in Fig.6.17 (d). The efficiency and the output power for the above waveforms are summarized in Table 6.7 below. At rated output power of 400W, the designed rotary transformer is 4 percent less efficient than the predicted value mentioned in Chapter 4, which is caused by the poor fill factor in the rotor side of the transformer. As a result, the rotor winding resistance is about eighty percent higher than the predicted value.

Table 6.7 Summarized information for sinusoidal input at standstill operation

Input Voltage (rms)	5V	15V	40V
Input Current (rms)	0.631A	3.396A	13.46A
Output Field Current (avg)	1.266A	8.33A	34A
Overall Transformer Efficiency	93.8%	85%	93%
Output Power	2.25W	32.5W	391W

To check if the airgap has been uniformly distributed through the rotary transformer, a measurement of the input current to the transformer was performed at different speeds while keeping the same input voltage of 15V. It can be observed from the plot in Fig.6.18 that a uniformly distributed airgap has been achived in the rotary transformer since the input current at standstill is the same as the input current during rotation, which also means the magnetizing inductance maintains a constant value at different rotor location.

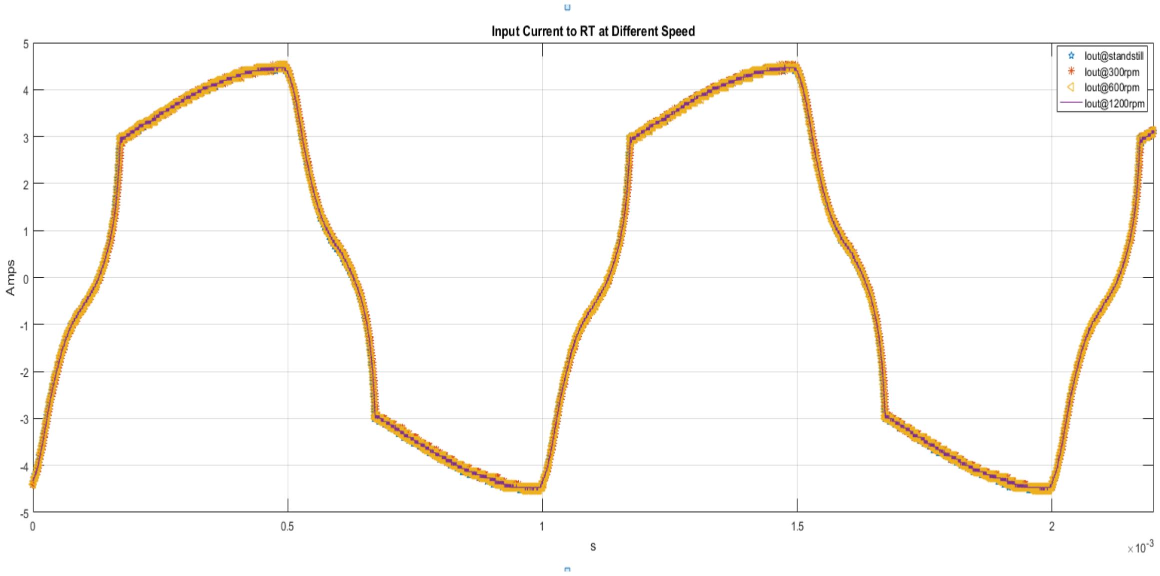

Figure 6.18 Input current to the rotary transformer at different speed

Fig.6.19 shows the generated three-phase back EMF at four different speeds while the input voltage is 15 Volts. The corresponding detailed information is summarized in Table 6.8.

Table 6.8 Generated back EMF at different speed

Speed (RPM)/Frequency(Hz)	300/10	600/20	1200/40	1800/60
EMF (Volts in rms) line to line	59.52	117.68	233.65	346.7

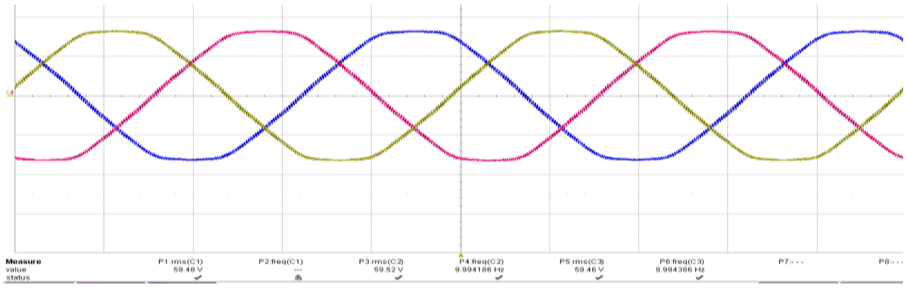

(a)

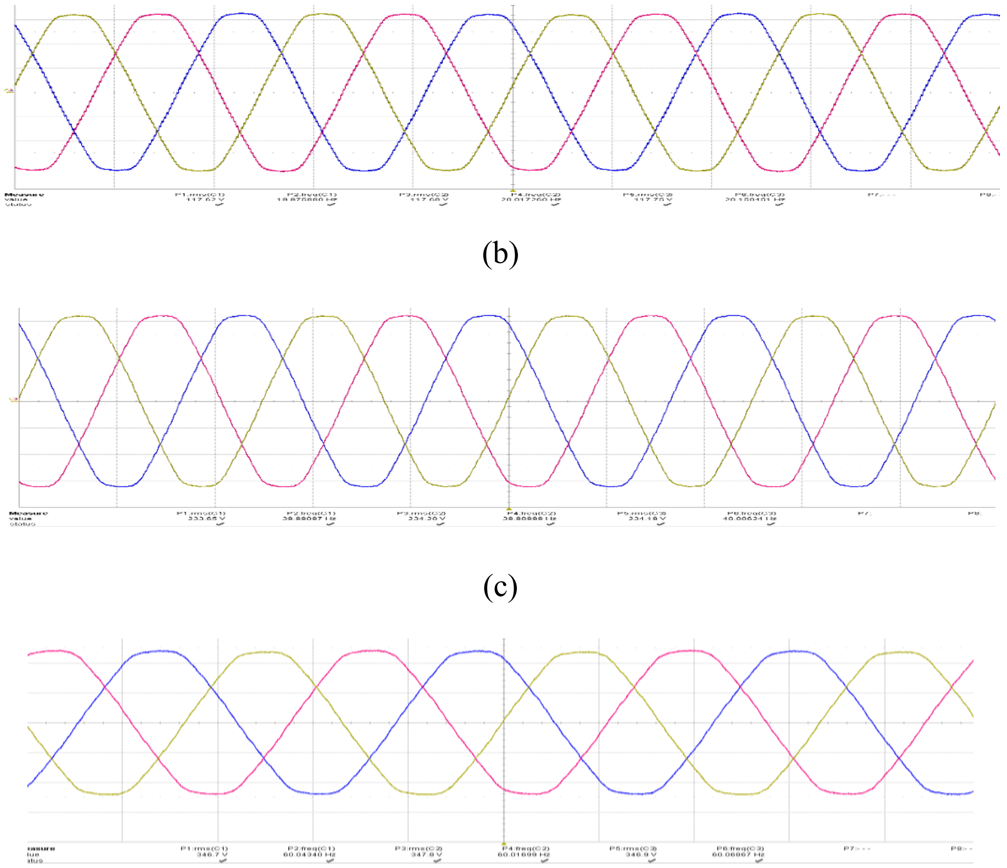

(b)

(c)

(d)

Figure 6.19 Generated back EMF at different speed (a) 300RPM (b) 600RPM (c) 1200RPM (d) 1800RPM

From Fig.6.19, it can be concluded that the desired back EMF has been successfully generated by the proposed rotary transformer system. Since the three-phase load consists of three 260Ω resistors with a limited heat dissipation property, the back EMF is not going higher than 350V rms. But it should be noted that the proposed system can produce rated 480 V rms, as the output power for the rotary transformer is less than 30 W in the 350V case, but it has a rated output power of 400W.

6.6.2 Experimental results with proposed constant volts per Hz modulation

A similar standstill set-up was also implemented for the proposed constant volts per Hz modulation. Fig.6.20 shows the input voltage, current to the rotary transformer (which is also the output voltage and current waveform produced by the single phase matrix converter) and the rectified output voltage and current waveforms for the proposed constant volts per Hz modulation when the machine is at standstill. The input voltage to the matrix converter is 60Hz sinusoidal wave with three different rms values of 30, 60 and 90 Volts.

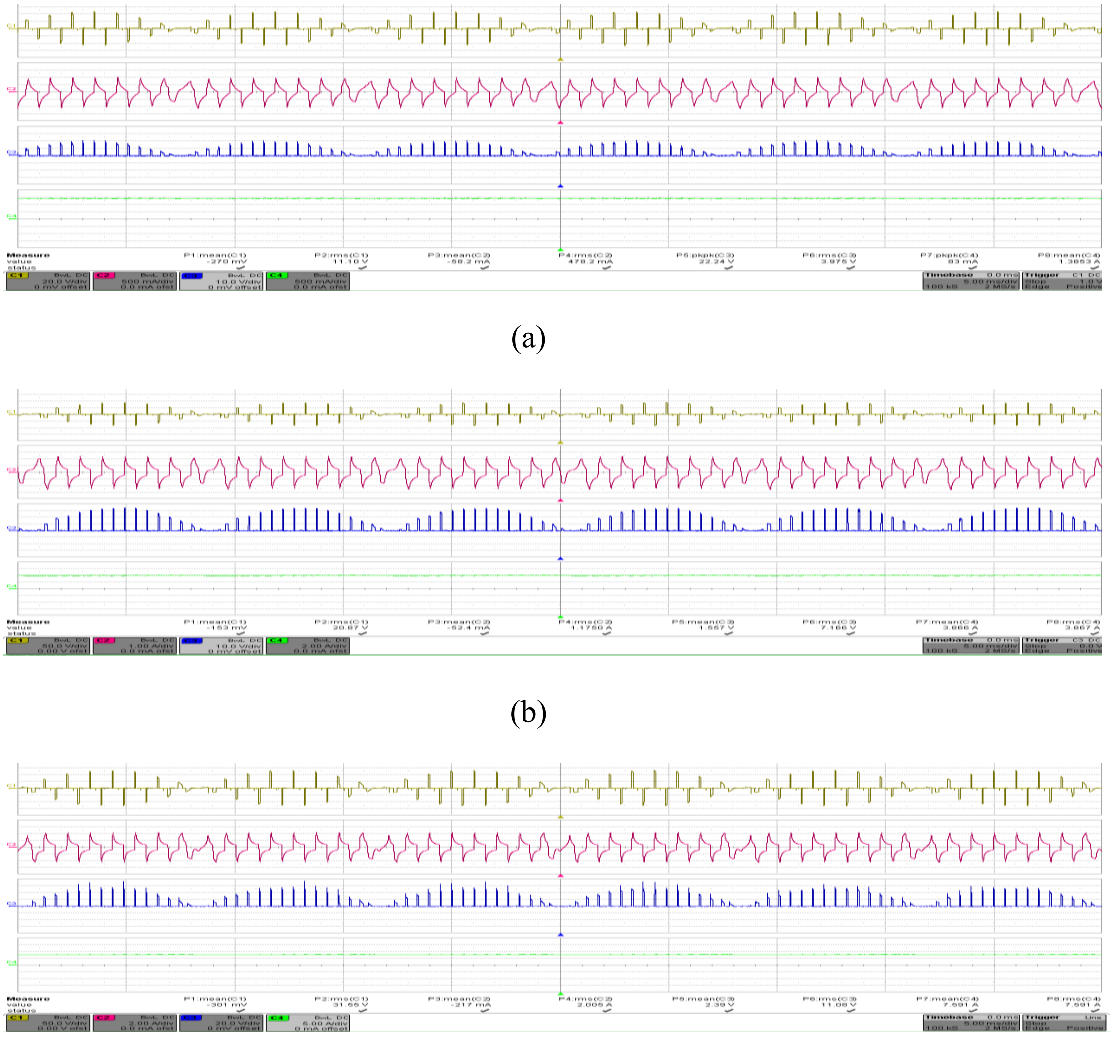

(a)

(b)

(c)

Figure 6.20. Input voltage, current to the rotary transformer and output voltage, current after the rectifier bridge for the propose constant volts per Hz modulation (a) 30V input (b) 60V input (c) 90V input

It can be observed from Fig.6.20 that there is a continuous and balanced transformer input current . Thus, the proposed safe commutation strategy is successfully implemented. It could also be observed from the waveform that there is a nearly constant field current from the proposed constant V/Hz modulation . Thus, the proposed modulation strategy has also been successfully applied. Fig.6.21 shows the input voltage and current waveform to the matrix converter when the input voltage is 90V rms. Because of the discontinuous output voltage of the converter, the input current to the converter is not purely sinusoidal as shown in Fig.6.21 (b).

The important characteristics of the proposed single phase matrix converter when the input voltage is 90V rms are summarized in Table 6.9. The overall system efficiency is 79% and 95 percent of loss are caused by the unavoidable conduction loss as the system operates at medium frequency. It should also be noted that the proposed system is designed to be operated at a rated power level of 400W due to an estimation of the field power requirement . However, it turns out that the field power of the real machine is only less than 50W . Thus, the designed system is not optimized for the proposed machine. Also, if the system is working at its rated power of 400W, the overall system efficiency will be higher than 80%.

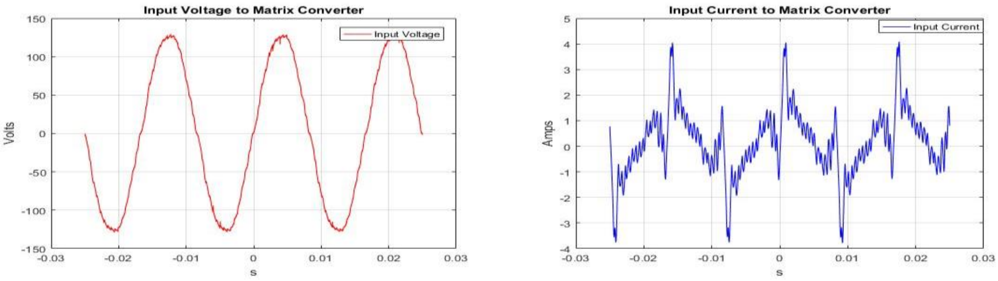

(a) (b)

Figure 6.21. (a) Input voltage to the matrix converter (b) Input current to the matrix converter

Table 6.9 Important characteristics for the proposed system with an input voltage of 90Vrms

Input Voltage (rms)	90V
Input Current (rms)	1.3A
Transformer Input Voltage (rms)	31.55V
Transformer Input Current (rms)	2A
Field Current	7.6A
Input Power	36W
Output Power of Matrix Converter	30.399W
Input Power Factor	54%
Output Field Power	17.28W
Rectifier Bridge Power Loss	9.86W
Snubber Loss	0.99W
Switch and Circuit Conduction Loss	4.89W
Transformer Loss	1.9W
Other Loss (Switching etc)	0.83W
Overall System Efficiency	79%

It may be seen from the Table 6.9 that the overall transformer loss for the proposed constant volts per Hz modulation is higher than that for the sinusoidal excitation shown in the last section at a same light load condition of 20W (3.67W loss for sinusoidal and 1.9W for constant) even though the proposed modulation has a higher core loss owing to the harmonics in the input voltage. Since the majority (85% or even higher) of the overall transformer loss is conduction loss for the medium frequency operation and for the proposed constant volts per Hz modulation, the transformer will only conduct full load current when there is a non zero input voltage (active Duty cycle) as mentioned in Chapter 4. It should also be noted that the constant V/Hz modulation will have even better efficiency than the sinusoidal excitation at heavy load (400W), because the difference in conduction loss is also larger at heavy load.

Following the same experiment set-up in the previous section, Fig.6.22 shows the generated three-phase back EMF at three different speed while the input voltage to the matrix converter is 60Hz 90Vrms. The detailed information is summarized in Table 6.10.

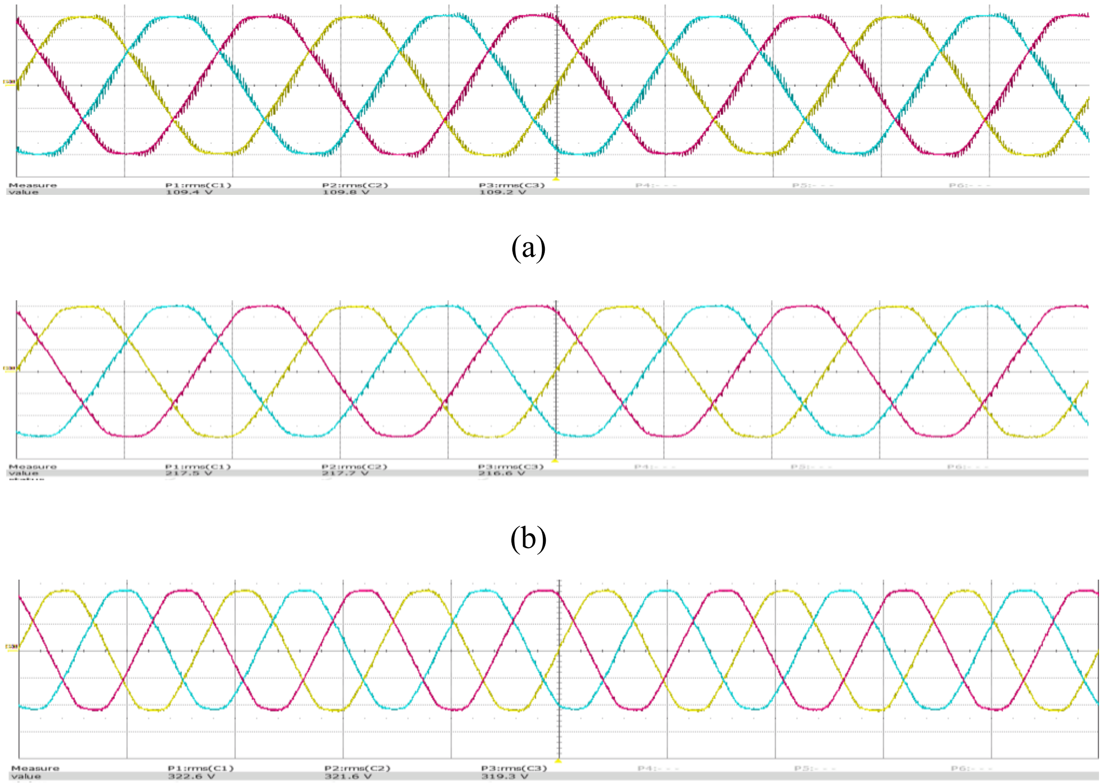

(a)

(b)

(c)

Figure 6.22. Three phase back EMF waveforms generated by the proposed modulation

Table 6.10 Generated back EMF at different speed

Speed (RPM)/Frequency(Hz)	600/20	1200/40	1800/60
EMF (Volts in rms) line to line	109	217	320

Fig.6.23 shows the rectifier side voltage waveforms for the sinusoidal and the constant V/Hz modulations. It can be observed from Fig.6.23 that the voltage overshoot for the constant V/Hz modulation is much smaller (at least 80 percent less) than that for the sinusoidal case. This is also due to the additional zero state that has been introduced in the constant V/Hz modulation. Because the energy stored in the leakage inductance is damped out in the additional zero state, there will be one and the only one diode which has a reverse recovery scenario when the input voltage polarity changes. On the other hand, there will be one pair (two) of diodes which have the reverse recovery scenarios on sinusoidal excitation since the energy stored in the leakage must be damped out by an active input voltage.

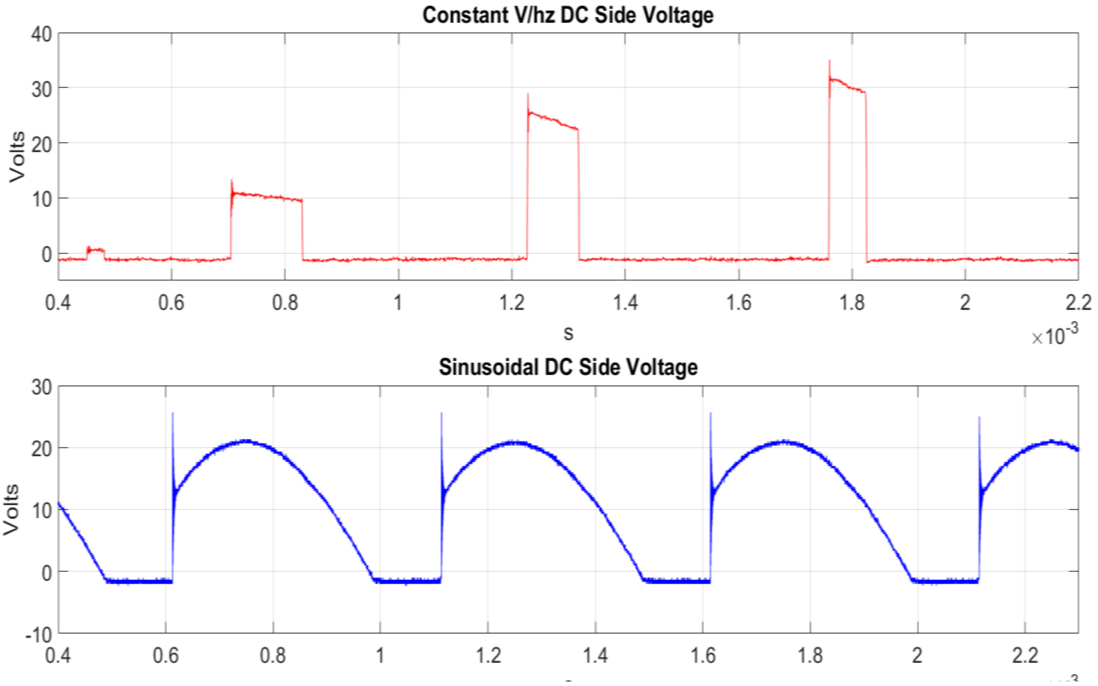

Figure 6.23 DC side voltage waveform

6.7 Summary

The proposed field excitation system with its experimental set-up has been explained in this chapter. Compared to a traditional brushless exciter, the proposed system can produce 6.5 (400W to 60W) times its rated power at one 7th (2.1kg to 14.4kg) of its weight.

A loss analysis has been made based on the use of a rotary transformer and the matrix converter. It can be observed that the overall system has an efficiency of 83 percent for a rated output power of 400W and has an efficiency of 78 percent for an output power of 35W to produce 330V line to line voltage at machine's rated speed of 1800 RPM, wherein the traditional brushless exciter has an efficiency around 70 percent at its rated power. The overall system efficiency can be further increased by increasing the fill factor of the rotary transformer and using an active switch with lower on resistance.

Chapter 7

CONTRIBUTIONS AND FUTURE WORK

7.1 Summary of contributions

1. A single phase matrix converter based rotary transformer for brushless field excitation system was first proposed and realized in this thesis.

2. A new constant volts per Hz modulation method based on the single phase matrix converter has been proposed, which will significantly reduce the size, increase the efficiency of the rotary transformer, and increase the reliability of the rectifier bridge as well. Compared to a traditional brushless exciter, the proposed system has reduced the system weight by 90 percent while increasing the output power by 500 percent.

3. A novel safe commutation strategy was proposed and verified through experiments based on the proposed modulation method.

4. The current flow during the zero state for the proposed modulation strategy was analyzed, and a comprehensive comparison made to prove the proposed modulation has the advantages of lower transformer loss under most conditions.

5. An accurate model to calculate the transformer primary and secondary side RMS current for a constant volts per Hz modulation method is proposed in this thesis, which can be used to calculate the power loss for the transformer.

6. A new generalized optimization procedure in designing a medium frequency rotary

transformer with minimum leakage inductance is proposed, which will generate a rotary transformer with both minimum weight and minimum power loss without iteration required. By simply replacing the RMS current calculation model, this generalized procedure is also applicable for other rotary transformer designs.

7. A detailed study of the rotary transformer characteristics was performed based on the proposed optimization model.

8. Two different topologies (rectifier bridge connected and back to back connected) for the matrix converter were built to verify the proposed modulation strategy and the benefits and the defects for the two topologies were discussed.

7.2 Recommended future work

7.2.1 Indirect matrix converter topology

It is always important to reduce the cost of any power electronics drive circuit. However, for a traditional matrix converter topology, the switches must conduct bi-direction current and block bi-directional voltage. Thus, compared to the inverter based circuit, the active switch number for the matrix converter system is doubled. To reduce the number of active switches, some researchers have proposed a current source ac to ac system [93]. The proposed system structure with its transformer's magnetizing current waveform is shown in Fig.7.1.

By proper control of the input voltage to the converter, a dc biased magnetizing current could be obtained shown in Fig.7.1 (b), thus the converter only needs to conduct a single direction output current. As a result, the system is capable of changing the two-active switch structure to one active switch plus one passive diode shown in Fig.7.1 (a), and the cost of overall system is reduced.

However, this system is, in fact, an ac based fly back converter. Compared to a traditional transformer, the flux area must be at least doubled for the same V/Hz input to avoid saturation of the transformer core (due to the dc component), which also means the transformer weight needs to be doubled.

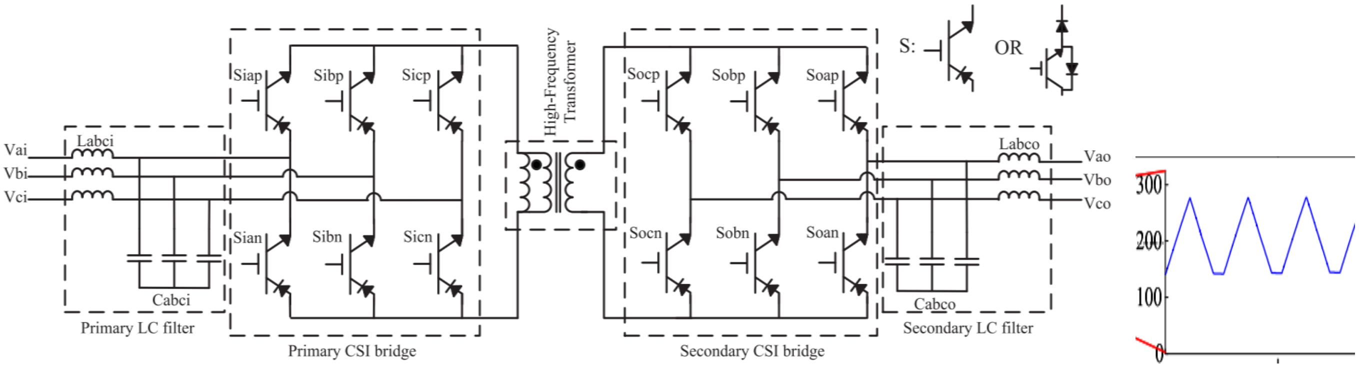

(a) (b)

Figure.7.1. Current source ac/ac system with reduced number of active switch (a) System structure (b) Transformer magnetizing current waveform [93]

To solve the above mentioned problems with the current source ac/ac converter, the in-direct dual bridge matrix converter will also be a possible substitution. The proposed system structure is shown in Fig.7.2, where the input line voltage is rectified through a diode bridge and fed to an inverter circuit through a very small link capacitor. The output voltage waveform of the inverter circuit will be the same as the proposed constant V/Hz modulation. This kind of matrix converter has the same switch counts as the current source ac/ac converter mentioned above and inherits the advantages of the proposed constant V/Hz modulation. However, it should be noted that the proposed system can only operate when there is a unity power factor at the load side, since the reactive power stored in the load side will keep charging the link capacitor and eventually causing an over-voltage issue. For the proposed rotary transformer with small leakage inductance, the transformer input voltage and current will be totally in phase in the steady state as shown in Fig.7.3. Thus, the proposed indirect matrix converter will be a perfect match for the rotary transformer application.

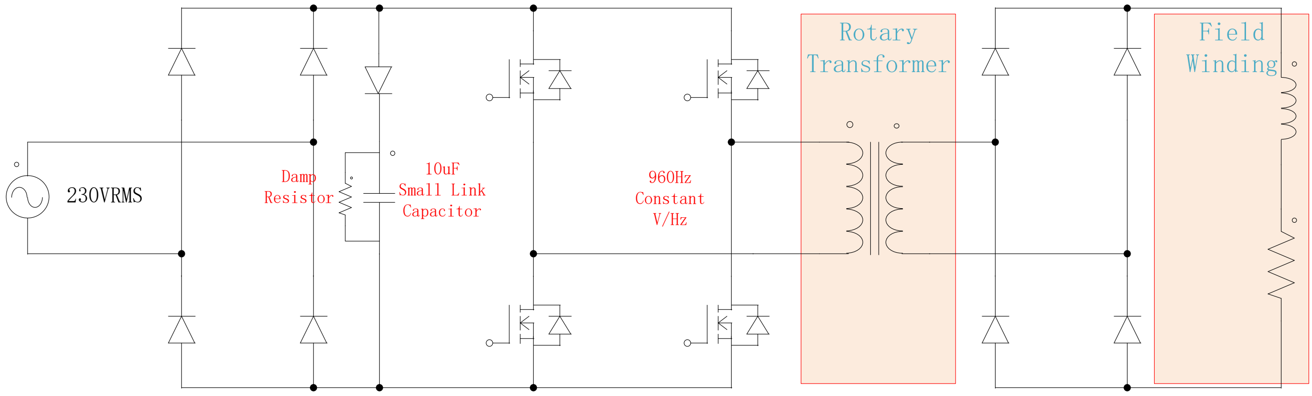

Figure.7.2. Proposed indirect matrix converter topology

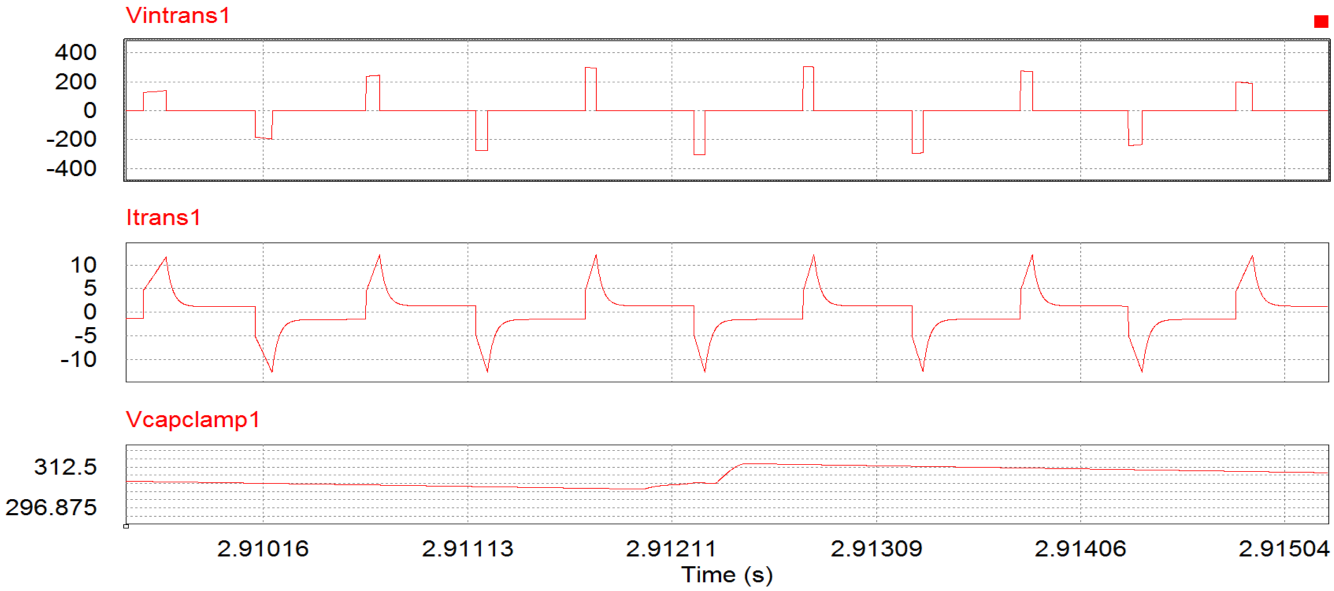

Figure.7.3. Steady state transformer input voltage, current waveform and clamp capacitor voltage waveform

However, when the system starts from zero field current, the magnetizing current will increase much faster than the load current because of the huge field inductance. The energy stored in the magnetizing branch of the transformer must be released to the clamp capacitor when the transformer input voltage polarity changes. Therefore, there will be a overshoot voltage in the clamp circuit if the system is not properly controlled shown in Fig.7.4. Fig.7.5 shows the input voltage and current waveform to the rotary transformer when the system starts.

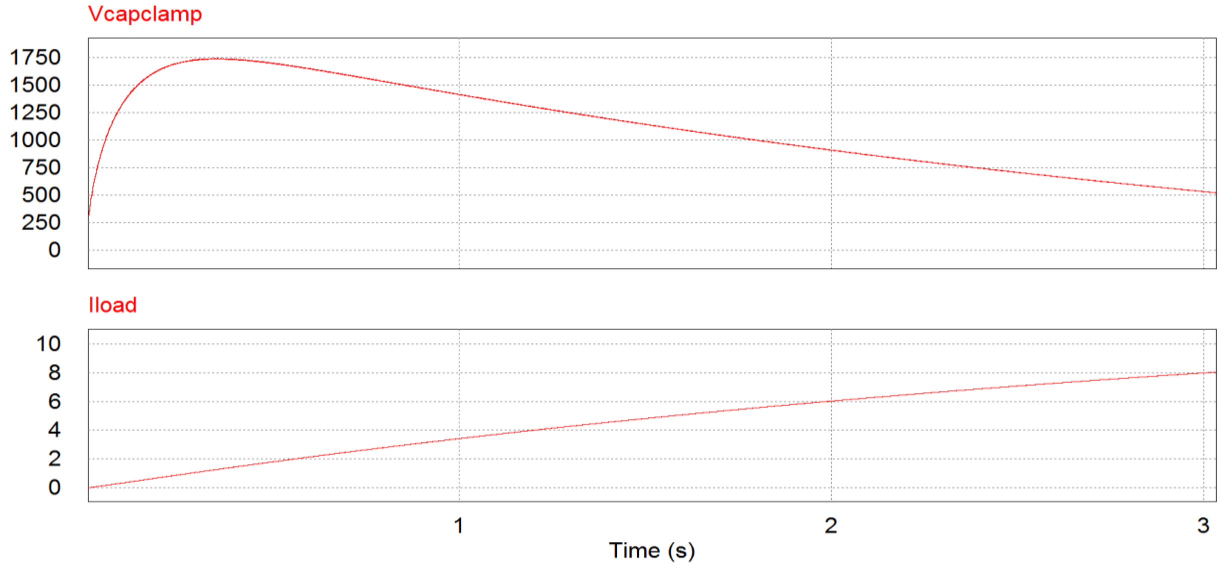

Figure.7.4. Transient voltage waveform for the clamp capacitor and field current waveform

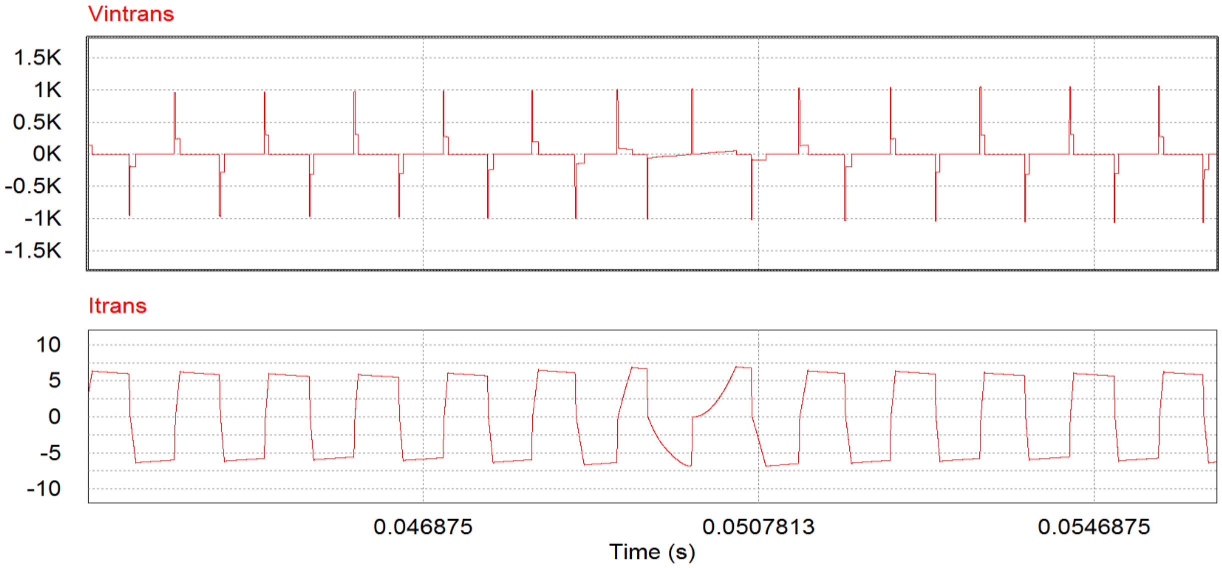

Figure.7.5. Transient transformer input voltage and current waveform

It has been discussed in the previous paragraph that once the load current reaches the peak value of the magnetizing current, the stored energy in the transformer will no longer transfer to the clamp capacitor. Thus, it will also be the moment when the clamp capacitor reaches its peak overshoot voltage. As a result, it is important to produce an equation to calculate the total energy transfer to the clamp capacitor during the transient starting period, since the overshoot voltage could also be controlled based on the variables in that equation. (7.1) shows the peak magnetizing current I_{mpeak} of the transformer, where f is the frequency, V_{avg} is the average voltage per half cycle, and L_m is the magnetizing inductance of the transformer.

$$\mathrm{I_{mpeak}} = \frac{\mathrm{V_{avg}}}{\mathrm{4f{*}L_m}} \tag{7.1}$$

The field winding current I_{field} can be estimated in (7.2) where L_{field} is the field winding inductance and T is the time to charge the inductor (if steady state load current is much larger than the peak magnetizing current).

$$\mathrm{I}_{field} = \frac{\mathrm{V_{avg}}{*}T}{\mathrm{L_{field}}} \tag{7.2}$$

Based on these two equations, the time (T_1) when the clamp capacitor reaches its peak voltage can be calculated in (7.3).

$$\mathrm{T_1} = \frac{\mathrm{L_{field}}{*}\mathrm{I_{mpeak}}}{\mathrm{V_{avg}}} \tag{7.3}$$

The total energy W_{tot} which will be transferred to the clamp capacitor is calculated in (7.4), where I_n is the current that goes to the clamp capacitor for every switching cycle. N_{max} is the cycle counts when the field current reaches the magnetizing current.

$$\mathrm{W}_{tot} = \frac{1}{2}\sum_{n=0}^{n=N_{max}} L_m * I_n^2 \tag{7.4}$$

$$I_n = \mathrm{I_{mpeak}} - n * \frac{\mathrm{V_{avg}}}{\mathrm{L_{field}}{*}2f} \tag{7.5}$$

$$N_{max} = T_1 * 2f = \frac{L_{field}}{2 * L_m} \tag{7.6}$$

Substitute I_n in (7.4) from (7.5), the total energy transferred to the clamp capacitor can be rewritten in (7.7).

$$W_{tot} = \frac{1}{4} * \frac{{V_{avg}}^2}{f^2 * L_m} * (N_{max} + N_{max} * (N_{max} - 1) * \frac{2N_{max} - 1}{6} + \frac{N_{max} * (N_{max} - 1)}{2}) \tag{7.7}$$

From (7.6) and (7.7), it is clear that the four control variables that determine the total energy that will be transferred to the clamp capacitor are the average half cycle voltage V_{avg}, input frequency f, field inductance L_{field} and the magnetizing inductance L_m. The only way to reduce this total energy is by reducing the L_{field} and V_{avg} or increasing L_m and f. But as L_{field} and L_m are determined by the machine and the transformer, it is only feasible to reduce the overall energy by manipulating V_{avg} and f. Because V_{avg} can be easily changed by the pulse width of the output without creating additional switching loss, it is chosen as the variable to reduce W_{tot}. Fig.7.6 shows the simulation results of clamp capacitor voltage after a proper control of the V_{avg} is implemented. And it can be also observed from Fig.7.6 that the overshoot of the clamp capacitor voltage is successfully suppressed.

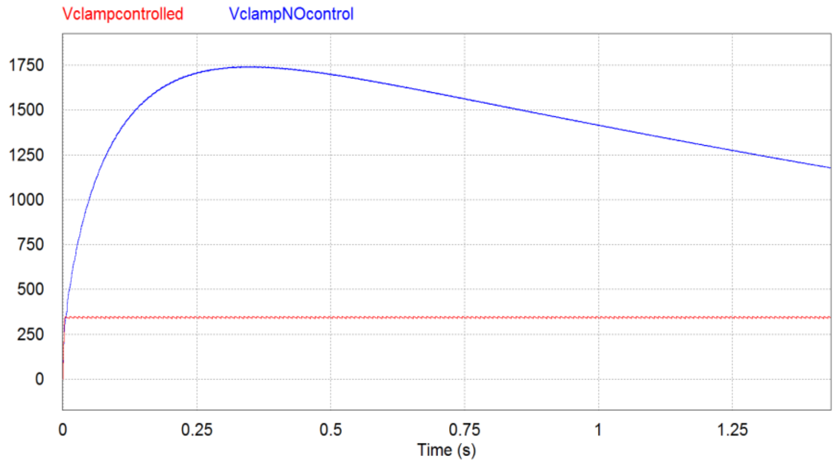

Figure.7.6. Controlled Vclamp versus uncontrolled Vclamp

7.2.2 Application on high voltage low frequency transmission lines

Another possible application for the proposed modulation method is on a high voltage low frequency transmission line. Owing to the low frequency input (60 or 50Hz) at the local distribution site, the transformer used to step down the high line voltage is usually bulky in volume. By using the proposed medium frequency modulation, the transformer in the local site can be more efficient and more compact.

On account of the large power level (MW level), the main issue which needs to be dealt with in this application is to increase the input side power factor, which needs to be solved by future researchers.

7.2.3 Closed-loop control of the field winding current

As experiments performed in this thesis are all open loop based, to adjust the output voltage for the wound field synchronous machine, a proper control of the field current should be implemented in the future work. Since the proposed constant V/Hz modulation has the voltage and the frequency as two control variables, it also has two ways to control the output voltage which needs to be determined by specific applications.

7.2.4 Resonant converter topology

The transformer designed in this project has a leakage inductance of 190uH, which is four times larger than the predicted value. The increase of the leakage inductance decreases the load side power factor by five percent and the overall transformer efficiency by one percent. A resonant converter may be a great candidate to incorporate this leakage inductance to its resonant tank, which increases the power factor and system efficiency. But it should be noted that the operating frequency of the transformer needs to be at least 10kHz for this kind of application, otherwise the size of the resonant tank may be a problem.

7.2.5 Investigate the possible rotary transformer structure for MW level wind turbine application

The proposed system can also be applied to MW level wind turbine system [94]. The main issue which needs to be solved in this application is the structure of the rotary transformer. Because for MW level application, ferrite material will be too fragile to operate, a robust laminated iron structure should be explored.

7.3 Summary

In conclusion, the proposed matrix converter based rotary transformer system is expected to be a competitive approach compared to the existing brush and brushless exciters for wound field synchronous machine.

List of References

[1] T. A. Lipo and Z. S. Du, "Synchronous motor drives-a forgotten option," in *2015 Intl Aegean Conference on Electrical Machines & Power Electronics (ACEMP), 2015 Intl Conference on Optimization of Electrical & Electronic Equipment (OPTIM) & 2015 Intl Symposium on Advanced Electromechanical Motion Systems (ELECTROMOTION)*, 2015, pp. 1-5.

[2] A. T. H. Houenouvo and W. Hofmann, "Diagnostics of the transmission properties of the slip ring system in doubly fed induction generators," in *2014 IEEE 60th Holm Conference on Electrical Contacts (Holm)*, 2014, pp. 1-7.

[3] K. Sawa, Y. Suzuki, N. Morita, T. Ueno, and K. Endo, "Effect of Lubricant on Degradation Process of Au-Plated Slip-Ring and Ag-Pd Brush System for Small Electric Power," in *2011 IEEE 57th Holm Conference on Electrical Contacts (Holm)*, 2011, pp. 1-6.

[4] R. C. Schaefer, "Brushless rotating exciter conversion to main field static exciter system," in *Conference Record of 2013 Annual IEEE Pulp and Paper Industry Technical Conference (PPIC)*, 2013, pp. 186-191.

[5] J. K. SkjØlberg, H. F. Ohma, and M. Runde, "Wear Rates and Current Distribution of Carbon Brushes on Steel Slip Rings," *IEEE Transactions on Energy Conversion,* vol. 24, pp. 835-840, 2009.

[6] R. W. Ferguson, R. Herbst, and R. W. Miller, "Analytical Studies of the Brushless Excitation System," *Transactions of the American Institute of Electrical Engineers. Part III: Power Apparatus and Systems,* vol. 78, pp. 1815-1821, 1959.

[7] E. C. Whitney, D. B. Hoover, and P. O. Bobo, "An Electric Utility Brushless Excitation System," *Transactions of the American Institute of Electrical Engineers. Part III: Power Apparatus and Systems,* vol. 78, pp. 1821-1824, 1959.

[8] D. C. Aliprantis, S. D. Sudhoff, and B. T. Kuhn, "A brushless exciter model incorporating multiple rectifier modes and Preisach's hysteresis theory," *IEEE Transactions on Energy Conversion,* vol. 21, pp. 136-147, 2006.

[9] Z. Shushu, L. Chuang, N. Yinhang, and T. Jie, "A Two-Stage Brushless Excitation Method for Hybrid Excitation Synchronous Generator," *IEEE Transactions on Magnetics,* vol. 51, pp. 1-11, 2015.

[10] A. Griffo, R. Wrobel, P. H. Mellor, and J. M. Yon, "Design and Characterization of a Three-Phase Brushless Exciter for Aircraft Starter/Generator," *IEEE Transactions on Industry Applications,* vol. 49, pp. 2106-2115, 2013.

[11] N. Jiao, W. Liu, T. Meng, J. Peng, and S. Mao, "Design and Control of a Two-Phase Brushless Exciter for Aircraft Wound-Rotor Synchronous Starter/Generator in the Starting Mode," *IEEE Transactions on Power Electronics,* vol. 31, pp. 4452-4461, 2016.

[12] N. Jiao, W. Liu, T. Meng, J. Peng, and S. Mao, "Detailed Excitation Control Methods for Two-Phase Brushless Exciter of the Wound-Rotor Synchronous

Starter/Generator in the Starting Mode," *IEEE Transactions on Industry Applications,* vol. 53, pp. 115-123, 2017.

[13] J. K. Noeland, F. Evestedt, J. J. Perez-Loya, a. j, and U. Lundin, "Design and characterization of a rotating brushless outer pole PM exciter for a synchronous generator," *IEEE Transactions on Industry Applications,* vol. PP, pp. 1-1, 2017.

[14] Z. Z. Su, D. Wang, Y. J. Guo, X. Q. Yi, and Y. X. Xiong, "Analysis and modeling of novel brushless exciter based on hybrid excitation topology," in *2015 IEEE International Conference on Applied Superconductivity and Electromagnetic Devices (ASEMD)*, 2015, pp. 512-514.

[15] X. Jia, L. Qingfu, L. Jih-Sheng, and S. Byeong-Mun, "Analysis of polyphase brushless exciter," *IEEE Transactions on Industry Applications,* vol. 37, pp. 1720-1726, 2001.

[16] J. K. Nøland, K. B. Hjelmervik, and U. Lundin, "Comparison of Thyristor-Controlled Rectification Topologies for a Six-Phase Rotating Brushless Permanent Magnet Exciter," *IEEE Transactions on Energy Conversion,* vol. 31, pp. 314-322, 2016.

[17] J. K. Nøland, F. Evestedt, J. J. Perez-Loya, J. Abrahamsson, and U. Lundin, "Evaluation of different power electronic interfaces for control of a rotating brushless PM exciter," in *IECON 2016 - 42nd Annual Conference of the IEEE Industrial Electronics Society*, 2016, pp. 1924-1929.

[18] D. C. Aliprantis, S. D. Sudhoff, and B. T. Kuhn, "Genetic algorithm-based parameter identification of a hysteretic brushless exciter model," *IEEE Transactions on Energy Conversion,* vol. 21, pp. 148-154, 2006.

[19] S. Rosado, X. Ma, G. Francis, F. Wang, and D. Boroyevich, "Model-Based Digital Generator Control Unit for a Variable Frequency Synchronous Generator With Brushless Exciter," *IEEE Transactions on Energy Conversion,* vol. 23, pp. 42-52, 2008.

[20] W. F. Wright, R. Hawley, and J. L. Dinely, "Brushless Thyristor Excitation Systems," *IEEE Transactions on Power Apparatus and Systems,* vol. PAS-91, pp. 1848-1854, 1972.

[21] R. Hong-Woo, S. Seung-Ki, and P. Min-Ho, "A new generator static excitation system using boost-buck chopper," in *Proceedings of the 1996 IEEE IECON. 22nd International Conference on Industrial Electronics, Control, and Instrumentation*, 1996, pp. 1023-1028 vol.2.

[22] A. Barakat, S. Tnani, G. Champenois, and E. Mouni, "Output voltage control of synchronous generator using diode and thyristor excitation structures combined with multivariable H∞ controllers," *IET Electric Power Applications,* vol. 6, pp. 203-213, 2012.

[23] S. Nadarajan, B. Bhangu, S. K. Panda, and A. K. Gupta, "Feasibility analysis of auxiliary winding for condition monitoring of wound field brushless synchronous generators," in *IECON 2015 - 41st Annual Conference of the IEEE Industrial Electronics Society*, 2015, pp. 003370-003375.

[24] L. Sun, X. Gao, F. Yao, Q. An, and T. Lipo, "A new type of harmonic current excited brushless synchronous machine based on an open winding pattern," in

2014 IEEE Energy Conversion Congress and Exposition (ECCE), 2014, pp. 2366-2373.

[25] Q. Ali, T. A. Lipo, and B. Kwon, "Design and analysis of a novel brushless wound rotor synchronous machine," in *2015 IEEE Magnetics Conference (INTERMAG)*, 2015, pp. 1-1.

[26] G. Jawad, Q. Ali, T. A. Lipo, and B. I. Kwon, "Novel Brushless Wound Rotor Synchronous Machine With Zero-Sequence Third-Harmonic Field Excitation," *IEEE Transactions on Magnetics,* vol. 52, pp. 1-4, 2016.

[27] F. Yao, Q. An, L. Sun, and T. A. Lipo, "Performance Investigation of a Brushless Synchronous Machine With Additional Harmonic Field Windings," *IEEE Transactions on Industrial Electronics,* vol. 63, pp. 6756-6766, 2016.

[28] F. Yao, Q. An, X. Gao, L. Sun, and T. A. Lipo, "Principle of Operation and Performance of a Synchronous Machine Employing a New Harmonic Excitation Scheme," *IEEE Transactions on Industry Applications,* vol. 51, pp. 3890-3898, 2015.

[29] S. Zhu, C. Liu, K. Wang, and Y. Hu, "The novel brushless excitation methods for wound rotor excitation synchronous generators," in *2016 Eleventh International Conference on Ecological Vehicles and Renewable Energies (EVER)*, 2016, pp. 1-7.

[30] Q. An, X. Gao, F. Yao, L. Sun, and T. Lipo, "The structure optimization of novel harmonic current excited brushless synchronous machines based on open winding pattern," in *2014 IEEE Energy Conversion Congress and Exposition (ECCE)*, 2014, pp. 1754-1761.

[31] Q. Ali, T. A. Lipo, and B. I. Kwon, "Design and Analysis of a Novel Brushless Wound Rotor Synchronous Machine," *IEEE Transactions on Magnetics,* vol. 51, pp. 1-4, 2015.

[32] D. C. Ludois, J. K. Reed, and K. Hanson, "Capacitive Power Transfer for Rotor Field Current in Synchronous Machines," *IEEE Transactions on Power Electronics,* vol. 27, pp. 4638-4645, 2012.

[33] D. C. Ludois, K. Hanson, and J. K. Reed, "Capacitive power transfer for slip ring replacement in wound field synchronous machines," in *2011 IEEE Energy Conversion Congress and Exposition*, 2011, pp. 1664-1669.

[34] A. D. Gioia, I. P. Brown, Y. Nie, R. Knippel, D. C. Ludois, J. Dai*, et al.*, "Design of a wound field synchronous machine for electric vehicle traction with brushless capacitive field excitation," in *2016 IEEE Energy Conversion Congress and Exposition (ECCE)*, 2016, pp. 1-8.

[35] S. Hagen, R. Knippel, J. Dai, and D. C. Ludois, "Capacitive coupling through a hydrodynamic journal bearing to power rotating electrical loads without contact," in *2015 IEEE Wireless Power Transfer Conference (WPTC)*, 2015, pp. 1-4.

[36] J. Dai, S. Hagen, D. C. Ludois, and I. P. Brown, "Synchronous generator field excitation via capacitive coupling through a journal bearing," in *2016 IEEE Energy Conversion Congress and Exposition (ECCE)*, 2016, pp. 1-8.

[37] "Rotary transformers developed to replace slip rings and brushes," *Electrical*

Engineering, vol. 80, pp. 469-471, 1961.

[38] E. E. Landsman, "Rotary transformer design," in *1970 IEEE Power Electronics Specialists Conference*, 1970, pp. 139-152.

[39] S. H. Marx and R. W. Bounds, "A Kilowatt Rotary Power Transformer," *IEEE Transactions on Aerospace and Electronic Systems,* vol. AES-7, pp. 1157-1163, 1971.

[40] J. Legranger, G. Friedrich, S. Vivier, and J. C. Mipo, "Design of a Brushless Rotor Supply for a Wound Rotor Synchronous Machine for Integrated Starter Generator," in *2007 IEEE Vehicle Power and Propulsion Conference*, 2007, pp. 236-241.

[41] B. A. Potter and S. A. Shirsavar, "Design, Implementation and Characterisation of a Contactless Power Transfer System for Rotating Applications," in *IECON 2006 - 32nd Annual Conference on IEEE Industrial Electronics*, 2006, pp. 2168-2173.

[42] R. Trevisan and A. Costanzo, "A 1-kW Contactless Energy Transfer System Based on a Rotary Transformer for Sealing Rollers," *IEEE Transactions on Industrial Electronics,* vol. 61, pp. 6337-6345, 2014.

[43] S. Ditze, A. Endruschat, T. Schriefer, A. Rosskopf, and T. Heckel, "Inductive power transfer system with a rotary transformer for contactless energy transfer on rotating applications," in *2016 IEEE International Symposium on Circuits and Systems (ISCAS)*, 2016, pp. 1622-1625.

[44] H. Krupp and A. Mertens, "Semi-analytical loss model for rotary transformers," in *2016 18th European Conference on Power Electronics and Applications (EPE'16 ECCE Europe)*, 2016, pp. 1-10.

[45] K. D. Papastergiou, D. E. Macpherson, and F. Fisher, "A 1kW Phase-Shifted Full Bridge Converter incorporating Contact-less Transfer of Energy," in *2005 IEEE 36th Power Electronics Specialists Conference*, 2005, pp. 83-89.

[46] C. Stancu, T. Ward, K. Rahman, R. Dawsey, and P. Savagian, "Separately excited synchronous motor with rotary transformer for hybrid vehicle application," in *2014 IEEE Energy Conversion Congress and Exposition (ECCE)*, 2014, pp. 5844-5851.

[47] J. N. Weber, A. Rehfeldt, S. A. Vip, and B. Ponick, "Rotary transformer with electrical steel core for brushless excitation of synchronous machines," in *2016 XXII International Conference on Electrical Machines (ICEM)*, 2016, pp. 884-889.

[48] N. L. Zietsman and N. Gule, "Design and evaluation of a 1.2 kVA single phase rotary transformer," in *2016 XXII International Conference on Electrical Machines (ICEM)*, 2016, pp. 1466-1472.

[49] A. Balakrishnan, W. T. Joines, and T. G. Wilson, "Air-gap reluctance and inductance calculations for magnetic circuits using a Schwarz-Christoffel transformation," in *Power Electronics Specialists Conference, 1995. PESC '95 Record., 26th Annual IEEE*, 1995, pp. 1050-1056 vol.2.

[50] N. L. Zietsman and N. Gule, "Optimal design methodology of a three phase rotary transformer for doubly fed induction generator application," in *2015*

IEEE International Electric Machines & Drives Conference (IEMDC), 2015, pp. 763-768.

[51] H. Zhong, L. Zhao, X. Wang, and X. Li, "Design and analysis of a three-phase rotary transformer for doubly fed induction generators," in *2014 IEEE Industry Application Society Annual Meeting*, 2014, pp. 1-6.

[52] H. R. Mohabati, J. S. Moghani, and S. T. Boroujeni, "Complex vector modelling and sequence analysis of the integrated three-phase rotating transformer for design of a symmetrical structure," *IET Electric Power Applications,* vol. 10, pp. 649-657, 2016.

[53] T. A. Stuart, R. J. King, and H. Shamseddin, "Rotary Transformer Design with Fixed Magnetizing and/or Leakage Inductances," *IEEE Transactions on Aerospace and Electronic Systems,* vol. AES-22, pp. 565-572, 1986.

[54] H. Krupp and A. Mertens, "Rotary Transformer Design for Brushless Electrically Excited Synchronous Machines," in *2015 IEEE Vehicle Power and Propulsion Conference (VPPC)*, 2015, pp. 1-6.

[55] H. Yu-Ting, C. Chi-Jen, and S. Wen-Ben, "Finite element analysis on characteristics of rotary transformers," *IEEE Transactions on Magnetics,* vol. 30, pp. 4866-4868, 1994.

[56] J. P. C. Smeets, D. C. J. Krop, J. W. Jansen, and E. A. Lomonova, "Contactless power transfer to a rotating disk," in *2010 IEEE International Symposium on Industrial Electronics*, 2010, pp. 748-753.

[57] J. P. C. Smeets, D. C. J. Krop, J. W. Jansen, M. A. M. Hendrix, and E. A. Lomonova, "Optimal design of a pot core rotating transformer," in *2010 IEEE Energy Conversion Congress and Exposition*, 2010, pp. 4390-4397.

[58] J. P. C. Smeets, L. Encica, and E. A. Lomonova, "Comparison of winding topologies in a pot core rotating transformer," in *2010 12th International Conference on Optimization of Electrical and Electronic Equipment*, 2010, pp. 103-110.

[59] D. Bortis, I. Kovacevic, L. Fässler, and J. W. Kolar, "Optimization of rotary transformer for high-speed applications," in *2013 IEEE 14th Workshop on Control and Modeling for Power Electronics (COMPEL)*, 2013, pp. 1-6.

[60] D. Bortis, L. Fässler, A. Looser, and J. W. Kolar, "Analysis of rotary transformer concepts for high-speed applications," in *2013 Twenty-Eighth Annual IEEE Applied Power Electronics Conference and Exposition (APEC)*, 2013, pp. 3262-3269.

[61] J. Veitengruber, F. Rinderknecht, and H. E. Friedrich, "Preliminary investigations of an inductive power transfer system for the rotor power supply of an electric traction drive," in *2014 Ninth International Conference on Ecological Vehicles and Renewable Energies (EVER)*, 2014, pp. 1-8.

[62] J. Legranger, G. Friedrich, S. Vivier, and J. C. Mipo, "Comparison of Two Optimal Rotary Transformer Designs for Highly Constrained Applications," in *2007 IEEE International Electric Machines & Drives Conference*, 2007, pp. 1546-1551.

[63] K. Veszpremi, "Comprehensive optimization of brushless excitation of

synchronous machine," in *30th Annual Conference of IEEE Industrial Electronics Society, 2004. IECON 2004*, 2004, pp. 1327-1332 Vol. 2.

[64] K. Veszpremi and M. Hunyar, "New application fields of the PWM IGBT AC chopper," in *2000 Eighth International Conference on Power Electronics and Variable Speed Drives (IEE Conf. Publ. No. 475)*, 2000, pp. 46-51.

[65] K. Veszpremi, I. Schmidt, and M. Hunyar, "Optimal operation of the rotating transformer brushless excitation of synchronous machine," in *2003 IEEE International Symposium on Industrial Electronics (Cat. No.03TH8692)*, 2003, pp. 627-632 vol. 1.

[66] K. Veszpremi, M. Hunyar, and I. Schmidt, "PWM AC chopper-ready for higher power applications," in *2001 IEEE Porto Power Tech Proceedings (Cat. No.01EX502)*, 2001, p. 6 pp. vol.4.

[67] M. Kang, P. N. Enjeti, and I. J. Pitel, "Analysis and design of electronic transformers for electric power distribution system," *IEEE Transactions on Power Electronics,* vol. 14, pp. 1133-1141, 1999.

[68] M. M. Swamy, "An Electronically Isolated 12-Pulse Autotransformer Rectification Scheme to Improve Input Power Factor and Lower Harmonic Distortion in Variable-Frequency Drives," *IEEE Transactions on Industry Applications,* vol. 51, pp. 3986-3994, 2015.

[69] R. A. Otto, T. H. Putman, and L. Gyugyi, "Principles and Applications of Static, Thyristor-Controlled Shunt Compensators," *IEEE Transactions on Power Apparatus and Systems,* vol. PAS-97, pp. 1935-1945, 1978.

[70] A. Zuckerberger, D. Weinstock, and A. Alexandrovitz, "Single-phase matrix converter," *IEE Proceedings - Electric Power Applications,* vol. 144, pp. 235-240, 1997.

[71] S. Firdaus and M. K. Hamzah, "Modelling and simulation of a single-phase AC-AC matrix converter using SPWM," in *Student Conference on Research and Development*, 2002, pp. 286-289.

[72] Z. Idris, S. Z. M. Noor, and M. K. Hamzah, "Safe Commutation Strategy in Single Phase Matrix Converter," in *2005 International Conference on Power Electronics and Drives Systems*, 2005, pp. 886-891.

[73] L. Wei, T. A. Lipo, and R. A. Lukaszewski, "Comparison of IGBT Cycling Capabilities for Different AC/AC Topologies," *IEEE Transactions on Industry Applications,* vol. 46, pp. 2475-2483, 2010.

[74] L. Helle, K. B. Larsen, A. H. Jorgensen, S. Munk-Nielsen, and F. Blaabjerg, "Evaluation of modulation schemes for three-phase to three-phase matrix converters," *IEEE Transactions on Industrial Electronics,* vol. 51, pp. 158-171, 2004.

[75] J. Kang, E. Yamamoto, M. Ikeda, and E. Watanabe, "Medium-Voltage Matrix Converter Design Using Cascaded Single-Phase Power Cell Modules," *IEEE Transactions on Industrial Electronics,* vol. 58, pp. 5007-5013, 2011.

[76] P. Fang Zheng, C. Lihua, and Z. Fan, "Simple topologies of PWM AC-AC converters," *IEEE Power Electronics Letters,* vol. 1, pp. 10-13, 2003.

[77] S. H. Hosseini and E. Babaei, "A new generalized direct matrix converter," in

ISIE 2001. 2001 IEEE International Symposium on Industrial Electronics Proceedings (Cat. No.01TH8570), 2001, pp. 1071-1076 vol.2.

[78] G. Aarthi and T. Porselvi, "Modeling and simulation of Single Phase Matrix Converter using PWM," in *2012 International Conference on Computing, Electronics and Electrical Technologies (ICCEET)*, 2012, pp. 168-173.

[79] A. Agarwal, P. Sanjeevikumar, V. Agarwal, S. Rajasekar, V. Fedák, and M. Cernat, "Harmonic minimization in modulated frequency single-phase matrix converter," in *2016 IEEE International Power Electronics and Motion Control Conference (PEMC)*, 2016, pp. 104-109.

[80] E. Babaei, S. H. Hosseini, and G. B. Gharehpetian, "Reduction of THD and low order harmonics with symmetrical output current for single-phase ac/ac matrix converters," *International Journal of Electrical Power & Energy Systems,* vol. 32, pp. 225-235, 3// 2010.

[81] A. Biswas, J. L. Jaiswal, and V. Agarwal, "A study of staircase modulation technique for single phase matrix converter," in *2012 2nd International Conference on Power, Control and Embedded Systems*, 2012, pp. 1-6.

[82] J. Sandoval, H. Krishnamoorthy, P. Enjeti, and S. Choi, "Reduced Active Switch Front End Multi-Pulse Rectifier with Medium Frequency Transformer Isolation," *IEEE Transactions on Power Electronics,* vol. PP, pp. 1-1, 2016.

[83] C. Gu, H. S. Krishnamoorthy, P. N. Enjeti, and Y. Li, "A novel medium-frequency-transformer isolated matrix converter for wind power conversion applications," in *2014 IEEE Energy Conversion Congress and Exposition (ECCE)*, 2014, pp. 1070-1077.

[84] P. Drabek, Z. Peroutka, M. Pittermann, and M. Cedl, "New Configuration of Traction Converter With Medium-Frequency Transformer Using Matrix Converters," *IEEE Transactions on Industrial Electronics,* vol. 58, pp. 5041-5048, 2011.

[85] B. Bednar, P. Drabek, and M. Pittermann, "The comparison of different variants of new traction drives with medium frequency transformer," in *2016 International Symposium on Power Electronics, Electrical Drives, Automation and Motion (SPEEDAM)*, 2016, pp. 1172-1177.

[86] M. Pittermann, P. Drabek, and B. Bednar, "Single phase high-voltage matrix converter for traction drive with medium frequency transformer," in *IECON 2015 - 41st Annual Conference of the IEEE Industrial Electronics Society*, 2015, pp. 005101-005106.

[87] M. Los, P. Drábek, and M. Cédl, "The control algorithms of traction drive with medium-frequency transformer and two modules of single phase matrix converters," in *Proceedings of 14th International Power Electronics and Motion Control Conference EPE-PEMC 2010*, 2010, pp. T3-143-T3-146.

[88] M. Pittermann, P. Drabek, and M. Cedl, "The traction drive topology using the matrix converter with middle-frequency transformer," in *2008 13th International Power Electronics and Motion Control Conference*, 2008, pp. 372-376.

[89] D. Al-Nimma and M. Altamemi, "Modeling and simulation of a single phase to

single phase (SPSP) matrix converter with an input filter and a clamp circuit," in *The 2nd International Conference on Control, Instrumentation and Automation*, 2011, pp. 1211-1216.

[90] P. W. Wheeler, J. Rodriguez, J. C. Clare, L. Empringham, and A. Weinstein, "Matrix converters: a technology review," *IEEE Transactions on Industrial Electronics,* vol. 49, pp. 276-288, 2002.

[91] W. Lixiang, T. A. Lipo, and C. Ho, "Matrix converter topologies with reduced number of switches," in *2002 IEEE 33rd Annual IEEE Power Electronics Specialists Conference. Proceedings (Cat. No.02CH37289)*, 2002, pp. 57-63 vol.1.

[92] C. Klumpner and F. Blaabjerg, "Experimental evaluation of ride-through capabilities for a matrix converter under short power interruptions," *IEEE Transactions on Industrial Electronics,* vol. 49, pp. 315-324, 2002.

[93] H. Chen, A. Prasai, R. Moghe, K. Chintakrinda, and D. Divan, "A 50-kVA Three-Phase Solid-State Transformer Based on the Minimal Topology: Dyna-C," *IEEE Transactions on Power Electronics,* vol. 31, pp. 8126-8137, 2016.

[94] Y. Suh and T. A. Lipo, "Field excitation scheme using a machine-side 4-leg converter in MW-range WRSG wind turbine systems," in *2017 IEEE Energy Conversion Congress and Exposition (ECCE)*, 2017, pp. 3316-3323.